Application of digital holography for metrology of inclusions in a droplet

Wisuttida Wichitwong

Thèse

présentée à
l'Institut National des Sciences Appliquées de Rouen
(INSA de Rouen)

En vue de l'obtention du grade de Docteur de l'Institut National des Sciences Appliquées de Rouen

Discipline : Physique - Spécialité : Optique

par

Wisuttida WICHITWONG

Soutenue le 16 Mars 2015

APPLICATION OF DIGITAL HOLOGRAPHY FOR METROLOGY OF INCLUSIONS IN A DROPLET

Directeurs de thèse : Marc BRUNEL, Gérard GREHAN

Pascal PICART	Professeur à l'université du Maine	Rapporteur
Fabrice LEMOINE	Professeur à l'université de Lorraine	Rapporteur
Sébastien COËTMELLEC	Maître de conférences à l'université de Rouen	Co-encadrant
Fabrice LAMADIE	Ingénieur de recherche à CEA-Marcoule	Examinateur

Thèse

présentée à
l'Institut National des Sciences Appliquées de Rouen
(INSA de Rouen)

En vue de l'obtention du grade de Docteur de l'Institut National des Sciences Appliquées de Rouen

Discipline : Physique - Spécialité : Optique

par

Wisuttida WICHITWONG

Soutenue le 16 Mars 2015

APPLICATION OF DIGITAL HOLOGRAPHY FOR METROLOGY OF INCLUSIONS IN A DROPLET

Directeurs de thèse : Marc BRUNEL, Gérard GREHAN

Pascal PICART	Professeur à l'université du Maine	Rapporteur
Fabrice LEMOINE	Professeur à l'université de Lorraine	Rapporteur
Sébastien COËTMELLEC	Maître de conférences à l'université de Rouen	Co-encadrant
Fabrice LAMADIE	Ingénieur de recherche à CEA-Marcoule	Examinateur

ACKNOWLEDGEMENTS

My research was carried out during October 2011 to December 2014 at CORIA (COmplexe de Recherche Interprofessionnel en Aérothermochimie) laboratory in Rouen, France. This work was supported by Ministère de l'Enseignement Supérieur et de la Recherche (MESR) of the French government. It would not has been possible for me to start my thesis without this financial support.

As a graduated student in nanomaterials and optics, my knowledge of digital holography was on general level to begin with this thesis. However, I am really fortunate to have three supervisors during my Ph.D. work. All of them are really kind and take a lot of time to pay attention for me. They are complementary to each other. It is my greatest pleasure to express my gratitude to Marc Brunel, Sébastien Coëtmellec, and Gérard Gréhan. I enjoyed to do the research with them.

Marc is a professor at University of Rouen and a researcher at CORIA laboratory. He is a specialist in laser diagnostic as out of focus imaging. He always used very simple sentences to describe the difficult points of my work. When I had experimental problems or coding problems, he always spent his valuable time and offered inspirational advices and solutions to me. I remember that the first question he asked me when I first came here was "Do you know what is the Gaussian beam?" and my answer was "no" at that time. Then he tried to explain me the Gaussian beam and its parameters. After that stupid answer, I asked to myself "What should I do next if I want to grow up?". From that period, I knew that where I was in the route to my thesis goal. Thank to him to let me know myself better and I think it is a very important view for a person like me. Besides this, I would like to thank him again for his helps to have a publication in *Optics Communication* and to allow me to attend a conference "Digital holography and 3-D imaging 2014" in Seattle, U.S.A.

Sébastien is a lecturer at University of Rouen and a researcher at CORIA. He specializes in solving mathematics related to optics problems . He always looks happy when talking about theoretical development and was excited all the time with my experimental results. Discussion with him tends to be highly motivative and gaves me a positive view of Mathematics. I also thank him for his helps to have another publication in *Journal of European Optical Society Rapid Publication*. He is patient enough to explain me the development of the new model that was proposed in this publication. He never gave up to describe when I asked him the same question for many times. I enjoy to speak French with him too.

Gérard is a CNRS (Centre National de la Recherche Scientifique) researcher and the director of Optics department at CORIA. He is very kind. He always helps me to see the better picture of this project. This is helpful for an inexperienced stu-

dent who can easily get lost in the vast field of knowledge. He always gives me the advices for giving a presentation about my work and spent his valuable time to listen my presentation. At the first time I came here, he gave a lot of advices for living in France including housing, food, language, and studying.

I sincerely wish to express my gratitude to the reviewers for their useful suggestions. Special thanks to Dr. Sawitree Seangkeaw who gave me an opportunity to be a Ph.D. student here. When I could not find some specific equipements, she always let me borrow them or gave me the other solutions. A lot of her advices in daily life were very useful. She is the best sister for me when I stay in Rouen. Many thanks to Danial Allano for his help when using CCD cameras at the beginning of my thesis work. I have learned a bit of French from him. I am also thankful to Denis Lebrun. He is the one who helped me to answer the questions when Marc or Sebastien were absent.

Thanks to all of my friends during my Ph.D. for spending time together. Special thanks to Dr. Huanhuan Shen, a previous Ph.D. student at CORIA, for her advice and help in finding some optical elements. Thanks to Dr. Clément Remacha, a previous PhD student at CORIA, for answering my questions. I also would like to thank Darawan Pejchang for her advices too. Besides this, I would like to thank to CORIA laboratory and all members of the CORIA.

Finally, I would like to thank my parents for giving birth to me and let me come here to have a new experience. Even though they do not know about physics, they always encourage me. Thanks to both of them for believing in me. Thanks to my brother and sister too. I always miss them.

ABSTRACT

In this thesis, the digital in-line holography (DIH) is the main optical method used to analyze inclusions in a droplet. The digital in-line holography is used to characterize the inclusions in terms of of their size, their 3D position, and their trajectories inside the droplet. Since the particles are located within a droplet, the incident wavefront is changed before it illuminates the inclusions. The challenge of this work has two points: first to take into account the shape of the droplet in the holographic model and secondly to extend the analysis to the transparent inclusions (phase object). To describe the hologram recorded by the CCD sensor, the Huygens-Fresnel integral and the ABCD matrix formalism were used. In this model, we introduce the Zernike polynomials to describe the transmission function of a particle. For the analysis of holograms, the 2D fractional Fourier transformation (2D-FRFT) is used to reconstruct the image of inclusions and in this case the size and their 3D position of the inclusions are performed. The trajectories of the inclusions in the drop are possible tracked with a long exposure shutter speed of the CCD. We also proposed a new simulation to describe objects of any phases and opaque particles. For this simulation, the same methods of reconstruction were used. In the case of micro-channel inclusions inside a cylindrical geometry such as a pipe, the interferometric imaging of multi-core pipe is proposed. In this case, summation of Dirac delta distribution, located along a line, introduced into the generalized Fresnel integral allows us to get a good agreement between the experiment and the simulation.

Keywords: Digital in-line holography, droplet with inclusions, fractional Fourier transform, Zernike polynomials

RÉSUMÉ

Dans cette thèse, l'holographie numérique dans l'axe (DIH) est la principale méthode optique utilisée pour analyser des inclusions dans une gouttelette. L'holographie numérique dans l'axe est utilisée pour caractériser des inclusions du point de vue de leur taille, leur position 3D et leur trajectoire à l'intérieur de la gouttelette. Comme les particules sont situées à l'intérieur d'une gouttelette, le front d'onde incident sur l'inclusion est modifié avant qu'il l'illumine. Le défi de ce travail est double : premièrement de prendre en compte la forme de la gouttelette dans le modèle d'holographie et deuxièmement détendre l'analyse aux inclusions transparentes (type objet de phase). Pour décrire l'hologramme enregistré par le capteur CCD, l'intégrale d'Huygens-Fresnel et le formalisme des matrices ABCD ont été utilisés. Dans ce modèle, nous introduisons les polynômes de Zernike pour décrire la fonction de transmission d'une particule. Pour l'analyse des hologrammes, l'outil mathématique de la transformation de Fourier fractionnaire 2D (2D-FRFT) est utilisé pour restituer l'image des inclusions et dans ce cas une mesure la taille de l'inclusion et de sa position 3D sont réalisées. Les trajectoires des inclusions dans la goutte est possible avec un long temps de pose de l'obturateur du capteur CCD. Nous avons également proposé un nouveau modèle pour décrire des objets de phases quelconque et des particules opaques. Pour ce nouveau modèle, les mêmes procédés ont été utilisés. Dans le cas d'inclusions filiformes à l'intérieur d'une géométrie cylindrique comme un canal, une méthode de simulation d'imagerie interférométrique multi-coeurs est proposée. Dans ce cas, une somme de distributions de Dirac, localisées le long d'une droite, introduite dans l'intégrale de Fresnel généralisée (c'est-à-dire le formalisme des matrices ABCD et l'intégrale de Fresnel) permet d'obtenir un bon degré de similitude entre l'expérience et la simulation.

Mots-clés: l'holographie numérique dans l'axe, gouttelettes avec inclusions, transformée de Fourier fractionnaire, polynômes de Zernike

CONTENTS

LIST OF FIGURES

LIST OF TABLES

1. INTRODUCTION

1.1 General introduction

The detection and characterization of particles inside droplets play an important role in many areas such as biology, climatology, public health, physics, etc. In biology, the foreign bodies or other organisms enclosed by a cell or a liquid can be considered as inclusions inside a droplet [1, 2, 3]. Those foreign bodies or other entities can live for a longer period within the protective liquid shell. In public health, the droplet can be considered as an expiratory aerosol and the inclusion can be considered as a bacterial cell inside the expiratory droplet [6, 7], (see Fig. 1.1). In this example in public health, the size of bacterial cellsl is important in their dispersion which is related to the spread of infectious respiratory diseases in the air. The insoluble particles inside the droplets of clouds are interesting for climatologists [9] for prediction of the weather or determination of the atmospheric aerosol composition for climate modelling and the detection of biological weapons agents in military applications [10]. For physicists, the scattering problem of water droplets with inclusions was studied by using Lorenz-Mie theory. The study of droplets or spray has many applications in industry to. For example, in the pharmaceuticals industry, spray drying or droplet drying is the key to analysing powder's properties [11]. Another application is in coating surface technology, as in [12, 13, 14, 15]. The original properties of the coated substrate are changed to the desired properties. In power plants, in case of an accident, each droplet from the spray can be used to reduce hazard and to limit the contamination to humans, animals, and the environment [16, 17]. Considering the wide variety of applications of droplets with inclusions, study of this topic is of great interest.

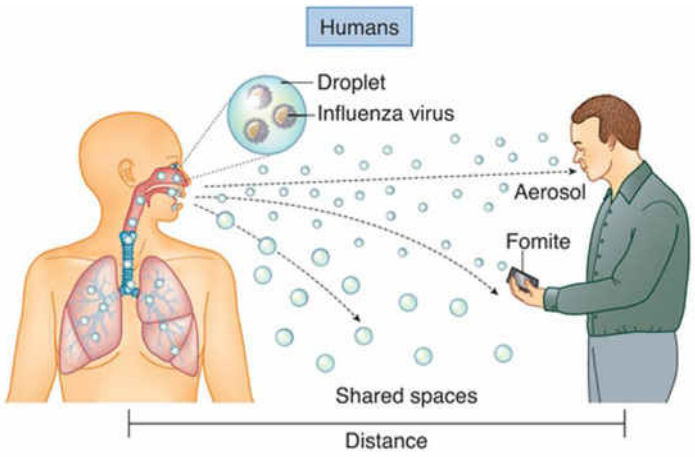

Fig. 1.1: The spread of disease via respiratory droplets [8].

In nuclear power plants, the cooling tower is used to reduce the temperature of wasted heat emitted to the atmosphere. In cooling tower, a water spray may be used to reduce the temperature of the waste. In the case of an accident, the water spray may be used to reduce the spread of radioactive particles that have leaked from the plant. Therefore, an understanding of the complex interaction between the water droplets and solid particles in the cooling tower is necessary and a fundamental understanding of the behaviour of particles captured by a droplet is essential. When particles enter the droplet, they will follow a fluid flow inside the droplet if they are small enough. One way that we can study a droplet with inclusions is by characterizing the properties of the inclusions. Then questions such as "How can we characterize the inclusions in a droplet?" and "Which method can we use?" appear. The answers are in the following paragraphs.

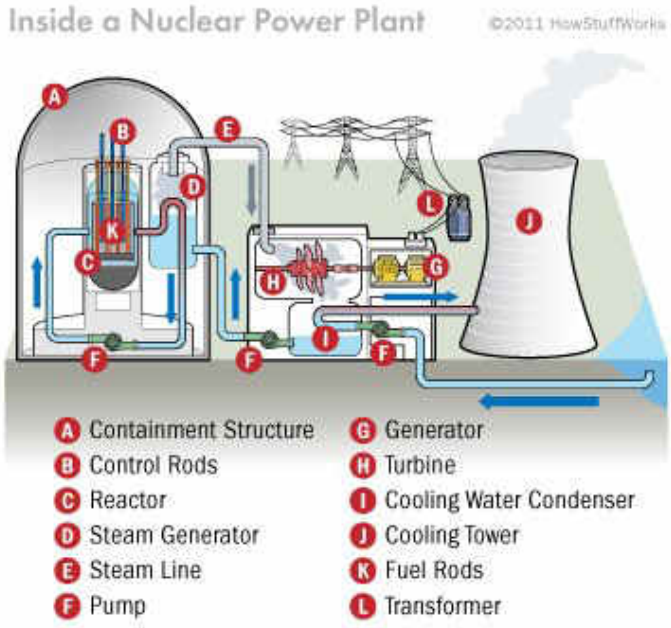

Fig. 1.2: Interior of a nuclear power plant*

An optical technique is a good choice to characterize the inclusion because it is a non-invasive and non-contact method for the particle. With the optical method, the particle does not change its original properties. Many kinds of optical techniques can be used to characterize the particle, such as particle imaging velocimetry (PIV), holography, scattering under Lorenz-Mie theory, etc. However, those techniques cannot give the actual 3D location of the particle except for the holography technique. Therefore, we choose holography for particle characterization.

In this thesis, characterization of inclusions inside a water droplet is investigated by digital in-line holography (DIH). The characterization process with the DIH technique allows us to measure the size, 3D location, and trajectories of the inclusions inside a droplet where the astigmatic aberration is introduced. The challenge of this problem is to take the effect of the droplet as a curved interface which deforms the wavefront of the incident wave. Without a droplet, the size and 3D location of the particle dis-

*http://sphweb.bumc.bu.edu/otlt/mph-modules/ph/ph709_c_transmission/ph709_c_transmission4.html

persed in the air or in the measured volume can be easily found because the wavefront of the incident beam is not modified or deformed. However, this problem is resolved by the DIH technique developped in CORIA.

1.2 Literature review

In this thesis, digital in-line holography is selected. Digital in-line holography is suitable for the visualization of particles inside a volume of interest. One advantage of the in-line configuration or Garbor hologram is the simplicity of the set-up. This technique can give the real 3D position of the inclusion in the droplet. Furthermore, this technique can track the particle's trajectory by analysing the holograms frame by frame or using a long exposure time of the CCD sensor, which will be presented later in this thesis. Before going into the details of the digital in-line holography used in this work, I would like to introduce some related techniques frequently used in flow measurement and in particle sizing.

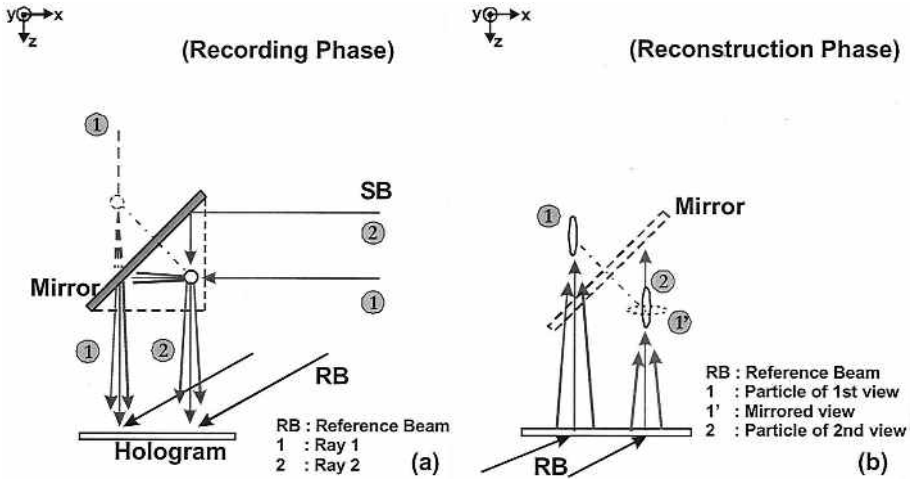

Fig. 1.3: Set-up of particle image velocimetry: (a) recording phase and (b) reconstruction phase [18].

Particle image velocimetry (or PIV) is an optical technique of flow visualization. This technique measures flow velocity by adding seed particles and measuring their velocity field in the measurement volume [19]. The seeded particles are assumed to follow the fluid flow. The degree to which the seeded particles follow the flow is represented by the Stokes number. The motion of the seeded particle is used to calculate the speed and direction of movement of the flow system of interest. The method makes it possible to measure the two-dimensional cross-section of the flow field, as presented in many applications [20, 21, 22, 23]. However, the density of the particles affects the motion of the fluid. Fig.1.4 shows an example of a 2D cross-section of the flow inside a droplet [20].

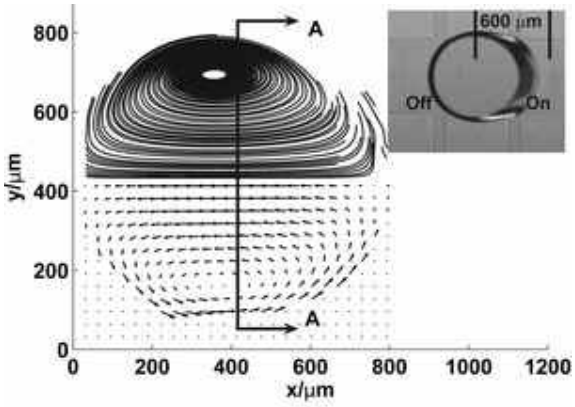

Fig. 1.4: The slab velocity field at $z = 148\mu m$ inside a droplet is shown in the bottom half and its streamline is shown in the top half [20].

Another technique used to measure flow is laser Doppler velocimetry. Laser Doppler velocimetry or Laser Doppler anemometry (LDA) is an optical technique that uses the Doppler effect on a laser beam to measure the velocity of small particles moving in gas, liquid, flames, in a domain such as combustion [24], channels [25, 26], wind or water tunnels [27], and in various areas of scientific and industrial research. The basic idea of LDA is to measure the velocity of small particles moving in the flow. If these particles are small enough, their velocity is assumed to be the velocity of that fluid. For a review of LDA, see [28].

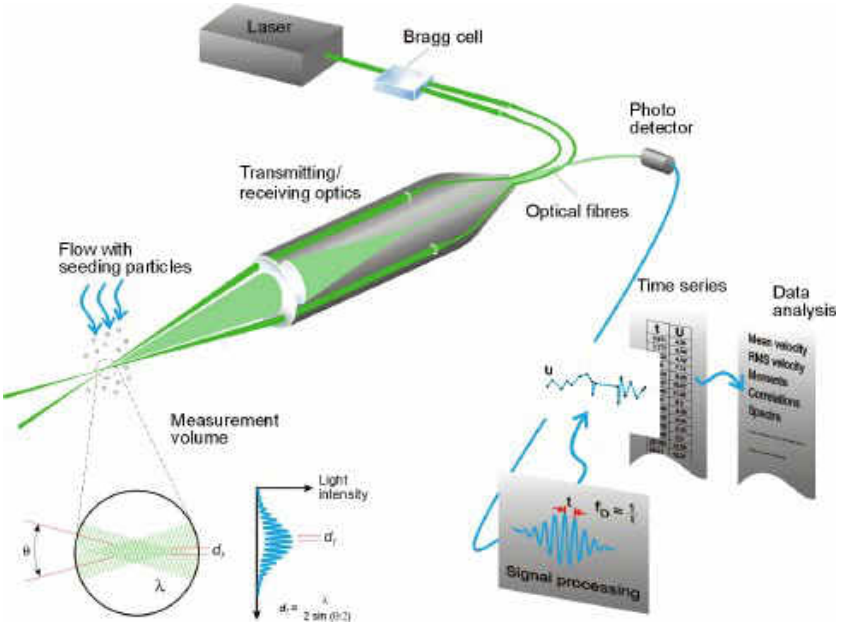

Fig. 1.5: Set-up of laser Doppler anemometry [29].

In aeronautical research, the flow velocity around the airplane model has been measured by the LDA technique in a water tunnel. The values of velocity are used to

determine the pressure coefficient along the wing's center span and along the cockpit [27].

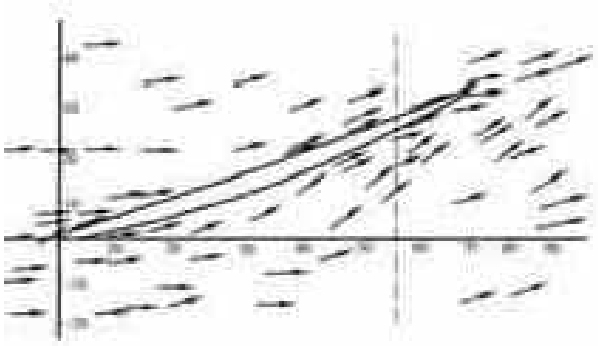

Fig. 1.6: Velocity vector around the hydrofoil with LDA measurement [27].

Fig.1.6 shows the velocity vectors of the upper surface of the wing model in a hydrofoil for angle of attack $\alpha = 25°$ and velocity $v = 5.32m/s$. This kind of study plays an important role in aeronautical research.

Many research groups in spray analysis use different techniques in order to measure the size and position of the droplet, such as the rainbow technique and ILIDS. Interferometric laser imaging for droplet sizing (ILIDS) was introduced in early 1986 by Koening et al. The droplets are illuminated by a light source and a CCD sensor is at an off-axis position, as shown in Fig. 1.7. The reflected and refracted rays are visible on the droplet surface. These two rays observed on the droplet surface are called glare points. When they are out of focus, an interference pattern becomes visible. If the two glare points are in focus, two bright dots can be observed on the sensor.

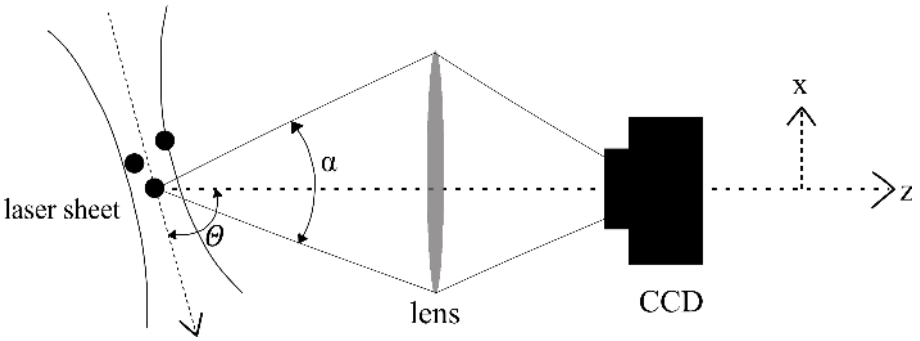

Fig. 1.7: Set-up of ILIDS [30].

For the rainbow technique, the scattered light at the rainbow angle is recorded. A fast Fourier transform (FFT) algorithm is used to analyse the pattern of the fringes. However, this technique can measure the size, refractive index, temperature, and the relative position, but not the real 3D position of the droplets. The experimental set-up of the rainbow technique is presented in Fig. 1.8.

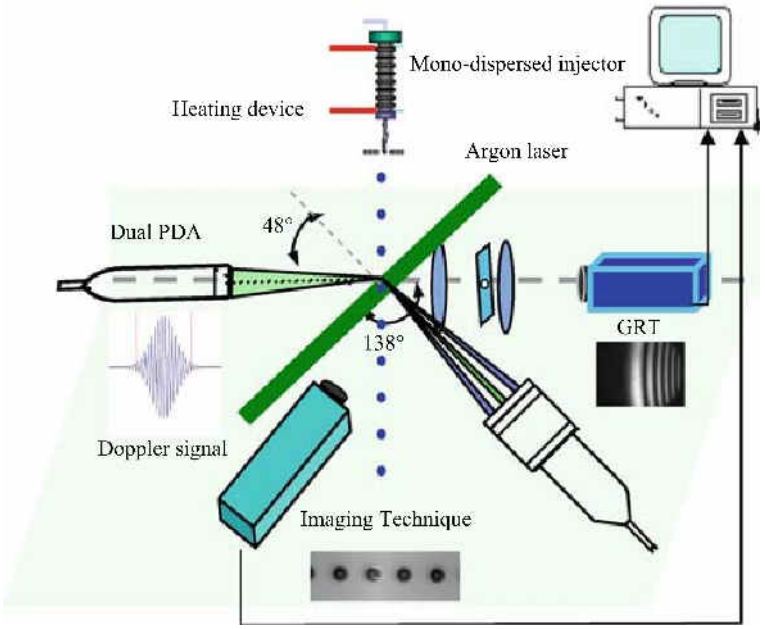

Fig. 1.8: Set-up of rainbow technique [31].

Holography was first invented in 1948 by Denis Gabor [32]. In a Gabor hologram, the total information has to be used, not only the amplitude, as in usual optical imaging, but also the phase. The phase of the object wave can be reconstructed optically but not measured directly. Gabor's original set-up (in-line configuration) is depicted in Fig. 1.9.

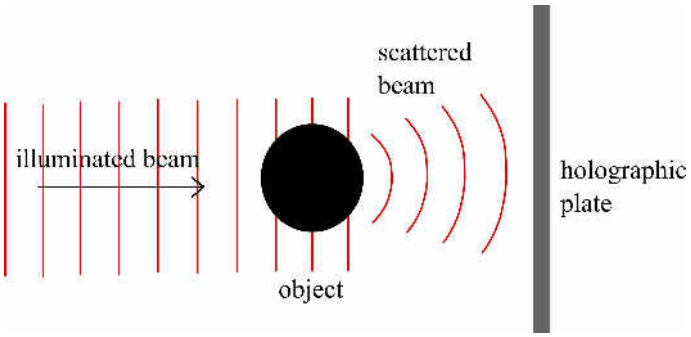

Fig. 1.9: Set-up of Gabor's hologram for recording.

His set-up was a two-step lensless imaging process in which the first step recorded an interference pattern generated by the interaction of scattered light from an object wave and a reference wave. The resulting interference pattern is called a "*hologram*". The second step in the procedure was the reconstruction of the wave field or image and this process was done through the diffraction of a coherence beam by the developed hologram.

However, the Gabor hologram caused a twin image. Leith and Upatnieks proposed off-axis holography [33, 34] to separate the two images and the reconstuction wave spatially. With the development of computer technology, computer-generated holography

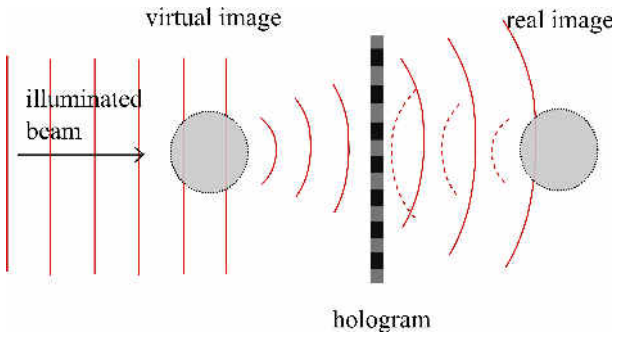

Fig. 1.10: Reconstruction process of Gabor's hologram.

(CGH) was invented instead of the classical holography. The hologram is recorded optically. Then, the hologram is analysed numerically and the object is reconstructed numerically [35]. Through the development of charged coupled devices (CCDs), the hologram is recorded on the CCD and is called a digital hologram. The intensity and phase of the electromagnetic wave can be measured, stored, and transfered into a computer for the recording and reconstruction process. CCDs are used instead of the holographic plates in classical holography. Since the development of digital holography in 1969, many significant applications have been studied. Some important studies [36] are:

- improvements of the experimental techniques and of the reconstruction algorithm
- applications in deformation analysis and shape measurement
- development of phase-shifting digital holography
- applications in imaging, particle-tracking and microscopy
- applications in encryption of information
- development of digital light-in-flight holography and other short-coherence-length applications
- combination of digital holography with heterodyne techniques
- development of methods to reconstruct the three-dimensional object structure from digital holograms
- development of comparative digital holography
- use of a digital mirror device (DMD) for optical reconstruction of digital holograms.

1.2.1 Holographic interferometry

Holographic interferometry (HI) is a method to detect optical path length variations which are caused by the object. HI is a non-invasive and non-contact method with very high sensitivity. This technique can be applied to stress, strain and vibration analysis. It can be used to measure optical path length variations in transparent media; for example, to visualize and analyse fluid flow. It can also be used to generate a fringe pattern corresponding to contour forms of the surface. In the double exposure method, two coherence waves illuminate two different states of the object and then interfere. The recording process of double exposure holography is presented in Fig. 1.11. The first exposure represents the object in its primary state, while the second

represents the object in its deformed state. The result is two overlapping waves which form a fringe pattern that contains the changes in optical path length.

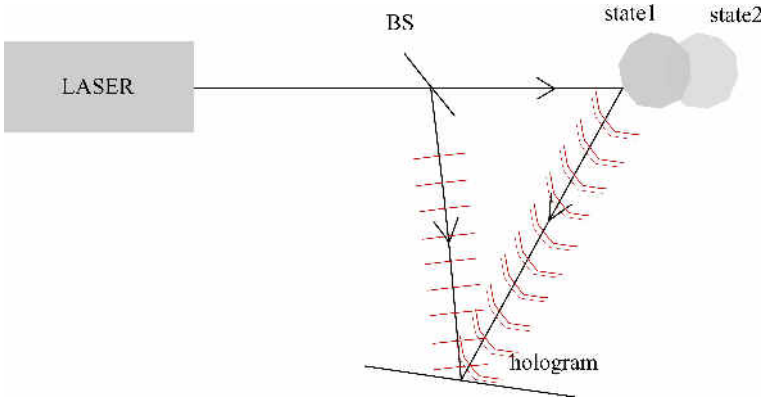

Fig. 1.11: Recording of a double exposed hologram.

When the hologram is illuminated by the reference wave, the reconstructed virtual image coincides with the object. In real-time technique, this allows us to observe instantaneously the effects of small changes in displacement on an object. This is done by superimposing a hologram over the object itself.

1.2.2 Digital holographic interferometry

The interferogram in HI is created by the superposition of two waves that are scattered from an object in different states. The interference fringe carries the information about phase change between the two waves in the form of bright and dark fringes. Digital holographic interferometry (DHI) is like conventional HI but using the CCD camera. The hologram image in DHI is recorded by the CCD and then it is restored in computer memory and reconstructed numerically. However, the interference phase cannot be extracted straightforwardly from a single hologram. It is usually extracted from three or more holograms by a phase-shifting method. The configuration of DHI is shown in Fig. 1.12.

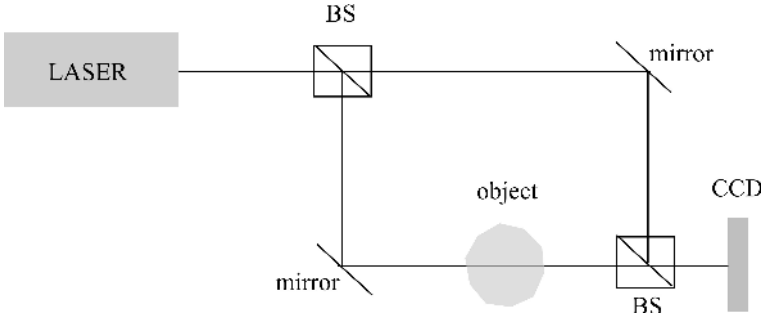

Fig. 1.12: DHI set-up.

The DHI technique can be used to determine the mechanical and thermal properties of a material, such as conductivity [37], Young's modulus [38], Poisson ratio [38], and thermal expansion coefficient[39]. Furthermore, it can be applied to shape measurement [38], refractive index measurement [40] and so on.

1.2.3 Digital holographic microscopy

Digital holographic microscopy (DHM) is digital holography applied to microscopy. The difference between DHM and conventional microscopy is that DHM does not record the projection image of the object. In DHM, the light wave field information from the object is recorded as a hologram for which a numerical reconstruction is required. The set-up of DHM is shown in Fig. 1.13.

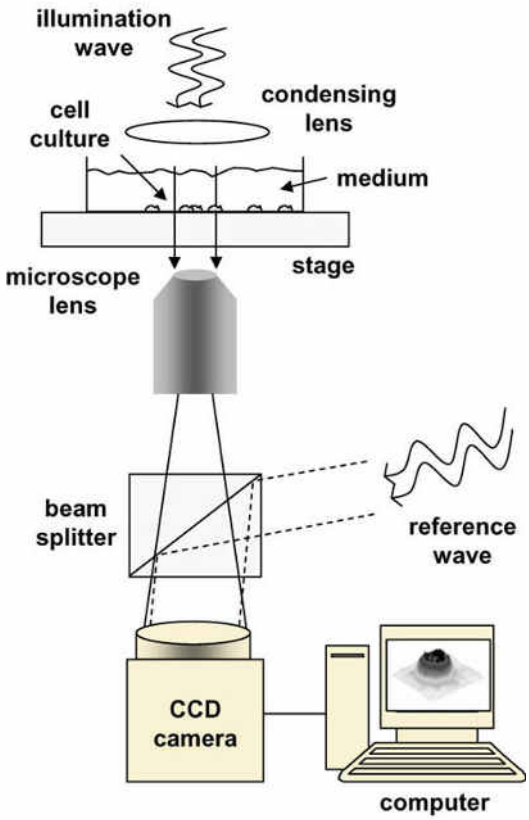

Fig. 1.13: DHM set-up for the characterization of living tumor cells [41].

The depth of field of the image decreases with increase of the magnification factor. Due to the high magnification in microscopy, the depth of field is limited. DHM has been successfully applied in many areas [41, 42], especially in biology.

In this thesis, digital in-line holography (DIH) is used to record the hologram of inclusions inside a droplet. In this case, the droplet introduces a lens effect to the diffraction patterns of the particles inside. To analyse the holograms, the 2D-FRFT with an appropriate fractional order is used.

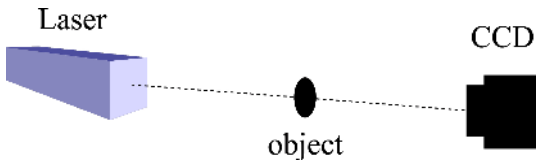

Fig. 1.14: Set-up of in-line holography.

Many methods for numerical reconstruction are proposed such as Fresnel transformation, the convolution approach, wavelet transform, Wigner distribution, and fractional Fourier transform, which is a generalized Fourier transform.

The Fresnel transformation enables reconstruction of the wavefield in a plane behind the hologram or in the plane of the real image. The Fresnel integral is the most often used numerical method for hologram reconstruction in digital holography. However, images reconstructed with this method always include different aberrations because of the neglect of the fourth- and higher-order phase terms in the calculation. The quality of the reconstructed image can be degraded by induced aberrations. The direct numerical processing of the Fresnel integral is more time-consuming than the convolution approach [43].

The convolution approach is a mathematical tool used to apply spatially filters to signals in image processing. The basic idea is that a window of some finite size and shape is scanned across the image. The output pixel value is the weighted sum of the input pixels within the window, where the weights are the values of the filter assigned to every pixel of the window itself. The window with its weights is called the convolution kernel. The kernel is a matrix of fixed numbers. The kernel is applied to the image by placing over the image to be convolved and sliding it around to center it over every pixel in the original image. The pixel values from the original image are multiplied by the kernel number. The sum of all these products is the output pixel value. Then this result is placed into the new image at the center position of the kernel. The kernel is then translated to the next pixel and the process is repeated until all the pixels have been done. One advantage of the convolution approach of reconstruction is an increase of lateral resolution or the digital zoom of the reconstructed image. Another advantage of the convolution approach is interesting since it allows the full calculation by Fast Fourier Transform (FFT) with high speed reconstructions [44, 45].

In conventional Fourier transform, the basis functions are sinusoidal functions. Such functions can provide frequency information but not temporal information. Unlike the conventional Fourier transform, the wavelet transform decomposes signals over dilated and translated functions called *wavelets*, which transform a continuous func-

tion into a highly redundant function. With wavelet transform, both frequency and temporal information can be obtained [46]. Wavelet transforms have advantages over traditional Fourier transform for representing functions that have discontinuities and sharp peaks, and for accurately deconstructing and reconstructing finite, non-periodic and/or non-stationary signals. Wavelet transform is one of a best tools to determine where the low frequency and high frequency areas are. There are two types of wavelet transforms: discrete wavelet transforms (DWTs) and continuous wavelet transforms (CWTs). The continuous two-dimensional wavelet transform is defined as

$$W_f(s,\theta,a,b) = \int_{-\infty}^{\infty} I(x,y)\Psi^*_{s,\theta}(x,y,a,b)\,dx\,dy, \tag{1.1}$$

where

$$\Psi_{s,\theta}(x,y,a,b) = \frac{1}{s^2}\Psi\left(\frac{x-a}{s}, \frac{y-b}{s}, \theta\right).$$

$I(x,y)$ is the intensity distribution recorded in the CCD plane. $s(>0)$ and θ are scale and rotation parameters. The shift parameters related to position are represented by a and b for the x and y directions, respectively. With wavelet transformation, the scaling and rotating parameters should be considered.

The concept of Wigner or Wigner-Ville distribution (WVD) is related to time-frequency representations of non-stationary signals. The approach was originally developed by Wigner for use in physics, but it was later applied to signal processing by Ville. This method can be introduced to phase-unwrapped problems [48]. WVD exhibits the highest signal energy concentration in the time-frequency domain for linear modulated signals. The main problem in this method is in the case of nonlinearly modulated signals. Furthermore, noise may appear in the time-frequency plane even though there is no noise in the signal [49]. The WVD belongs to a large class of bilinear distributions known as the Cohen's class. The WVD of a 2D image is a 4D function that includes Fourier transformation for every point of the original image. The discrete WVD of a 1D signal is periodic in the frequency variable with a period of π while the periodicity of the Fourier spectrum is 2π. This can be considered as the signal oversampling by a factor of 2. To overcome the problems of aliasing and cross terms in discretization problem, pseudo Wigner distribution (PWD) is used. The PWD has two smoothing windows: a spatial averaging window and a spatial-frequency averaging window. The cross terms problem can be diminished by spatial and spatial-frequency smoothing [50]. The used of Wigner distribution function (WDF) has already been proposed for the extraction of three-dimensional locations from holograms, as presented in [51].

Fractional Fourier transform (FRFT) is a generalization of classical Fourier transform. Wave propagation in optics can be interpreted by FRFT. For fractional Fourier transform in digital holography, one fractional order is needed for satisfactory reconstruction, instead of using the other parameters such as distance, wavelength, scaling parameter and resolution of the recording sensor required in the Fresnel reconstruction. Many studies have found that Fresnel diffraction can be expressed as an FRFT

whose orders depend on the distance between the object and the observation field [52, 53]. The FRFT was used initially as a mathematical tool in quantum mechanics [54] in 1980. Then the FRFT was used in various applications for signal analysis. In all time-frequency representations, it normally uses a plane with two orthogonal axes which correspond to time and frequency. If a signal $x(t)$ is represented along the time axis and its classical Fourier transform $X(f)$ is represented along the frequency axis, then the Fourier transform operator F can be visualized as a change in the representation domain of the signal that corresponds to the counterclockwise rotation of the axis by an angle $\pi/2$. Unlike the classical Fourier transform, the rotation of the signal in FRFT does not need to be a multiple of $\pi/2$.

Recently, FRFT has been combined with digital holography and used in several applications, such as analysis of the diffraction patterns of a particle field hologram [55, 56] generated by elliptic and astigmatic Gaussian beams [57], optical information security [58, 59], visualization of the particle in a thick pipes system [60], and reconstruction of particle holograms recorded with a pulsed laser beam [61, 62, 63]. A two-dimensional FRFT of a function $f(x, y)$ of order ($\alpha = a\pi/2$) is given by $F(x_\alpha, y_\alpha)$ as in [55, 56]

$$F(x_\alpha, y_\alpha) = K \int\int f(x, y) \times \exp\left(j\pi \frac{x^2 + y^2 + x_\alpha^2 + y_\alpha^2}{\lambda f_1 \tan\alpha} - 2j\pi \frac{xy + x_\alpha y_\alpha}{\lambda f_1 \sin\alpha}\right) dx\, dy.$$

(x, y) and (x_α, y_α) represent the space and fractional domain coordinates, respectively. The parameter K is a complex constant. In the case of the reconstruction of the hologram, the function $f(x, y)$ corresponds to the recorded intensity at CCD sensor. f_1 is the focal length of the lens in the optical set-up type I, which is proposed by Lohmann [64] and λ is the wavelength of the reconstructed wave.

1.3 Objectives

In this thesis, digital in-line holography is used to analyse inclusions inside a droplet. In the classical case where the particles are suspended in the air or other fluids, the diffracted wavefront is deformed due to the effect of the particle itself, whereas the diffracted wavefront in the case of particles inside a droplet is deformed due to the particle itself and the curvature of the droplet surrounding the particles. Therefore, in this thesis, the effect of the droplet is taken into account by considering the droplet as a lens. With ABCD formalism, the inclusions located near the optical axis is considered.

The principal objective of this study is to show the possibility of the digital in-line holography developed by our group in CORIA to visualize and characterize inclusions inside droplets. The model already developed is well adapted for the visualization of particles in micro-pipes, as shown in the previous work [60]. The aim is to compare the results of the droplet-inclusion system obtained from simulation and experiment for size, 3D position , and the trajectories of inclusions inside a droplet. In addition, a clear differentiation of opaque and phase objects is needed for better interpretation

of the results obtained with different types of aerosol particles.

In chapter 2, the fundamental knowledge related to digital holography is summarized to give the reader a broader idea. In chapter3, a model of an aberrating object at the center of a droplet is studied. Here the Zernike polynomial is used to represent the object's transmission function. The resulting intensity recorded by a CCD sensor is determined under ABCD matrix formalism. Next, a model of abitrarily shaped non-center objects is presented in chapter 4. Both opaque and constant phase objects with irregular shapes are studied. The simulational process for generating constant phase objects is described. In chapter 5, the simulated and experimental holograms and reconstructed images of different sizes of inclusions are presented. Next, the visualization of particles inside a droplet under a long exposure regime is studied in chapter 6. With this model, the 3D trajectories of the inclusions inside a droplet are achieved. Chapter 7 is a study on interferometric imaging of multi-channel pipes. In this chapter, the interference patterns introduced by many channels in a pipe are analyzed. Finally, the conclusions and perspectives are presented in chapter 8.

2. BASIC BACKGROUNDS

2.1 Digital holography

Holography is a non-invasive imaging technique which basically consists of a laser, an object of interest, and a recording medium, *e.g.* a photographic plate. The laser illuminates the object. The light diffracted by the object is called the object wave. The non-diffracted part is called the reference wave. When the two waves are superimposed on each other, an interference pattern is formed at the recording plane. This pattern is called a "*hologram*", from the Greek word *holos*, meaning "*whole*". The entire information of the object (both phase and amplitude) is recorded on the holographic plate in terms of black and white fringes. The object can be reconstructed by illuminating the same reference light source on to the hologram again. The virtual image will be reconstructed and appears at the location formerly occupied by the object, even though the object is no longer in its original position.

Conventional holography consists of two parts: recording and reconstruction steps as shown in Fig. 2.1 and Fig. 2.2, respectively, in the case of in-line (Gabor) holography.

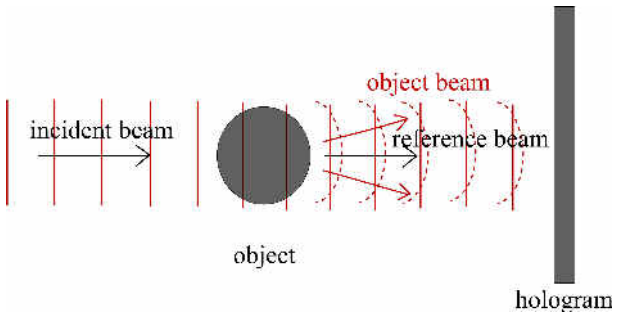

Fig. 2.1: Recording process

In the recording process, a plane wave is traditionally used to illuminate the object. Some part of wave is diffracted by the object and is called the object wave. The other is not diffracted by the object, but directly illuminates the recording medium. This is called the reference wave. When the two waves interfere with each other, the interference pattern is observed on the recording medium that we call the hologram.

For the reconstruction process, the same reference wave is used to illuminate the holographic plate. The hologram acts as a diffraction grating. The reconstructing beam, after passing through the hologram, produces the virtual image of the object at the same position as the original object. The real image of the object can be observed behind the holographic plate symmetrically.

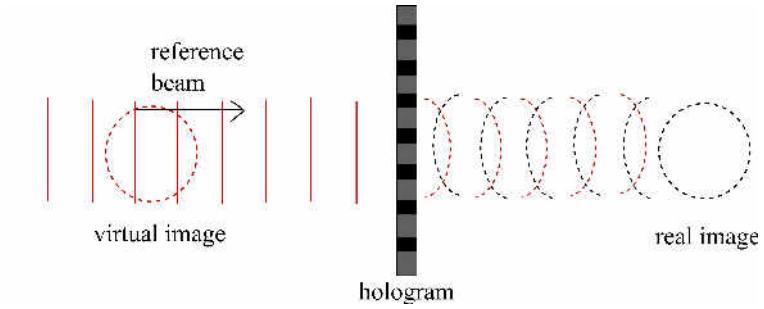

Fig. 2.2: Reconstructing process

In digital holography, the reference wave and the object wave interfere at the surface of a charge coupled device (CCD) instead of a photographic plate. The interference fringes are recorded electronically and they are transferred to the computer. In numerical reconstruction, the virtual image of the object will appear at the same position as the original object and the real image will appear in the opposite direction.

2.2 ABCD matrix

In geometrical optics, light travelling through an optical element can be described by a 2×2 matrix, called an ABCD transfer matrix. The ABCD matrix is a method for tracing the propagation of waves in an optical system. This ABCD method uses the paraxial approximation.

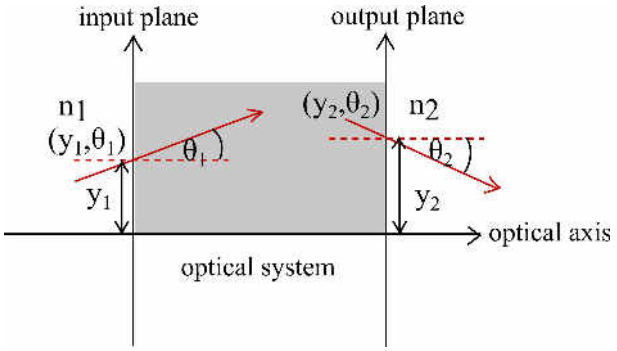

Fig. 2.3: Ray analysis

From Fig. 2.3, two parameters y and θ are considered. A ray is defined by its heigth, y, and its direction from the optical axis, θ. A light ray enters an optical system at the input plane at coordinates (y_1, θ_1) and leaves the system at the output plane at (y_2, θ_2). n_1 and n_2 are the refractive index of the medium before and after the optical system, respectively. The propagation of the ray can be described by the mathematical expression as

$$\begin{pmatrix} y_2 \\ \theta_2 \end{pmatrix} = \begin{pmatrix} A & B \\ C & D \end{pmatrix} \begin{pmatrix} y_1 \\ \theta_1 \end{pmatrix}. \tag{2.1}$$

All the parameters of Eq.(2.1) are presented in Fig. 2.3. The vector $(y\ \theta)$ is called the "*ray vector*". If the optical system has several components, the combined optical system can be calculated by multiplying these ABCD matrices:

$$\begin{pmatrix} y_2 \\ \theta_2 \end{pmatrix} = \begin{pmatrix} A_n & B_n \\ C_n & D_n \end{pmatrix} \cdots \begin{pmatrix} A_1 & B_1 \\ C_1 & D_1 \end{pmatrix} \begin{pmatrix} y_1 \\ \theta_1 \end{pmatrix}. \tag{2.2}$$

The following examples of a transfer matrix for some commonly used optical components are presented in [84] (Appendix B.3, pp.404-407).

- For light travelling in free space with a distance L, the ABCD matrix is

$$\begin{pmatrix} A & B \\ C & D \end{pmatrix} = \begin{pmatrix} 1 & L \\ 0 & 1 \end{pmatrix}. \tag{2.3}$$

- For light travelling through any medium that has a refractive index, n_2, and that propagates through a distance L, the ABCD matrix is

$$\begin{pmatrix} A & B \\ C & D \end{pmatrix} = \begin{pmatrix} 1 & \frac{L}{n_2} \\ 0 & 1 \end{pmatrix}. \tag{2.4}$$

- For light travelling through a thin lens with focal length f, the ABCD matrix is

$$\begin{pmatrix} A & B \\ C & D \end{pmatrix} = \begin{pmatrix} 1 & 0 \\ -\frac{1}{f} & 1 \end{pmatrix}. \tag{2.5}$$

- For light refracting at a spherical surface with radius of curvature R, the ABCD matrix is

$$\begin{pmatrix} A & B \\ C & D \end{pmatrix} = \begin{pmatrix} 1 & 0 \\ \frac{n_1-n_2}{R} & 1 \end{pmatrix}, \tag{2.6}$$

where n_1 is the refractive index of the first medium and n_2 is the refractive index of the second medium.

- If the refracted surface has a non-symmetric radius of curvature in the x- and y-direction, the ABCD matrix in x- and y-components is

$$\begin{pmatrix} A_x & B_x \\ C_x & D_x \end{pmatrix} = \begin{pmatrix} 1 & 0 \\ \frac{n_1-n_2}{R_x} & 1 \end{pmatrix} \qquad \text{and} \qquad \begin{pmatrix} A_y & B_y \\ C_y & D_y \end{pmatrix} = \begin{pmatrix} 1 & 0 \\ \frac{n_1-n_2}{R_y} & 1 \end{pmatrix}, \tag{2.7}$$

where $A_{x,y}, B_{x,y}, C_{x,y}$, and $D_{x,y}$ are matrix elements in the x- and y-components. $R_{x,y}$ is the radius of curvature of the surface in x- and y-direction.

2.2.1 Propagation of wave under Fresnel transform

The relation between diffraction theory and ray optics can be used to describe the propagation of light through a lens systems. A diffraction integral relates the electric field on the input plane and on the output plane. However, this integral is limited by the paraxial approximation. The Fresnel integral can be written as the coefficients of the transfer matrix between the two planes as follows:

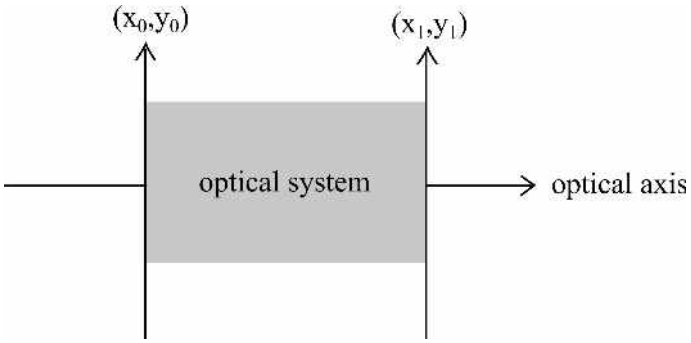

Fig. 2.4: Illustration of the input and output plane coordinates.

$$E_1(x_1, y_1) = \frac{\exp(i\frac{2\pi}{\lambda}L_0)}{i\lambda B} \int\int E_0(x_0, y_0) \exp\left[\frac{i\pi}{\lambda B}\left(A(x_0^2 + y_0^2) - 2(x_0x_1 + y_0y_1) + D(x_1^2 + y_1^2)\right)\right] dx_0\, dy_0, \tag{2.8}$$

where L_0 is the optical path of a ray lying on the axis of the system between the input and output planes [69, 70]. $E_0(x_0, y_0)$ is the electric field amplitude at the (x_0, y_0) plane. This expression is very useful in holography.

2.3 Gaussian beam

A Gaussian beam is an electromagnetic wave whose intensity distribution is well described by a Gaussian function. The Gaussian beam is described by a few parameters such as the beam's size, radius of curvature, and Gouy phase shift. The beam parameters are presented in Fig. 2.5.

The complex electric field amplitude of a Gaussian beam can be expressed as

$$E(r, z) = E_0 \frac{\omega_0}{\omega(z)} \exp\left(\frac{-r^2}{\omega(z)^2} + ikz + ik\frac{r^2}{2R(z)} - i\zeta(z)\right). \tag{2.9}$$

The radial distance from the beam axis is denoted r and z is the axial distance from the beam waist. E_0 is the amplitude at $(0, 0)$, ω_0 is the beam waist radius at $z = 0$ whose amplitude is $1/e$ of its maximum value, $\omega(z)$ is the beam radius or spot size at distance z from the beam waist, and k is wave number, $k = 2\pi/\lambda$. $R(z)$ is the radius

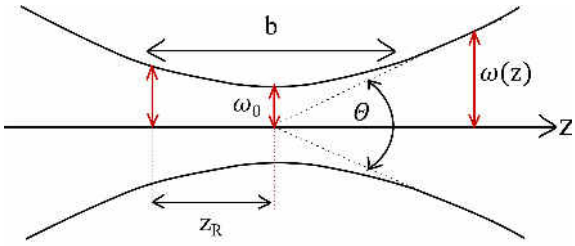

Fig. 2.5: Gaussian beam's parameters

of curvature of the beam's wavefront and $\zeta(z)$ is the Gouy phase shift. The beam size, $\omega(z)$, at a distance z along the beam from the beam waist is

$$\omega(z) = \omega_0 \sqrt{1 + \left(\frac{z}{z_R}\right)^2}, \tag{2.10}$$

where $z_R = \frac{\pi\omega_0^2}{\lambda}$. The radius of curvature of the wavefronts as a function of axial position, $R(z)$, is

$$R(z) = z\left[1 + \left(\frac{z_R}{z}\right)^2\right], \tag{2.11}$$

and the Gouy phase of the beam, $\zeta(z)$, is

$$\zeta(z) = \arctan\left(\frac{z}{z_R}\right). \tag{2.12}$$

When a Gaussian beam propagates through an optical system with optical length L_0, the beam output, $E_{out}(x, y)$, under Fresnel transformation and ABCD matrix formalism, is

$$\begin{aligned} E_{out}(x,y) = \frac{\exp(ikL_0)}{\sqrt{iB}} \int_{-\infty}^{\infty} E_{in}(x',y') \exp\left[\frac{i\pi}{B}\left(Dx^2 - 2xx' + Ax'^2\right)\right] \\ \exp\left[\frac{i\pi}{B}\left(Dy^2 - 2yy' + Ay'^2\right)\right] dx'\, dy', \end{aligned} \tag{2.13}$$

where E_{in} is the beam input. In this case, it is not possible to define the Gouy phase shift as in Eq. (2.12). Thus the phase accumulated by a Gaussian beam passing through an optical system, the denoted Gouy phase shift (ζ_{out}), can be defined as

$$-\zeta_{out} = \arg\left[E_{out}(0,0)\right] - \arg\left[E_{in}(0,0)\right] - kL_0, \tag{2.14}$$

$\arg[\cdot]$ denotes the argument (phase). From [67], the output parameters are related to the input parameters through transformation of ABCD matrix elements of the medium. Now consider a Gaussian beam with the input parameters ω_{in} and R_{in} that

propagates through an optical system characterized by an ABCD matrix. By considering a complex beam parameter q which is defined as

$$\frac{1}{q} = \frac{1}{R(z)} + i\frac{\lambda}{\pi\omega^2(z)}. \tag{2.15}$$

q_{out} is related to q_{in} through matrix elements as [67]

$$\lambda q_{out} = \frac{A\lambda q_{in} + B}{C\lambda q_{in} + D}. \tag{2.16}$$

From the above equation, we then find the output parameters ω_{out}, R_{out}, and ζ_{out} from the input parameters ω_{in}, R_{in}, and ζ_{in} through the ABCD matrix as

$$\omega_{out}^2 = \left(A + \frac{B}{\lambda R_{in}}\right)^2 \omega_{in}^2 + \frac{B^2}{\omega_{in}^2}, \tag{2.17}$$

$$\frac{1}{\lambda R_{out}} = \frac{\left(C + \frac{D}{\lambda R_{in}}\right)\left(A + \frac{B}{\lambda R_{in}}\right) + \frac{BD}{\omega_{in}^4}}{\left(A + \frac{B}{\lambda R_{in}}\right)^2 + \frac{B^2}{\omega_{in}^4}}, \tag{2.18}$$

$$\zeta_{out} = \zeta_{in} + \arctan\left[\frac{B}{\left(A + \frac{B}{\lambda R_{in}}\right)\omega_{in}^2}\right], \tag{2.19}$$

where A, B, C, and D are matrix elements of the ABCD matrix. The corresponding intensity distribution at the input plane denoted $I(r, z)$ is

$$I(r, z) = I_0 \left(\frac{\omega_0}{\omega_z}\right)^2 \exp\left(-\frac{2r^2}{\omega^2(z)}\right), \tag{2.20}$$

where I_0 is the intensity of the beam at its waist. As can be seen in Eq.(2.20), the intensity distribution has a Gaussian form. In my thesis, I will use the Gaussian beam to characterize inclusions inside a suspended water droplet.

2.4 In-line configuration

For in-line holography, the system can be divided into two parts: before the object plane and after the object plane. The coordinates at the input plane are (μ, ν), at the object plane are (ξ, η) and at the recording plane are (x, y). The optical system between the incident plane and the object plane can be described by transfer matrix $M_1^{x,y}$ where x, y refer to the components of the transfer matrix, M_1 in x- and y-direction. The system between the object plane and the recording plane can be described by another transfer matrix $M_2^{x,y}$. A light wave illuminates the object. Some part of the wave is diffracted by the object while the remaining part passes without

being diffracted. The former part is called the reference wave and the latter part is called the object wave. When two waves interfere, a typical diffraction pattern is observed on the recording plane.

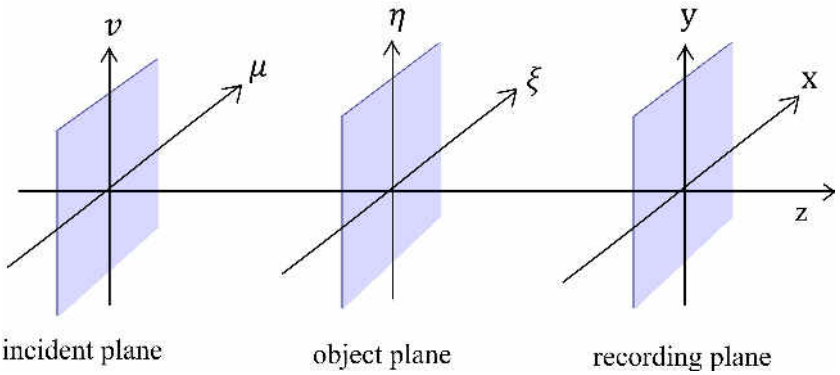

Fig. 2.6: Planes of consideration.

The generalized Fresnel integral tells us how to calculate the field G_1 before the object plane by using the field distribution in the incident plane as

$$G_1(\xi,\eta) = \frac{\exp(i\frac{2\pi}{\lambda}E_1)}{i\lambda\sqrt{B_1^x B_1^y}} \int_{\mathbb{R}^2} G_0(\mu,\nu) \exp\left(i\frac{2\pi}{\lambda B_1^x}[A_1^x\mu^2 - 2\xi\mu + D_1^x\xi^2]\right) \exp\left(i\frac{2\pi}{\lambda B_1^y}[A_1^y\nu^2 - 2\eta\nu + D_1^y\eta^2]\right) d\mu\, d\nu, \tag{2.21}$$

where $G_0(\mu,\nu)$ is the field amplitude at the incident plane. In our case, G_0 is a Gaussian function. E_1 is the optical path along the system between the incident plane and the object plane, and $A_1^{x,y}$, $B_1^{x,y}$, $D_1^{x,y}$ are the matrix elements of $M_1^{x,y}$. This expression describes the propagation of light through optical systems; it relates diffraction theory to ray optics. After the propagation through the system of matrix $M_2^{x,y}$, the complex field amplitude at the recording plane is

$$G_2(x,y) = \frac{\exp(i\frac{2\pi}{\lambda}E_2)}{i\lambda\sqrt{B_2^x B_2^y}} \int_{\mathbb{R}^2} G_1(\xi,\eta)[1 - T(\xi,\eta)] \exp\left(i\frac{2\pi}{\lambda B_2^x}[A_2^x\xi^2 - 2\xi x + D_2^x x^2]\right) \exp\left(i\frac{2\pi}{\lambda B_2^y}[A_2^y\eta^2 - 2\eta y + D_1^y y^2]\right) d\xi\, d\eta, \tag{2.22}$$

where $G_1(\xi,\eta)$ is the field amplitude at the object plane in Eq.(2.21), E_2 is the optical path along the system after the object plane, and $A_2^{x,y}$, $B_2^{x,y}$, $D_2^{x,y}$ are the matrix elements of $M_2^{x,y}$. The function $1 - T(\xi,\eta)$ is the transmission function of the particle. Equation (2.22) can be separated into two parts: the reference beam, denoted $R(x,y)$, and the object beam, denoted $O(x,y)$, such that

$$G_2(x,y) = \frac{\exp(i\frac{2\pi}{\lambda}E_2)}{i\lambda\sqrt{B_2^x B_2^y}}[R(x,y) - O(x,y)], \tag{2.23}$$

where the reference beam is

$$R(x,y) = \int_{\mathbb{R}^2} G_1(\xi,\eta) \exp\left(i\frac{2\pi}{\lambda B_2^x}[A_2^x\xi^2 - 2\xi x + D_2^x x^2]\right) \exp\left(i\frac{2\pi}{\lambda B_2^y}[A_2^y\eta^2 - 2\eta y + D_1^y y^2]\right) d\xi\, d\eta, \tag{2.24}$$

and the object beam is

$$O(x,y) = \int_{\mathbb{R}^2} G_1(\xi,\eta)T(\xi,\eta) \exp\left(i\frac{2\pi}{\lambda B_2^x}[A_2^x\xi^2 - 2\xi x + D_2^x x^2]\right) \exp\left(i\frac{2\pi}{\lambda B_2^y}[A_2^y\eta^2 - 2\eta y + D_1^y y^2]\right) d\xi\, d\eta. \tag{2.25}$$

From Eqs.(2.24) and (2.25), the intensity, denoted $I(x,y)$, recorded by the CCD sensor is

$$I(x,y) = G_2(x,y)\overline{G_2(x,y)} = \frac{1}{\lambda^2 B_2^x B_2^y}\left[|R|^2 - 2\Re(R\bar{O}) + |O|^2\right], \tag{2.26}$$

where the upper bar denotes to the complex conjugate. Now we have the intensity distribution or the hologram recorded by a CCD camera. The next step is to reconstruct the image of the particle from the recording hologram.

In order to obtain analytical expression of the transmission function of the particle, $T(\xi,\eta)$ can be expressed as [71]

$$T(\xi,\eta) = \begin{cases} 1 & \text{when} \sqrt{\xi^2+\eta^2} \le D/2 \\ 0 & \text{when } \sqrt{\xi^2+\eta^2} > D/2 \end{cases} = \sum_{k=1}^{N} A_k \exp\left[-\frac{B_k}{b^2}(\xi^2 + R_{ell}^2\eta^2\right], \tag{2.27}$$

where D is the diameter of the particle. For our previous development, the particle transmission function for an opaque disk, $T(\xi,\eta)$, can be derived from the summation of a Gaussian series [71] as described in the above equation. To simulate the opaque disk, N is fixed at 10. The A_k and B_k coefficients are determined by numerical resolution of the Kirchhoff equation [71]. $R_{ell} = b/a$ represents the particle ellipticity where a and b refer to the major and minor axis of the ellipse, respectively. $R_{ell} = 1$ refers to a circular particle. In my work, the particle shape considered most is circular ($R_{ell} = 1$).

Most of the previous publications on digital holography consider the particle as a pure amplitude (or an opaque) object. The definition of the transmission function of the particle, denoted $1 - T$, can be written as in Eq. (2.27). This kind of transmission function can be adapted to describe elliptical opaque objects. For more general objects, we need to modify this function into a more general form, which is presented in chapter 3.

2.5 Fractional Fourier transformation

To reconstruct the image of the particle in this thesis, the 2D fractional Fourier transformation (2D-FRFT) is used. The fractional Fourier transform is a Fourier transform with the fractional order. The mathematical expression of 2D-FRFT of order α is

$$\mathcal{F}_{\alpha_x,\alpha_y}\left[I(x,y)\right](x_a,y_a) = \int_{\mathbb{R}^2} N_{\alpha_x}(x,x_a)\, N_{\alpha_y}(y,y_a)\, I(x,y)dxdy, \tag{2.28}$$

where N_{α_x} and N_{α_y} are the kernel of the fractional operator in two dimensions, which is defined by

$$N_{\alpha_p}(p,p_a) = C(\alpha_p)\exp\left(i\pi\frac{p^2+p_a^2}{s_p^2\tan\alpha_p}\right)\exp\left(-\frac{i2\pi p_a p}{s_p^2\sin\alpha_p}\right) \tag{2.29}$$

where the coefficient $C(\alpha_p)$ is

$$C(\alpha_p) = \frac{\exp\left(-i(\frac{\pi}{4}sign(\sin\alpha_p) - \frac{\alpha_p}{2})\right)}{|s_p^2\sin\alpha_p|^{1/2}}. \tag{2.30}$$

The parameter p refers to x, y. $s_p^2 = N_p\delta_p^2$. N_p is the number of samples in the x and y axes. δ_p is the sample size along both axes.

In digital holography, the digital reconstruction can be viewed as the digital refocusing on the object. From Eq.(2.26), the first and the last terms are concerned with the reference and the object wave, respectively. Only the second term relates to the interference pattern. By considering the phase of the interference part (ϕ) and the quadratic phase in the FRFT kernel (ϕ_a), the best reconstruction plane is obtained when

$$\phi \pm \phi_a = 0. \tag{2.31}$$

The quadratic phase from the interference, ϕ, is

$$\phi = \frac{\pi}{\lambda}\left[\left(\frac{M_x - D_2^x}{B_2^x}\right)x^2 + \left(\frac{M_y - D_2^y}{B_2^y}\right)y^2\right] \tag{2.32}$$

and the quadratic phase from the FRFT kernel,ϕ_a, is given by

$$\phi_a = \pi\left[\frac{\cot\alpha_x}{s_x^2}x^2 + \frac{\cot\alpha_y}{s_y^2}y^2\right] \tag{2.33}$$

From the condition in Eq.(2.31), the optimal fractional orders are

$$\begin{aligned}\alpha_x^{opt} &= \arctan\left[\mp\frac{B_2^x\lambda}{s_x^2(M_x - D_2^x)}\right],\\ \alpha_y^{opt} &= \arctan\left[\mp\frac{B_2^y\lambda}{s_y^2(M_y - D_2^y)}\right],\end{aligned} \tag{2.34}$$

When the hologram is reconstructed with optimal fractional orders, α_x^{opt} and α_y^{opt}, the best focus plane of the particle is selected. Then the image of the particle is recovered.

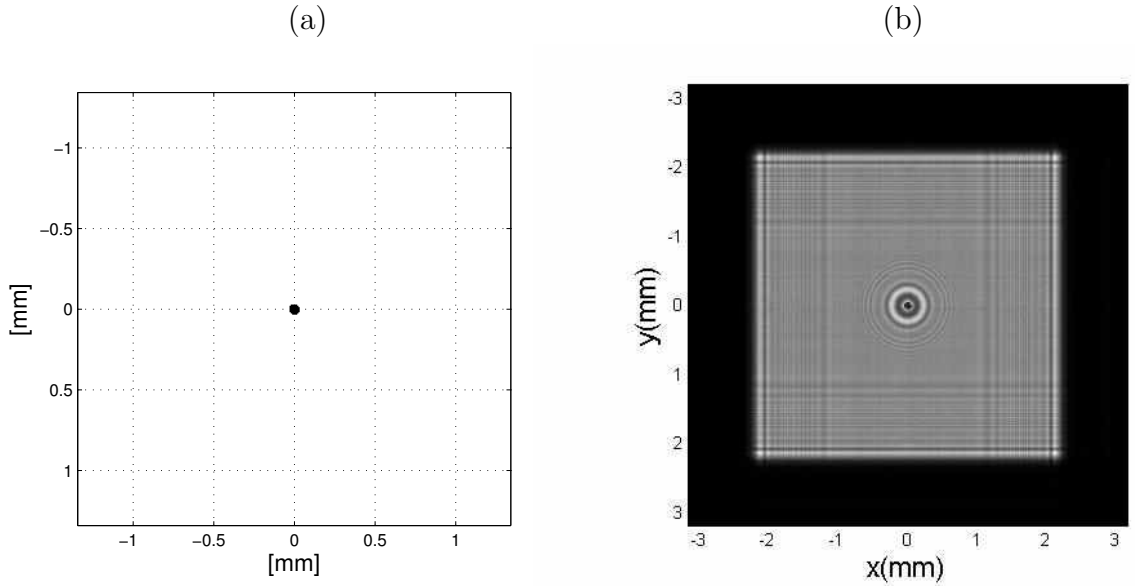

Fig. 2.7: Example of one opaque particle (a) and its reconstructed image (b).

Fig. 2.7 is an example of an opaque disk particle (a) and its reconstructed image (b) by 2D-FRFT. In this case, an opaque particle is illuminated by a plane wave. The hologram is recorded by a CCD camera behind the opaque particle.

If the incident wave is not a plane wave, the magnification factor needs to be considered as proposed by [72]:

$$g_{x,y} = \frac{\omega_{tot_{x,y}}}{\omega_{1_{x,y}}}, \tag{2.35}$$

where $\omega_{1_{x,y}}$ is the beam waist dimension along the x and y direction in the inclusion's plane and $\omega_{tot_{x,y}}$ is the beam waist dimension along the x and y direction in the CCD plane.

3. GENERAL MODEL FOR A CENTRED ABERRATING OBJECT

In this chapter, an extended mathematical description of the digital in-line hologram of a spherical transparent/semi-transparent particle is presented. Most of the previous studies concerned opaque particles or homogeneous transparent particles [73, 74, 75]. From the opaque disk point of view, the refractive index of the particle is not taken into account. Therefore, erroneous interpretations can be obtained when considering phase particles experimentally such as droplets or bubbles or another transparent particles such as glass particles.

In the first part of this chapter, a general expression for the intensity distribution of the hologram of a particle in the plane of the CCD sensor is proposed. To do this, a new model based on ABCD transfer matrix formalism and Zernike polynomials is developed. In this chapter, the droplet is sometimes considered as a part of the system with an inclusion inside. This inclusion can be a transparent or opaque particle whose transmission function is described by a Zernike polynomial. A Zernike polynomial is chosen to describe the particle because this kind of function can be used to describe any astigmatism introduced by the particle. Sometime a droplet is considered as a transparent particle described by a circle polynomial without inclusions. The details of some mathematical functions are given in the Appendix. For the hologram reconstruction, the two-dimensional fractional Fourier transform is used to reconstruct the image of the particle.

The second part focuses on a transparent particle or droplet without inclusion. Three approximations for the particle's transmission function are compared: opaque disk, the quadratic phase, and the quasi-spherical phase approximation. Furthermore, the Zernike coefficients that describe the considered transparent particles are evaluated by using the double exponential (DE) method, which will be presented in this chapter.

In the last part of this chapter, a glass particle inside a droplet is considered. The hologram of the experiment and its reconstruction image of a glass particle inside a droplet are presented here. The intensity profile of the hologram of a transparent particle is presented. The difference between the intensity profile of this glass particle and that of an opaque particle is noticeable.

3.1 In-line configuration of the system

As in the previous chapter's section, "In-line Configuration", the system is composed of two parts: before and after the particle plane. The in-line configuration is represented in Fig. 3.1. The two parts can be described by two 4×4 symplectic matrices, denoted M_i and M_t, respectively. These symplectic matrices can easily deal with

the polarisation of light in the future applications. M_i describes the system between the source (with waist ω_0) and the particle plane. M_t describes the system between the particle plane and the CCD sensor. (μ, ν) are the transverse coordinates at the input plane, (ξ, η) are the transverse coordinates at the object plane and (x, y) are the transverse coordinates at the recording plane. Each symplectic matrix is composed of 2×2 matrices A, B, C, and D.

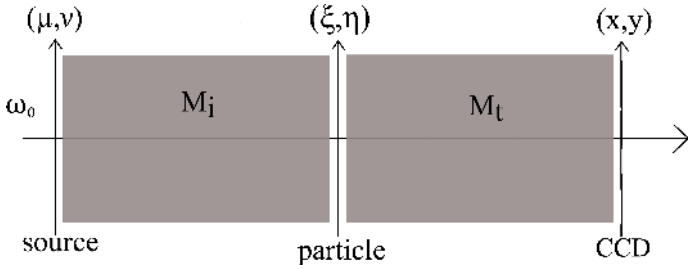

Fig. 3.1: In-line configuration of digital holography

The matrices M_i and M_t are defined as

$$M_i = \begin{pmatrix} A_i & B_i \\ C_i & D_i \end{pmatrix}, \qquad M_t = \begin{pmatrix} A_t & B_t \\ C_t & D_t \end{pmatrix} \tag{3.1}$$

where

$$A_i = \begin{pmatrix} a_{i,1} & 0 \\ 0 & a_{i,2} \end{pmatrix}, \quad B_i = \begin{pmatrix} b_{i,1} & 0 \\ 0 & b_{i,2} \end{pmatrix}, \quad C_i = \begin{pmatrix} c_{i,1} & 0 \\ 0 & c_{i,2} \end{pmatrix}, \quad D_i = \begin{pmatrix} d_{i,1} & 0 \\ 0 & d_{i,2} \end{pmatrix} \tag{3.2}$$

and

$$A_t = \begin{pmatrix} a_{t,1} & 0 \\ 0 & a_{t,2} \end{pmatrix}, \quad B_t = \begin{pmatrix} b_{t,1} & 0 \\ 0 & b_{t,2} \end{pmatrix}, \quad C_t = \begin{pmatrix} c_{t,1} & 0 \\ 0 & c_{t,2} \end{pmatrix}, \quad D_t = \begin{pmatrix} d_{t,1} & 0 \\ 0 & d_{t,2} \end{pmatrix}. \tag{3.3}$$

All the matrix elements are defined by the optical components along the propagation direction of the beam. The indices "i" and "t" indicate the incident part and transmitted part, respectively. The indices 1 and 2 indicate the transverse coordinates (x or y coordinates).

A source in this study is a Gaussian light source propagated through a system represented by transfer matrix, M_i. In this work, a particle is described by a Zernike polynomial which is introduced in the next section.

3.2 Zernike polynomials

Zernike polynomials are mathematical functions which consist of a sequence of polynomials. These polynomials form a complete orthogonal basis on the unit disk.

The mathematical expression of Zernike polynomials is

$$Z_n^m(s,\theta) = R_n^{|m|}(s)\exp(i\,m\theta), \qquad 0 \le s \le 1,\ 0 \le \theta < 2\pi, \tag{3.4}$$

where n is non-negative integers, m describes all integers between $-n$ to n, and $n-|m|$ is an even number. The two coordinates (s,θ) refer to the radial distance and the azimuthal angle, respectively. These polynomials are used in the characterization of circular optical imaging systems with non-uniform pupil functions [76, 77]. The radial polynomials, $R_n^m(s)$, are given by

$$R_n^{|m|}(s) = \sum_{k=0}^{(n-|m|)/2} (-1)^k \frac{(n-k)!}{k!\left(\frac{n+|m|}{2}-k\right)!\left(\frac{n-|m|}{2}-k\right)!} \tag{3.5}$$

The important property of the Zernike polynomials is their orthogonality. The orthogonality property of Zernike polynomials is

$$\int_0^1 \int_0^{2\pi} Z_n^m(s,\theta)\overline{Z_{n'}^{m'}(s,\theta)}\, s\, ds\, d\theta = \frac{\pi}{n+1}\delta_{mm'}\delta_{nn'} \tag{3.6}$$

The symbol δ is Kronecker's delta function. The first few of the Zernike polynomials are presented in the following table.

n	m	Z_n^m	name
0	0	1	Piston
1	1	$2s\cos\theta$	Tilt
1	-1	$2s\sin\theta$	Tilt
2	0	$\sqrt{3}(2s^2-1)$	Defocus
2	2	$\sqrt{6}s^2\cos 2\theta$	Astigmatism
2	-2	$\sqrt{6}s^2\sin 2\theta$	Astigmatism
3	1	$\sqrt{8}(3s^3-2s)\cos\theta$	Coma
3	-1	$\sqrt{8}(3s^3-2s)\sin\theta$	Coma

Tab. 3.1: Order and name of Zernike polynomials.

Some examples of the Zernike polynomials of the unit disks of different orders are presented in Fig. 3.2.

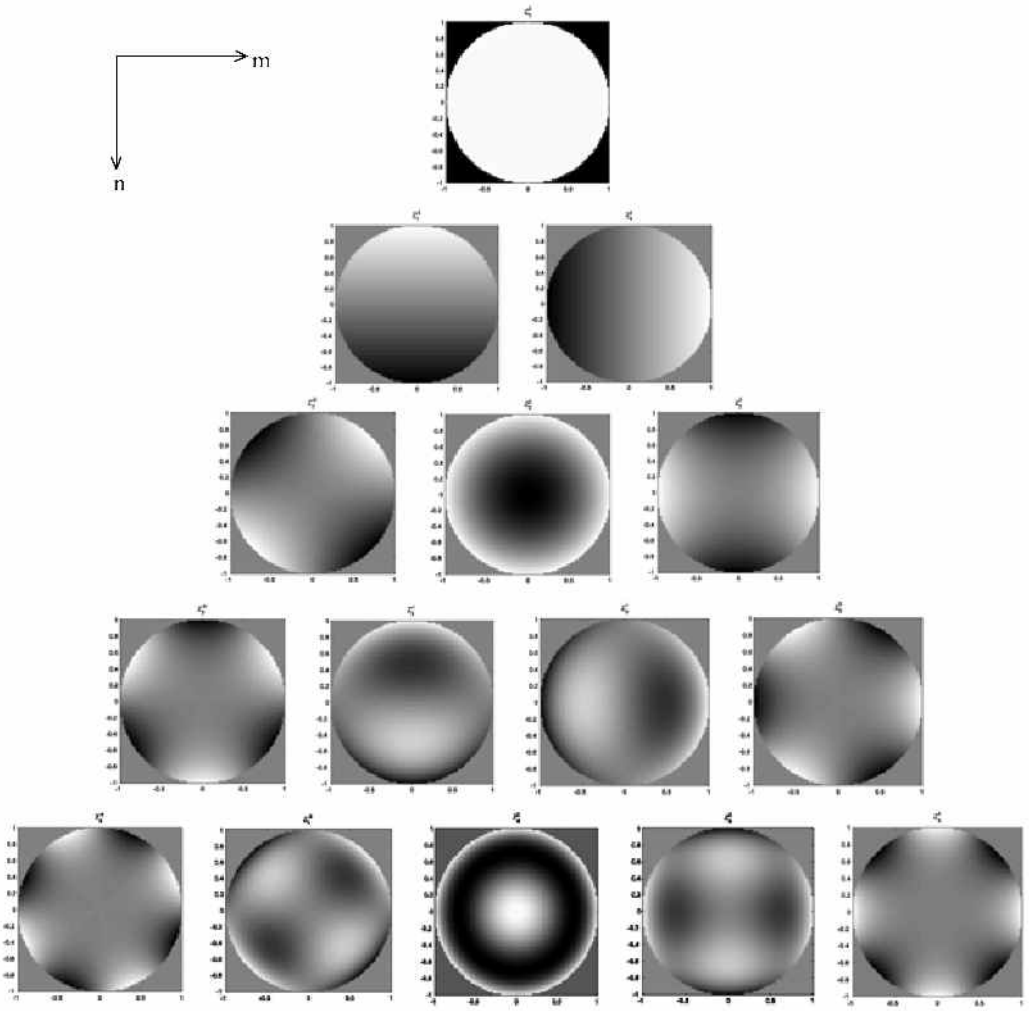

Fig. 3.2: Figure representing the different orders of Zernike polynomials.

These Zernike polynomials are used in what follows to describe the objects under study (both opaque and transparent objects which introduced any kind of aberrations) in the digital in-line holography.

3.3 Intensity distribution in the plane of the CCD sensor

From Fig. 3.1, the propagation of the Gaussian beam from the incident plane to the CCD plane can be described by two linear canonical transformations. Each linear canonical transformation has the same integral structure. The first part of the propagation as in Eq.(2.21) can be written in the matrix form by

$$G_1(\mathbf{r}) = \frac{\exp(ikE_i)}{i\lambda\sqrt{\det(B_i)}} \int_{\mathbb{R}^2} G_0(\boldsymbol{\rho}) \exp[i\frac{\pi}{\lambda}(\boldsymbol{\rho}^T B_i^{-1} A_i \boldsymbol{\rho} - 2\boldsymbol{\rho}^T B_i^{-1}\mathbf{r} + \mathbf{r}^T D_i B_i^{-1}\mathbf{r})] d\boldsymbol{\rho}. \quad (3.7)$$

The G_0 function refers to the incident Gaussian beam and is defined as

$$G_0(\boldsymbol{\rho}) = \exp(-\boldsymbol{\rho}^T Q_0^{-1} \boldsymbol{\rho}), \tag{3.8}$$

where the vector $\boldsymbol{\rho} = (\mu \quad \nu)^T$. The matrix Q_0^{-1} is due to the Gaussian beam waist, denoted ω_0, and its inverse is given by

$$Q_0 = \begin{pmatrix} \omega_0^2 & 0 \\ 0 & \omega_0^2 \end{pmatrix} \tag{3.9}$$

E_i in Eq.(3.7) is the optical path between the incident plane and the particle plane. λ is the wavelength of the light source and $k = 2\pi/\lambda$ is the wave number. By substituting Eq.(3.8) into Eq.(3.7) and integrating over ρ (see Appendix A, B and D.1 of this thesis), the complex field amplitude of the beam at the particle plane is given by

$$G_1(\mathbf{r}) = \frac{\pi}{i\lambda} \frac{\exp(ikE_i)}{\sqrt{\det(B_i Q_0^{-1} - i\frac{\pi}{\lambda} A_i)}} \exp\left[-\frac{\pi^2}{\lambda^2} \mathbf{r}^T Q_i^{-1} \mathbf{r}\right], \tag{3.10}$$

where

$$Q_i^{-1} = B_i^{-1T} \left(Q_0^{-1} - i\frac{\pi}{\lambda} B_i^{-1} A_i\right)^{-1} B_i^{-1} - i\frac{\pi}{\lambda} D_i B_i^{-1} \tag{3.11}$$

and $\mathbf{r}^T = (\xi \quad \eta)$ is the transverse plane coordinates of the particle plane. The field amplitude in Eq.(3.10) can be rewritten in the form:

$$G_1(\mathbf{r}) = \frac{\pi}{i\lambda} \frac{\exp(ikE_i)}{\sqrt{\det(B_i Q_0^{-1} - i\frac{\pi}{\lambda} A_i)}} E(\mathbf{r}), \tag{3.12}$$

where $E(\mathbf{r})$ is the Gaussian incident beam before the particles plane and is defined as

$$E(\xi, \eta) = \exp\left[-\left(\frac{\xi^2}{\omega_x^2} + \frac{\eta^2}{\omega_y^2}\right)\right] \exp\left[-i\frac{\pi}{\lambda}\left(\frac{\xi^2}{R_x} + \frac{\eta^2}{R_y}\right)\right], \tag{3.13}$$

where the waist along the transverse coordinates, *i.e.* (x, y), is given by

$$\omega_x = \frac{\lambda}{\pi}\sqrt{\frac{1}{\Re(Q_i^{-1}(1,1))}}, \qquad \omega_y = \frac{\lambda}{\pi}\sqrt{\frac{1}{\Re(Q_i^{-1}(2,2))}}. \tag{3.14}$$

$\Re[.]$ refers to the real part of the function. The radius of curvature in the same coordinate system is

$$R_x = \frac{\frac{\lambda}{\pi}}{\Im(Q_i^{-1}(1,1))}, \qquad R_y = \frac{\frac{\lambda}{\pi}}{\Im(Q_i^{-1}(2,2))} \tag{3.15}$$

where $\Im[.]$ refers to the imaginary part of the function.

However, most of the previous publications on digital holography consider the particle as a pure amplitude (no phase) object or an opaque object. The definition

of the particle function, denoted $1-p$, can be written in the Gaussian series [60] as in Eq.(2.27). This kind of transmission function is adapted to describe quasi-homogeneous elliptical opaque objects. For more general objects, we need to modify this function into a more general form. Therefore, in this chapter, a Zernike series is introduced to describe the particle function in the case of inhomogeneous phase objects. This description will be further adapted to homogeneous objects as opaque particles. Here we expand the complex function p as Zernike polynomials, presented as follows:

$$p(s,\theta) = [1 - A(s,\theta)\exp(i\Phi(s,\theta))]Z_0^0(s,\theta) = \left[1 - \sum_{n,m} \gamma_n^m Z_n^m(s,\theta)\right] Z_0^0(s,\theta). \quad (3.16)$$

The order n is non-negative integers, m describes all integers between $-n$ to n, and $n-|m|$ is an even number. Zernike polynomials are defined in Eq.(3.4)

The Zernike polynomials are separated into a radial part $R_n^{|m|}(s)$ and an angle dependence part $exp(im\theta)$. The Zernike coefficients, denoted γ_n^m, in Eq.(3.16) can be obtained by using the orthogonality of the Zernike polynomial functions. Then the coefficients are

$$\gamma_n^m = \frac{n+1}{\pi} \int_0^1 \int_0^{2\pi} A(s,\theta) \cdot \exp[i\Phi(s,\theta)] \cdot \overline{Z_n^m(s,\theta)}\, s\, ds\, d\theta. \quad (3.17)$$

The constant before the integral represents the normalization factor. The upper bar refers to the complex conjugate of the corresponding Zernike polynomials function, Z_n^m. In case of an opaque disk ($m=0, n=0$), the amplitude $A(s,\theta)$ is equal to unity and the phase $\Phi(s,\theta)$ is equal to zero. Then the function $p(s,\theta)$ becomes

$$p(s,\theta) = \gamma_0^0\ Z_0^0(s,\theta), \quad (3.18)$$

where $\gamma_0^0 = 1$. The field amplitude at the CCD sensor can be described by linear canonical transformation and its integral structure is the same as in Eq.(3.7). Then the field amplitude , G_2, can be written as

$$\begin{aligned} G_2(\mathbf{r}') = \frac{\exp(ikE_t)}{i\lambda\sqrt{\det(B_t)}} \exp\left[i\frac{\pi}{\lambda}\mathbf{r}'^T B_t^{-1} D_t \mathbf{r}'\right] \int_{\mathbb{R}^2} G_1(\mathbf{r}) \cdot [1 - p(s,\theta)] \times \\ \exp\left[i\frac{\pi}{\lambda}\mathbf{r}^T B_t^{-1} A_t \mathbf{r}\right] \exp\left[-i\frac{2\pi}{\lambda}\mathbf{r}^T B_t^{-1}\mathbf{r}\right] d\mathbf{r}, \end{aligned} \quad (3.19)$$

where E_t is an optical path between the particle plane and CCD sensor. Let us introduce the dimensionless variables $\mathbf{s} = 2\mathbf{r}/D$ and $\mathbf{s}' = 2\mathbf{r}'/D$ where D is the diameter of the particle. Then Eq.(3.19) becomes

$$\begin{aligned} G_2(\mathbf{s}'D/2) = -\frac{\pi D^2}{4\lambda^2} \frac{\exp[ik(E_i+E_t)]}{\sqrt{\det(B_t)\det(B_i Q_0^{-1} - i\frac{\pi}{\lambda}A_i)}} \exp\left[i\frac{\pi D^2}{4\lambda}\mathbf{s}'^T B_t^{-1} D_t \mathbf{s}'\right] \times \\ \int_{\mathbb{R}^2} [1 - p(s,\theta)] \exp\left[i\mathbf{s}^T L_t \mathbf{s}\right] \exp\left[-2i\pi\mathbf{s}^T P_t \mathbf{s}'\right] d\mathbf{s} \end{aligned} \quad (3.20)$$

with

$$L_t = \frac{\pi D^2}{4\lambda} B_t^{-1} A_t + i \left(\frac{\pi D}{2\lambda}\right)^2 Q_i, \qquad P_t = \frac{D^2}{4\lambda} \cdot B_t^{-1} \tag{3.21}$$

Let $\boldsymbol{\sigma} = P_t \mathbf{s}'$ to simplify the calculations, then the integration on Eq. (3.20) changes to the form

$$\begin{aligned} G_2(DP_t^{-1}\boldsymbol{\sigma}/2) = -\frac{\pi D^2}{4\lambda^2} \frac{\exp[ik(E_i + E_t)]}{\sqrt{\det(B_t)\det(B_i Q_0^{-1} - i\frac{\pi}{\lambda} A_i)}} \exp\left[i \frac{\pi D^2}{4\lambda} \boldsymbol{\sigma}^T S_t \boldsymbol{\sigma}\right] \\ \times \int_{\mathbb{R}^2} [1 - p(s,\theta)] \exp\left[i\mathbf{s}^T L_t \mathbf{s}\right] \exp\left[-2i\pi \mathbf{s}^T \boldsymbol{\sigma}\right] d\mathbf{s} \end{aligned} \tag{3.22}$$

with $S_t = P_t^{-1T} D_t B_t^{-1} P_t^{-1}$. Now, we have a mathematical expression of the field amplitude, G_2, in the CCD plane. Therefore, the intensity distribution recorded on the CCD sensor can be written as

$$I = |G_2(DP_t^{-1}\boldsymbol{\sigma}/2)|^2 = \frac{\pi D^2}{4\lambda^2} \frac{|G(\boldsymbol{\sigma}) - G_0^0(\boldsymbol{\sigma}) + \epsilon G_n^m(\boldsymbol{\sigma})|^2}{\left|\sqrt{\det(B_t)\det(B_i \det(Q_0^{-1} - i\frac{\pi}{\lambda} A_i))}\right|^2}, \tag{3.23}$$

where

$$G(\boldsymbol{\sigma}) = \int_{\mathbb{R}^2} \exp\left[i\mathbf{s}^T L_t \mathbf{s}\right] \exp\left[-2i\pi \mathbf{s}^T \boldsymbol{\sigma}\right] d\mathbf{s} \tag{3.24}$$

and

$$G_n^m(\boldsymbol{\sigma}) = \sum_{n,m} \gamma_n^m \times \int_{\mathbb{R}^2} Z_0^0(s,\theta) Z_n^m(s,\theta) \exp\left[i\mathbf{s}^T L_t \mathbf{s}\right] \exp\left[-2i\pi \mathbf{s}^T \boldsymbol{\sigma}\right] d\mathbf{s} \tag{3.25}$$

The value of ϵ in Eq.(3.23) depends on the kind of particle that is considered. If the particle is an opaque object, $\epsilon = 0$, and if the particle is a transparent object, $\epsilon = 1$. The solution of $G(\boldsymbol{\sigma})$ and $G_n^m(\boldsymbol{\sigma})$ is presented in the next section.

3.4 Expression for $G(\boldsymbol{\sigma})$ and $G_n^m(\boldsymbol{\sigma})$

The solution of the integral in Eq.(G) can be solved more easily than Eq.(3.25) and it is given by

$$G(\boldsymbol{\sigma}) = \frac{i\pi}{\sqrt{\det(L_t)}} \exp[-i\pi^2 \boldsymbol{\sigma}^T L_t^{-1} \boldsymbol{\sigma}] \tag{3.26}$$

For more details, see [78], page 57, Eq.(2.303). The difficulty is how to find the solution of the integral in Eq.(3.25). To achieve the solution, it is necessary to use mathematical results on (i) a special circle polynomial expansion, (ii) the linearization of products of

circle polynomials [79], and (iii) the extended Nijboer-Zernike theory (ENZ) [80]. The details of the calculation are given in Appendix **??**. The semi-analytical expression of $G_n^m(\boldsymbol{\sigma})$ is

$$G_n^m(\boldsymbol{\sigma}) = 2\pi \sum_{q=-\infty}^{+\infty} \sum_{n,m,p}^{\infty} \sum_{t} \gamma_n^m (-i)^{m+q} A_{n,|2q|+2p,t}^{m,2q,m+2q} \beta_{|2q|+2p}^{|2q|}(\delta) V_t^{m+2q}(2\pi\sigma, \chi) e^{i(m+2q)\varphi}. \tag{3.27}$$

The summation over t has to respect the following condition:

$$t = \max(|m+2q|, |m-|2q|-2p|)(2)(n+|2q|+2p), \tag{3.28}$$

where a(2)b is $a, a+2, \ldots, b$ when $b-a$ is non-negative and even.

The parameter χ in Eq.(3.27) is the trace of the matrix L_t which is defined by $\chi = \frac{1}{2}Tr(L_t)$. The parameter δ in Eq.(3.27) is linked to the ellipticity of the system, i.e., the optical components and the droplet, and is defined by $\delta = \frac{1}{2}(L_{t(1,1)} - L_{t(2,2)})$ where $L_{t(i,j)}$ are the diagonal elements of L_t in Eq.(3.21). In the particular case of a circular system, $\delta = 0$ and $\beta_{|2q|+2p}^{|2q|}(0) = 1$ if $q = p = 0$, and $\beta_{|2q|+2p}^{|2q|}(0) = 0$ otherwise. The coefficients β can be expressed explicitly in terms of the hypergeometric function ${}_2F_3$ as in [57], Appendix A, Eq.(A12) and Eq.(A13). In the case where $2r-p=0$, the coefficients β are

$$\beta_{|2q|+2p}^{|2q|}(\delta) = d_0^0(-1)^r(2|2q|+4r+1)\left(\frac{1}{2}\delta\right)^{|2q|+2r} {}_2F_3\left(\begin{matrix} r+\frac{1}{2} & |2q|+r+\frac{1}{2} \\ \frac{1}{2} & |2q|+2r+\frac{3}{2} \end{matrix} \quad |2q|+2r+1; -\frac{1}{4}\delta^2\right) \tag{3.29}$$

and

$$\beta_{|2q|+2p}^{|2q|}(\delta) = d_0^1(-1)^r(2|2q|+4r+1)\left(\frac{1}{2}\delta\right)^{|2q|+2r} {}_2F_3\left(\begin{matrix} r+\frac{1}{2} & |2q|+r+\frac{1}{2} \\ \frac{3}{2} & |2q|+2r+1 \end{matrix} \quad |2q|+2r+\frac{1}{2}; -\frac{1}{4}\delta^2\right) \tag{3.30}$$

when $2r-p=1$. The coefficients d_0^0 in Eq.(3.29) and d_0^1 in Eq.(3.30) are defined as follows

$$d_0^0 = \frac{(2r)!(2|2q|+2r)!}{r!(|2q|+r)!(2|2q|+4r+1)!}, \qquad d_0^1 = \frac{(2r)!(2|2q|+2r)!}{r!(|2q|+r)!(2|2q|+4r)!} \tag{3.31}$$

From [81], Eq.(142), the parameters A in Eq.(3.27) are related to the Clebsch-Gordon coefficients as

$$A_{n,|2q|+2p,t}^{m,2q,m+2q} = \left| C_{\frac{m}{2},\frac{2q}{2},\frac{m+2q}{2}}^{\frac{n}{2},\frac{|2q|+2p}{2},\frac{t}{2}} \right|^2, \tag{3.32}$$

where C are the Clebsch-Gordon coefficients. The functions V in Eq.(3.27) are given by the following series expansions

$$V_n^m(r,f) = \varepsilon_m \exp(if) \sum_{l=1}^{\infty} (-2if)^{l-1} \sum_{j=0}^{P} \upsilon_{lj} \frac{J_{|m|+l+2j}(r)}{l(r)^l}, \tag{3.33}$$

where n and $|m|$ are integers greater than 0 with $n-|m|$ even and non-negative and the function υ_{lj} is

$$\upsilon_{lj} = (-1)^P(|m|+l+2j)\binom{|m|+j+l-1}{l-1}\binom{j+l-1}{l-1}\binom{l-1}{P-j}/\binom{Q+l+j}{l}, \quad (3.34)$$

for $l = 1, 2, \ldots, j = 0, 1, \ldots, P, P = \frac{n-|m|}{2}$ and $Q = \frac{n+|m|}{2}$. For odd $m < 0$, ε_m in Eq.(3.33) is equal to $\varepsilon_m = -1$ and $\varepsilon_m = 1$ otherwise. Now, there are two particular cases to consider: $\epsilon = 0$ for an opaque object and $\epsilon = 1$ for a phase object.

3.5 Reconstruction by the fractional Fourier transformation

In the reconstruction process, the 2D fractional Fourier transformation (2D-FRFT) is used to reconstruct the object [82]. The fractional order varies from $0 \leq a_{x,y} \leq 1$. The 2D fractional Fourier transform of an intensity image $I(x, y)$ is defined as

$$\mathcal{F}_{a_x,a_y}[I(x,y)](x_a, y_a) = \int_{\mathbb{R}^2} N_{a_x}(x, x_a) N_{a_y}(y, y_a) I(x, y) dx\, dy \quad (3.35)$$

where $N_{a_x}(x, x_a)$ and $N_{a_y}(y, y_a)$ are the kernel operators and are defined by

$$N_{a_p}(p, p_a) = C(a_p) \exp\left(i\pi \frac{p^2 + p_a^2}{s_p^2 \tan\left(\frac{a_p\pi}{2}\right)}\right) \exp\left(-\frac{i2\pi p_a p}{s_p^2 \sin\left(\frac{a_p\pi}{2}\right)}\right), \quad (3.36)$$

and

$$C(a_p) = \frac{\exp\left[-i\left(\frac{\pi}{4} sign\left(\sin\left(\frac{a_p\pi}{2}\right)\right) - \frac{a_p\pi}{4}\right)\right]}{|s_p^2 \sin\left(\frac{a_p\pi}{2}\right)|^{1/2}}, \quad (3.37)$$

where $p = x, y$. The 2D-FRFT is a mathematical tool which is a good operator to analyse linearly chirped functions in signal processing (or holograms in the present case). These linearly chirped functions can be different along the two orthogonal axes x and y and these match the kernel operators in 2D-FRFT, which are separable as presented in Eq.(3.35). The image of the particle can be reconstructed with fractional orders called "*optimal fractional order*", and denoted by $a_{x,y}^{opt}$, which corresponds to the best reconstruction plane. To find the best reconstructed plane, the following conditions must be satisfied:

$$\tan\left[\frac{a_x^{opt}\pi}{2}\right] = -\frac{\pi}{s_x^2 \Re[\phi_{11}]} \qquad and \qquad \tan\left[\frac{a_y^{opt}\pi}{2}\right] = -\frac{\pi}{s_y^2 \Re[\phi_{22}]}, \quad (3.38)$$

where $[\phi_{kl}]$ is the 2×2 matrix and is defined by

$$[\phi_{kl}] = -\frac{\pi D^2}{4\lambda} B_t^{-1T} \overline{L_t^{-1}} B_t^{-1}, \quad (3.39)$$

with $(k, l) \in [1, 2] \times [1, 2]$ and $\Re[\phi_{kl}]$ refers to the real part of $[\phi_{kl}]$. Eq.(3.38) can be

rewritten in another form as

$$\tan(\alpha_x^{opt}) = \frac{4\lambda}{s_x^2 D^2} \frac{1}{\Re[B_t^{-1T} \overline{L_t^{-1}} B_t^{-1}]} \tag{3.40}$$

$$\tan(\alpha_y^{opt}) = \frac{4\lambda}{s_y^2 D^2} \frac{1}{\Re[B_t^{-1T} \overline{L_t^{-1}} B_t^{-1}]} \tag{3.41}$$

where $\alpha_{x,y}^{opt} = a_{x,y}^{opt}\pi/2$. The next section is devoted to the hologram of an opaque inclusion inside a water droplet. The experimented and simulated holograms from the new model of a pupil function of an opaque inclusion inside a droplet are compared in order to confirm our developed model.

3.6 Hologram of an opaque inclusion

In this section, the above theoretical development of the intensity distribution and an experimental hologram of an opaque inclusion at the centre of a droplet are compared. The experimental and numerical set-up is represented in Fig. 3.3.

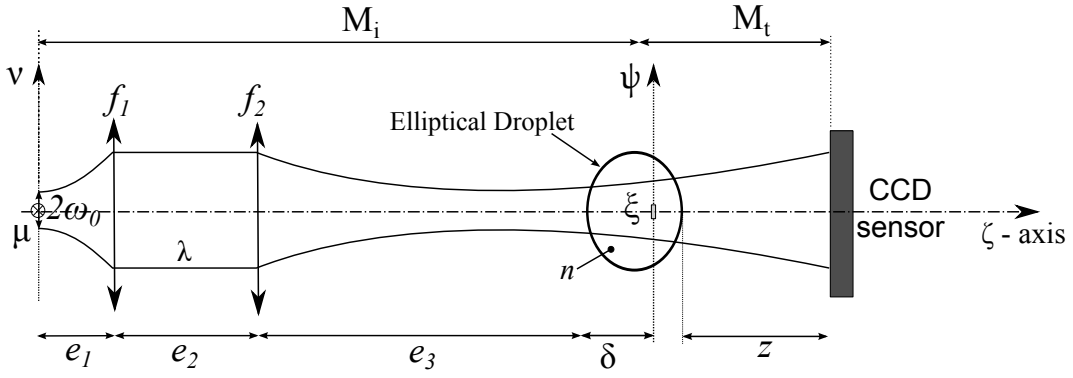

Fig. 3.3: Configuration representing the numerical and experimental set-up with $\lambda = 642nm, \omega_0 = 2.5\mu m, f_1 = 50.4mm, e_1 = f_1, f_2 = 5.5mm, e_2 = 409.56mm, e_3 = 12mm$, and $z = 6.1mm$.

The incident beam is a Gaussian laser diode emitting at the wavelength $642nm$, operating at temperature $25°C$. The beam propagates across an optical system to illuminate a water droplet of d diameter and with a refractive index $n = 1.33$. A hologram image is recorded with a CCD sensor (1234×1624 pixels; each pixel size is $4.4 \times 4.4\mu m$). A $20\mu m$ opaque polymer microsphere from Cospheric Innovations in Microtechnology is inserted into the centre of the droplet. Note here that the optical path E_i in Eq.(3.7) is equal to $E_i = e_1+e_2+e_3+n\delta$ and the optical path E_t in Eq.(3.19) is $E_t = n(d-\delta)+z$ according to the set-up where d is the diameter of the droplet. In the experiment, the powder of opaque particles is mixed with pure water at low (as low as possible) concentration. A syringe is used to form a suspended droplet at its tip. The size of the created droplet is on a millimetric scale. However, the exact size of

the droplet in the experiment could not be determined. The way to predict a droplet's size is using the shadowgraphy technique. When the hologram image of the droplet is recorded, the tip of the needle holding it is included in the image. Fortunately, the size of the real needle is a known parameter and from the image, its image size can be measured. Immediately, we know how big the needle is from the real size. Otherwise, the magnification of an image is known. Then the real size of the droplet can be obtained with the same consideration. In this experiment, the estimated droplet size in the x- and y-direction is not the same - $1.7mm$ in the x-axis and $1.8mm$ in the y-axis. Here, in simulation, the opaque inclusion is considered as a disk-like shape and the droplet is considered as an elliptical shape.

Therefore, we can consider two possiblilities of the imaging system: a circular system and a non-circular system, as discussed in the following sections.

3.6.1 Case of an axisymmetric imaging system

In the case of an opaque particle ($n = m = 0$) in a circular system ($\delta = 0$) or in the case of a spherical droplet, G_n^m in Eq.(3.27) takes the following form:

$$G_0^0(\sigma, \varphi) = 2\pi V_0^0(2\pi\sigma, \chi), \tag{3.42}$$

with $A_{0,0,t}^{0,0,0} = 1$ for all t in Eq.(3.28). This case is a particular case for axisymmetric optical systems. Actually, the millimetric-scale droplet is not spherical due to gravity. The diameters along two perpendicular axes are not the same. The following subsection allows us to better understand non-axisymmetric systems.

3.6.2 Case of an anamorphic system

An anamorphic system is a non-circular system where $\delta \neq 0$ and G_n^m in Eq.(3.27) for an opaque particle is given by

$$G_0^0(\sigma, \varphi) = 2\pi \sum_{q=-\infty}^{+\infty} \sum_{p,t} (-i)^q \beta_{|2q|+2p}^{|2q|}(\delta) \cdot V_t^{2q}(2\pi\sigma, \chi) \cdot e^{i2q\varphi} \tag{3.43}$$

The simulated and experimental images of the intensity distribution recorded on the CCD sensor for an opaque micro-inclusion located at the center of a droplet are given in Fig. 3.4 (a) and Fig. 3.4 (b), respectively. Due to gravity, the millimetric droplet is not a sphere: it is an ellipsoid with different radii of curvature in the x- and y-axes. In the simulation, the radii of curvatures of the droplet are $1.7mm$ along the x-axis and $1.8mm$ along the y-axis.

In Fig. 3.5, the simulated and experimental intensity profiles along both the x- and y-axes of the holograms of the opaque inclusion inside a droplet in Fig. 3.4 are compared. From the results, the simulated and experimental intensity profiles are in very close agreement, confirming the theoretical developments of this chapter.

In this simulation, the diameter of an opaque micro-inclusion is $D = 23.5\mu m$ and its position in the droplet along the propagation direction (z-axis) is $\delta = 0.99mm$.

All parameters used in the simulation are indicated in the caption of Fig. 3.3. The hologram image in the experiment is captured by a 1624×1234 pixels camera with $4.4 \times 4.4 \mu m$ pixel size.

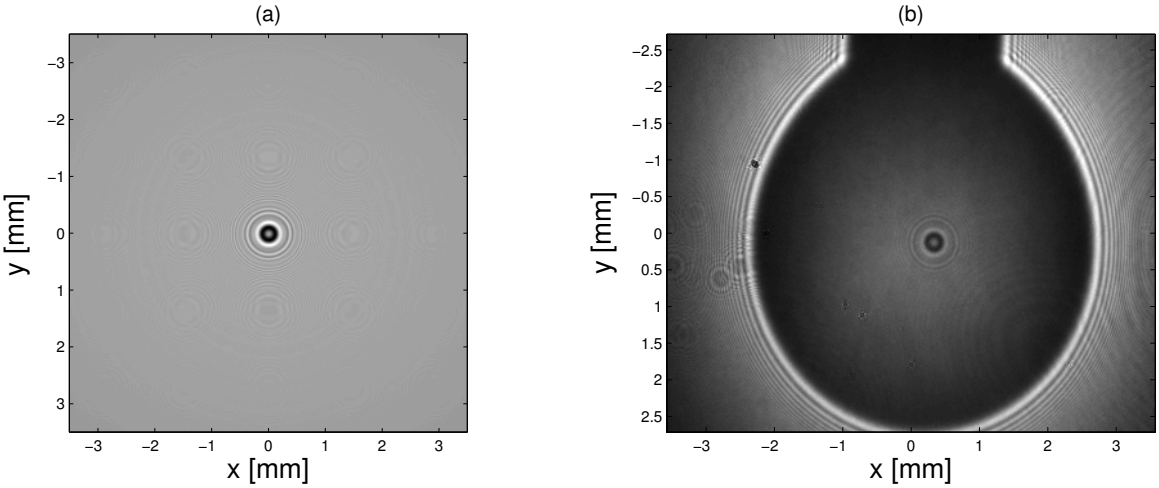

Fig. 3.4: Hologram of an opaque micro-inclusion in a droplet obtained from (a) theoretical development and (b) experimental result.

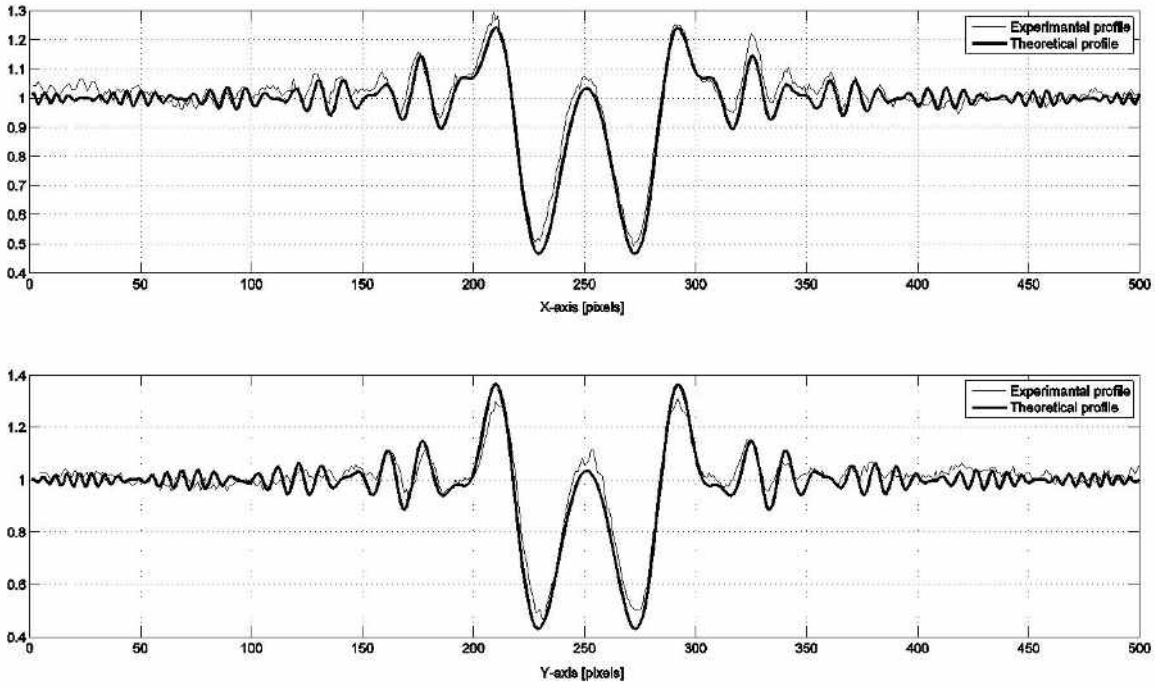

Fig. 3.5: Comparison of the intensity profile of the hologram in Fig. 3.4 between theoretical development and experiment along x-axis (above) and y-axis (below).

3.7 Reconstruction of the opaque inclusion

In this section, the hologram image of an opaque inclusion at the centre of a droplet is reconstructed by using the 2D fractional Fourier transform (2D-FRFT). This reconstruction is a numerically refocused plane of the inclusion. The theoretical details have been described already in Section 3.3. The reconstructed images of the theoretical and experimental holograms in Fig. 3.4 are shown in Fig. 3.6 (a) and (b), respectively.

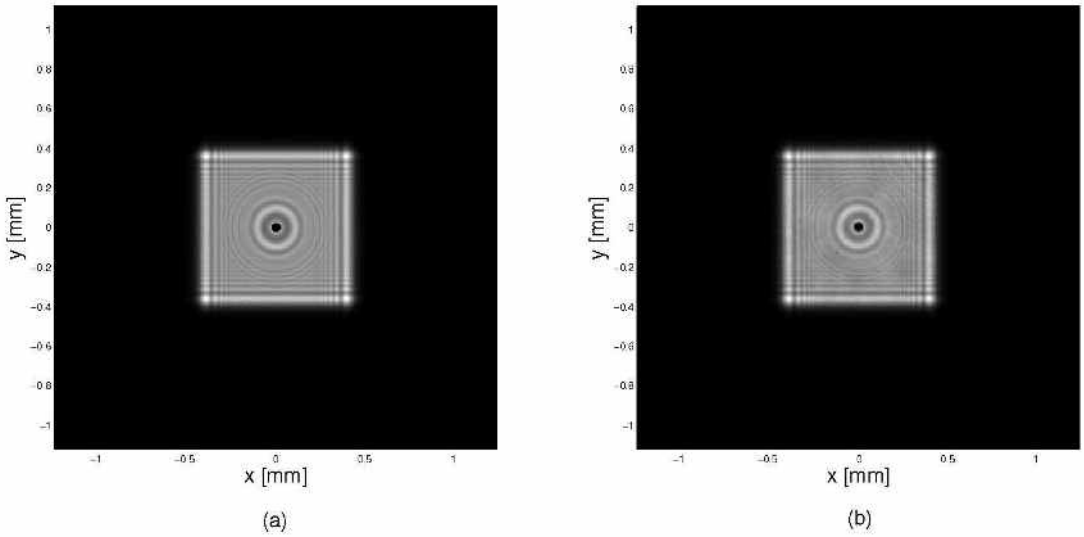

Fig. 3.6: Reconstructed image of an opaque micro-inclusion in a droplet obtained from (a) theoretical development and (b) experimental hologram. The optimal fractional orders are $\alpha_x^{opt} = 0.766\pi/2$ and $\alpha_y^{opt} = 0.763\pi/2$.

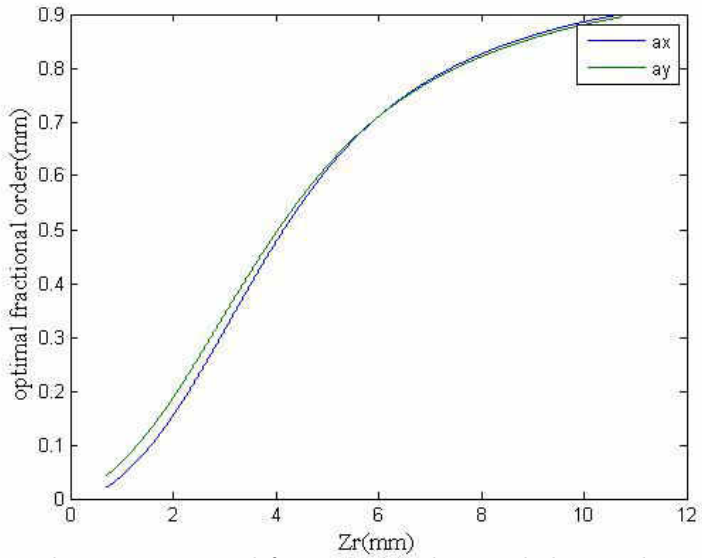

Fig. 3.7: Relationsip between optimal fractional orders and the axial position from the CCD sensor presented in blue and green curves for $a_x^{opt} = 0.766$ and $a_y^{opt} = 0.763$, respectively.

The calculated optimal fractional orders from our theoretical development are $\alpha_x^{opt} = 0.766\pi/2$ and $\alpha_y^{opt} = 0.763\pi/2$. The 2D shape of an inclusion is well recovered

as a circle. From the previous studies, we know already that the optimal fractional orders are related to the axial position of the reconstructed inclusion by the relationship in Fig. 3.7. This finding derived from the theory and we then know that these two fractional orders a_x^{opt} and a_y^{opt} as indicated above correspond to the axial position (position of inclusion from CCD) $z + (d - \delta) = 6.80mm$, whereas the axial position in the simulation is $z_{sim} + (d - \delta) = 6.81mm$. The uncertainty for measuring the axial position is about $\triangle z = 0.01mm$ or $10\mu m$.

To obtain the real size of the inclusion, a scale factor (or magnification factor) must be applied. From the shadowgraphy technique, the experimental magnification factor, denoted g is equal to 2.9. By plotting the intensity profile of the reconstructed inclusion in Fig. 3.6(b), the measured size of an inclusion is $24.6\mu m$, whereas the measured size from the simulation is $24.0\mu m$.

3.8 Hologram of a spherical particle

In this section, only a numerical study was done. There is no inclusion inside a droplet but the droplet itself is considered as a spherical particle. Therefore the refractive index and the spherical shape of the droplet are considered. The droplet here is a very small droplet (in micro-scale, not millimetric scale). Here, we have chosen to compare our holographic model with a general numerical standard of holograms of particles based on rigorous near-field Lorenz-Mie scattering theory (LMT) [83]. The comparison between the developed model and LMT is based on a particle with diameter $D = 20\mu m$ and refractive index $n_i = 1.33$ and the surrounding medium index $n = 1$. In LMT, the incident beam has to be a plane wave. Therefore, the configuration set-up in this study is as represented in Fig. 3.8. In this section, there are three ways to model the droplet. The first approximation is an opaque disk approximation of the droplet. The second is the classical approximation where a droplet is treated like a thin lens. The third way is based on a second description of the pupil function $p(s, \theta)$. The pupil function in this approximation depends on the refractive index and the thickness of the particle. All approximations will be introduced later in this section.

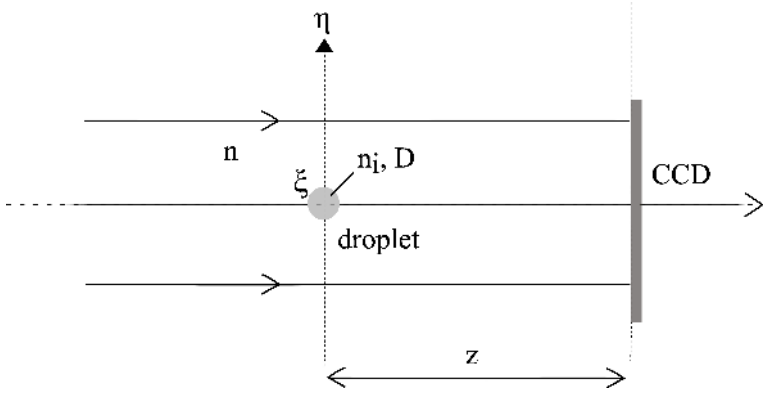

Fig. 3.8: The configuration under study for phase particle (droplet with refractive index n_i). The distance between droplet and CCD is $z = 3mm$.

3.8.1 Case of the opaque disk approximation

The compared intensity distribution between the near-field LMT and an opaque disk approximation of the droplet is shown in Fig. 3.9.

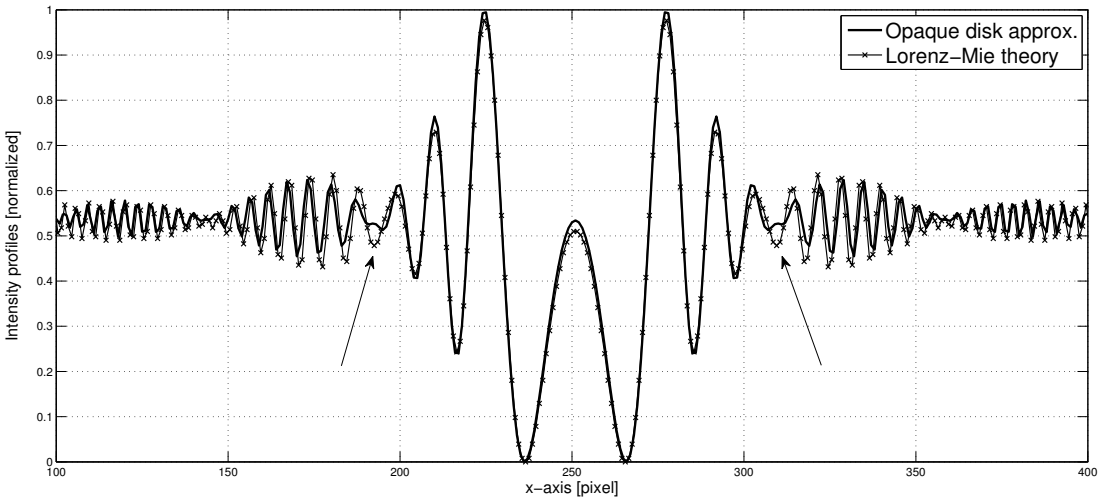

Fig. 3.9: Simulated intensity profile diffracted by a droplet with opaque disk approximation for $\lambda = 642nm, n = 1, n_i = 1.33, D = 20\mu m$, and $z = 3mm$. Comparison with the near-field LMT.

The arrows indicate the position where the zero-th crossing modulation functions of the intensity distribution do not match. Moreover, the reconstructed images of the droplet are different.

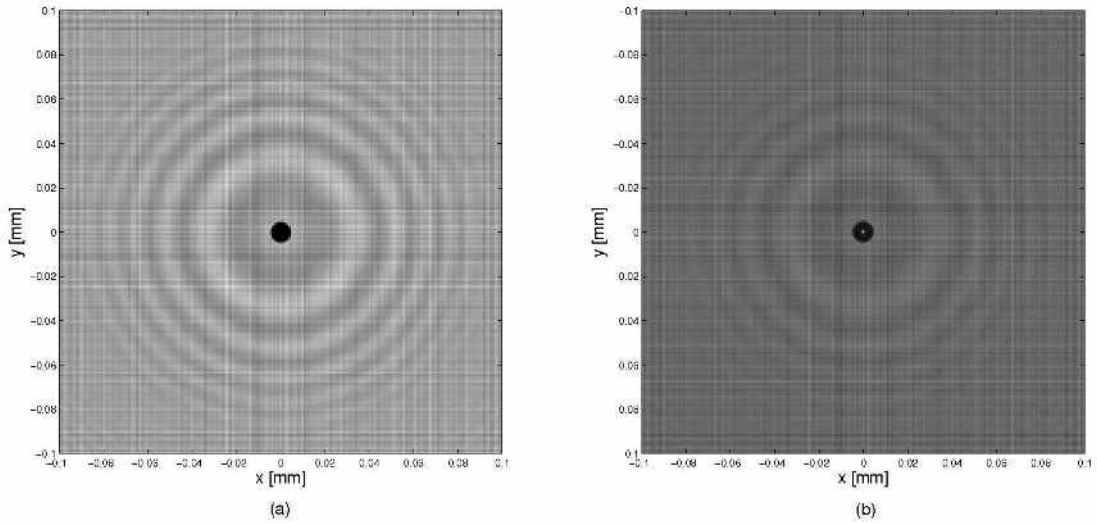

Fig. 3.10: Reconstructed image of a droplet with opaque disk approximation obtained from (a) opaque disk approximation and (b) the near-field Lorenz-Mie scattering theory. The optimal fractional orders are $a_x^{opt} = a_y^{opt} = 0.701$.

Fig. 3.10 (a) shows a digital reconstruction by 2D fractional Fourier transform

in the case of the opaque disk approximation. The calculated optimal fractional orders from Eq.(3.38) are $a_x^{opt} = a_y^{opt} = 0.701$. In the reconstructed image in Fig. 3.10 (b) obtained from LMT, a centred light spot is observed, whereas the opaque disk approximation did not show it and only the disk shape structure is observed BUT THERE IS NO CENTERED LIGHT SPOT. The absence of the light spot in the reconstructed image indicates that the modulation functions for these two cases do not agree. Therefore, we have to find another way to interpret the hologram of a droplet. As indicated above, there are the other methods to approximate a droplet: classical thin lens approximation and the pupil function with a refractive index and its thickness approximation.

3.8.2 Case of the quadratic phase approximation

Under paraxial Gauss conditions, we assume that the droplet is equivalent to a thin lens. Then, the pupil function p of the droplet with aperture D can be described by

$$p(s,\theta) = \left[1 - \exp\left(-i\pi\kappa s^2\right)\right] \cdot Z_0^0(s,\theta), \tag{3.44}$$

where $\kappa = D^2/(4\lambda f)$ and $f = \frac{n_i D}{4(n_i - n)}$ is the effective focal length of the ball-shaped lens. Note that κ can be a complex number, for any absorption in the droplet, but this point will not be addressed here. The second term of Eq.(3.44) can be written as

$$\exp\left(-i\pi\kappa s^2\right) \cdot Z_0^0(s,\theta) = \sum_{\substack{n=0 \\ n\ even}}^{\infty} \gamma_n^0(\kappa) \cdot Z_n^0(s,\theta), \tag{3.45}$$

where $n = 0, 2, 4, \ldots$ and the Zernike moments $\gamma_n^0(\kappa)$ are defined by

$$\gamma_n^0 = (n+1)\exp\left(-i\pi\frac{\kappa}{2}\right)(-i)^{\frac{n}{2}} \cdot j_{\frac{n}{2}}\left(\kappa\frac{\pi}{2}\right). \tag{3.46}$$

For an axisymmetric circular system $\delta = 0$, the semi-analytical expression for G_n^m in Eq.(3.27) is

$$G_n^0(\boldsymbol{\sigma}) = 2\pi \sum_{\substack{n=0 \\ n\ even}}^{\infty} \gamma_n^0(\kappa) \cdot V_n^0(2\pi\sigma, \chi). \tag{3.47}$$

Fig. 3.11 shows the intensity distribution of the quadratic phase approximation compared with LMT. Only the central lobe agrees well using both models. There is a minor shift in the second lobe. This is because the modulation function in this case does not describe the droplet well. However, the centred light spot is observed in the reconstructed image, as shown in Fig. 3.12.

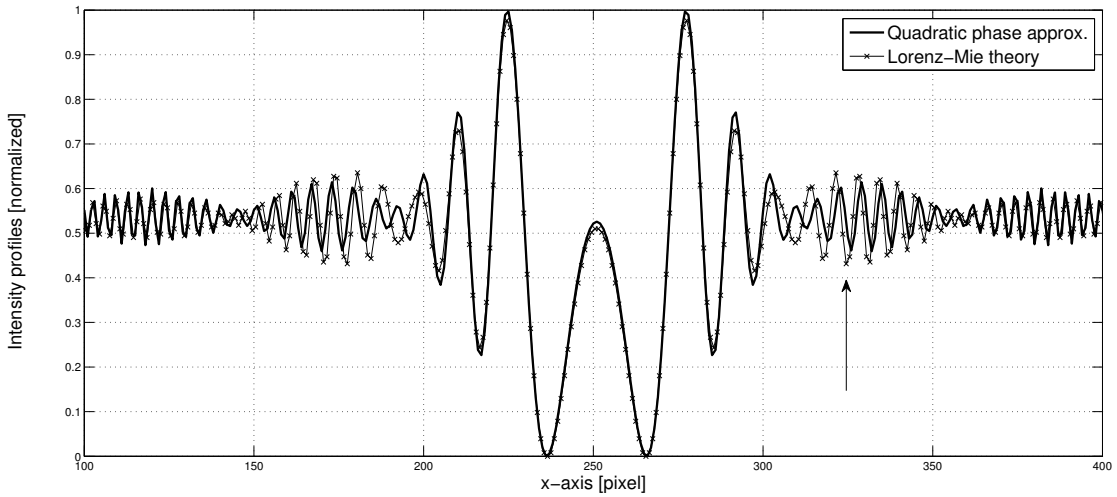

Fig. 3.11: Simulated intensity profile of a droplet with quadratic phase approximation.

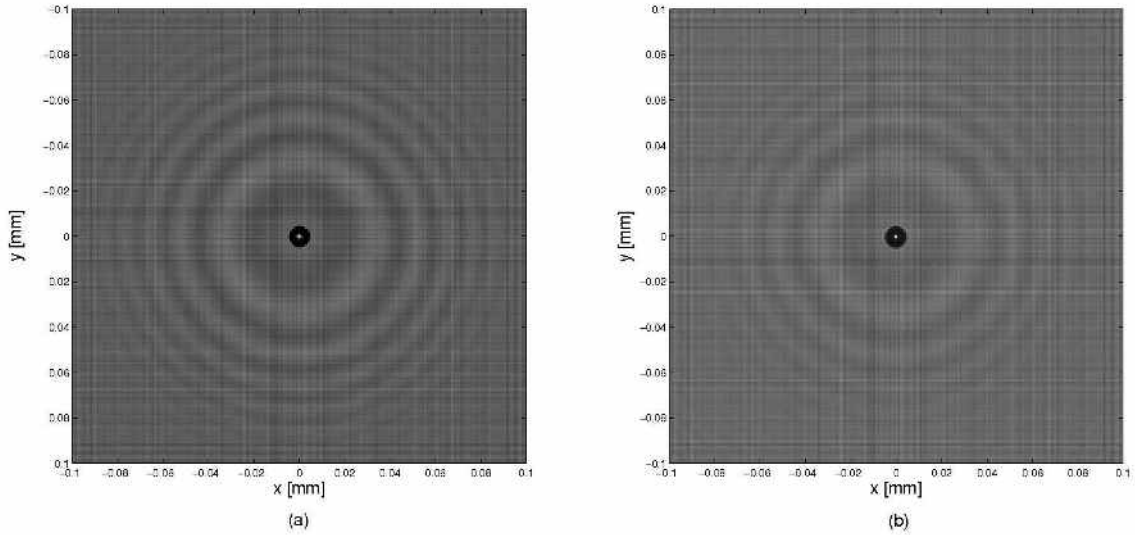

Fig. 3.12: Reconstructed image of the hologram in Fig.3.11 obtained from (a) quadratic phase approximation and (b) the near-field Lorenz-Mie scattering theory. In this case, the optimal fractional orders α_x^{opt} and α_y^{opt} are equal to $0.701\pi/2$.

Fig. 3.12 (a) shows a digital reconstruction image of a droplet by 2D-FRFT under quadratic phase approximation. Fig. 3.12 (b) is a reconstruction image deriving from LMT. The theoretical optimal fractional order is $a_x^{opt} = a_y^{opt} = 0.701$. With quadratic phase approximation, the centred bright spot is observed in the reconstructed image.

3.8.3 Case of the quasi-spherical phase approximation

From Goodman's book, light propagation through a lens is considered, where the lens is considered as a thin lens. Therefore, the ray entering the droplet at coordinates

(x, y) on the entrance face is said to be the same as the exit face and the refraction effect or bending of the ray inside the lens is negligible. With this approximation, the phase delays introduced by a thin lens are proportional to the thickness of the lens at each position.

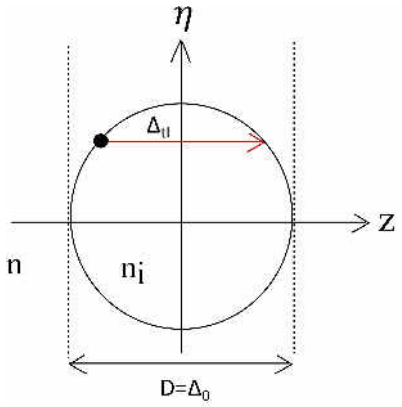

Fig. 3.13: Configuration under study for a glass inclusion illuminated by a plane wave.

In Fig. 3.13, $\triangle_0$ is the maximum thickness of the lens or the thickness on the optical axis and $\triangle_{tl}$ is the thickness at any (ξ, η) position. Thus the phase introduced by a thin lens when it is illuminated by a plane wave is

$$\phi(\xi, \eta) = \frac{2\pi}{\lambda} n_i \triangle_{tl} + \frac{2\pi}{\lambda} n \left(\triangle_0 - \triangle_{tl}\right), \tag{3.48}$$

with

$$\triangle_{tl} = D\sqrt{1 - \frac{4(\xi^2 + \eta^2)}{D^2}}. \tag{3.49}$$

All parameters in Eq.(3.48) are presented in Fig. 3.13. n_i is the refractive index of the droplet ($n_i = 1.33$) and n is the refractive index of the surrounding medium ($n = 1$). The first term of Eq.(3.48) is the phase delay introduced by the droplet and the second term is the phase delay introduced by the remaining region. Eq.(3.48) can be rewritten as

$$\begin{aligned} \phi(\xi, \eta) &= \frac{2\pi}{\lambda} n_i \triangle_{tl} + \frac{2\pi}{\lambda} n \left(\triangle_0 - \triangle_{tl}\right) \\ &= \frac{2\pi}{\lambda} n_i \triangle_{tl} + \frac{2\pi}{\lambda} n \triangle_0 - \frac{2\pi}{\lambda} n \triangle_{tl} \\ &= 2\pi n \frac{D}{\lambda} + \frac{2\pi}{\lambda} \left(n_i - n\right) \triangle_{tl}. \end{aligned} \tag{3.50}$$

But this approximation is not good for a big droplet that cannot be considered as a thin lens. This imposes a need to take into account the refractive law. In this case, the model of the droplet with an approximation called quasi-spherical phase approximation is proposed. This approximation is based on the idea of using a thickness

function to extend the model beyond the thin lens approximation. Here, the droplet is considered to have a spherical shape with constant refractive index n_i. An appropriate transmittance function for the droplet will allow us to evaluate the pupil function. For quasi-spherical phase approximation, only the second term in Eq.(3.50) is considered.

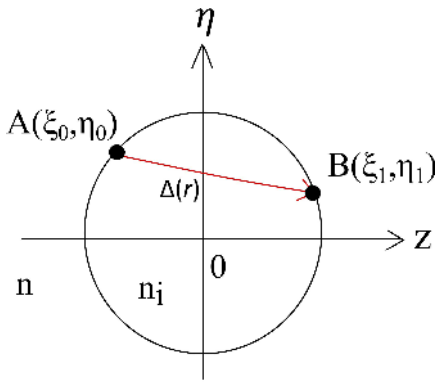

Fig. 3.14: Image showing the entrance and exit ray of the droplet.

From the development introduced, the total phase delay $\phi(\boldsymbol{r})$ of the wave at transverse plane $\boldsymbol{r} = (\xi, \eta)$ when it is passing through the droplet is

$$\phi(\boldsymbol{r}) = 2\pi(n_i - n)\frac{\triangle(\boldsymbol{r})}{\lambda}, \tag{3.51}$$

where $\triangle(\boldsymbol{r})$ is the thickness function which is indicated in Fig. 3.14. Recall that $\boldsymbol{r} = \boldsymbol{s}D/2$, and we have $\triangle(\boldsymbol{r}) = D \cdot (1 - c^2 s^2)^{1/2}$ [for more details, see Appendix F]. The numerical aperture is $c = (n/n_i)$ with $0 \leq c \leq 1$. In Eq.(3.51), we assume that the coordinates of the entrance ray (ξ_0, η_0) at point A and the exit ray (ξ_1, η_1) at point B of the droplet in Fig. 3.14 are not the same. In other words, the bending of the light ray is taken into account. Consequently, in this approximation, the pupil function p can be written as

$$p(s, \theta) = \left[1 - \exp\left(i\pi\kappa_{n_i}\sqrt{1 - c^2 s^2}\right)\right] \cdot Z_0^0(s, \theta), \tag{3.52}$$

where $\kappa_{n_i} = 2(n_i - n)D/\lambda$. The pupil function in Eq.(3.52) can be expanded in terms of circle polynomials as

$$\exp\left(i\pi\kappa_{n_i}\sqrt{1 - c^2 s^2}\right) \cdot Z_0^0(s, \theta) = \sum_{\substack{n=0 \\ n\ even}}^{\infty} \gamma_n^0(-\pi\kappa_{n_i} \cdot u_c) \cdot Z_n^0(s, \theta), \tag{3.53}$$

where $u_c = 1 - \sqrt{1 - c^2}$ and the Zernike moments are

$$\gamma_n^0(x) = (n + 1) \cdot \left[\frac{x}{2} \cdot \boldsymbol{j}_{\frac{n}{2}} \cdot \boldsymbol{h}_{\frac{n}{2}}^{(2)} - \frac{x}{2\nu_c}\boldsymbol{j}_{\frac{n}{2}} \cdot \boldsymbol{h}_{\frac{n}{2}+1}^{(2)}\right], \qquad \nu_c = \frac{1 - \sqrt{1 - c^2}}{1 + \sqrt{1 - c^2}} \tag{3.54}$$

The functions $\boldsymbol{j}_n$ are the spherical Bessel functions of the first kind and $\boldsymbol{h}_n^{(2)}$ are

the spherical Hankel functions of the second kind. In the case of a circular system ($\delta = 0$),the semi-analytical expression of G_n^m is

$$G_n^0(\boldsymbol{\sigma}) = 2\pi \sum_{\substack{n=0 \\ n\ even}}^{\infty} \gamma_n^0 \cdot V_n^0(2\pi\sigma, \chi) \tag{3.55}$$

Fig. 3.15 illustrates the relation $|\triangle_{tl} - \triangle|$ versus $r = \sqrt{\xi^2 + \eta^2}$ where $\triangle_{tl}$ is the thickness without refraction effect or the thickness in thin lens approximation. $\triangle$ is the real thickness when the refraction inside a droplet is taken into account or the thickness with quasi-spherical approximation. In this figure, the relation $|\triangle_{tl} - \triangle|$ versus $r = \sqrt{\xi^2 + \eta^2}$ is plotted for different particle diameters. For smaller particles, the different between the estimated thickness and the real thickness function is very small. Therefore, the interpretation of the droplet as a thin lens is closed to the quasi-spherical approximation of the droplet. For big droplet, *i.e.* $100\mu m$, the thin lens approximation fails when compared to the quasi-spherical phase approximation.

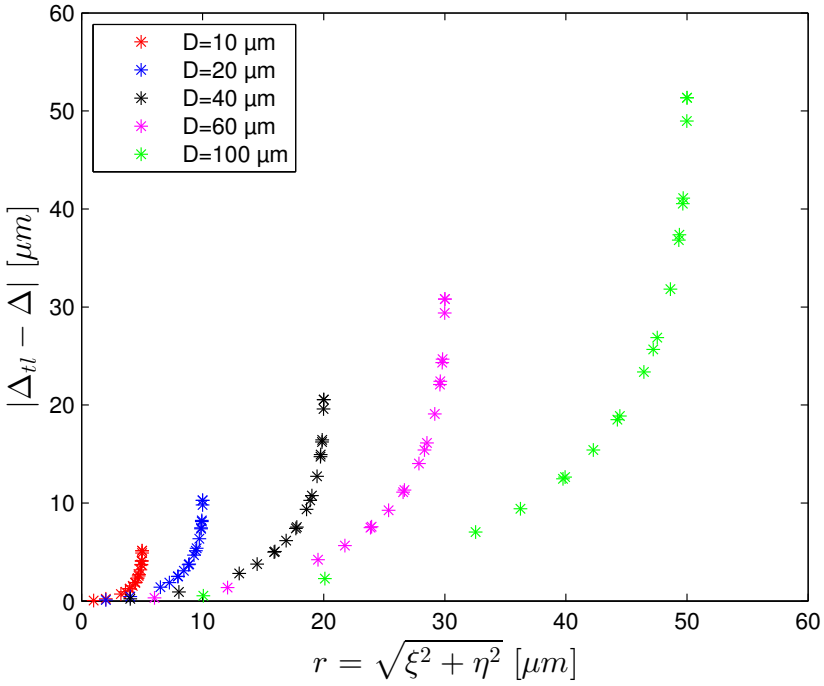

Fig. 3.15: Thickness $\triangle_{tl}$ as thin lens approximation and the real thickness $\triangle$ from quasi-spherical approximation of droplet is plotted versus r for different droplet diameters D

The intensity profile of the hologram of a droplet is illustrated in Fig. 3.16, where the solid line belongs to the proposed quasi-spherical approximation and the cross-faded line belongs to the standard LMT.

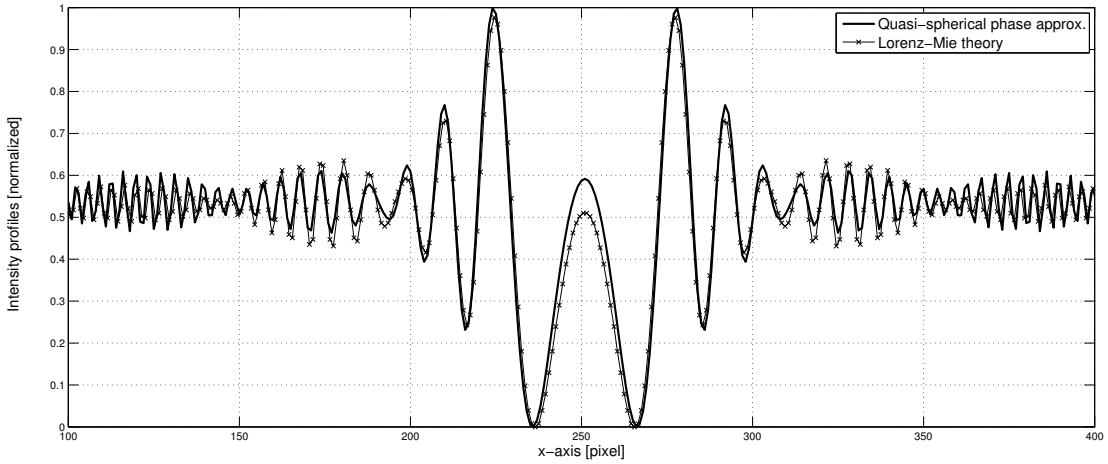

Fig. 3.16: Simulated intensity profile of a droplet with quasi-spherical phase approximation.

From this result, the quasi-spherical phase approximation of a droplet is close to the numerical standard LMT. The reconstructed image of this hologram is shown in Fig. 3.17 with fractional orders $a_x = a_y = 0.701$ in both images. In this case, the centred light spot is observed in both cases. As a result, the model describing the droplet as a thickness function seems to be a very good approximation.

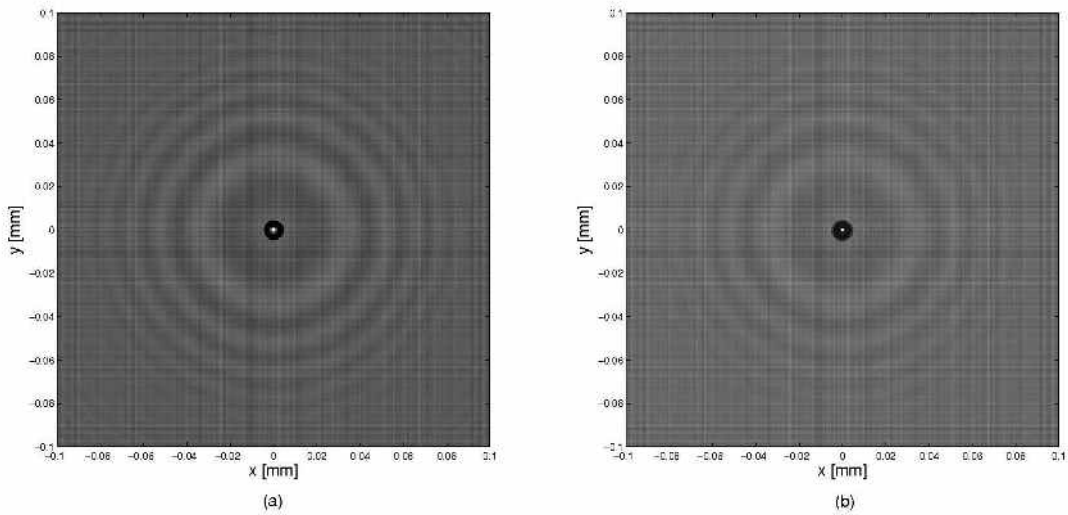

Fig. 3.17: Reconstructed image of a droplet with its intensity distribution as in Fig. 3.16 obtained from (a) quasi-spherical phase approximation and (b) the near-field Lorenz-Mie scattering theory.

Finally, the profiles of the reconstructed droplet using the three approximations are plotted in Fig. 3.18. However, at this moment, only the qualitative results are compared.

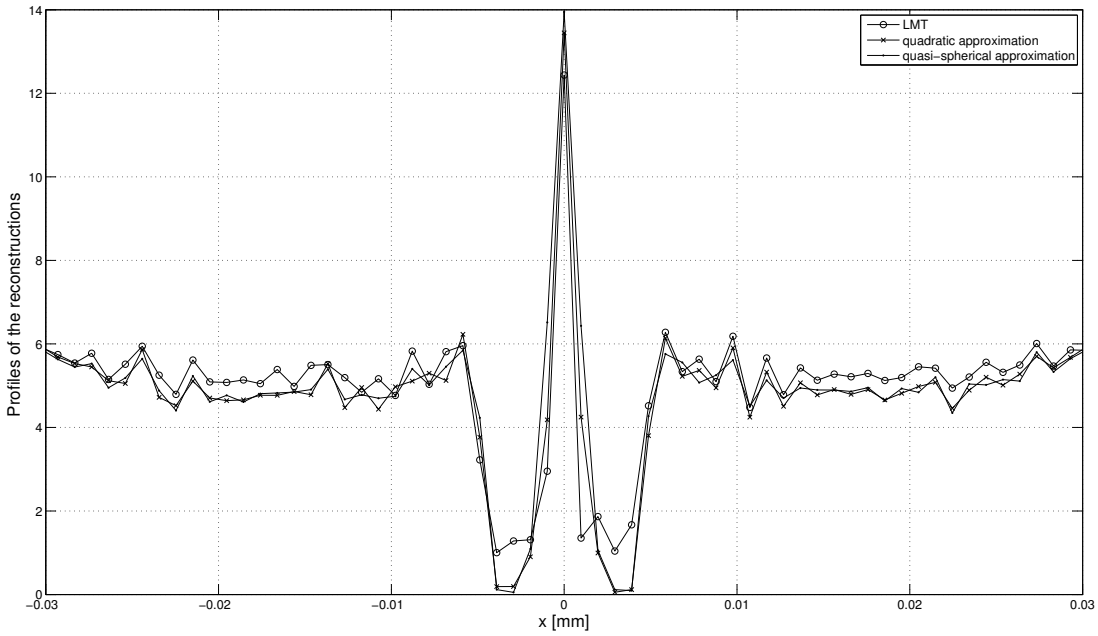

Fig. 3.18: Intensity profiles of reconstructed images of the droplet in the two cases: (i) quadratic phase, and (ii) quasi-spherical phase approximation, compared to LMT.

3.9 Numerical estimation of the Zernike coefficients

In previous sections, the Zernike coefficients were clearly defined from the shape of the particle or inclusion. If the phase $\Phi(s,\theta)$ of the pupil function in Eq.(3.16) contains non-linear chirps, the Zernike coefficients do not have a closed form. Then the Zernike coefficients have to be numerically evaluated. In this section, numerical estimations of the Zernike coefficients γ_n^m are compared to theoretical values. A good evaluation means that the estimated Zernike coefficients can reconstruct the initial function that may contain the higher order spatial frequencies. For a good evaluation, a double exponential formula (DE) is used. This formula allow us to find the optimal change of variable that transforms the original integral over a finite interval to an integral over an infinite interval. In this case, we will change the limit of s and θ from $0 \leq s \leq 1$ and $0 \leq \theta \leq 2\pi$ to an infinite interval. This kind of transformation allows us to apply the trapezoidal rule over $]-\infty,+\infty[$. For variables s and θ, they become

$$\begin{aligned} s = \phi(u) &= \frac{1}{2}\left[1+\tanh\left(\frac{\pi}{2}\sinh(u)\right)\right], \\ \theta = \psi(v) &= \pi\left[1+\tanh\left(\frac{\pi}{2}\sinh(v)\right)\right], \end{aligned} \tag{3.56}$$

where

$$\phi(-\infty)=0, \qquad \phi(\infty)=1, \qquad \psi(-\infty)=0, \qquad \psi(\infty)=2\pi \tag{3.57}$$

By this changing of variables, the estimated Zernike coefficients in Eq.(3.17) become

$$\Gamma_n^m = \frac{(n+1)}{\pi}\cdot\int_{\mathbb{R}^2} F_n^m\left(\phi(u),\psi(v)\right)\cdot\phi(u)\phi'(u)\psi'(v)\,du\,dv \tag{3.58}$$

where

$$F_n^m(s,\theta) = A(s,\theta)\cdot\exp\left[i\Phi(s,\theta)\right]\cdot\overline{Z_n^m(s,\theta)} \tag{3.59}$$

The amplitude $A(s,\theta)$ can be a constant or a Gaussian function. The phase $\Phi(s,\theta)$ is a real value of s and θ. The prime refers to the derivative of that function. Therefore,

$$\phi'(u) = \frac{\pi}{4}\frac{\cosh(u)}{\cosh^2\left(\frac{\pi}{2}\sinh(u)\right)} = O\left(\exp\left(-\frac{\pi}{2}(1-\alpha)\exp|u|\right)\right), \quad |u|\to\infty \tag{3.60}$$

and

$$\psi'(v) = \frac{\pi^2}{2}\frac{\cosh(v)}{\cosh^2\left(\frac{\pi}{2}\sinh(v)\right)} = O\left(\exp\left(-\frac{\pi}{4}(1-\alpha)\exp|v|\right)\right), \quad |v|\to\infty \tag{3.61}$$

with $0<\alpha<1$. The integrand in Eq.(3.58) decays by double exponential after the transformation. That is why this formula is called the double exponential formula. After this transformation, the integrand $\phi'(u)$ has singular points ($\phi'(u_0)=0$) where u_0 is a complex value which is given by

$$\cosh(u_0) = 0, \qquad u_0 = \pm i\frac{\pi}{2} + i2\pi\mathbb{Z}, \tag{3.62}$$

where $\mathbb{Z}$ is an integer and the poles p_0 are given by

$$\cosh^2\left(\frac{\pi}{2}\sinh(p_0)\right) = 0, \qquad p_0 = \pm i\ \arcsin(1) = \pm i\frac{\pi}{2} + i2\pi\mathbb{Z}. \tag{3.63}$$

To find the sampling period, we need to avoid the singular points and poles, which corresponds to [85]

$$|\Im[u]| < d = \frac{\pi}{2}, \tag{3.64}$$

where d is the minimum distance between the singular points and the real axis in a complex plane. Then we used the trapezoidal formula as in [85] and Eq.(3.58) becomes

$$\Gamma_n^m = \frac{(n+1)}{\pi}\cdot\delta_n\delta_v\sum_{k=-N}^{+N}\sum_{l=-N}^{+N} F_n^m\left[\phi(k\delta_u),\psi(l\delta_v)\right]\cdot\phi(k\delta_u)\ \phi'(k\delta_u)\ \psi'(l\delta_v) + \triangle\gamma_\delta. \tag{3.65}$$

$\delta_{u,v}$ is the constant sampling period along the $u-$ and $v-$axis. To get Eq.(3.65), Eq.(3.58) is transformed from an integral with an infinite interval to summation with infinite interval first. Then it is transformed again to the summation with a finite interval $(-N,+N)$. $\triangle\gamma_\delta$ is linked to the discretization and truncation errors as in [85], Eq.(3.13) and (3.19), pp.909-910.

$$\triangle\gamma_\delta = O\left(\exp\left[-\frac{2\pi d}{\delta_{u,v)}}\right]\right) + O\left(\frac{\pi}{4}\exp\left[-\frac{\pi}{2}(1-\alpha)\exp(N\delta_{u,v})\right]\right) \tag{3.66}$$

The sampling period $\delta_{u,v}$ is chosen such that the discretization and truncation errors have the same orders of magnitude. Therefore,

$$\exp\left[-\frac{2\pi d}{\delta_{u,v)}}\right] = \frac{\pi}{4}\exp\left(-\frac{\pi}{2}(1-\alpha)\exp(N\delta_{u,v})\right). \tag{3.67}$$

Then we can determine the sampling period $\delta_{u,v}$ or the number of evaluation N. The plotted curves between the Zernike coefficient and n of Eq.(3.46) with quadratic approximation and Eq.(3.58) are compared as shown in Fig. 3.19. This figure compares the numerical Zernike coefficient γ_n^m and the estimated Zernike coefficient Γ_n^m under quadratic approximation. The comparison is of both the imaginary part and the real part of the Zernike coefficient. This comparison introduces an error $\triangle_e$ and is defined by

$$\triangle_e = \max\left(||\Re(\Gamma_n^m) - \Re(\gamma_n^m)| + |\Im(\Gamma_n^m) - \Im(\gamma_n^m)||\right). \tag{3.68}$$

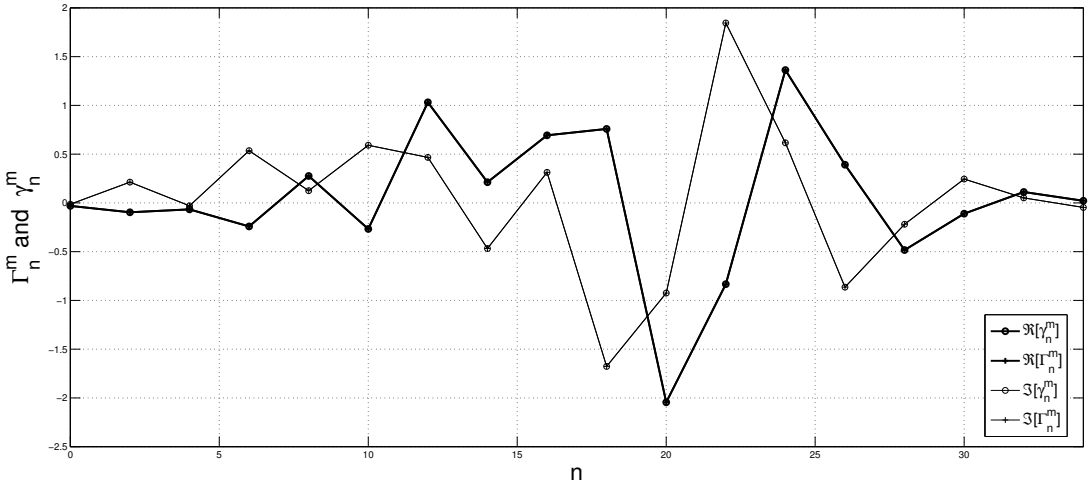

Fig. 3.19: Graph comparing the theoretical Zernike coefficients (γ_n^m) and the estimated Zernike coefficients (Γ_n^m) with n for the case of quadratic phase approximation.

Fig. 3.19 represents in the case of $m = 0$ and the κ coefficient equal to 7.7296. The maximum error obtained is 0.557×10^{-13} over interval $n = (0, 34)$.

The comparison curve between the Zernike coefficients and n of Eq.(3.54) with quasi-spherical phase approximation and Eq.(3.58) is illustrated in Fig. 3.20.

In this figure both theoretical and numerical estimated Zernike coefficients are compared under quasi-spherical phase approximation. The maximal error of the comparison in Fig. 3.20 is 0.519×10^{-13} over interval $n = (0, 34)$. From these comparisons, the error between the theoretical Zernike coefficients and the estimated coefficients is very small. We can conclude that this approximation works well for a pure phase pupil function.

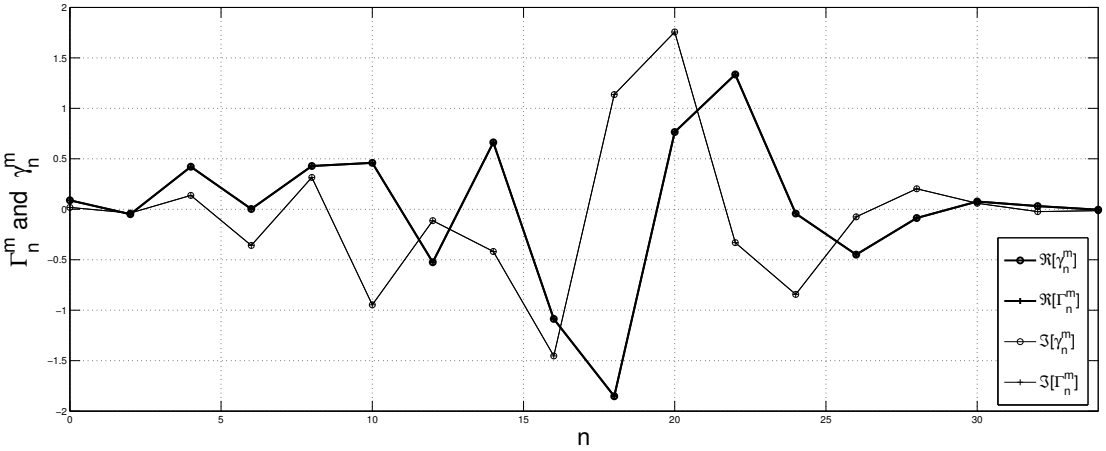

Fig. 3.20: Graph comparing the numerical Zernike coefficients (γ_n^m) and the estimated Zernike coefficients (Γ_n^m) with n for the case of quasi-spherical phase approximation.

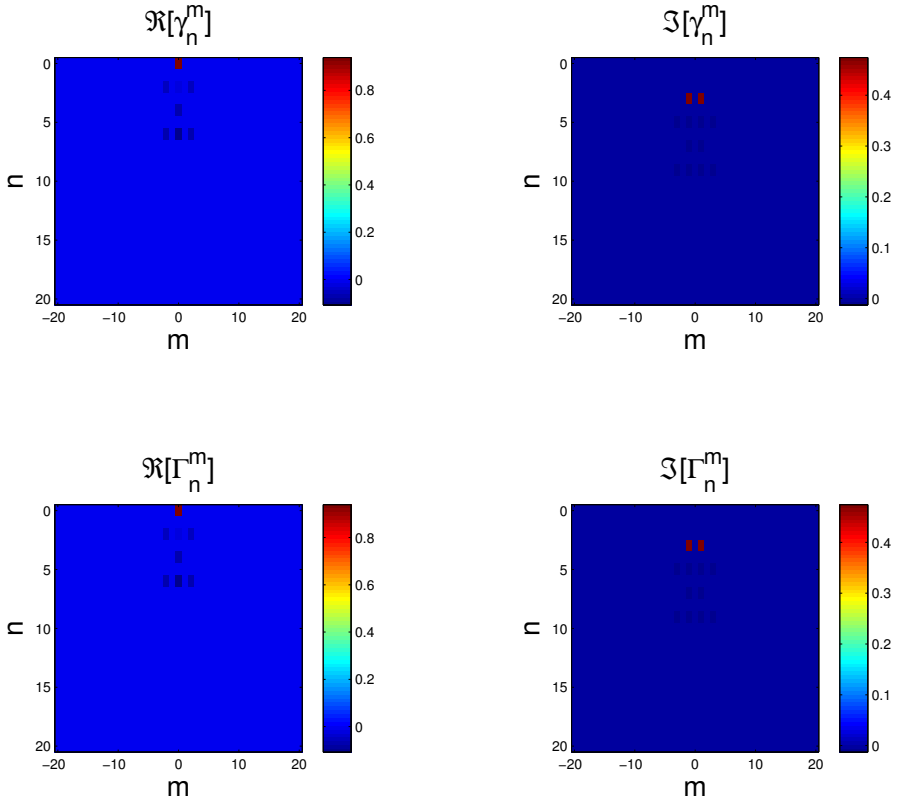

Fig. 3.21: Comparison between the theoretical Zernike coefficients γ_n^m and the estimated Zernike coefficients Γ_n^m of coma function with $N = 100$ and $\delta_u = \delta_v = 0.0486167$.

For example, if the pupil function $p(s,\theta)$ is a coma function and it is defined by

$$p(s,\theta) = \exp(i\alpha R_3^1(s)\cos\theta) \simeq \sum_{n,m} \Gamma_n^m \cdot Z_n^m(s,\theta), \quad \alpha = 1 \tag{3.69}$$

The numerical estimation of the Zernike coefficients Γ_n^m can be compared to the theoretical Zernike coefficients γ_n^m as shown in Fig. 3.21, with both real and imaginary parts which are represented by $\Re$ and $\Im$, respectively. The maximum error is equal to 0.854×10^{-15} over the range $(n, m) = [0, 20] \times [-20, 20]$.

3.10 Hologram of a glass inclusion

In this section, the quasi-spherical phase approximation is used to describe a glass inclusion inside a droplet. The experimental study of a glass inclusion inside the droplet is performed. The experimental setup is presented in Fig. 3.22. A glass inclusion is located at the centre of a transverse plane of a droplet. The experimental parameters in Fig. 3.22 are: $\lambda = 642nm, \omega_0 = 2.5\mu m, f_1 = e_1 = 50.4mm, f_2 = 5.5mm$, and $z = 6.1mm$. The radius of curvature of droplet in the x and y directions is $R_x = 0.785mm$ and $R_y = 0.815mm$ with refractive index $n_1 = 1.33$. The diameter of the glass inclusion is $D = 20\mu m$ with refractive index $n_2 = 1.5$.

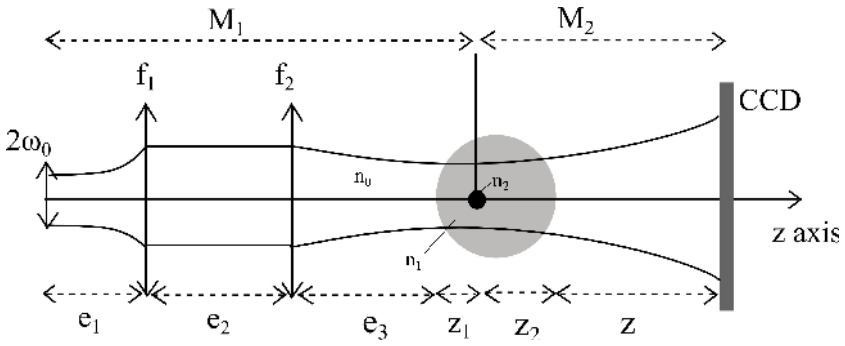

Fig. 3.22: Configuration under study for droplet with a glass inclusion (side or top view).

The hologram of a glass inclusion located at the centre of the droplet is first recorded by a 1234×1234 pixels CCD sensor and each pixel's size is $4.4\mu m$. Then the hologram is cropped for the region of interest with 500×500 pixels as in Fig.3.23 (a). According to the previous section which mention that the reconstructed phase particle under quadratic phase and quasi-spherical phase approximation gives a white spot at the centre of the reconstructed particle, an example of a hologram and its reconstruction image of a droplet with a $20\mu m$ glass inclusion are presented in Fig. 3.23 (a) and (b), respectively.

In Fig. 3.23(b), the white spot is observed at the centre of the reconstructed glass inclusion. The estimated diameter of this glass inclusion is $20.13\mu m$ where the magnification factor is 2.9. To consider the axial position in the drop of the inclusion, see Fig. 3.7.

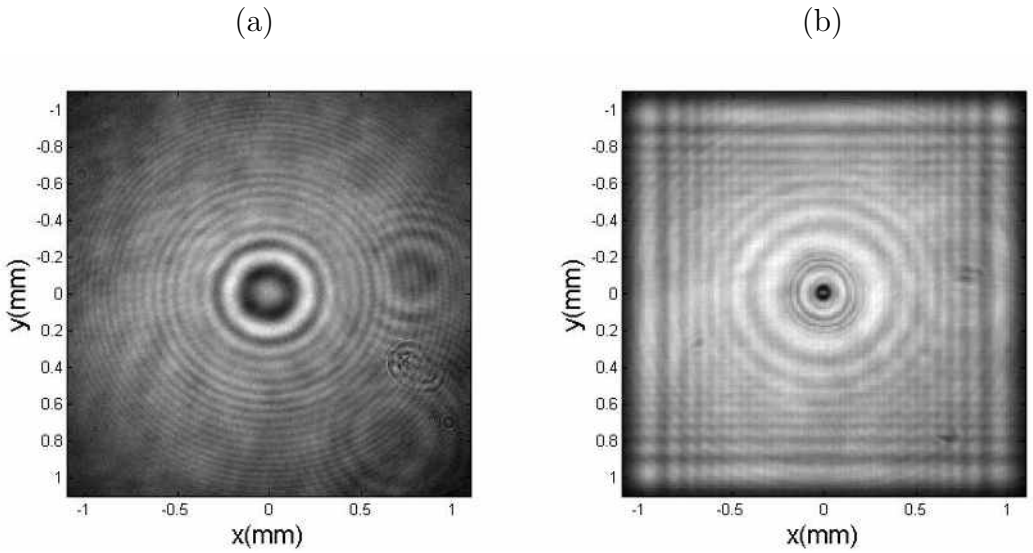

Fig. 3.23: (a) is the hologram of $20\mu m$ glass inclusion inside a droplet. (b) is the reconstruction image of (a) with fractional orders $a_x = 0.8\pi/2$ and $a_y = 0.77\pi/2$

Fig. 3.24 shows the intensity profile along the x- and y-axis of the hologram presented in Fig. 3.23 (a). For the high frequency signal, a shift between the profile of the x- and y- axis can be observed.

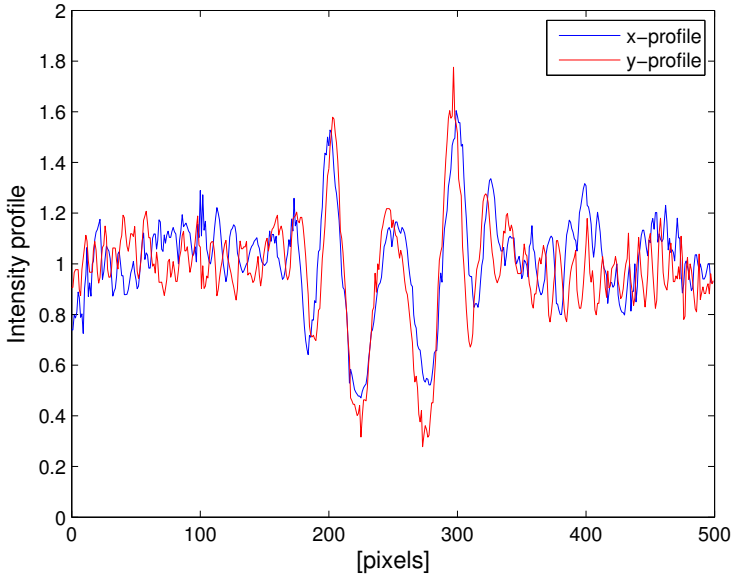

Fig. 3.24: Intensity profile along x- and y- axis of the hologram in Fig. 3.23(a).

Fig. 3.25 shows the intensity profiles along the x- and y-axis of the reconstructed particle from Fig. 3.23(b). The central peak of Fig. 3.25 shows the white spot at the centre of the reconstruction particle. From this result, it is confirmed that the bright spot could be observed in the reconstructed image of a transparent particles (in this case, a glass particles) but not in an opaque particle.

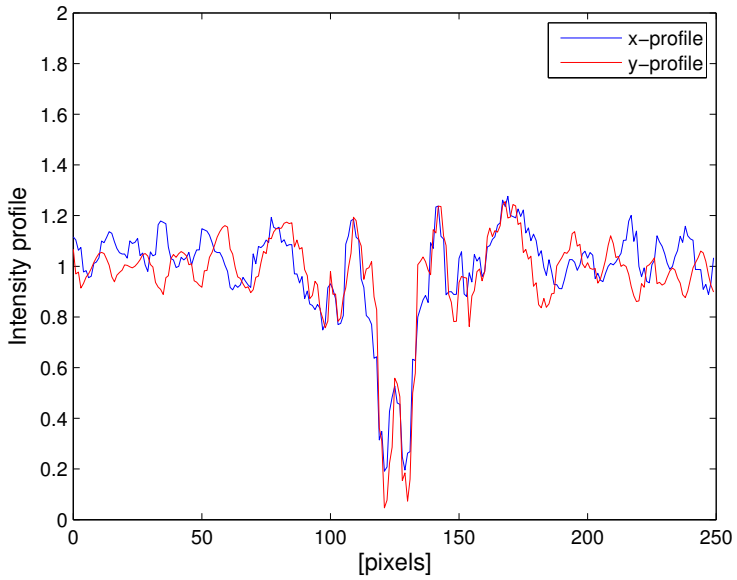

Fig. 3.25: Intensity profile along x- and y- axis of the reconstructed particle in Fig. 3.23(b).

3.11 Conclusions

In this chapter, a mathematical model giving the intensity distribution for the hologram of a particle is proposed. Three approximations have been proposed to describe the pupil function: opaque disk, quadratic phase approximation, and quasi-spherical phase approximation. The holograms obtained with these three approximations were compared with the near-field Lorenz-Mie scattering theory. Both the quadratic and quasi-spherical phase approximations represent the pupil in terms of the circle polynomials. From the results obtained, the opaque disk approximation fails to describe a centred light spot present in the reconstructed image of the particle, while the other two do not. The quasi-spherical phase approximation is the best of the three approximation proposed in this chapter. This approximation considers the true thickness function. In conclusion, our proposed model is well suited to determine both opaque and phase particles (with quasi-spherical phase approximation). However, this model has some limitations: the refractive index of the particle has to be higher than the index of the surrounding medium. It cannot describe an air bubbles in a liquid.

4. GENERAL MODEL OF ARBITRARILY SHAPED NON-CENTERED OPAQUE/PHASE OBJECT

In the previous chapter, we proposed a model to describe various kinds of pupil functions of spherical opaque or transparent particles. Nevertheless, the model is limited to one particle located on the centre of the optical axis of the incident Gaussian beam. In this chapter, a general numerical model that can create arbitrarily shaped non-centered opaque or phase objects is introduced. The possibility of analysing such transparent phase objects using digital in-line holography and 2D fractional Fourier transform is then demonstrated numerically. With this technique, the study of opaque objects is well understood already. However, in the general case, the object under investigation is not necessarily opaque. It can be transparent, for example in the study of biological cells. Research on phase contrast metrology by digital holography has been proposed in [86, 87, 61].

There are two configurations under study in this chapter. Firstly, we consider two irregularly shaped opaque and phase objects located at two different planes as represented in Fig. 4.10. The second is the study of two irregularly shaped phase and opaque objects located inside a droplet, as will be shown later in Fig. 4.15. The irregularly-shaped objects in this chapter are produced by defining numerically arbitrarily-shaped transmission functions. An object will be created as a collection of many small circular particles. All these small circular particles are connected in order to form the irregularly shaped object. In this study, "N" elementary circular particles are generated to create an object. The collection of these elementary particles is generated randomly. Note that only a numerical study is performed in this chapter.

In section 4.1, a mathematical expression of the electric field in the object's plane is evaluated. This mathematical development is based on ABCD matrix formalism. The definition of the transmission function of irregularly-shaped opaque and phase objects is considered in this section. The field amplitude at the CCD sensor is briefly described in this section and a brief mathematical analysis of the hologram is presented. The holograms generated by phase and opaque objects located in different planes are then simulated and reconstructed in section 4.2. In section 4.3, the hologram and reconstructed images of phase and opaque objects located in the same longitudinal planes inside a water droplet are presented. An example of the different object shapes is given in section 4.4. Next, we propose the possiblility of adding noise into the simulated hologram image in section 4.5. After that, the conclusion of this work is presented.

4.1 Mathematical development

4.1.1 Amplitude distribution of the beam in the plane of the object

Recall that the basic idea of digital in-line holograhy is to record the intensity distribution of the diffraction pattern by an object on a CCD camera. Fig. 4.1 is the numerical set-up with a Gaussian incident beam.

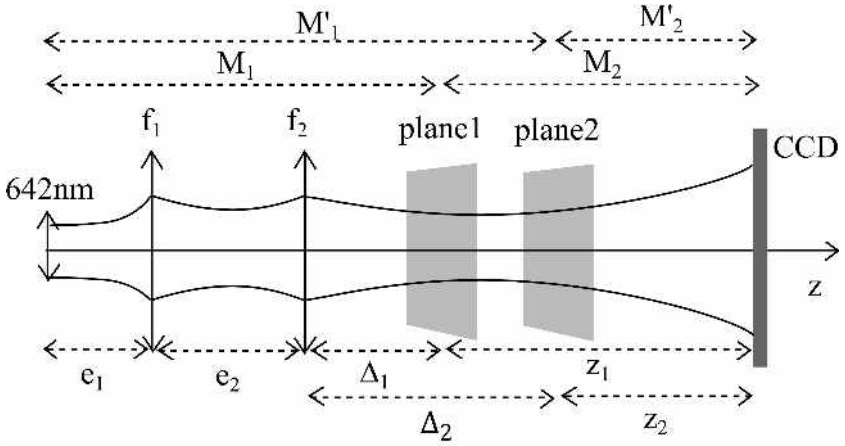

Fig. 4.1: Numerical set-up of the objects located in two different planes with $\omega_0 = 2.3\mu$ m, $e_1 = 58.8$mm, $e_2 = 342.84$mm, $f_1 = 42.8$mm, $f_2 = 5.5$mm,$\triangle_1 = 9.5$mm, $\triangle_2 = 10$mm, $z_1 = 8.5$mm,and $z_2 = 8$mm.

At the beginning of the propagation, the waist of the incident Gaussian beam is located at the origin ($z = 0$). The electric field amplitude in the incident plane is

$$G(\mu, \nu, z = 0) = G(\mu, \nu) = \exp\left(-\frac{\mu^2 + \nu^2}{\omega_0^2}\right), \tag{4.1}$$

where ω_0 is the waist of the beam as shown in Fig. 2.5. Then the incident light source propagates through the first optical system between the incident plane and the particle plane, which is denoted by a transfer matrix M_1 as seen in Fig. 4.1. The complex field amplitude of the wave at the particle's plane, G_1, can be described by a generalized Fresnel integral. G_1, is defined by

$$\begin{aligned} G_1(\xi, \eta) = \frac{\exp(i\frac{2\pi}{\lambda}E_1)}{i\lambda\sqrt{B_1^x B_1^y}} \int_{\mathbb{R}^2} G(\mu, \nu) \exp\left(i\frac{\pi}{\lambda B_1^x}[A_1^x\mu^2 - 2\xi\mu + D_1^x\xi^2]\right) \\ \exp\left(i\frac{\pi}{\lambda B_1^y}[A_1^y\nu^2 - 2\eta\nu + D_1^y\eta^2]\right) d\mu\, d\nu, \end{aligned} \tag{4.2}$$

where E_1 is an optical path between the incident plane and the object's plane. $A_1^{x,y}$, $B_1^{x,y}$, and $D_1^{x,y}$ are the matrix elements of the matrix $M_1^{x,y}$, where $M_1^x = M_1^y = M_1$, for an axisymmetric system. Substituting Eq.(4.1) into Eq.(4.2), the complex amplitude $G_1(\xi, \eta)$ at the particle's plane becomes

$$G_1(\xi, \eta) = \frac{\exp(i\frac{2\pi}{\lambda}E_1)}{i\lambda\sqrt{B_1^x B_1^y}} G_0 K_1^x K_1^y \exp\left[-\left(\frac{\xi^2}{\omega_{1_x}^2} + \frac{\eta^2}{\omega_{1_y}^2}\right)\right] \exp\left[-\frac{i\pi}{\lambda}\left(\frac{\xi^2}{R_{1x}} + \frac{\eta^2}{R_{1y}}\right)\right], \tag{4.3}$$

with

$$K_1^{x,y} = \left(\frac{\pi\omega_0^2}{1 - i\frac{\pi\omega_0^2}{\lambda}\left(\frac{A_1^{x,y}}{B_1^{x,y}}\right)} \right)^{1/2}, \tag{4.4}$$

$$\omega_{1_{x,y}} = \left(\frac{\lambda B_1^{x,y}}{\pi\omega}\right)\left[1 + \left(\frac{\pi\omega_0^2}{\lambda}\frac{A_1^{x,y}}{B_1^{x,y}}\right)^2\right]^{1/2}, \tag{4.5}$$

$$R_{1_{x,y}} = -\frac{B_1^{x,y}}{D_1^{x,y} - \frac{A_1^x\left(\frac{\pi\omega_0^2}{\lambda B_1^{x,y}}\right)^2}{1+\left(\frac{\pi\omega_0^2}{\lambda}\frac{A_1^{x,y}}{B_1^{x,y}}\right)^2}}, \tag{4.6}$$

where $\omega_{1_{x,y}}$ and $R_{1_{x,y}}$ are the beam waist radii and the beam curvature at the object plane, respectively. For more details, see Appendix A.

4.1.2 Definition of the objects

In this section, the numerical definitions of the irregularly-shaped opaque and phase objects are explained. The irregularly-shaped object is created from a collection of small circular disks. These small circular particles are collected in one and two directions that will be explained in 1D and 2D description. Both opaque and phase objects description will be described in the following topics.

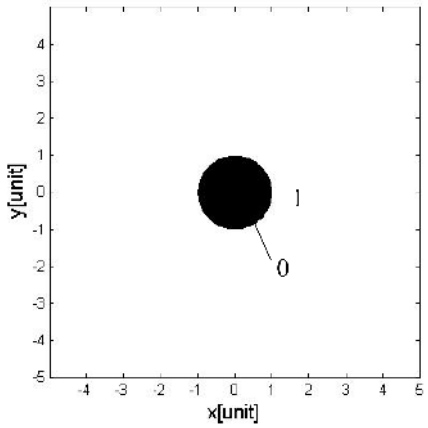

Fig. 4.2: Opaque disk locates at $(x, y) = (0, 0)$.

Creation of an opaque object

-1D description

In the simulation, the irregular shape of an opaque object can be created by first

considering one opaque disk. The opaque disk is presented in Fig. 4.2. In the simulation, we assume that the diameter of the opaque disk is equal to 2 units.

For the opaque particle, the transmission function is defined as

$$T(x,y) = \begin{cases} 0, & \text{if } \sqrt{x^2+y^2} < \frac{D}{2} \\ 1, & \text{otherwise} \end{cases}, \tag{4.7}$$

where D is the diameter of the disk. The transmission function of one opaque disk in Fig. 4.2 located at the centre of the $x-y$ plane is shown versus the x-axis (for $y=0$) in the following figure.

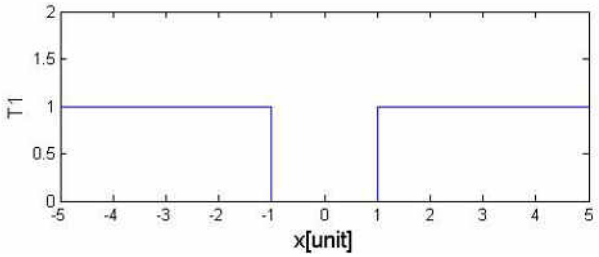

Fig. 4.3: Transmission function of an opaque disk located at the centre of x axis. The diameter of the opaque disk is 2 units.

Fig. 4.3 shows the transmission function of the opaque disk plotted along the x-axis. The transmittance inside the disk is equal to zero and equal to one outside the disk. For 1D description of an arbitrarily-shaped opaque object, the other opaque disks are located along one direction (x or y direction). To do this, the second opaque disk is generated with distance $\triangle$ far away from the first disk along one direction or the x-direction in this example. The third opaque disk is located far from the second disk with the same distance $\triangle$ in the x-direction and so on. For "N" opaque disks, the 1D opaque object can be obtained and it is composed of "N" opaque disks. If "N" is high enough and the distance $\triangle$ is small enough, the shape of this opaque object will look like a rod or wire shape. An example of an opaque object composed of three opaque disks is presented in Fig. 4.4.

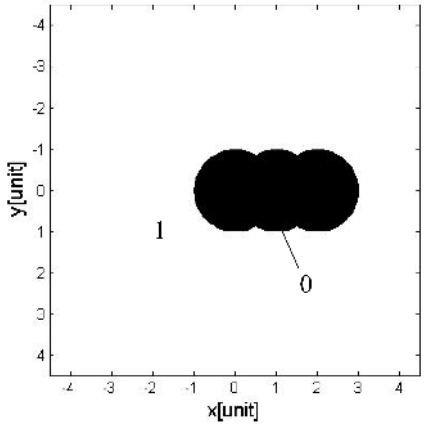

Fig. 4.4: Three opaque disks separated by distance $\triangle = 1$unit.

In Fig. 4.4, three opaque disks are created along the x-direction. All three disks have a diameter of 2 units and each of them is separated by distance $\triangle = 1$ unit.

-2D description

The 2D description of the opaque object can be generated by varying the position of each opaque disk in both the x and y directions. The displacement in the x and y directions are represented by $\triangle_x$ and $\triangle_y$, respectively. The first opaque disk with diameter, D, is located at its original position (x_0, y_0). The position of the second disk is generated randomly and it can be defined in different ways. Fig. 4.5 shows an example of how to define the random position in 2D. In this case, one random number J is generated numerically and $0 \leq J \leq 1$. Let $J \leq 0.5$, the opaque disk changes in the x direction with displacement $\triangle_x$. Let $0.5 < J \leq 1$, then the disk changes its position in the y direction with displacement $\triangle_y$. The example of 10 opaque disks is shown in Fig. 4.5.

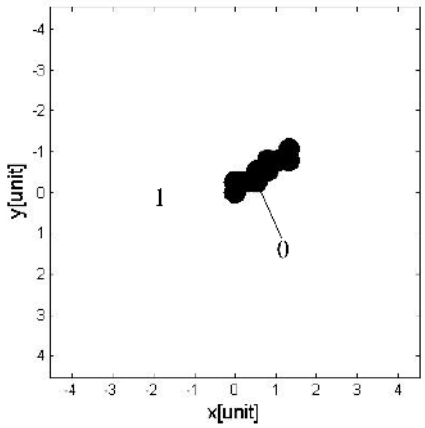

Fig. 4.5: Ten opaque disks located in two directions. They are separated by displacement $\triangle_x = 0.25$ and $\triangle_y = 0.25$.

The diameter of the opaque disk in Fig. 4.5 is 0.5 unit. The displacements are $\triangle_x = 0.25$ and $\triangle_y = 0.25$. From this description, the arbitrary shape of the opaque object can be generated.

Creation of a phase object

In this section, I will describe how to create an irregularly-shaped phase object. In the simulation, the irregular shape of a constant phase object can be created by first considering one phase disk. For a phase particle, the transmission function is defined as

$$T(x,y) = \begin{cases} e^{i\phi}, & \text{if } \sqrt{x^2+y^2} < \frac{D}{2} \\ 1, & \text{otherwise} \end{cases}, \tag{4.8}$$

where D is the diameter of a disk.

-1D description

A circular phase disk located at $(x, y) = (0, 0)$ is presented in Fig. 4.6. The diameter of the disk is 2 units. The transmission value inside the disk is equal to $e^{i\phi}$ and the value outside the disk is equal to 1.

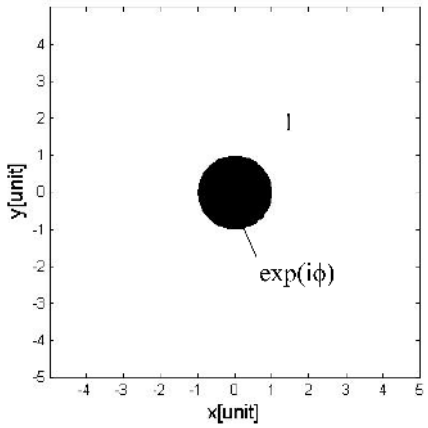

Fig. 4.6: A phase disk located at the origin.

The transmission function of the phase particle is developed from the opaque particle's transmission function as shown in Fig. 4.7.

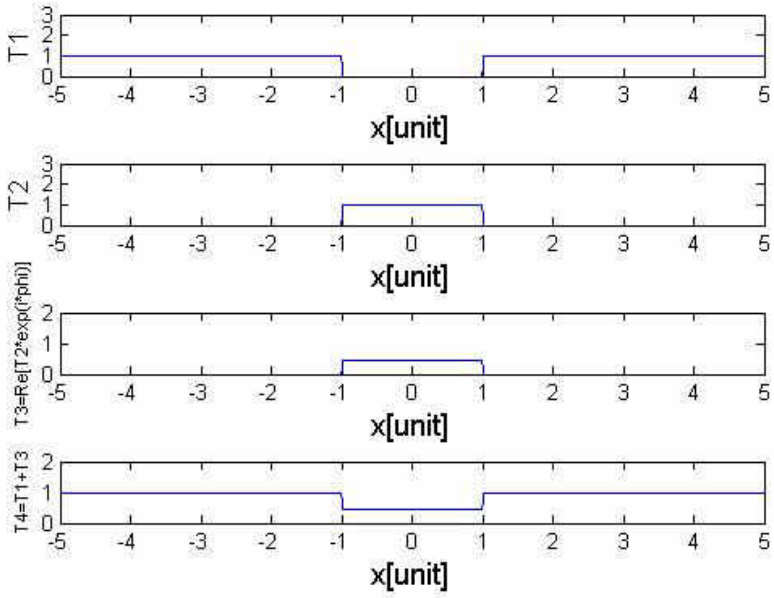

Fig. 4.7: Development of the transmission function of one phase particle from the opaque particle.

The first graph of Fig. 4.7 is the transmission function T_1 of the opaque particle. The second is the complementary of the opaque particle and it can be obtained from $T_2 = 1 - T_1$. The third graph (T_3) is the real part of T_2 multiplied by $e^{i\phi}$ and is called an "incomplete phase particle". The constant phase of the object is presented by ϕ. The bottom graph is the complete phase particle and it is found from $T_4 = T_3 + T_1$.

-2D description

The 2D phase object as in Fig. 4.8 is composed of 10 phase particles. The diameter of each phase particle is $D = 0.25$. The positions of the second to the tenth particles are generated randomly as described for the 2D opaque object. Fig. 4.8 shows the transmission function in the (x, y) plane. The transmission function equals $e^{i\phi}$ in the black part of the figure and 1 elsewhere.

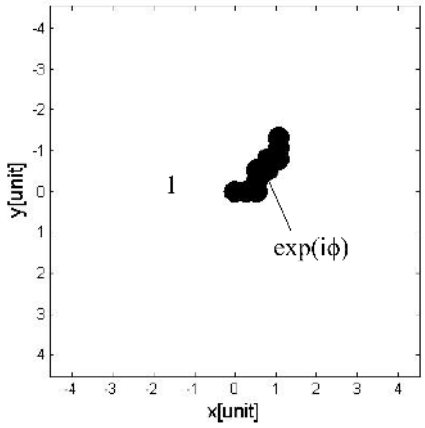

Fig. 4.8: Ten phase disks located in two directions. They are separated by displacement $\triangle_x = 0.5$ and $\triangle_y = 0.5$.

Now, the irregularly-shaped opaque and/or phase object can be simulated. Next, the intensity distribution in the CCD plane of the phase object is analysed.

4.1.3 Fresnel transform for the field in the CCD plane

A second Fresnel transform of the field G_1 gives the field G_2 in the CCD plane. The second Fresnel transformation for any kind of object is given by

$$G_2(x,y) = \frac{\exp(i\frac{2\pi}{\lambda}E_2)}{i\lambda\sqrt{B_2^x B_2^y}} \int_{\mathbb{R}^2} G_1(\xi,\eta)T(\xi,\eta) \exp\left[i\frac{\pi}{\lambda B_2^x}(A_2^x\xi^2 - 2\xi x + D_2^x x^2)\right] \exp\left[i\frac{\pi}{\lambda B_2^y}(A_2^y\eta^2 - 2\eta y + D_1^y y^2)\right] d\xi\, d\eta, \tag{4.9}$$

where $T(\xi,\eta) = T1$ for an opaque object and $T(\xi,\eta) = T4$ for a phase object. T is the transmittance of the object. $T1$ and $T4$ are defined in Fig. 4.7 (top) and (bottom), respectively. This second integral is evaluated numerically and the intensity in the plane of the CCD sensor will be described later.

4.1.4 Hologram analysis by fractional Fourier transform

In previous section, the electric field amplitude in the CCD plane has been presented already. The intensity distribution recorded by a CCD sensor can be found from

$$I(x,y) = G_2(x,y) \cdot \overline{G_2(x,y)}, \tag{4.10}$$

where the overline refers to its complex conjugate. Next, we use the 2D-FRFT to converse the hologram to an image of the object or to reconstruct the object.

The best reconstruction plane is reached when [60]

$$\varphi_a \pm \varphi = 0, \tag{4.11}$$

where φ_a is the phase contained in 2D-FRFT and φ is the phase contained in its intensity. From this condition, the optimal fractional order can be obtained.

4.2 Simulation of opaque and phase object

In this section, two irregular objects are generated at two different planes. Each object has a different size and shape, as shown in Fig. 4.9. The numerical set-up is presented in Fig. 4.10. The first object is located at $\triangle_1 = 9.5$mm and the second object is located at $\triangle_2 = 10$mm from the second lens, as seen in Fig. 4.10. The distance from the second lens to the CCD sensor is fixed as 18mm. From Fig. 4.9, the object in Plane 1 is a phase object and the object in Plane 2 is an opaque object.

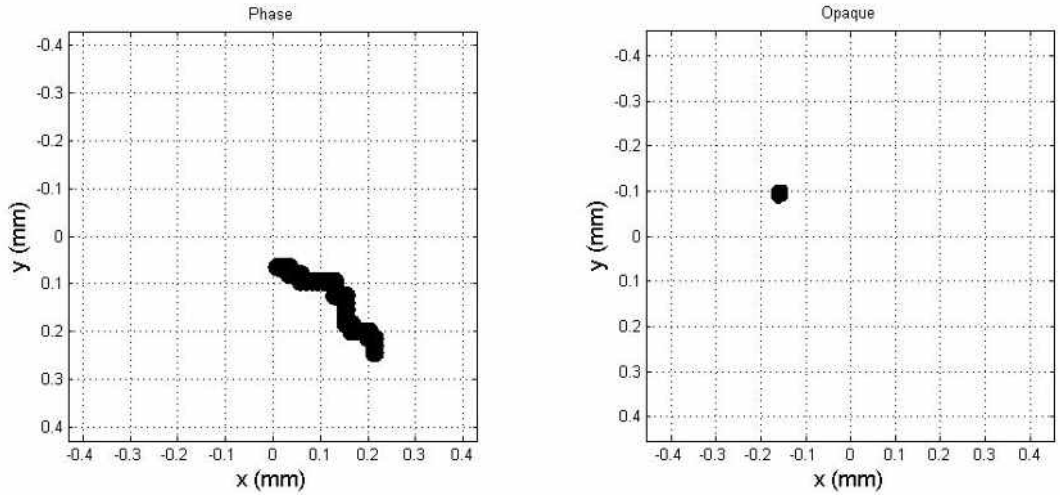

Fig. 4.9: Simulated phase particle (left) with phase shift $\varphi = 0.3\pi$ and opaque particle (right) at two different planes.

The incident beam is a Gaussian beam with beam waist $\omega_0 = 2.3\mu$m. According to the numerical set-up in Fig. 4.10, the beam then propagates through Plane 1 and Plane 2, respectively. The diffracted beam gives the pattern on the CCD camera.

For the two objects, the magnification factors between the objects' plane and the CCD's plane differ. Following the set-up in Fig. 4.10, the object in Plane 1 has a magnification factor equal to 6.76 while the object in Plane 2 has 5.32. The magnification factor can be found easily by [72]

$$g_{1,2_{x,y}} = \frac{w_{tot_{x,y}}}{w_{1,2_{x,y}}}, \tag{4.12}$$

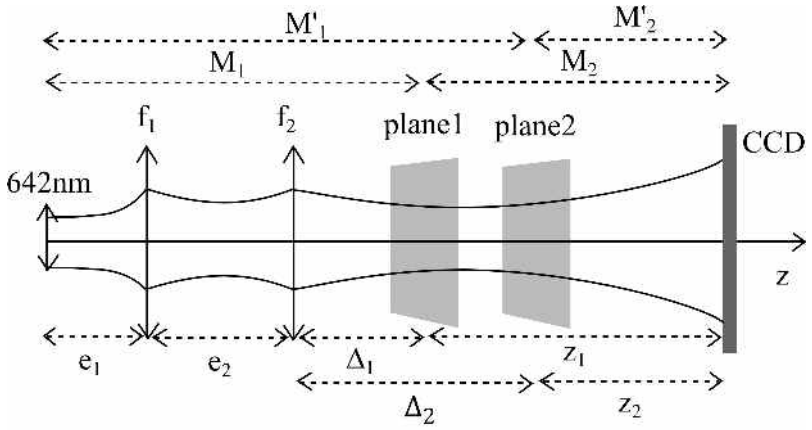

Fig. 4.10: Simulated configuration of the system showing two different object planes with $e_1 = 58.8$mm, $f_1 = 42.8$mm, $e_2 = 342.84$mm, $f_2 = 5.5$mm, $\triangle_1 = 9.5$mm, $\triangle_2 = 10$mm, and distance from the second lens to CCD is 18mm.

where $g_{1,2_{x,y}}$ are the magnification factors between the objects in Plane 1 (or Plane 2) and the CCD's plane, respectively. $w_{1,2_{x,y}}$ are the beam waist dimensions (along x and y, respectively) of the initial Gaussian beam in Plane 1 and Plane 2, respectively, and expressed in Eq.(4.5). $w_{tot_{x,y}}$ is the beam waist dimension of the original Gaussian beam at the CCD plane and is given by [72]

$$w_{tot_{x,y}} = \left(\frac{\lambda B_{tot}^{x,y}}{\pi\omega_0}\right)\left[1 + \left(A_{tot}^{x,y}\frac{\pi\omega_0^2}{\lambda B_{tot}^{x,y}}\right)^2\right]^{1/2} \tag{4.13}$$

$A_{tot}^{x,y}$ and $B_{tot}^{x,y}$ are the matrix elements of the matrix transfer describing the whole system between the laser source and the CCD sensor: $M_{tot} = M_2 \times M_1$. In the simulation, the sensor's size is 1024×1024 pixels and each pixel is $4.4 \times 4.4\mu$m.

Fig. 4.11 (a) is the hologram of the two objects recorded by CCD camera. Fig. 4.11 (b) and (c) show the optimal reconstruction of the two objects. For reconstruction of the objects, the 2D-FRFT is applied to the hologram. The optimal fractional orders for the objects in Fig. 4.11(b) and (c) are $-0.600\pi/2$ and $-0.686\pi/2$, respectively. For the pure phase object in Fig. 4.11 (b), the reconstruction object is indicated by the arrow. In this case, fringes due to the discontinuity are observed around the edge of the object. The intensity inside the reconstructed object is higher than the background. For the opaque object in Fig. 4.11 (c), the intensity in the reconstructed object is zero. The optimal fractional orders of the reconstructed objects give the longitudinal position along the z-axis of the two objects. Moreover, the analysis of the patterns of the reconstructed objects leads to the size and the 2D-shape of the objects.

If we zoom in on the reconstructed object, we observe a discontinuity which is different for the opaque and phase objects as shown in Fig. 4.12(a) and (b).

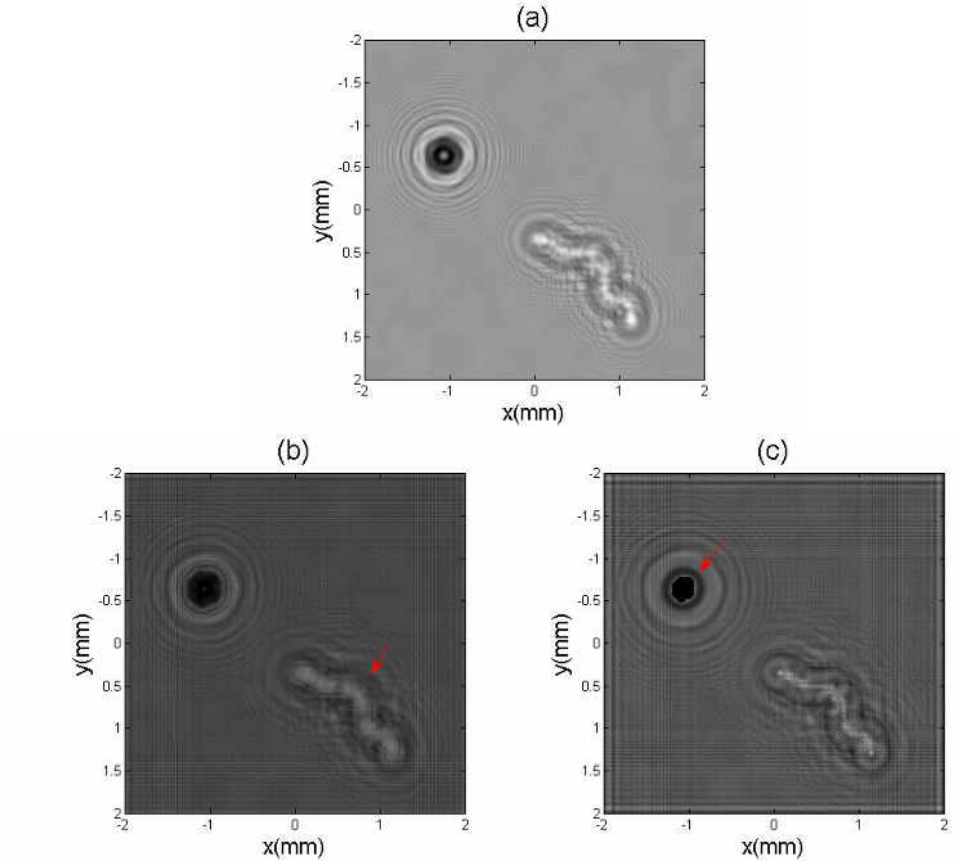

Fig. 4.11: (a) Simulated hologram of phase and opaque objects at two different planes. (b) Reconstructed image of the phase object with order $\alpha_{x,y} = -0.600\pi/2$ as indicated by the red arrow. (c) Reconstructed image of opaque object with order $\alpha_{x,y} = -0.686\pi/2$.

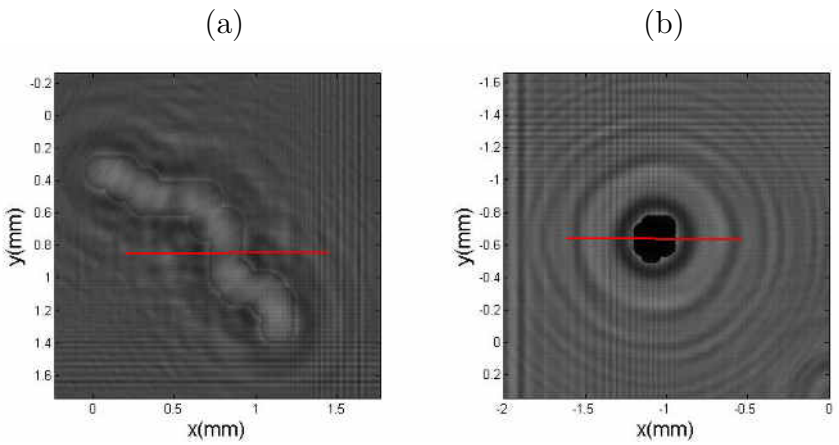

Fig. 4.12: Zoom in on the reconstructed phase and opaque object.

The intensity profiles of this phase and opaque reconstructed object are plotted in Fig. 4.13(a) and (b), respectively. The size of the phase object can be estimated from the distance between the discontinuities which are indicated by the two arrows in Fig. 4.13(a). For the opaque object, the width between the two discontinuities of the intensity profile represents its size. From the intensity profiles of the two objects

and their magnification factors (5.32 and 6.76, for the phase and opaque objects, respectively), the real size of the phase object along the x-axis is 24.81μm and the real size of the opaque object along the x-axis is 20.12μm, respectively. The size measurements correspond to the original sizes of the two simulated objects in Fig. 4.9.

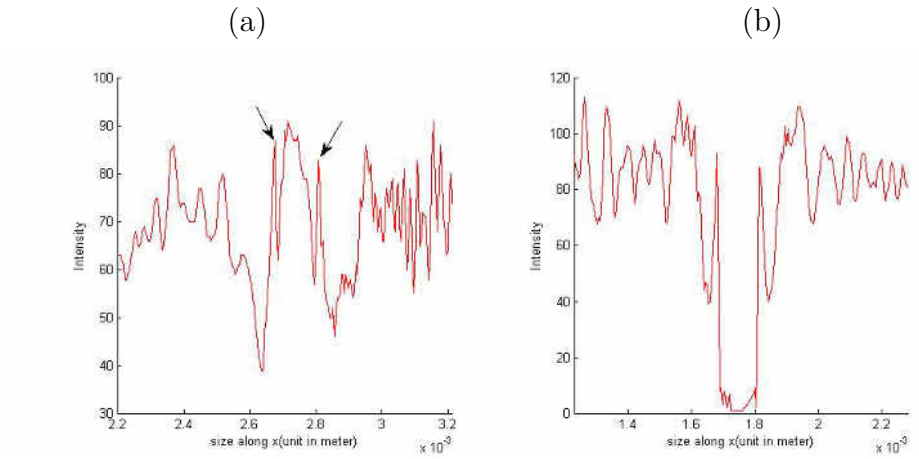

Fig. 4.13: Lateral intensity profile of the reconstructed phase (a) and opaque (b) object.

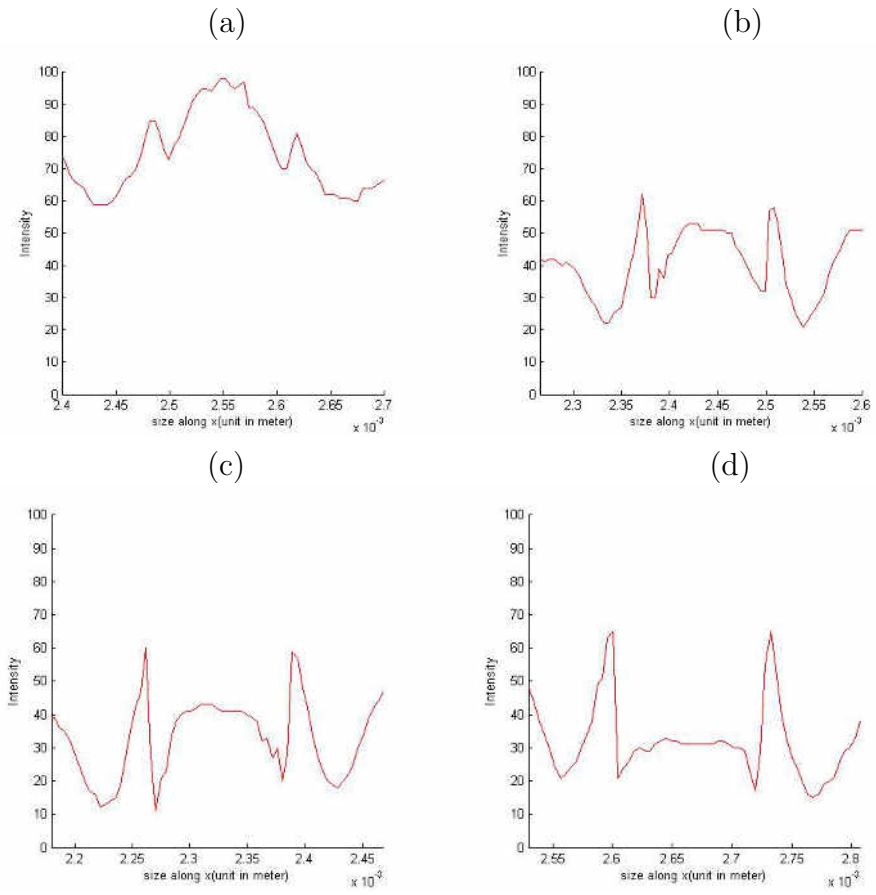

Fig. 4.14: Transversel intensity profile of the reconstructed phase of (a) $\varphi = 0.25\pi$, (b) $\varphi = 0.5\pi$, (c) $\varphi = 0.75\pi$, and (d) $\varphi = \pi$.

For different values of the phase shift introduced by the irregularly-shaped phase object, the transverse reconstructed intensity profiles for $\varphi = 0.25\pi, 0.5\pi, 0.75\pi$ and π are presented in Fig. 4.14 (a), (b), (c) and (d), respectively.

A comparison of the experimental result with our simulation should then allow us to determine the phase shift introduced by arbitrarily-shaped phase object.

4.3 Simulation of irregularly-shaped phase/opaque objects in a droplet

In this section, two irregularly-shaped phase and opaque objects are generated at one longitudinal plane inside a water droplet. The numerical set-up is presented in Fig. 4.15. The wavelength of the incident beam is 642nm. The diameter of the water droplet is 1.5mm and its refractive index is 1.33. The numerical parameters are presented in the caption of Fig. 4.15.

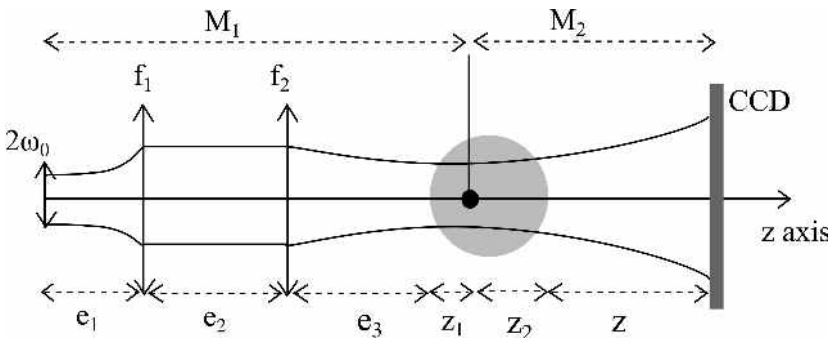

Fig. 4.15: Simulated configuration of the two different objects in a plane with $e_1 = 42.8$mm, $f_1 = 42.8$mm, $e_2 = 135.6$mm, $f_2 = 5.5$mm, $e_3 = 10$mm, $z_1 = 1.125$mm, $z_2 = 0.375$mm, and $z = 9.7$mm.

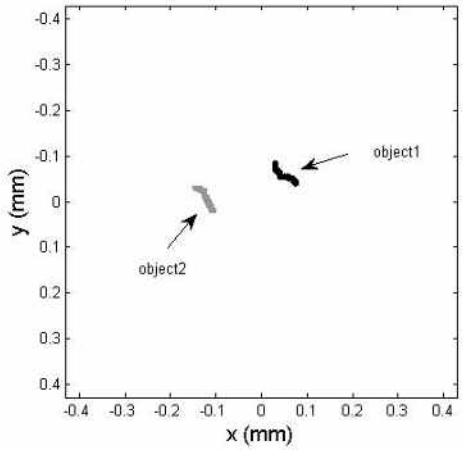

Fig. 4.16: The simulated object1 (opaque) and object2 (phase).

Object 1 and object 2 shown in Fig. 4.16 (a) and (b) are located at $z_1 = 1.125$mm inside a droplet. Object1 is an opaque object and object2 is a phase object. Object1 and object2 are generated by the collection of 20μm opaque and phase particles,

respectively. The phase shift introduced by object2 is equal to $\varphi = 0.3\pi$. By the calculation of magnification factors as in Eq.(4.12) and (4.13), the magnification factor introduced by the optical system for the two objects in one plane is 5.61.

Fig. 4.17(a) shows the hologram of these two objects located in the droplet. Fig. 4.17(b) is the reconstructed image of object 1 and object 2 with a fractional order 0.644.

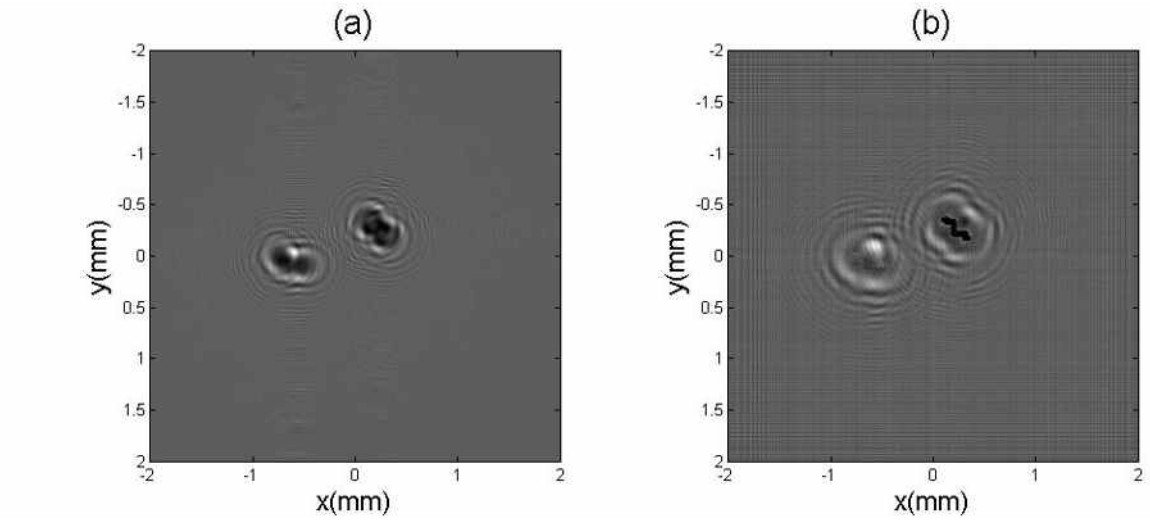

Fig. 4.17: (a) Simulated hologram of phase objects at one longitudinal plane inside a droplet. (b) Reconstructed image of the phase and opaque object with the optimal fractional order $a_{x,y} = 0.644$.

From Fig. 4.17, if we realize a zoom of the two reconstructed objects, we see the discontinuity around the edge of the phase object as shown in Fig. 4.18.

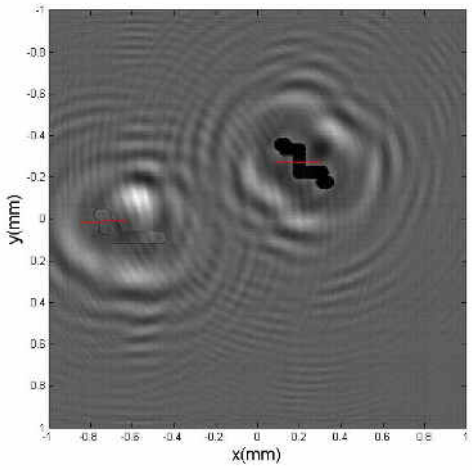

Fig. 4.18: Zoom of the two reconstructed objects.

Intensity profiles along the x-axis of the two objects are plotted in Fig. 4.19. Fig.

4.19 (a) is the intensity profile of the opaque object and Fig. 4.19 (b) is the intensity profile of the phase object which presents the discontinuity around the edge of the object. The width of the intensity profile of the reconstruction of the irregularly-shaped objects divided by the magnification factors gives the real size of the objects.

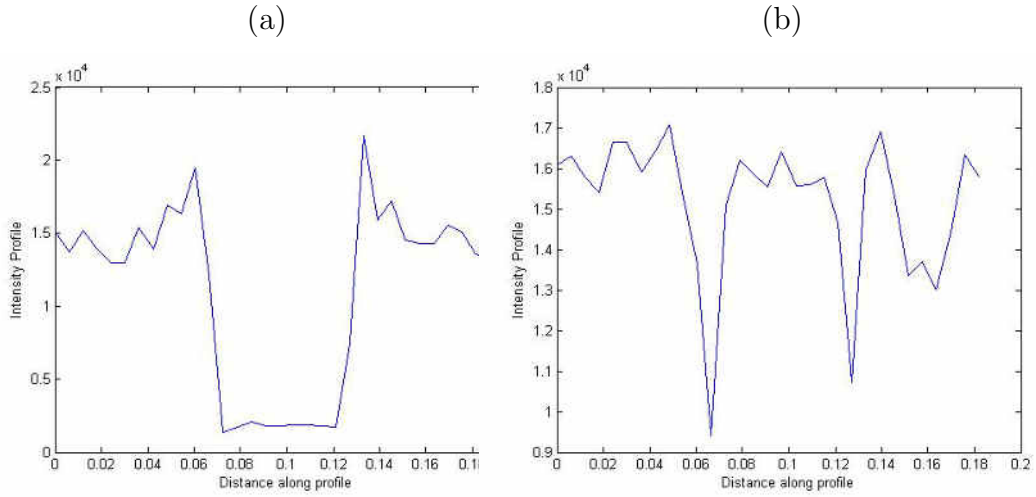

Fig. 4.19: Intensity profile along x-axis of two objects : (a) profile of the opaque object and (b) profile of the phase object.

From these results, we found the difference between the opaque and phase objects. In future work, we may use our developed simulator to distinguish opaque and phase objects inside a droplet.

4.4 Library of objects

In this section, we have made a library of different shapes of objects. For a cross-like opaque object, Fig. 4.20 shows the object (a), the hologram of the cross-shaped object (b) and its optimal reconstruction (c), respectively.

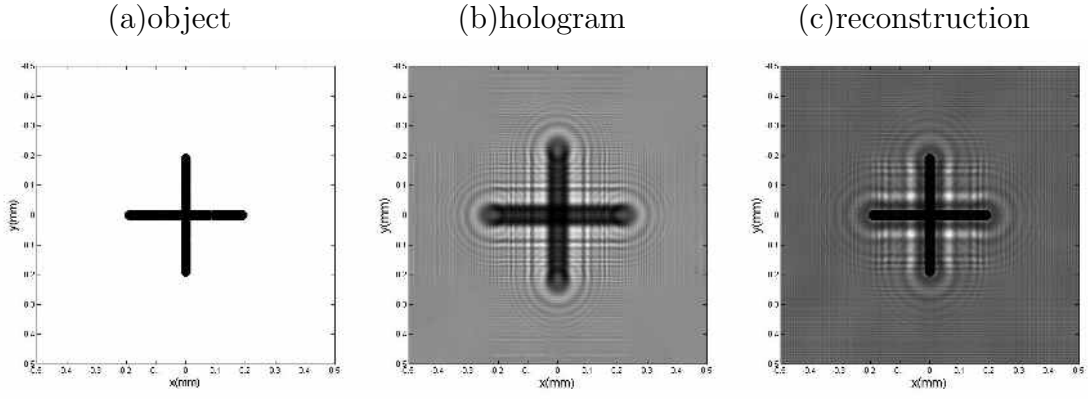

Fig. 4.20: Image of the cross-shape object (a), its hologram (b), and its reconstruction image (c).

For an asterisk-like object, the object, the hologram and the reconstructed object are shown in the first row of Fig. 4.21(a), (b), and (c), respectively.

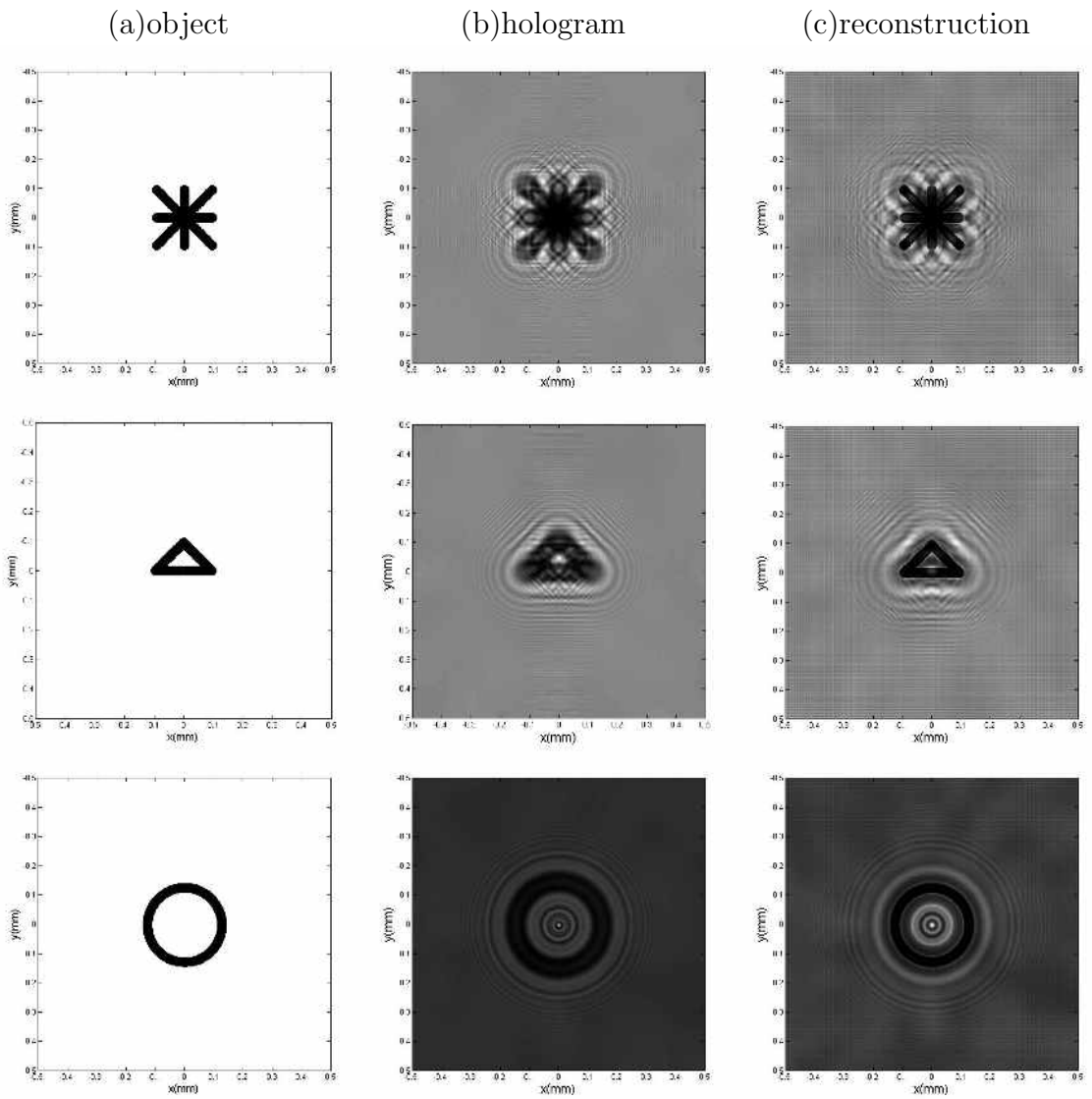

Fig. 4.21: First column (a) shows the image of the object, the second column (b) shows its hologram, and the third column (c) shows its reconstructed image .

The second and the third rows refer to triangle- and ring-shaped objects. With our definition of the object presented in the previous section, any kind of object shap can be simulated. Objects can be opaque or phase objects. Any optical system can be considered by the choice of the appropriated transfer matrices.

4.5 Possiblility to add noise

In the simulation, we can add noise into the hologram. We have developed a procedure to add noise with a spatial frequency that we can adjust. By using MATLAB, the

meshgrid command is used to generate two arrays containing x- and y-coordinates at each position in a grid. Firstly, a square $N \times N$ mesh grid is created. Using MATLAB, the syntax for creating a 2D meshgrid is $[X, Y] = meshgrid(u, v)$ which replicates the grid vectors u and v to produce a 2D grid.

First, we create a grid where the noise is obtained as shown in Fig. 4.22 (a) with spatial frequency $k1 = 2$. The scaling of this grid is then enlarged to the scaling of the hologram. Next, another grid that has the same number of pixels (with spatial frequency $k2 = 1$) as the hologram grid (called a hologram-like grid) is generated.

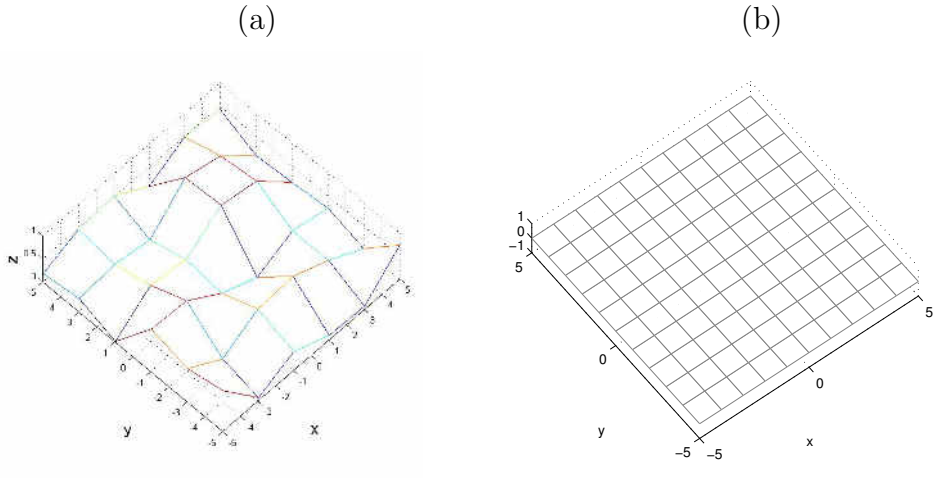

Fig. 4.22: (a) Noise grid. (b) Hologram-like grid. (c) Resulting noise grid.

Unfortunately, the pixel sizes of the two grids (noise grid and hologram-like grid) are unequal. We thus realize an interpolation or resampling of the noise grid in the hologram-like grid.

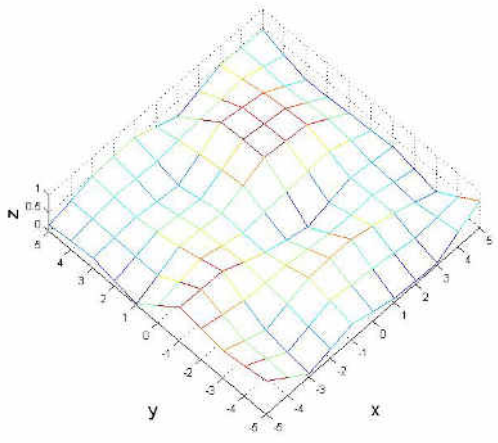

Fig. 4.23: The resulting noise grid.

Now Fig. 4.22 (b) is the generated hologram-like grid with the same number of pixels as the hologram. Fig. 4.23 is the resulting noise grid derived from the interpolation between Fig. 4.22 (a) and (b). In the next figure, we will show an example of a generated 2D noise grid for $k1 = 50, k2 = 1$ and number of pixels $N = 500$. The noise

can be generated as in Fig.4.24. This figure shows the 2D projection of a meshgrid with a noise value. Noise is generated randomly in this case.

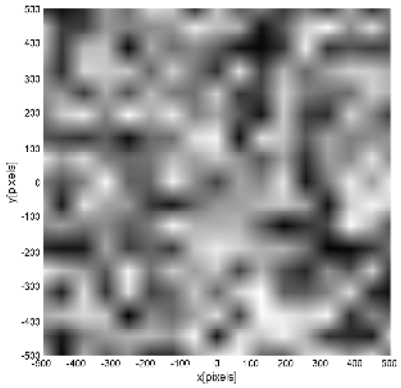

Fig. 4.24: An interpolated grid.

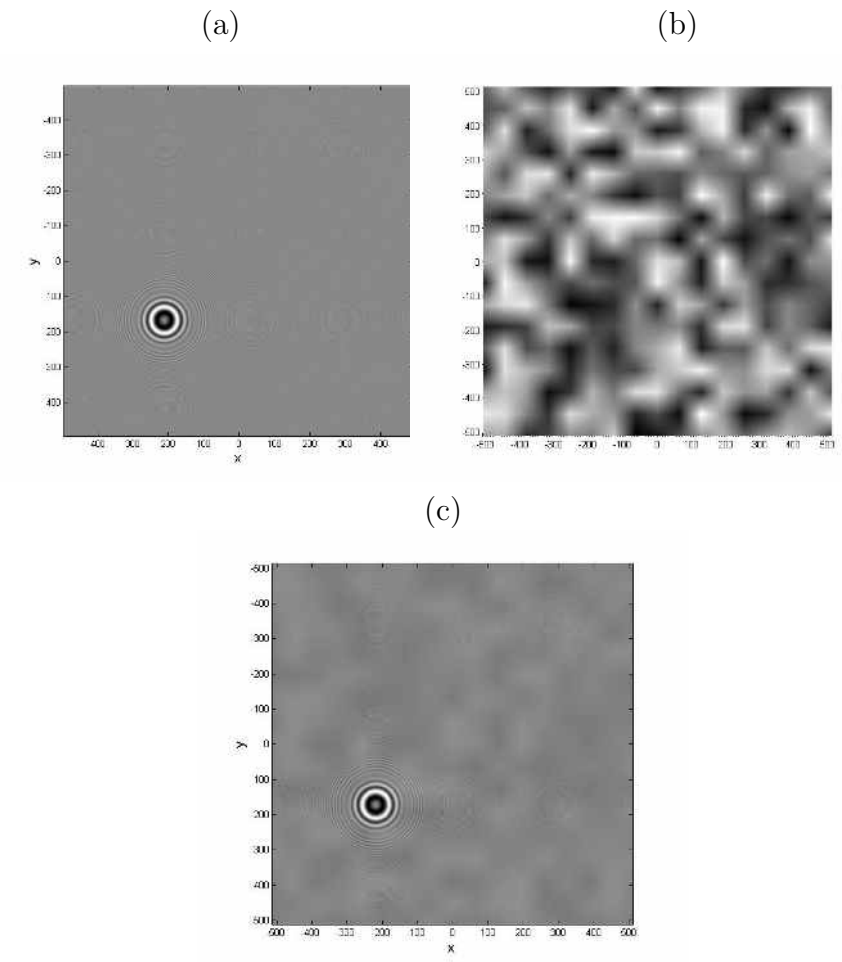

Fig. 4.25: (a) Hologram without any noise. (b) Generated noise. (c) Interpolated image between hologram in (a) and noise in (b).

Actually, the hologram image in the simulation did not generate noise in the image. The following figure, Fig. 4.25 (a) is a simulated hologram without any noise. Then

noise is generated by the "*meshgrid*" command in MATLAB following the procedure in section 4.4. The simulation is produced with $N = 512, k1 = 64, k2 = 1$ as shown in Fig. 4.25 (b). Finally, in the hologram, noise can be added into our simulated hologram as presented in Fig. 4.25 (c).

4.6 Conclusions

In this chapter, irregularly-shaped objects are simulationally created at differrent planes in a general system. We are able to simulate any optical in-line configurations by the choice of the appropriate transfer matrices. The objects can be opaque or phase objects. In this chapter, two configurations have been studied: objects in free space or objects within a droplet. With our model, irregularly-shaped phase and opaque objects can be produced simultaneously at the same longitudinal plane and different transverse positions inside a droplet. We can add noise, whose spatial frequency can be arbitrarily defined to the hologram. Note here that only simulational studies are performed in this chapter. This numerical simulator should become a very powerful tool for the analysis and simulation of experimental results in a wide range of optical configurations such as in the characterization of ice crystals.

5. DIGITAL RECONSTRUCTION OF INCLUSIONS IN A DROPLET

In this chapter, the inclusions inside a suspended water droplet are visualized both in simulation and in experiment. Moreover, the inclusions sizes and their 3D locations in the drop are characterized. The simulated and experimental set-up are shown in Fig. 5.1. The challenge of this problem is that the field amplitude of the incident beam is modified by the droplet size and shape and by the position of the inclusion in the drop. In other words, the radius of curvature of the beam is changed by the droplet's curvature, the shape, and the position of the inclusion in the drop . The inclusion here means the micro-particle inside a droplet. This modification will modify the diffraction pattern of the inclusions inside a droplet. With this problem, finding the droplet's size and locations is not straightforward. More parameters are needed to find the size and the 3D positions such as the radii of curvature of the droplet, the shape, and the position of the inclusion in the drop. The number of unknown parameters in this study is more important than the classical problem where only the particle's longitudinal location and size are determined.

According to the previous work [60, 89], digital in-line holography (DIH) offers the possibility to describe a system with droplet and inclusions. In the recording process, the intensity distribution recorded on the CCD sensor can be determined by the ABCD matrix formalism and the generalized Huygens-Fresnel integral under paraxial approximation. The numerical reconstruction is introduced to "refocus" the plane where the inclusion is located inside the droplet. The hologram reconstruction is carried out by using the 2D fractional Fourier transform (2D-FRFT). Deformations due to an optical astigmatism introduced by the inclusion can be described. The originality of this approach is to see an individual droplet as a spherical micro-channel and the inclusions as seeding particles which trace the fluid flow. In this chapter, both simulated and experimental measurements of the size and the 3D positions will be presented.

5.1 Hologram of an opaque particle as an inclusion

The experimental and numerical set-up is illustrated in Fig. 5.1. The incident Gaussian beam propagates across an optical system, denoted M_1, and illuminates a water droplet (with refractive index equal to $n = 1.33$) of diameter d.

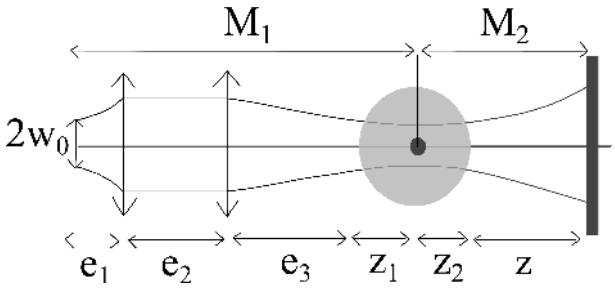

Fig. 5.1: Numerical and experimental optical set-up for $\lambda = 642$nm, $\omega_0 = 2.5\mu$m, $f_1 = 42.8$mm, $f_2 = 5.5$mm, $e_1 = f_1$, $e_2 = 135.6$mm, $e_3 = 14.32$mm, $z = 11.1$mm.

Inside the droplet, spherical particles of diameter D are added to create the inclusions. In the experiment, the inclusions are put inside a droplet by adding the solid particles into a certain amount of water and mixing them together until it becomes a solution of those particles. A simple way to form a drop is to flow the liquid solution by pushing the pistol of the syringe. The surface tension of the liquid causes the liquid hanging from the tip of the syringe's tube to form a pendant drop as in Fig. 5.2.

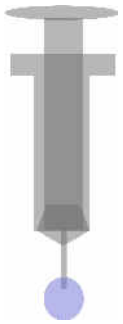

Fig. 5.2: Suspended droplet.

In the theoretical developments, the finite droplet size is not taken into account. On the other hand, the radii of curvature of the droplet are involved in the model. After the beam illuminates a droplet, it propagates again through another optical system, denoted M_2. Behind the droplet, the CCD sensor is located at a distance z to record the intensity distribution of the diffraction pattern. Note here that the matrices, M_1 and M_2 are refered to transfer matrices describing the optical systems before and after the inclusion's plane, respectively. The detail of matrices M_1 and M_2 are explained in Appendix A.1 and B.1.

For an opaque particle, the intensity distribution recorded by the CCD sensor is

$$I(x,y) = \frac{1}{\lambda^2 B_2^x B_2^y}\left[|R|^2 - 2\Re(R\bar{O}) + |O|^2\right] \tag{5.1}$$

where the upper bar denotes the complex conjugate and $\Re$ is the real part. The square

modulus $|R|^2$ corresponds to the directly transmitted beam and $|O|^2$ corresponds to the diffracted beam. The reference beam R and the object beam O are defined as [60, 57].

$$\begin{aligned} R(x,y) = \int_{\mathbb{R}^2} G_1(\xi,\eta) \exp\left(i\frac{2\pi}{\lambda B_2^x}[A_2^x\xi^2 - 2\xi x + D_2^x x^2]\right) \\ \exp\left(i\frac{2\pi}{\lambda B_2^y}[A_2^y\eta^2 - 2\eta y + D_1^y y^2]\right) d\xi\, d\eta, \end{aligned} \tag{5.2}$$

and

$$\begin{aligned} O(x,y) = \int_{\mathbb{R}^2} G_1(\xi,\eta) T(\xi,\eta) \exp\left(i\frac{2\pi}{\lambda B_2^x}[A_2^x\xi^2 - 2\xi x + D_2^x x^2]\right) \\ \exp\left(i\frac{2\pi}{\lambda B_2^y}[A_2^y\eta^2 - 2\eta y + D_1^y y^2]\right) d\xi\, d\eta. \end{aligned} \tag{5.3}$$

5.2 Reconstruction of the hologram

As previously, the two-dimensional fractional Fourier transformation is used for the image processing. This tool is well suited for these studies. For clarity, we recall briefly the main definitions and results. The mathematical expression of 2D-FRFT is

$$\mathcal{F}_{\alpha_x,\alpha_y}[I(x,y)](x_a,y_a) = \int_{\mathbb{R}^2} N_{\alpha_x}(x,x_a) N_{\alpha_y}(y,y_a) I(x,y)\, dx\, dy \tag{5.4}$$

where the kernel function N_{α_p} is defined in Chapter 2, Eq.(2.29). The numerical reconstruction can be considered as a numerical refocusing over the object. The quadratic phase φ must be evaluated. The quadratic phase is contained in the term $2\Re(R\bar{O})$ of Eq.(5.1). This term is composed of a linear chirp function and a complex Gaussian series. The linear chirp is inversely proportional to the recording distance z and a summation of complex Gaussian functions relates to the diameter of the particle. The analytical expression of the quadratic phase is as follows:

$$R\bar{O} = |R\bar{O}| \exp(i\varphi) \tag{5.5}$$

where

$$\varphi = \frac{\pi}{\lambda}\left[\left(\frac{M_x - D_2^x}{B_2^x}\right)x^2 + \left(\frac{M_y - D_2^y}{B_2^y}\right)y^2\right] \tag{5.6}$$

The quadratic phase of the kernel of the 2D-FRFT denoted φ_a is

$$\varphi_a = \pi\left(\frac{\cot\alpha_x}{s_x^2}x^2 + \frac{\cot\alpha_y}{s_y^2}y^2\right) \tag{5.7}$$

The best reconstruction of the particle is achieved when one of the quadratic phase terms is equal to zero.

$$\varphi + \varphi_a = 0 \tag{5.8}$$

$$\varphi - \varphi_a = 0 \tag{5.9}$$

The first condition , $\varphi - \varphi_a = 0$, corresponds to the reconstruction of the real image and the second condition, $\varphi + \varphi_a = 0$, corresponds to the virtual image. With these conditions, the optimal fractional orders α_x^{opt} and α_y^{opt} are

$$\alpha_x^{opt} = \arctan\left[\mp\frac{B_2^x\lambda}{s_x^2(M_x - D_2^x)}\right]$$

$$\alpha_y^{opt} = \arctan\left[\mp\frac{B_2^y\lambda}{s_y^2(M_y - D_2^y)}\right] \tag{5.10}$$

Finally, the optimal fractional order allows us to reconstruct the image of the particle.

5.3 Hologram and its reconstruction

In this section, the holograms of different particle sizes are shown using both simulations and experiments. In the simulation, 20μm opaque particles are considered at two different planes: a first particle is located at distance $z_1 = 1.125$mm within the droplet and a second particle is located at $z_1 = 0.5625$mm along the z-axis inside the droplet. For 10μm particles, the first plane is at $z_1 = 1.35$mm and the second plane is at $z_1 = 0.5625$mm. For the simulation of 5μm particles, they are assumed to be located at two different planes $z_1 = 1.35$mm and 0.15mm. The diameter of the droplet is fixed to 1.5mm for 20μm and 10μm particles and the droplet size is 1.4mm for 5μm particles. Other parameters in the simulation are indicated in Fig. 5.1, which corresponds to the experiment. The holograms derived from the simulation are shown in Fig. 5.3(a), (c), and (e). In the experiment, holograms are recorded by a 1234×1624 CCD sensor with pixel size 4.4μm $\times$4.4μm.These particles are calibrated borosilicate glass particles of diameter 19.3μm $\pm$1.0μm, 9.9μm $\pm$1.0μm, and 5.4μm $\pm$0.3μm from Duke Standards. The experimental holograms are presented in Fig. 5.3(b), (d), and (f). These holograms show only the region of interest where the particles are present, and not the whole droplet.

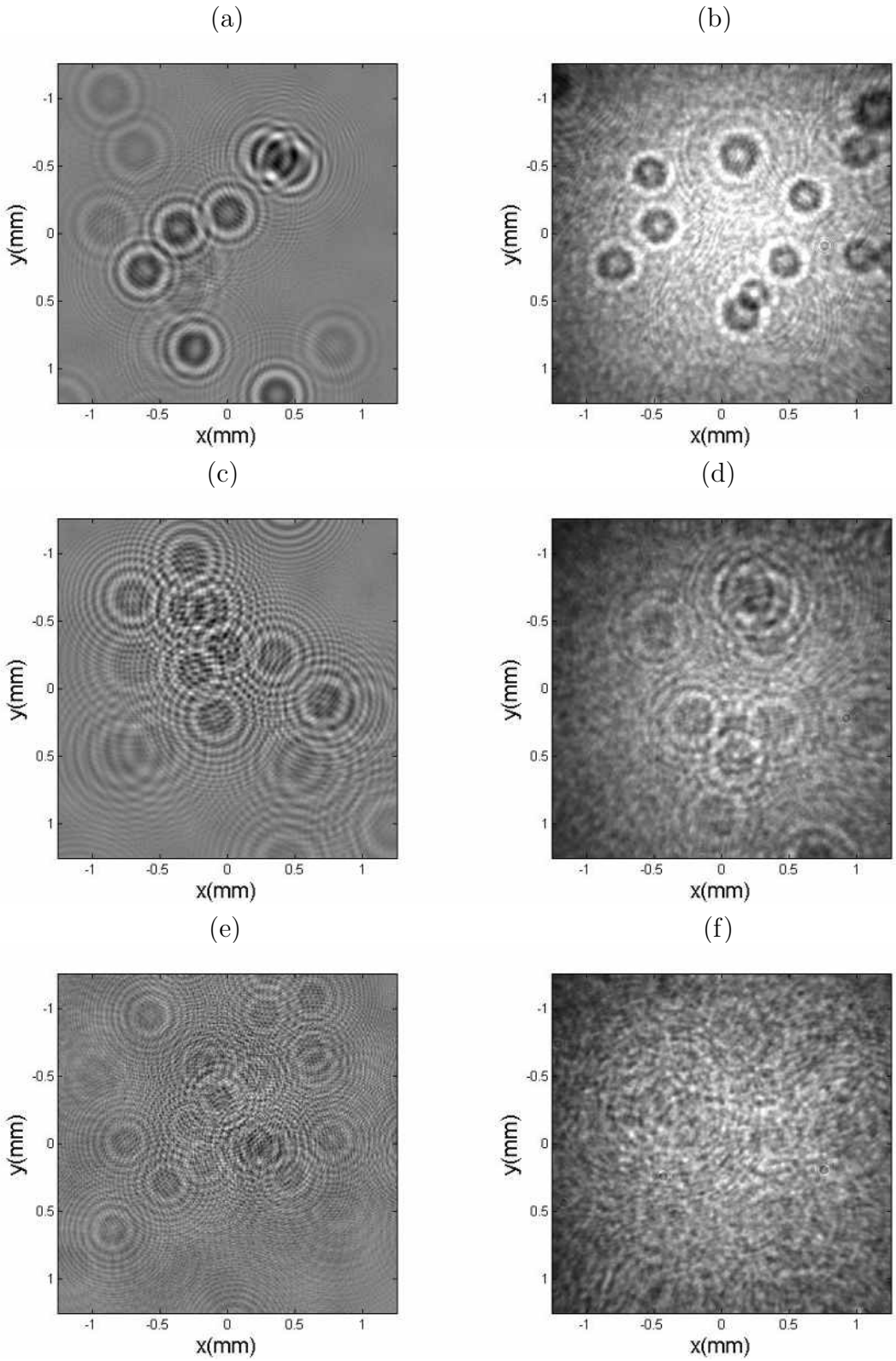

Fig. 5.3: Simulated hologram of 20μm, 10μm, and 5μm particles are shown in (a),(c), and (e). Experimental holograma of 20μm, 10μm, and 5μm particles are shown in (b),(d), and (f), respectively.

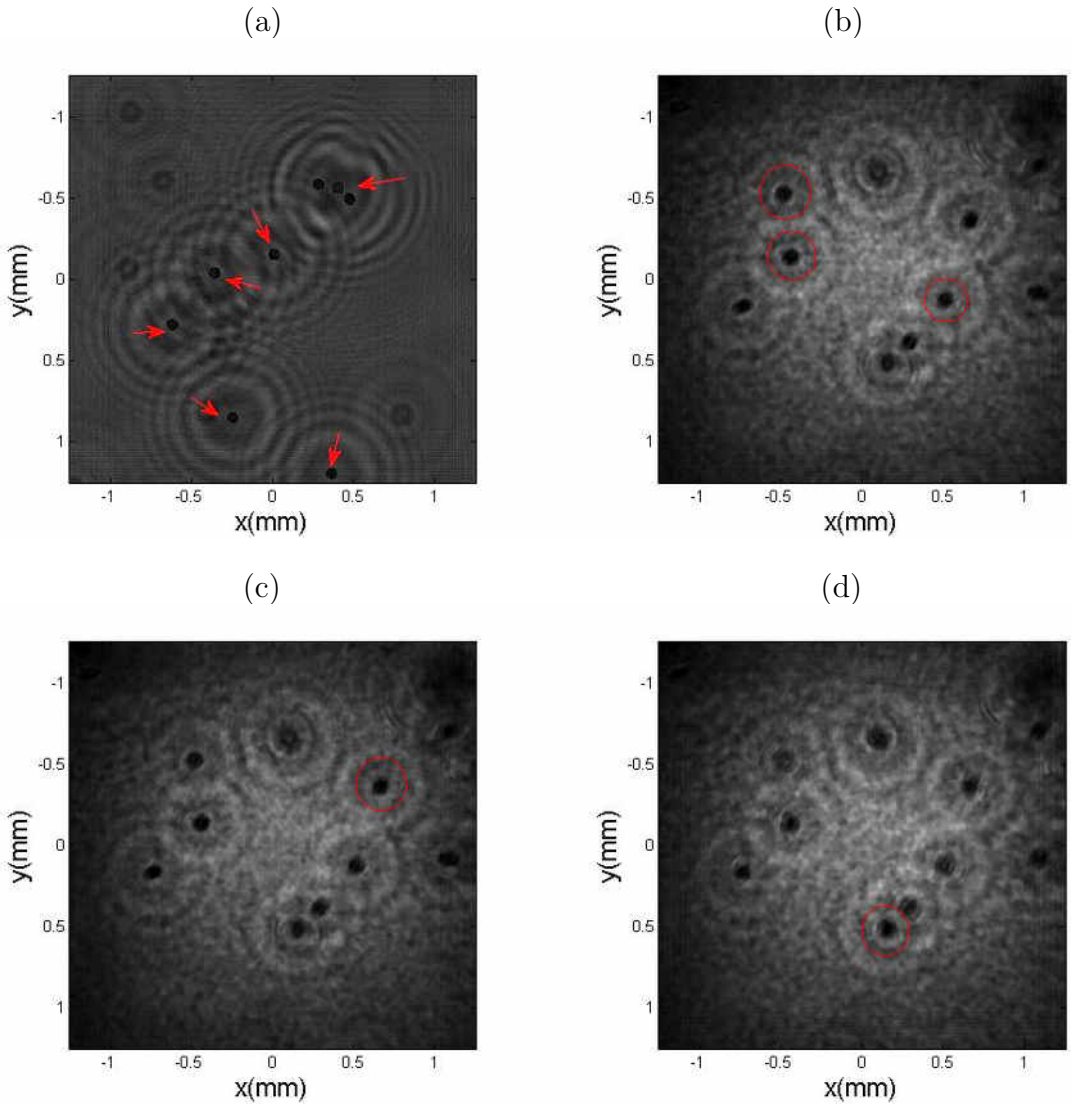

Fig. 5.4: Reconstructed images of 20μm particles in different planes presented numerically and experimentally. (a) Reconstructed image of simulated hologram of Fig. 5.3(a) with fractional order $\alpha_{x,y} = 0.48\pi/2$. (b), (c) and (d) Reconstructed images of the experimental hologram of Fig. 5.3(b) with fractional order $\alpha_{x,y} = 0.48\pi/2, 0.49\pi/2$, and $\alpha_{x,y} = 0.53\pi/2$, respectively.

To characterize the particle's size, we have to do the numerical reconstruction. The reconstructed images of 20μm particles are shown in Fig. 5.4 for both simulations and experimental results. Fig. 5.4(a) is the reconstructed image from the simulation and the reconstructed image of the particles is indicated by arrows. These images are reconstructed with fractional order $\alpha_{x,y}^{opt} = 0.48\pi/2$. Fig. 5.4(b), (c), and (d) are the reconstruction images from the experiment with fractional orders $\alpha_{x,y}^{opt} = 0.48\pi/2, 0.49\pi/2$, and $0.53\pi/2$, respectively. The reconstructed particles are indicated in circles.

The numerical and experimental reconstructed images of 10μm particles are presented in Fig. 5.5.

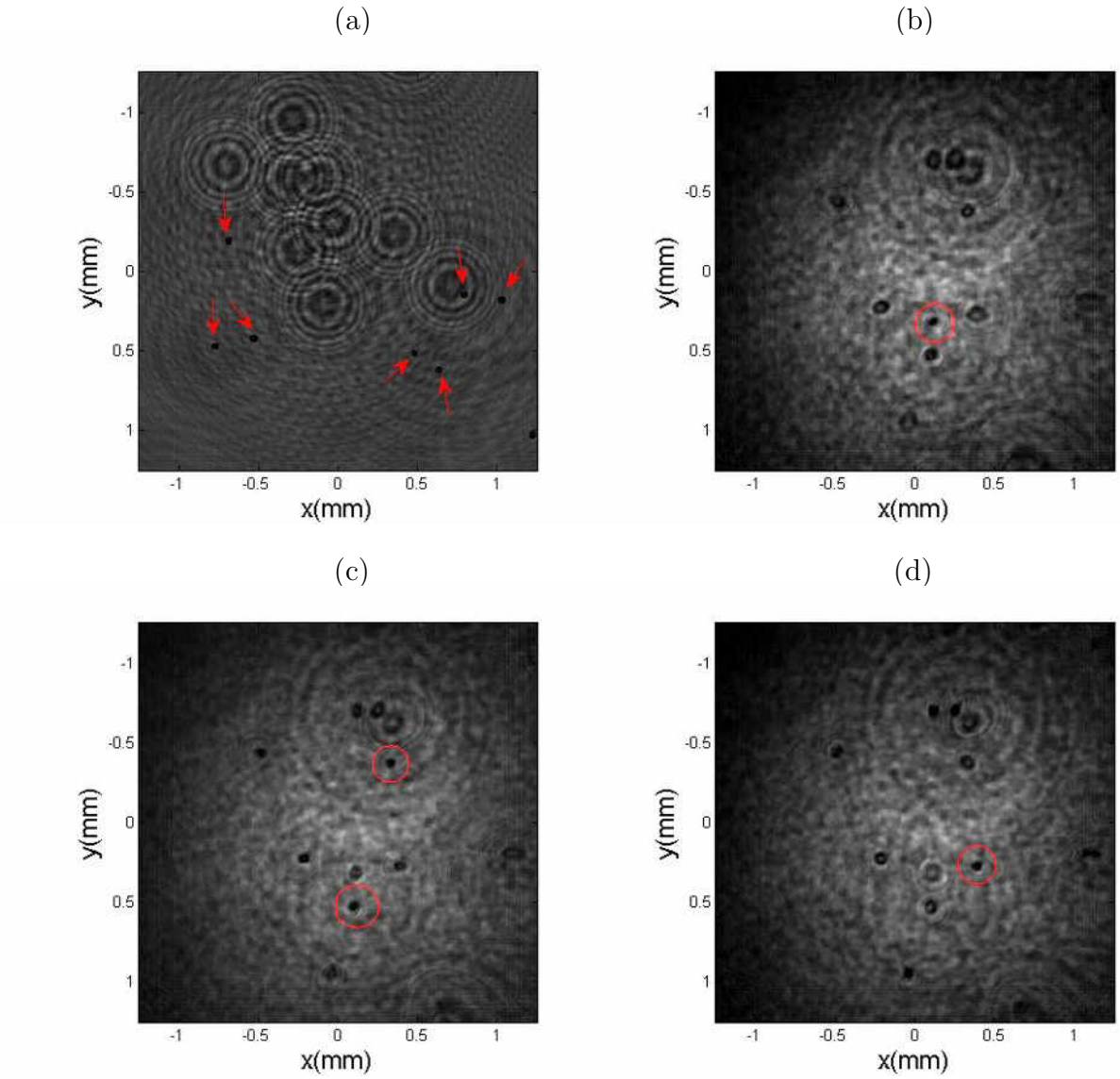

Fig. 5.5: (a) Simulated reconstruction image of 10μm in Fig. 5.3(c) with fractional order $\alpha_{x,y} = 0.619\pi/2$. (b), (c), and (d) Experimental reconstruction images of Fig. 5.3(d) with fractional order $\alpha_{x,y} = 0.50\pi/2, 0.54\pi/2$, and $0.57\pi/2$, respectively.

Fig. 5.5(a) is the simulated reconstruction. The reconstructed particles are indicated by the arrows with fractional order $\alpha_{x,y}^{opt} = 0.619\pi/2$. Fig. 5.5(b), (c), and (d) are the experimental reconstruction images with $\alpha_{x,y}^{opt} = 0.50\pi/2, 0.54\pi/2$, and $0.57\pi/2$, respectively, and are indicated in the circles.

For 5μm particles, the reconstruction images are shown in Fig. 5.6.

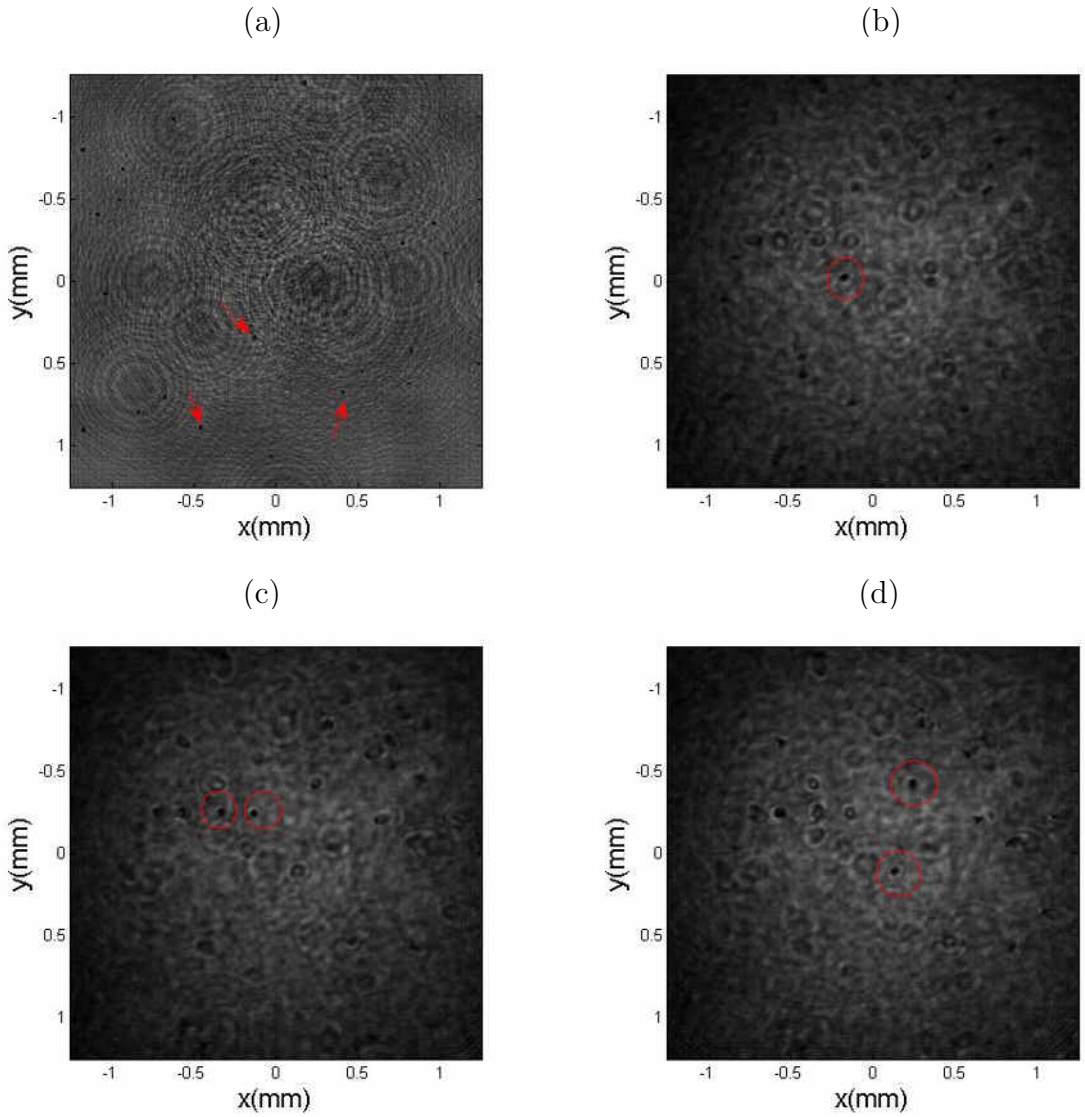

Fig. 5.6: (a) Reconstructed image of simulated hologram of 5μm in Fig. 5.3(e) with fractional order $\alpha_{x,y} = 0.59\pi/2$. (b) Reconstructed image of the experimental hologram of Fig. 5.3(f) with fractional order $\alpha_{x,y} = 0.55\pi/2$. (c) and (d) Reconstructed images of the experimental hologram with fractional order $\alpha_{x,y} = 0.59\pi/2$ and $\alpha_{x,y} = 0.61\pi/2$, respectively.

Fig. 5.6(a) is the simulated reconstruction. The reconstructed particles are indicated by the arrows with fractional order $\alpha_{x,y}^{opt} = 0.59\pi/2$. Fig. 5.5(b), (c), and (d) are the experimental reconstruction images with $\alpha_{x,y}^{opt} = 0.55\pi/2, 0.59\pi/2$, and $0.61\pi/2$, respectively, and are indicated in the circles.

All holograms and reconstruction images are not in the true scale. The magnification factor should be taken into account to find the estimated diameter of the inclusions. The transverse positions of the inclusions inside the droplet are easily obtained from the reconstruction image. The longitudinal position can be found from the optimal fractional order.

5.3.1 *Size measurement*

This section is about how to find the inclusion's size. The profile width at 10% of the maximum intensity is considered to be the inclusion's size. For 20μm, 10μm,and 5μm particle, the intensity profiles along the horizontal axis of the reconstructed particles are plotted in Fig. 5.7.

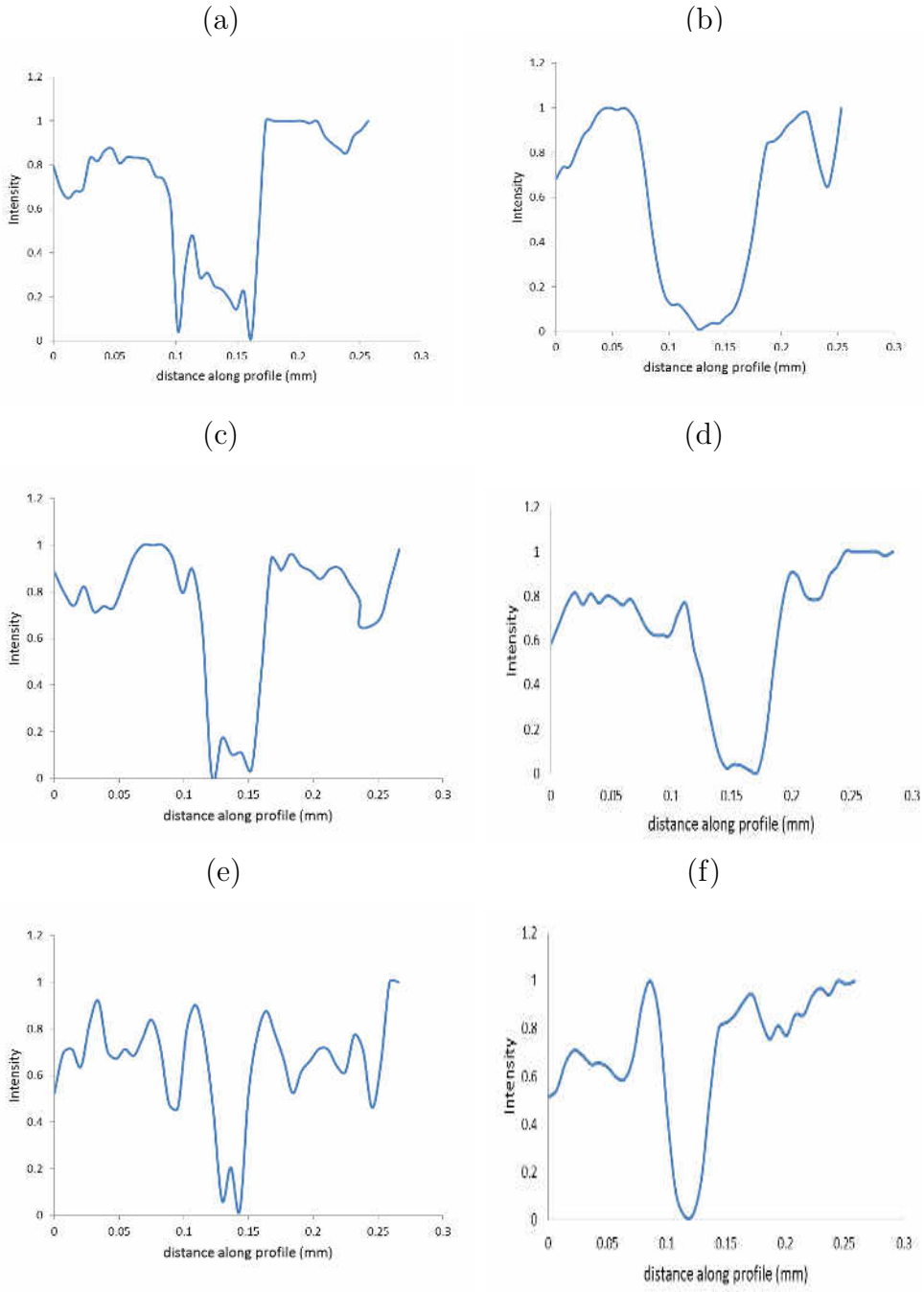

Fig. 5.7: Intensity profile of simulated reconstruction particle with 20μm diameter (a), 10μm diameter (c), and 5μm diameter (e). (b), (d), and (f) are the experimented intensity profile of 20μm, 10μm, 5μm particle, respectively.

In our case, the inclusion has a circular shape, so the profile along the x- and y- axis

should be equal. Therefore, we considered only the profile along the x-axis. For the 20μm particle, the reconstructed size is equal to 20.4μm for the simulation and 20.1μ m for the experiment where the magnification factor is 3.3. For the 10μm particle, its reconstructed size is 11.3μm for the simulation and 10.7μm for the experiment where the magnification factor is 3.4. The size of a 5μm particle after reconstruction of the simulated hologram is 6.0μm and its experimental size is 6.0μm where the magnification equal to 3.4.

In the simulation, the magnification factor can be found as in chapter 4, section 4.6, Eq.(4.12). The magnification factor in the experiment can be obtained by shadowgraphy.

5.3.2 Method for finding axial position of the particle

From the optimal fractional orders, the axial location of the particle can be found by plotting the relationship between the fractional order and the axial position numerically. The curve plotting the optimal fractional order versus the longitudinal location of the particle is shown in Fig. 5.8. Note that there is a difference between the three curves because the droplet radius (d) was different: $d = 1.5$mm for 20μm and 10μm, and $d = 1.4$mm for 5μm particles.

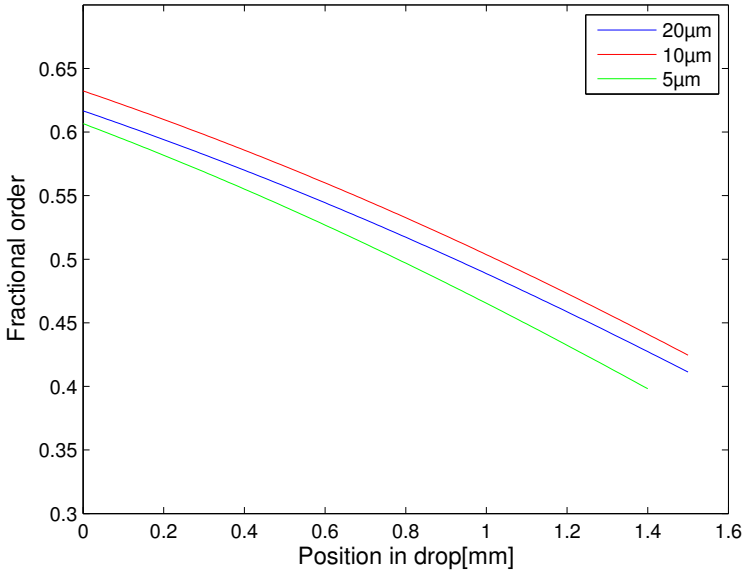

Fig. 5.8: Theoretical optimal order of reconstruction and longitudinal position of the different inclusions' sizes.

From Fig. 5.8 in the blue line, the 20μm particle with fractional order $a = 0.48, 0.49, 0.53$ corresponds to the positions $z_2 + z = 1.1, 1.03, 0.76$mm in the droplet. The inclusions with diameter 10μm are reconstructed at $a = 0.5, 0.54, 0.57$ and correspond to $z_2 + z = 1.03, 0.77, 0.54$mm, respectively. For 5μm particles with fractional order $a = 0.55, 0.59, 0.61$, the longitudinal locations are $z_2 + z = 0.84, 0.58, 0.44$mm.

If we can fix the axial position of the particles in the droplet, then we can compare

the optimal fractional orders obtained from the experiment and the theoretical values. The difference between these two values corresponds to the error in the evolution of the longitudinal position in the measurement. Unfortunately, this experiment cannot fix the axial position of the inclusions inside a droplet because the inclusions move following the fluid flow inside the droplet. Therefore, we need to find another way of describing the limitation in the measurement of the axial position. The limitation of the technique for the evaluation of the longitudinal displacement of the particles can be considered by varying the fractional orders in the reconstruction process. For example, in Fig. 5.4 (c) the particle is reconstructed with the optimal fractional order $0.49\pi/2$. The Fig. 5.9 realizes a zoom of the reconstructed particle in Fig. 5.4 (c) with different fractional orders $\alpha = 0.47\pi/2, 0.48\pi/2, 0.49\pi/2, 0.50\pi/2$, and $0.51\pi/2$.

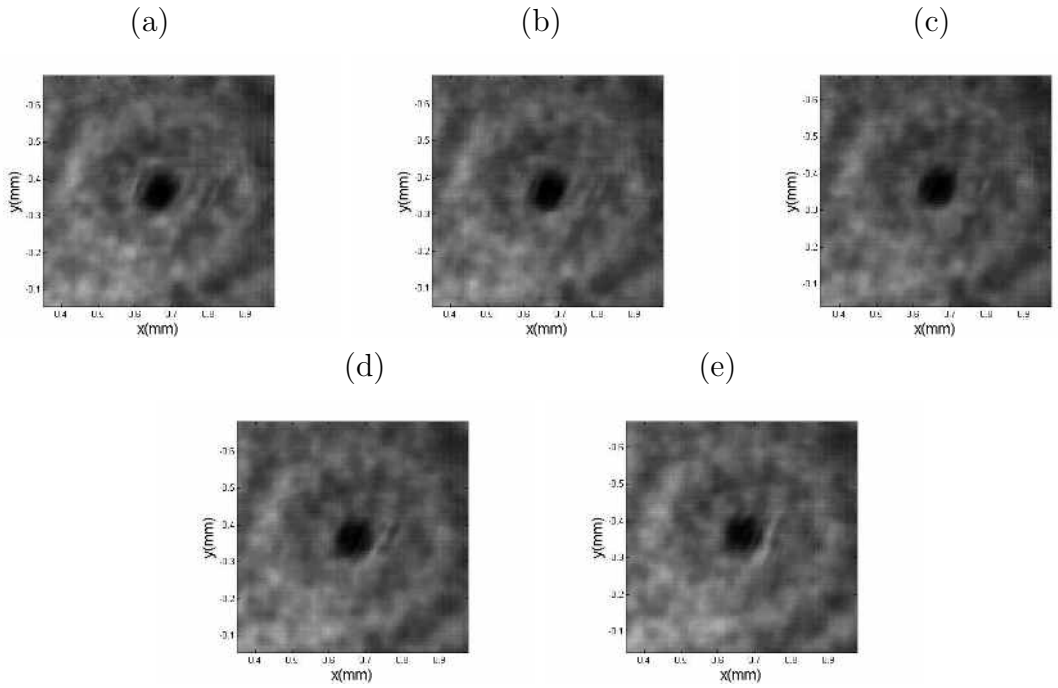

Fig. 5.9: (a) $\alpha = 0.47\pi/2$, (b) $\alpha = 0.48\pi/2$, (c) $\alpha = 0.49\pi/2$, (d) $\alpha = 0.50\pi/2$, (e) $\alpha = 0.51\pi/2$

From Fig. 5.9, the best reconstruction particle is in figure (c). The images of the reconstructed particle in (b) and (d) are different from (c). From these results, we found that the second decimal number affects the reconstruction image of the particle with $\triangle\alpha = \pm 0.01\pi/2$. Then the corresponding uncertainty of the measurement of the axial position for 20μm particle is $\triangle z = 0.07$mm. The transverse accuracy can be obtained by counting thel number of pixels divided by the magnification factor.

5.3.3 Tracking the particle's trajectory

By recording a series of holograms, the trajectories of the particles can be tracked. Then we can trace the trajectory of the particle inside a droplet. For 20μm particles, their trajectories can be tracked as shown in Fig. 5.10. The 3D location of the particle

in the droplet is obtained from the different holograms. The time between two holograms is known. Then we can find the average velocity of the particle between two successive holograms. From the experiment, ten holograms are recorded. The frame rate of the CCD camera is 14.7 fps (frames per second).

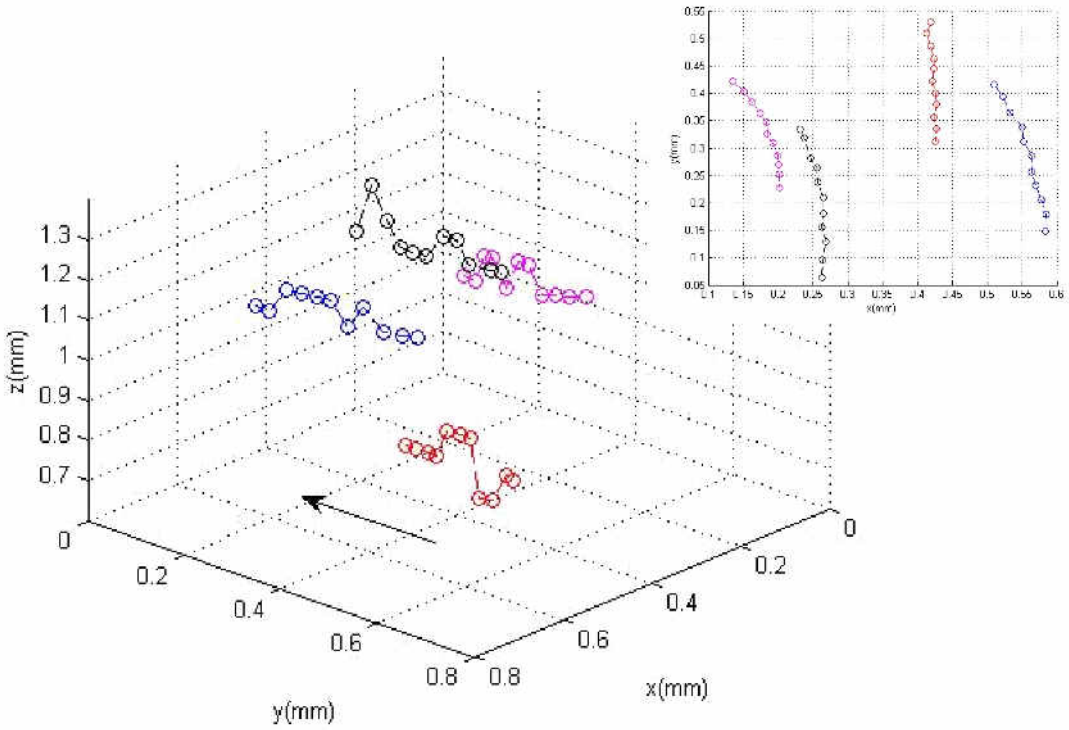

Fig. 5.10: The circles represent the 3D locations of each hologram series. In this figure, ten holograms were recorded. The different colors refer to different particles in the drop. The arrow shows the direction of movement of the particles. The upper right image shows the trajectory of the particles in a 2D plane.

From Fig. 5.10, the circles refer to the 3D location of the inclusions inside the droplet. The distance between two circles refers to the displacement between two holograms. From this information, the velocity of the inclusion can be obtained. The direction of travel of the inclusion follows the black arrow in the figure. For the 2D trajectory, the inclusions move upwards along the y-direction which is the result of the capillary force of the needle that suspended the droplet.

5.4 Conclusions

This technique allows us to visualize the inclusions inside a droplet. The size, shape and 3D locations of the inclusions can be determined. The trajectories of the inclusions can be analysed by recording series of holograms and it is possible to measure the velocity of the inclusions inside the droplet. In this study, the droplet is suspended from the tip of a syringe which produces the capillary action to the droplet and makes the inclusion inside the droplet move upwards into the tube. This technique should allow

us to characterize the inclusion in 3D and real time. However, tracing the inclusion's trajectory by reconstruction the hologram series takes time to analyse.

6. TRAJECTORIES OF PARTICLES IN A DROPLET BY LONG EXPOSURE TIME MEASUREMENT

From the previous chapter, the trajectory of the inclusion can be obtained by analysing the hologram series frame by frame. However, this method takes a lot of time. Therefore in this chapter, we propose another method to trace the inclusion's trajectory inside a droplet.

Studying the trajectory of particles is very interesting in flow measurement. Many techniques are proposed for measuring the velocity of the particles [3, 62, 90, 19]. For the holography technique, the multiple exposure method [101] and video holographic microscope [100, 102] are proposed in order to track the trajectories of individual particles in the flow. A long exposure time method is proposed by [99, 103] for tracking particles in the measurement volume. In this chapter, we propose a long exposure time method to analyse the trajectory of the particles inside a droplet. This technique can measure moving particles inside a millimetric droplet [104]. This is of great interest when measuring the 3D flow of micronic particles in a millimetric droplet. A long exposure time experiment consists in using a long duration shutter speed of the camera. In this chapter, we show that it is possible to reconstruct the trajectory of particles within a droplet by the digital in-line holography (DIH) technique. When a slow shutter speed (long time exposure) is used, the particles' trajectory inside the droplet can be detected.

In the experiment, we consider a suspended droplet with inclusions. The inclusions or particles are inserted by mixing water with the powder of solid particles and making a suspended drop with a syringe. The inclusions used in this experiment are calibrated $20\mu m$ particles and the droplet's diameter is on a millimeter scale. The holograms are recorded by a CCD sensor. The exposure time of the CCD sensor is set from $0.15s$ to $0.25s$. The 2D fractional Fourier transform (2D-FRFT) is used to reconstruct the holograms.

6.1 Theoretical description of digital in-line holography set-up

The theoretical development in this chapter is the same as in the previous chapter. A Gaussian light source is used. The light source propagates through an optical system, denoted M_1, and illuminates the object. Then the transmitted light and scattered light propagate through another optical system, denoted M_2, and are collected by a CCD sensor with a slow shutter speed. The parameters used in the experiment are indicated in the caption of Fig. 6.1. To derive the intensity distribution of the hologram, the Huygens-Fresnel transformation is used two times: first it is used to transform the field amplitude in the incident plane to the field in the particle's plane;

second, the field in the particle's plane is transformed to the field in the CCD's plane. The intensity distribution of the hologram recorded by the CCD sensor is

$$I(x, y = G_2(x, y)\overline{G_2(x, y)} \tag{6.1}$$

where G_2 is the field in the CCD's plane and the upper bar refers to the complex conjugate.

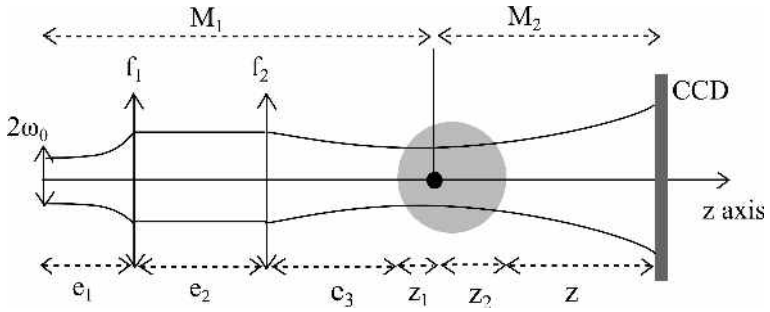

Fig. 6.1: Configuration of numerical and experimental set-up of long exposure time measurement with $\omega_0 = 2.3\mu m, f_1 = 42.8mm, e_1 = 42.8mm, e_2 = 342.84mm, f_2 = 5.5mm, e_3 = 10.9mm, z = 13.14mm$.

For digital reconstruction, the 2D fractional Fourier transform is used to convert the hologram to the image of the particle as in the following equation

$$\mathcal{F}_{\alpha_x,\alpha_y}\left[I(x, y)\right](x_a, y_a) = \int_{\mathbb{R}^2} N_{\alpha_x}(x, x_a)N_{\alpha_y}(y, y_a)I(x, y)dx\ dy \tag{6.2}$$

where N_{α_x} and N_{α_y} are the kernel operators of the 2D-FRFT. The numerical reconstruction can be considered as a numerical refocusing in the particle's plane. The details of the mathematical development are already described in [60, 57]. The optimal fractional order is reached if the hologram is refocused to the right plane. The optimal fractional order is given by

$$\alpha_{x,y}^{opt} = \frac{2}{\pi}\arctan\left[\mp\frac{B_2^{x,y}\lambda}{s_{x,y}^2(M_{x,y} - D_2^{x,y})}\right] \tag{6.3}$$

This relation links the optimal fractional order of reconstruction to the position of the particle. The experimental results of the holograms and their reconstructions are presented in the next section.

6.2 Experimental results using a long exposure time

The experimental set-up was installed as described in Fig. 6.1. The parameters used in the experiment are indicated in the caption of this figure. The light source is a laser diode with wavelength $\lambda = 642nm$ operating at $25°C$. The CCD sensor used

in this experiment has 1624×1234 pixels. Each pixel size is $4.4\mu m \times 4.4\mu m$. In the previous chapter, the normal shutter duration that we used to capture the holograms was $0.04s$. The exposure time of the CCD sensor is now set to $0.15s, 0.20s$, and $0.25s$. Calibrated $20\mu m$ spheres of borosiligate glass are used as inclusions.

For noise reduction, all holograms in the experiments are treated with the following steps: first the holograms are recorded on the CCD sensor. Next, we apply a Gaussain filter to a hologram in order to obtain a blurred image of the hologram. Then a filtered hologram is obtained from the division of the original hologram by the blurred image. Finally, we then use the filtered holograms for characterization of the moving particles.

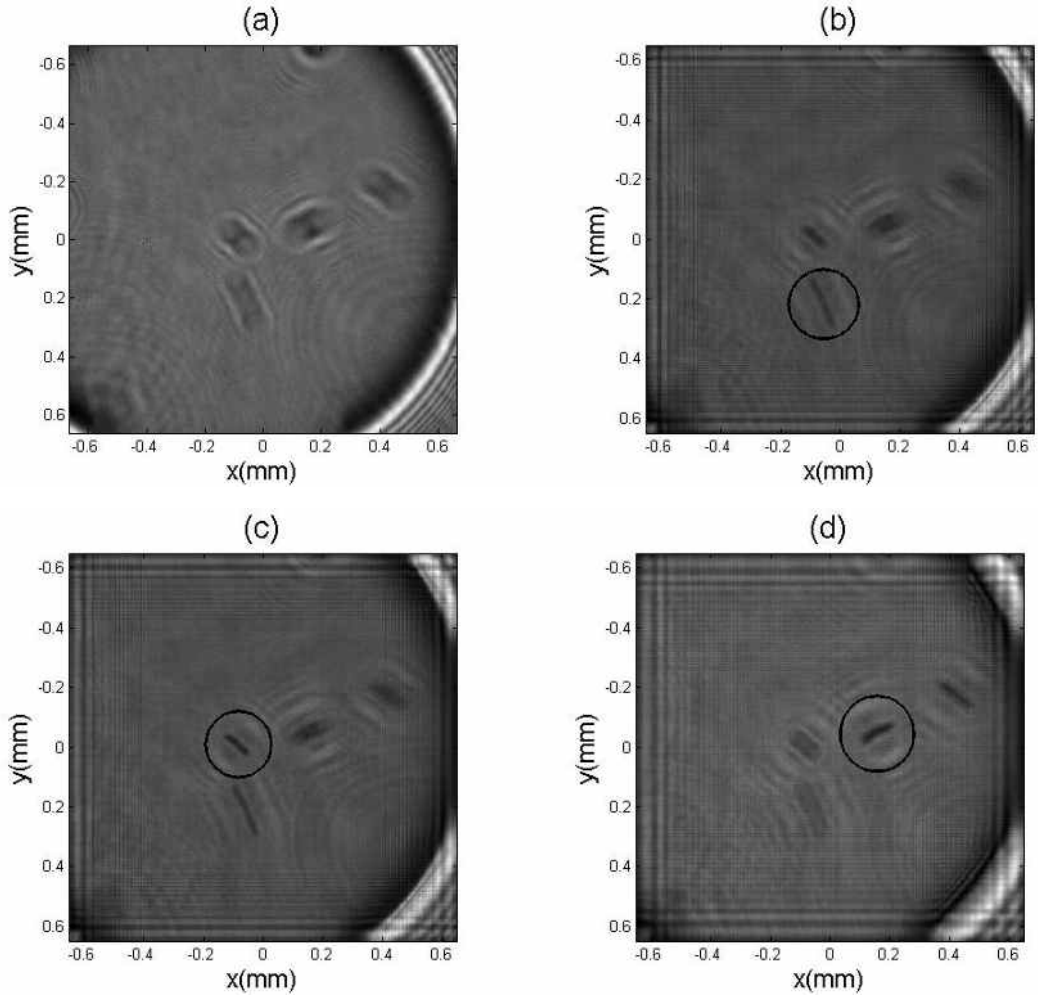

Fig. 6.2: (a) Hologram of $20\mu m$ glass particle inside the droplet with $0.15s$ shutter time. (b)-(d) Reconstructed images of $20\mu m$ glass particle inside the droplet under $0.15s$ shutter time with optimal fractional order: $0.56\pi/2, 0.6\pi/2$, and $0.73\pi/2$.

For $0.15s$ of exposure time, an example of the filtered hologram of the moving particles is presented in Fig. 6.2 (a). The diameter of the droplet is $1.7mm$ in this case. Three optimal reconstructed images of the inclusions are presented in Fig. 6.2(b), (c), and (d) for the following three fractional orders: $\alpha = 0.56\pi/2, 0.6\pi/2$, and $0.73\pi/2$, respectively. In each case, the reconstructed particle is indicated by the circle.

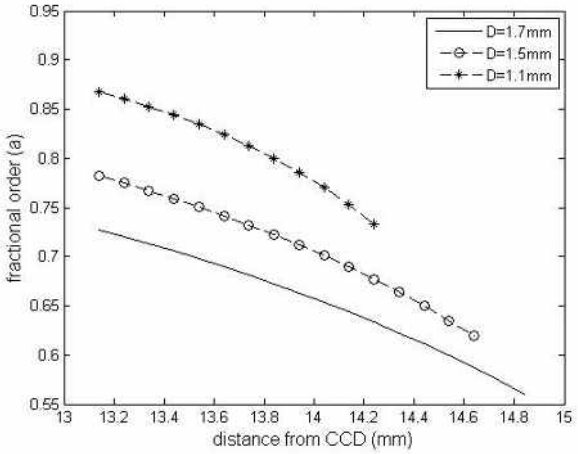

Fig. 6.3: Theoretical fractional order of reconstruction versus the longitudinal distance of $20\mu m$ particles for three droplet sizes.

To find the longitudinal position of the particles, the curve in Fig.6.3 is considered. This curve shows the relationship between the optimal fractional order and the axial position of the particles for three different droplet sizes. This graph is obtained from theoretical analysis. The particles in Fig. 6.2(b), (c), and (d) are thus located at distances $z_2 + z = 14.8mm, 14.6mm$, and $13.2mm$, respectively, from the CCD sensor. The magnification factor is evaluated experimentally. It is equal to 3.4 ± 0.1. This uncertainty of the magnification factor is not sensitive for the different reconstructed planes that are presented here. After considering the magnification factor, the evaluated velocity in the x and y components (v_x, v_y) of the particles in Fig. 6.2(b), (c), and (d) are $(0.45, 0.95)mm/s$, $(0.41, 0.47)mm/s$, and $(0.49, 0.26)mm/s$, respectively. The resolution depth along the z-axis is not accurate enough to evaluate the velocity in the z-direction. The direction of the moving particle (or the sign of the velocity) can be obtained by using a double exposure source (short and long exposure). First, we use the short exposure which acts as a precursor that indicates the starting point of the particle. Second, we use the long exposure that tracks the trajectory of the particle, as shown in Fig. 6.4.

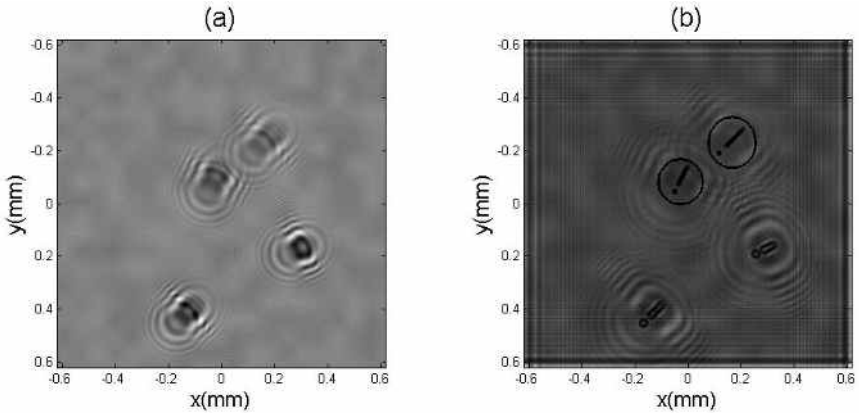

Fig. 6.4: Hologram recorded under a double exposure light source with $0.03s$ and $0.15s$ exposure time (a) and its reconstruction image (b) with fractional order $\alpha = 0.67\pi/2$.

Fig. 6.4 (a) is the recorded hologram from the double exposure light source. Fig. 6.4(b) is the reconstructed image of the hologram in (a). The particles enclosed by the two circles are reconstructed. In the reconstruction image, dark dots and dark rod shapes are observed. Dark dots refer to the starting point of the moving particles.

For a $0.20s$ exposure time, the hologram is presented in Fig. 6.5 (a), as recorded by the CCD sensor. Fig. 6.5 (b-d) are the reconstructed images of three different reconstruction planes with the fractional orders: $0.73\pi/2, 0.735\pi/2$, and $0.75\pi/2$, respectively. In this case, the droplet's diameter is $1.5mm$. The observed trajectories are indicated by the circles. The theoretical curve between the axial position and the optimal fractional order of reconstruction can be seen in Fig. 6.3 (middle curve).

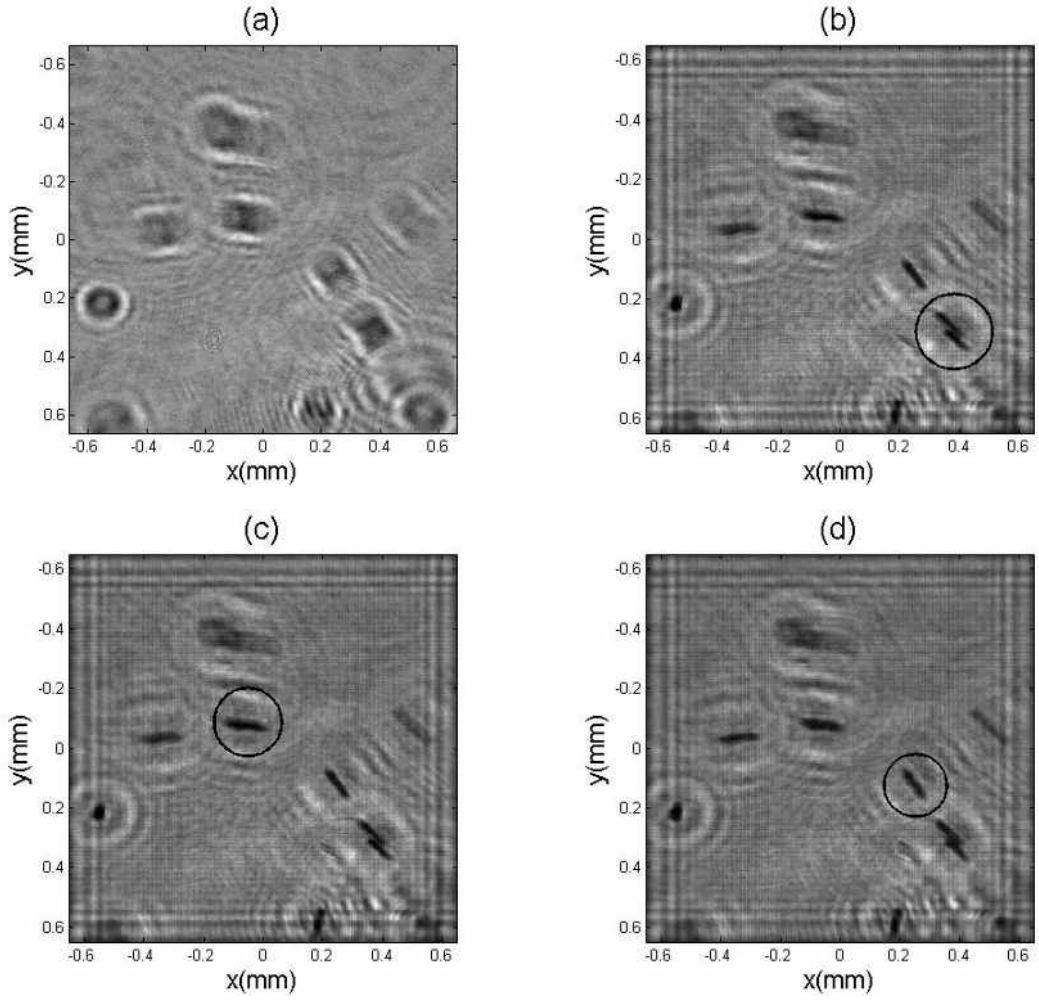

Fig. 6.5: Hologram of $20\mu m$ particle (a), and the reconstructed images of 20m glass particle under $0.20s$ shutter time (b-d). The optimal fractional order of (b-d) are $0.73\pi/2, 0.735\pi/2$, and $0.75\pi/2$, respectively.

From the curve in Fig. 6.3, we then know that these particles are located at the axial positions $z_2 + z = 13.8mm$, $13.75mm$, and $13.6mm$, respectively. The magnification factor is the same as in the first case. The evaluated x- and y-components (v_x, v_y) of the particle velocities in Fig. 6.5 (b), (c), and (d) are $(0.32, 0.27)mm/s$ (for

the lower encircled particle in Fig. 6.5 (b)), $(0.28, 0.25)mm/s$ (for the upper particle in Fig. 6.5 (b)), $(0.54, 0.08)mm/s$ (for the reconstructed particle in Fig. 6.5 (c)), and $(0.30, 0.39)mm/s$ (for the reconstructed particle in Fig. 6.5 (d)). The z-accuracy in this case is not accurate enough to evaluate the z-component velocity. For more description of the z-accuracy, see in section 6.3.2 Precision of axial position.

For a $0.25s$ exposure time, the experimental results are presented in Fig. 6.6. The hologram is presented in Fig. 6.6(a). Two optimal planes are reconstructed with fractional orders $\alpha = 0.76\pi/2$ and $0.8\pi/2$ as presented in Fig. 6.6(b) and (c), respectively. In this case, the droplet's diameter is $1.1mm$. According to Fig. 6.3, the longitudinal positions of the particle in Fig. 6.6(b) and (c) are $14.2mm$ and $13.9mm$, from the CCD sensor. After evaluation of the transverse magnification factor introduced by the imaging system, the x- and y-components of the particle velocities can be determined.

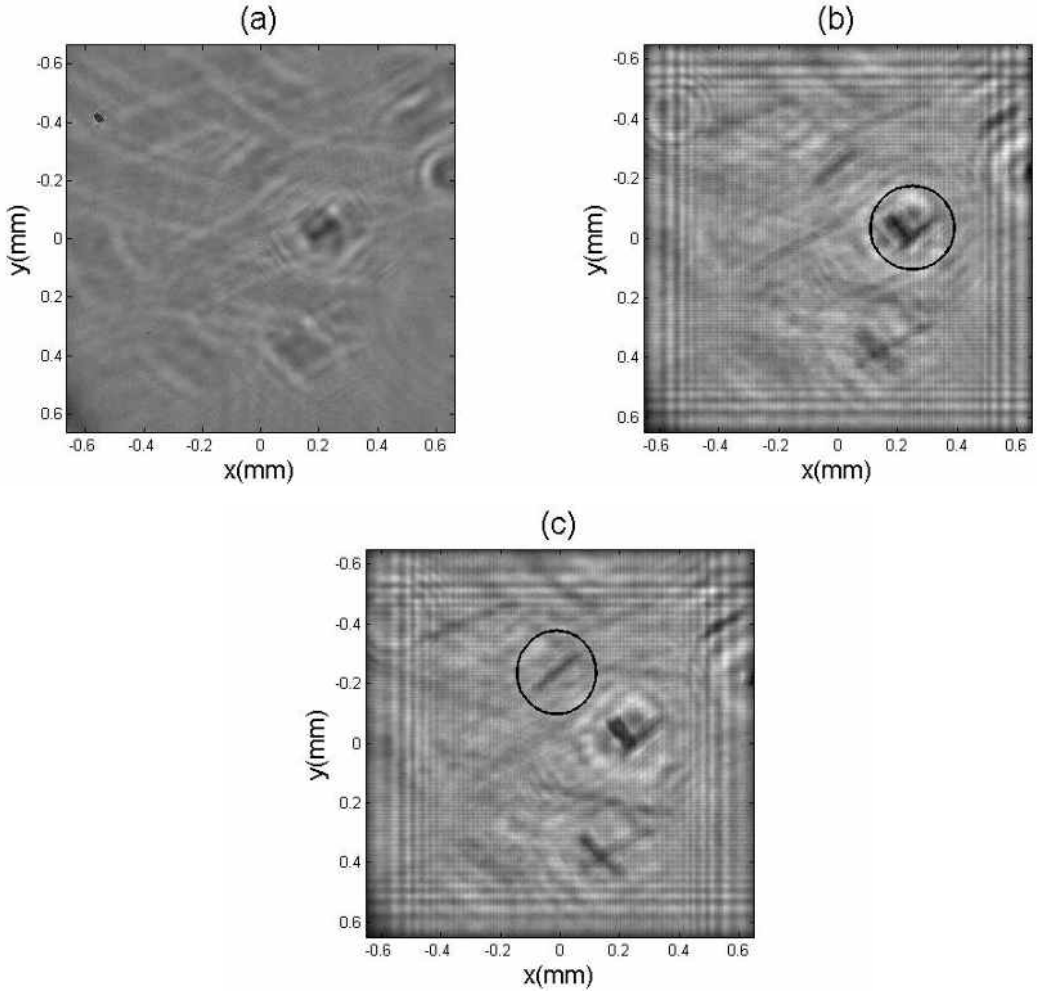

Fig. 6.6: (a) Hologram under $0.25s$. (b) and (c) Reconstructed images of $20\mu m$ glass particle under $0.25s$ shutter time. The optimal fractional orders are $0.76\pi/2$ and $0.80\pi/2$.

The velocity components (v_x, v_y) of the particles in Fig. 6.6 (b) and (c) are $(0.24, 0.29)mm/s$ (for the upper particle in Fig. 6.6 (b)), $(0.41, 0.38)mm/s$ (for the

lower particle in Fig. 6.6 (b)) and $(0.52, 0.45)mm/s$ (for the particle in Fig. 6.6 (c)). In this case, the image quality is poor because there is a lot of noise introduced in the image. Therefore, when the reconstruction process is done, the visibility of the reconstructed particles is poor. Again, the particles in this case move in the transverse plane.

6.3 Signal-to-noise ratio (SNR)

One of the methods to specify the quality of the reconstructed images is calculation of the signal-to-noise ratio (SNR). The better the quality, the higher the SNR value that should be obtained. In this section, the calculation of the SNR ratio is evaluated for each reconstructed image. The SNR in decibels is defined as

$$SNR = 10\log(\frac{I_{mean} - I_{min}}{\sigma}) \tag{6.4}$$

where σ is the standard deviation of the background intensity. I_{mean} is the average background intensity. I_{min} is the minimum intensity of the reconstructed particle.

To find these parameters, we need to treat the image by using "ImageJ" as shown in Fig.6.7.

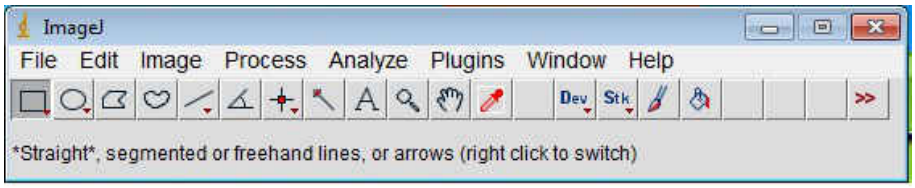

Fig. 6.7: The software "Image J".

The treatments of the reconstructed image are the following steps: select the background area in the reconstructed image and find I_{mean} and σ from the histogram of the selected area, rotate the particle if necessary, select the reconstructed particle's area and plot its intensity profile to see the minimum intensity I_{min}. From these steps, we can calculate the value of the signal-to-noise ratio of the reconstructed image of the particle.

Fig. 6.8 shows the example of the treatment processes as described above. The $20\mu m$ particle in Fig. 6.8 is reconstructed with fractional order $\alpha = 0.56\pi/2$ for exposure time $\tau = 0.15s$. From the measurement, the average intensity is $I_{mean} = 75.648$, the minimum intensity is $I_{min} = 54.330$, and the standard deviation is $\sigma = 3.888$. Therefore, from Eq.(6.4), the signal-to-noise ratio (SNR) is $SNR = 7.39$. The following table shows the SNR of all reconstructed particles.

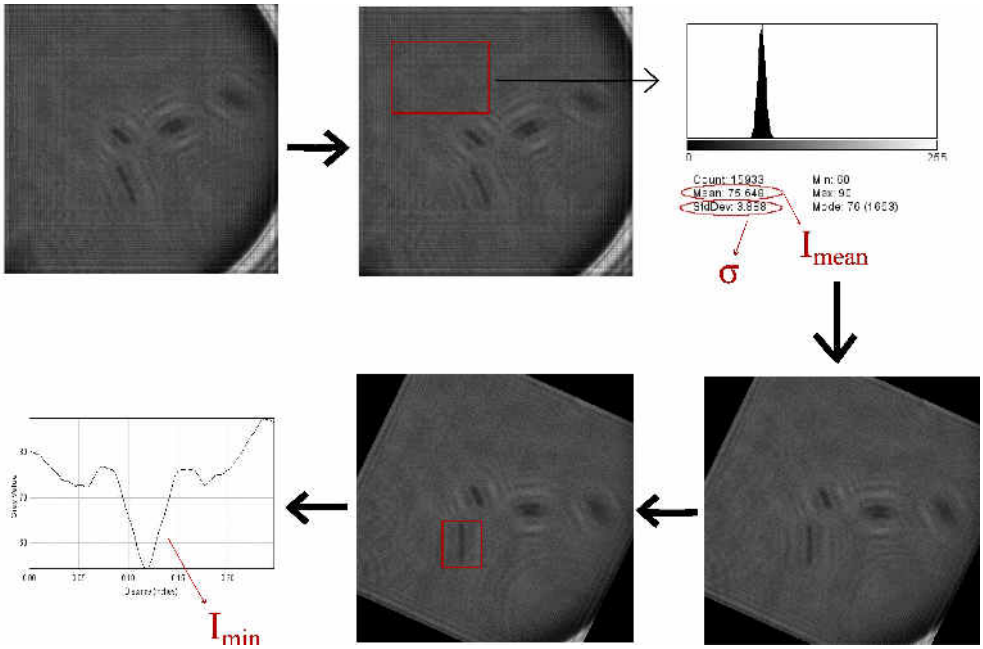

Fig. 6.8: Figure showing the process of signal-to-noise ratio (SNR) measurement.

Exposure time (τ)	Optimal order of reconstruction	SNR(dB)
0.15 s	0.56	7.387
	0.60	7.727
	0.73	8.112
0.20 s	0.73	8.010
	0.735	8.257
	0.75	7.479
0.25 s	0.76	6.523
	0.80	5.534

Tab. 6.1: Table of SNR

From Tab. 6.1, the exposure time $\tau = 0.25s$ gives the lowest signal-to-noise ratio. This means that the reconstructed image has more background noise than the signal. This technique for tracking the trajectories of the particles is limited to the exposure time $\tau < 0.25s$ because the diffraction pattern of the moving particle spreads and is blurred, as observed in the holograms in Fig. 6.2(a), Fig. 6.5(a), and Fig. 6.6(a). With this exposure time, the SNR is very low (less than 7.0 dB). This value is the limited value that we can distinguish the reconstructed particles from the background noise [101, 103, 97]. Therefore, this technique cannot be used for tracking full path of the particles inside a suspended droplet.

6.4 Displacement in z-component

During the recording process, the position of the particles in the droplet changes with time. To measure the displacement of the particles in the z-component, reconstructions with slightly different orders are performed. Let us consider Fig. 6.9 (a). One particle is reconstructed with fractional order α. If the particle moves in the z-direction, the top part of the reconstructed particle is reconstructed with fractional order α_1 while the bottom part is reconstructed with another fractional order α_2. Fig. 6.9(b) shows the positions where the intensity profile of the reconstructed particle is plotted. In this case, the intensity profile of the top part is plotted in red colour and the intensity profile of the bottom part is plotted in blue. The typical intensity profiles obtained in the different reconstructed planes are illustrated in Fig. 6.9(c). Blue lines refer to the profile at the bottom part and the red lines refer to the top part of the reconstructed particle.

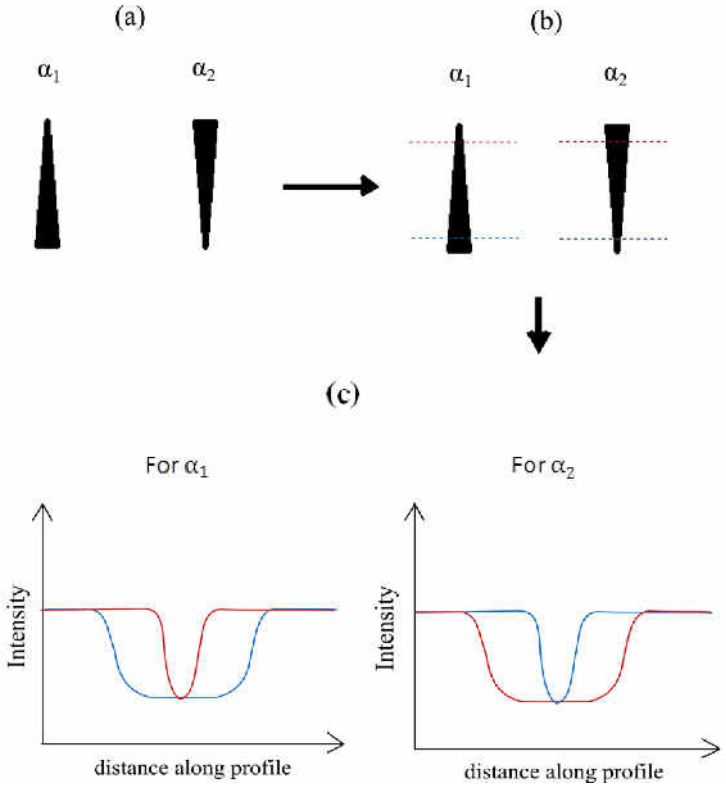

Fig. 6.9: (a) Two reconstructed particles with different fractional orders α_1 and α_2. (b) The position of intensity profile plotting in red and blue colors. (c) The intensity profiles for different fractional orders α_1 (left) and α_2 (right).

In our experiments, the widths of the intensity profiles obtained in the different reconstructed planes are the same. This means that the particles move in the transverse plane not in the longitudinal direction.

The graph in Fig. 6.10 shows the relationship between the signal-to-noise ratio (SNR) in decibels (dB) and the magnitude of transverse velocity multiplied by the ex-

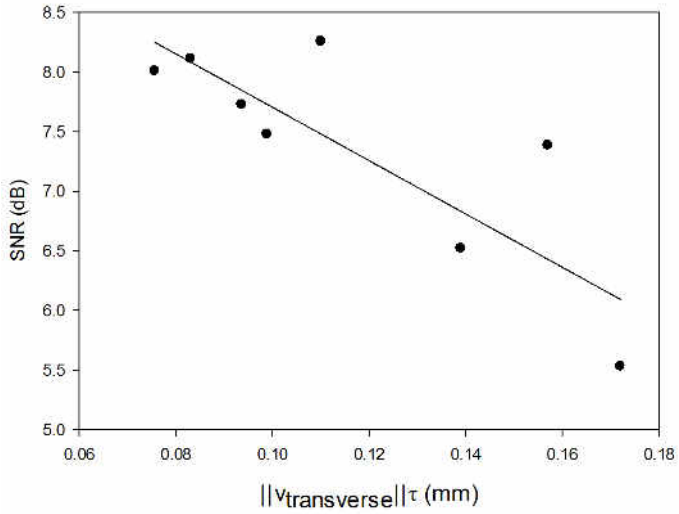

Fig. 6.10: Graph between SNR versus $||v_{transverse}||\tau$.

posure time (we call this the "*transverse length*" or "*transverse displacement*"). For longer exposure time, the contrast of the holograms decreases. The displacement of the particles induces a smoothing effect in the diffraction patterns, which makes unclearly reconstructed particles. From these experiments, we found that the reconstruction is correct (SNR>7.0 dB) when the transverse displacement is $||v_{transverse}||\tau < 0.12mm$ (approximately), where $||v_{transverse}|| = \sqrt{v_x^2 + v_y^2}$.

From the experimental results of different exposure times, we found that each reconstruction image of the particle cannot distinguish when the optimal fractional orders of the two reconstruction planes differ by less than $\triangle a_{avr} = 0.016\pi/2$. From the theoretical graph between the fractional order and longitudinal distance in Fig. 6.3, the corresponding uncertainty of the measurement of the axial position is $\triangle z = 0.16mm$. This is why we cannot evaluate the z-displacement with this technique.

6.5 Conclusions

In this chapter, a long exposure time is applied to the recording process of holograms. The trajectory of particles inside a droplet can be traced by using digital in-line holography with a long exposure time. The transverse trajectory of the particles can be achieved by reconstructing the holograms. In the different reconstruction planes, the length of the particle's trajectory can differ. Moreover, we can determine the x- and y-components of the particle's velocity. However, in this experiment, the z-accuracy is not good enough to determine the z-component velocity.

Tracing the particle's trajectory with long exposure saves on processing time. The hologram with frame by frame recording as in the previous chapter needs the reconstruction of each hologram. This method requires us to evaluate the 3D coordinates of the moving particle for each frame. In contrast, by using a long exposure time, only one reconstruction is done.

7. INTERFEROMETRIC IMAGING OF MULTI-CORE MICROPIPES

I showed in previous chapters that it was possible to reconstruct inclusions located inside a droplet using digital in-line holography. In the last years, our team has been working on microfluid systems. It was demonstrated that it was possible to reconstruct seeding particles in a microflow : i.e. inside a cylindrical, 100 micrometer diameter microchannel [88]. Different types of microchannels exist (squared, circular, mono-core, or multi-core) depending on the microflow systems used. It is an interesting challenge to develop techniques that can control the geometry of the micropipes. Based on previous chapters, we thought that DIH could be a well-suited technique to characterize quantitatively the geometry of multi-core micropipes (separation between the pipes, orientation of the inner multi-cores). In such systems, the multi-core pipes can indeed be viewed as inclusions located within a plexiglas or quartz cylinder whose diameter is more or less 1mm. This appears to be a specific case of cylindrical inclusions located within a cylindrical geometry, and the set-up previously developed in chapters 5 and 6 appears to be a good characterization technique. In this work, double-core and quard-core pipes are considered. The double-core pipe has 2 cylindrical holes and the quard-core pipe has 4 cylindrical holes, as shown in Fig. 7.1.

Fig. 7.1: Double core and quard core tube*

We thus decided to adapt the set-up of Fig. 6.1 (chapter 6) to record the digital in-line holograms generated by a laser beam focused in the vicinity of multi-core micropipes.

*www.vitrocom.com

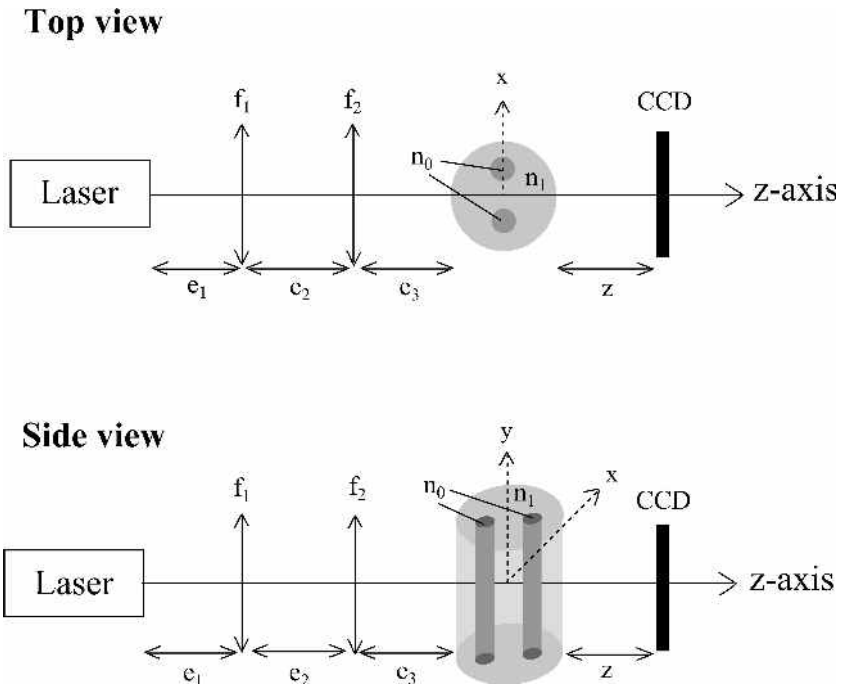

Fig. 7.2: Experimental set-up: side view and top view. The experimental parameters are $e1 = 46.05mm, f1 = 46.05mm, e2 = 300.57mm, f2 = 5.5mm, e3 = 13.20mm, z = 63.40mm$.

The set-up of Fig. 7.2 was realized. The diffracted patterns were recorded on a CCD sensor. An exemple of a recorded image is presented in Fig. 7.3 in the case of a double-core micropipe.

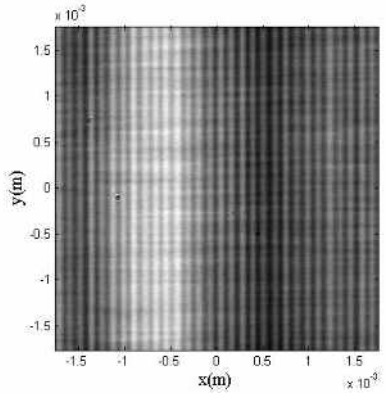

Fig. 7.3: Example of recorded interferogram from the experiment.

A first observation shows that the main effect is the presence of well-contrasted interference fringes. The characteristic diffraction pattern expected when illuminating a slit is partially masked by this interference. It appears that an interferometric analysis should allow us to characterize the position of the inner pipes where digital reconstruction would probably fail. Let us consider the system from an interferometric point of view. We consider the standard interferometric set-up indicated in Fig. 7.4.

In Young's double slit experiment, the spacing between two slits affects the spacing between bright and dark fringes. If the space between the two slits is very small, the interfringe is large. Inversely, if the space between the two slits is bigger, the interfringe is narrower. In our case, the goal is to determine the interdistance "s" between the pipe's cores. The observed interference patterns link to the interdistance "s" between the cores of the pipe.

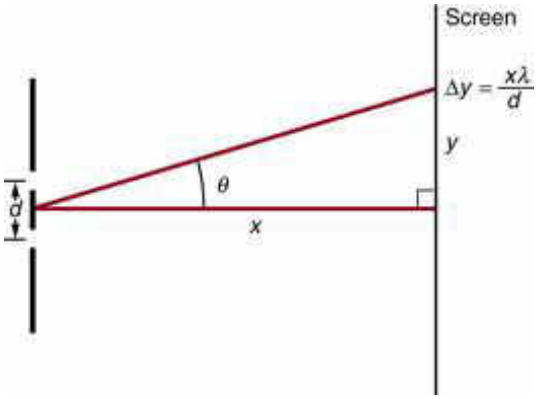

Fig. 7.4: Double slit interference*

An inner cylindrical tube can be considered as a column of many point sources, as presented in Fig. 7.5 (side view). For double cores, the two columns of light sources are located at the origin, as shown in Fig. 7.5. Light from the two sources propagates through the thickness of the tube where the refractive index is n_1. Then light propagates again through the outer curvature of the tube. After that, light goes out from the tube, propagates through the air and forms the interference pattern in the CCD sensor.

In section 1, a mathematical analysis of the intensity distribution recorded on the CCD sensor is investigated by ABCD matrix formalism. By considering the phase difference between the two light sources (which represent the two cores), the spatial fringes' frequency is obtained. The mathematical analysis shows that the spatial frequency depends directly on the interdistance between the two cores and the rotation angle around vertical axis (or y-axis). In section 2, the experimental and the simulated results are compared. Finally, in the last section, the conclusion is presented.

7.1 Mathematical analysis for multi-core micropipes

In this section, a mathematical analysis of two or four channels inside a cylindrical geometry is proposed. The development of interferometric laser imaging for droplet sizing (ILIDS) simulator based on generalized Huygens-Fresnel integrals associated with ABCD matrices was introduced in [30]. In out-of-focus imaging, the analysis of fringe patterns allows us to determine the diameter of droplets,as proposed by [87].

*http://cnx.org/content/m42508/latest/?collection=col11406/latest

In our case, the two/four cylindrical cores are considered to be extended light sources. These two sources illuminate an optical system and the interference of these sources gives fringe patterns in the CCD sensor. The analysis of interferogram allows us to evaluate the relative position between the different channels which are located inside a pipe. In our case, an in-line configuration is considered. In the simulation, light from the extended light sources propagates inside the pipe's thickness and then propagates through the curvature of the outer edge of the pipe as presented in Fig. 7.5: top view.

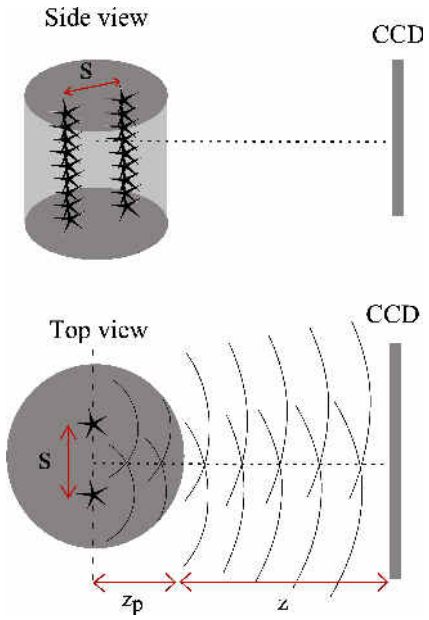

Fig. 7.5: Simulational set-up: side view and top view.

In our model, shown in Fig. 7.5, the two channels can be considered as two columns of light sources. Each column of light source is composed of N glare points. The 3D position of each glare point is defined. We assume the electric field amplitude emitted by each glare point is equal to unity. By using MATLAB, we then simulated N glare points for each column of light sources. The two columns are located along the y-direction. Their position in (x, z) are at $(-s/2, 0)$ and $(+s/2, 0)$.

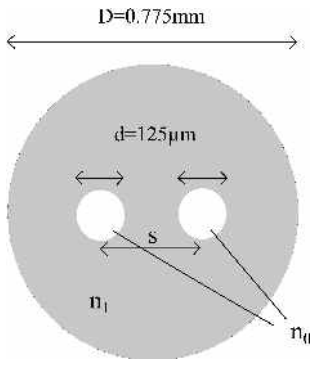

Fig. 7.6: Top view of pipe with indicated parameters.

The physical parameters of the double-core pipe are indicated in Fig. 7.6. The outer diameter of the pipe is equal to $D = 0.775mm$ and the inner diameter is equal to $d = 125\mu m$. These physical parameters of double-core pipe (model:DB531Q) and of quard-core pipe (model:FB531Q) can be found from *www.vitrocom.com* as shown in Fig. 7.6. The refractive index of quartz pipe is 1.54427. The inter-distance $s = 0.25mm$.

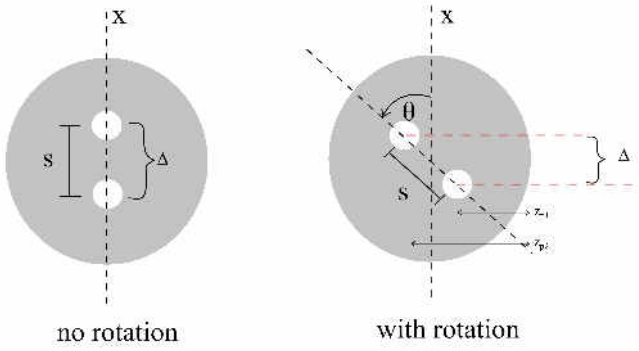

Fig. 7.7: Top view configuration of the channels with and without rotation.

The pipe's core can be rotated around the y-axis. When the cores are rotated, the axial distances of the two cores z_p as indicated in Fig. 7.5's top view are not equal. The distance z_p depends on the rotation angle θ as indicated in Fig. 7.7.

The total electric field emitted from two columns of point sources can be written as

$$G_0(x,y,z) = \sum_n^N A_n \delta(x-a_n, y-b_n, z-c_n)\exp(i\varphi_n) + \sum_n^N A_n \delta(x-d_n, y-e_n, z-f_n)\exp(i\phi_n), \tag{7.1}$$

where A_n is the electric field amplitude emitted by each point source which is assumed to be 1. δ is the Dirac delta function. φ_n and ϕ_n are the initial phases of each point in the first and second columns, respectively. The 3D positions of each point in the first column are (a_n, b_n, c_n) and the positions of each point in the second column are (d_n, e_n, f_n). The first term of Eq.(7.1) represents the first column of point sources and the second term in Eq.(7.1) represents the second column of point sources.

When light passes through these channels, light from the first channel and from the second channel will interfere. When the light is constructively superposed, the bright fringe is observed on the screen. The dark fringes will be observed when destructive interferences occurs. The interference pattern changes (the distance between the two bright fringes changes) due to the inter-distance s between the two channels.

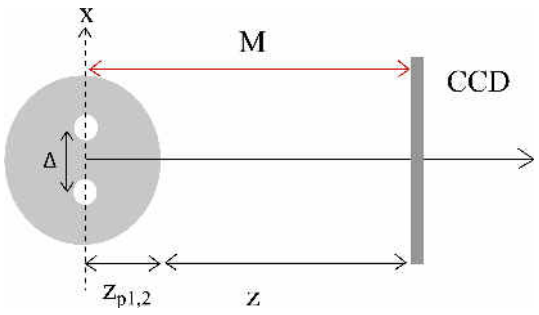

Fig. 7.8: Matrix system in the simulation.

Looking at Fig. 7.7, when there is no rotation around the y-axis , $\triangle$ is equal to the inter-distance (s), $\triangle = s$, as in Fig. 7.7 (left hand side). To make the rotation around the y-axis, we define the rotation angle, θ, as in Fig. 7.7. The smaller $\triangle$, the bigger the distance between two consecutive bright fringes that will be observed. Fig. 7.8 presents the system considered in the simulation. Here, we generate two sources which are located at $z + z_p$ far from the CCD sensor.

In the simulation, we use an ABCD matrix to describe the system. The matrix, M, consists of three matrices $M_{z_{p1,2}}$, $M_R^{x,y}$, and M_z. The matrix $M_{z_{p1,2}}$ can be written as

$$M_{z_{p1,2}} = \begin{pmatrix} 1 & z_{p1,2}/n_1 \\ 0 & 1 \end{pmatrix}, \tag{7.2}$$

where n_1 is the refractive index of the pipe ($n_1 = 1.54427$). The matrix $M_R^{x,y}$ is:

$$M_R^{x,y} = \begin{pmatrix} 1 & 0 \\ \frac{(n_1 - n_0)}{R^{x,y}} & 1 \end{pmatrix}, \tag{7.3}$$

where n_0 is the refractive index of the air ($n_0 = 1$) and $R^{x,y}$ is the radius of curvature of the pipe in the x- and y-direction. Here, we set the pipe along the y-axis. Therefore, the radius of curvature of the pipe is infinity along the y-direction and is $-D/2$ along the x-direction.

The matrix, M_z, can be written as

$$M_z = \begin{pmatrix} 1 & z/n_0 \\ 0 & 1 \end{pmatrix} \tag{7.4}$$

The total matrix, M, can be written as

$$M^{x,y} = M_z \times M_R^{x,y} \times M_{z_{p1,2}} \tag{7.5}$$

or

$$M = \begin{pmatrix} A_{x,y} & B_{x,y} \\ C_{x,y} & D_{x,y} \end{pmatrix} \tag{7.6}$$

When the two channels are rotated, the distance z_p changes from the initial value

($z_p = R$, where R is the radius of outer cylinder), as seen in Fig. 7.7. Assume that the two channels located along the y-axis and placed on the x-axis at the positiosn $x = a1$ and $x = a2$, respectively, as in Fig. 7.9.

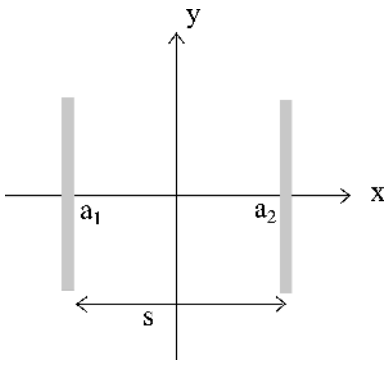

Fig. 7.9: Side view of the two channels. $|a_1 - a_2| = s$ when there is no rotation and $|a_1 - a_2| = \triangle$ with rotation.

By using the generalized Huygens-Fresnel integral, the field amplitude in the plane where the CCD sensor is located is

$$G(x', y', z') = \frac{\exp\left(i\frac{2\pi}{\lambda}E_1\right)}{i\lambda B_{x,y}} \int_{\mathbb{R}^{\not\vdash}} G_0(x, y, z) \exp\left[i\frac{\pi}{\lambda B_x}\left(A_x x^2 - 2x'x + D_x x'^2\right)\right] \exp\left[i\frac{\pi}{\lambda B_y}\left(A_y y^2 - 2y'y + D_y y'^2\right)\right] dx\, dy \tag{7.7}$$

where E_1 is an optical path which is equal to $E_1 = z_{p1,2} + z$. G_0 is the field amplitude of the two columns of light sources, defined in Eq.(7.1). x', y', and z' are the coordinates in the CCD plane. $A_{x,y}, B_{x,y}$, and $D_{x,y}$ are the matrix elements of the transfer matrix M.

For two columns of light sources as indicated in Fig. 7.9, the field amplitude at the CCD sensor can be written as

$$G \propto \gamma_1 \exp\left[i\frac{\pi}{\lambda B_x}\left(A_x a_1^2 - 2a_1 x' + D_x x'^2\right)\right] + \gamma_2 \exp\left[i\frac{\pi}{\lambda B_x}\left(A_x a_2^2 - 2a_2 x' + D_x x'^2\right) + i\varphi_0\right] \tag{7.8}$$

where φ_0 is the initial phase different between the two columns of light sources ($\varphi_0 = \varphi_n - \phi_n$).

The intensity is $I = G^* G$, where the asterisk means the complex conjugate. Assume that $\gamma_1 = \gamma_2 = 1$. Therefore, the intensity is

$$\begin{aligned} I &\propto 1 + 1 + e^{i\left[\frac{\pi}{\lambda B_x} 2(a_1 - a_2)x' + \varphi_0\right]} + e^{-i\left[\frac{\pi}{\lambda B_x} 2(a_1 - a_2)x' + \varphi_0\right]} \\ &\propto 1 + 1 + 2\cos\left[\frac{\pi}{\lambda B_x} 2(a_1 - a_2)x' + \varphi_0\right], \end{aligned} \tag{7.9}$$

where the third term represents the interference term. The phase difference $\triangle\varphi$ of the intensity distribution is

$$\triangle\varphi = \frac{\pi}{\lambda B_x} 2(a_1 - a_2)x' + \varphi_0 \tag{7.10}$$

which is equal to $\frac{2\pi}{\lambda}\delta$ (δ =path difference) and for the constructive interference the path different could differ by the full number of wavelength ($\delta = m\lambda$), where $m = 0, \pm 1, \pm 2, \pm 3, \ldots$. Let the initial phase difference $\varphi_0 = 0$ (in the case of no rotation) and the spacing between the two bright fringes be δx. If $x' = \delta x$ (the distance between the two successive bright fringes), the phase difference is 2π. Then

$$\frac{\pi}{\lambda B_x} 2(a_1 - a_2)\delta x = 2\pi. \tag{7.11}$$

The spacing between the two bright fringes, δx, becomes

$$\delta x = \frac{\lambda B_x}{(a_1 - a_2)} \tag{7.12}$$

Remember that the $\triangle = a_1 - a_2$. According to the rotation in Fig. 7.7, when the two channels are rotated, $\triangle$ is also changed as:

$$\triangle = s\ \cos\theta \tag{7.13}$$

Therefore, the fringes' space, δx is:

$$\delta x = \frac{\lambda B_x}{s\ \cos\theta} \tag{7.14}$$

The inverse of the fringes' space is the spatial frequency of the interference fringes. Thus the spatial frequency of the interference fringes is

$$F = \frac{1}{\delta x} = \frac{s\ \cos\theta}{\lambda B_x} \tag{7.15}$$

which depends on the orientation of the channels. B_x is the matrix element of the matrix M.

The mathematical development for the intensity distribution of the quard-core pipe is developed in the same way as for the double-core pipe. However, the system is more complex than in the case of double-core pipe. The geometry of the quard-core pipe is shown in Fig. 7.10.

The inner diameter of the channel is $d = 125\mu m$ and the outer diameter of the pipe is $D = 0.775mm$. The channels are separated with the distance $s = 0.25mm$. When the four channels are rotated with the angle θ, the $\triangle$ is changed. In this case, there are six values of $\triangle$: $\triangle_1, \triangle_2, \triangle_3, ..., \triangle_6$ as indicated in Fig. 7.12, in which the channels are number as 1, 2, 3, and 4.

The distance $\triangle_1$ is the distance between channel 1 and 2. $\triangle_2$ is the distance between channel 1 and 4. $\triangle_3$ is the distance between channel 1 and 3. $\triangle_4$ is the distance

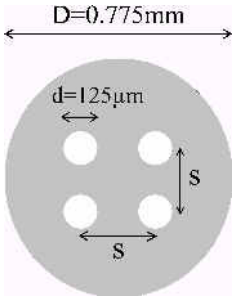

Fig. 7.10: Top view of the quard-core pipe indicating its parameters.

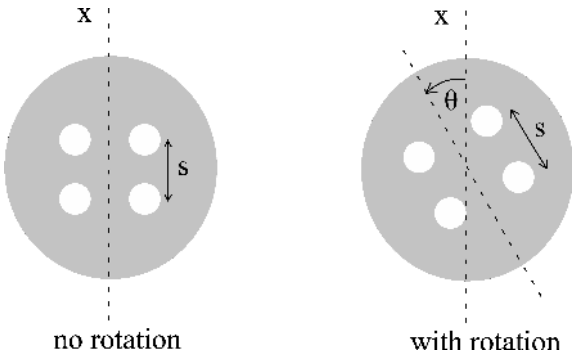

Fig. 7.11: Top view of the quard-core pipe with and without rotation.

between channel 2 and 3. $\triangle_5$ is the distance between channel 3 and 4. $\triangle_6$ is the distance between channel 2 and 4.

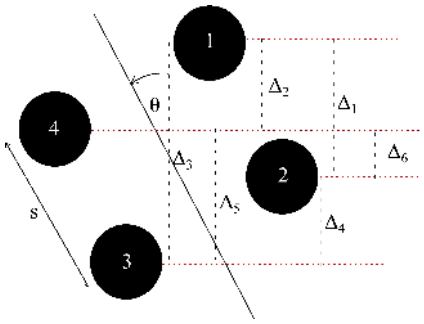

Fig. 7.12: Four channels with rotation angle θ and their interdistances $\triangle_1, \triangle_2, \triangle_3$, and $\triangle_4$.

However, we have $\triangle_1 = \triangle_5$ and $\triangle_2 = \triangle_4$. The interdistances between the channels are defined as the following relations:

$$\begin{aligned} \triangle_1 &= s\ \cos\theta, \quad \triangle_2 = s\ \sin\theta, \quad \triangle_3 = \sqrt{2}\, s\ \left|\sin\left(\frac{\pi}{4}+\theta\right)\right| \\ \triangle_4 &= s\ \sin\theta, \quad \triangle_5 = s\ \cos\theta, \quad \triangle_6 = \sqrt{2}\, s\ \left|\sin\left(\frac{\pi}{4}-\theta\right)\right| \end{aligned} \tag{7.16}$$

From the spatial frequency of the double-core pipe in Eq.(7.15), the spatial frequencies $F_1, F_2, F_3, ..., F_6$ are:

$$F_1 = \frac{\triangle_1}{\lambda\, B_1} \qquad F_2 = \frac{\triangle_2}{\lambda\, B_2} \qquad F_3 = \frac{\triangle_3}{\lambda\, B_3}$$
$$F_4 = \frac{\triangle_4}{\lambda\, B_4} \qquad F_5 = \frac{\triangle_5}{\lambda\, B_5} \qquad F_6 = \frac{\triangle_6}{\lambda\, B_6} \tag{7.17}$$

The parameters B_1, B_2, B_3, and B_4 depend on the distances $z_{p1}, z_{p2}, z_{p3}, z_{p4}$ along the z-axis between each channel 1, 2, 3, and 4, respectively, to the curvature of the pipe. $\triangle_1$ to $\triangle_6$ are defined in Eq.(7.16).

B_1 relates to channel 1 and channel 2, and the distance z_p between these two channels is the average between z_{p1} and z_{p2}. B_2 relates to channel 1 and channel 4, and the distance z_p between these two channels is the average between z_{p1} and z_{p4}. B_3 relates to channel 1 and channel 3, and the distance z_p between these two channels is the average between z_{p1} and z_{p3}. B_4 relates to channel 2 and channel 3, and the distance z_p between these two channels is the average between z_{p2} and z_{p3}. B_5 relates to channel 3 and channel 4, and the distance z_p between these two channels is the average between z_{p3} and z_{p4}. B_6 relates to channe l2 and channel 4, and the distance z_p between these two channels is the average between z_{p2} and z_{p4}. For all description, see Fig. 7.13.

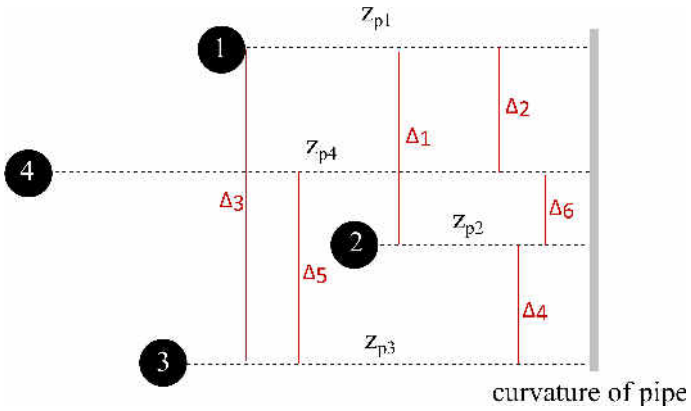

Fig. 7.13: The configuration showing $\triangle_1, ..., \triangle_6$ and $z_{p1}, ..., z_{p6}$.

7.2 Experimental Results

7.2.1 Double-core pipe

In this section, we present the possiblility of our simulation predicting the interferogram created by two channels inside a cylindrical geometry (pipe). In the double-core pipe experiment (model: DB 531Q), the experimental set-up is presented in Fig. 7.2. All parameters used in the experiment are indicated in the caption of Fig. 7.2. The configuration set-up in this study is the same as in the previous study. The difference

is in replacing a droplet with inclusions by a double-core pipe. This pipe can be rotated around the y-axis as already discussed in the previous section. The pipe is made from quartz with refractive index $n_1 = 1.54427$. Light from a light source is used to illuminate the pipe. A CCD sensor is located at distance z from the pipe.

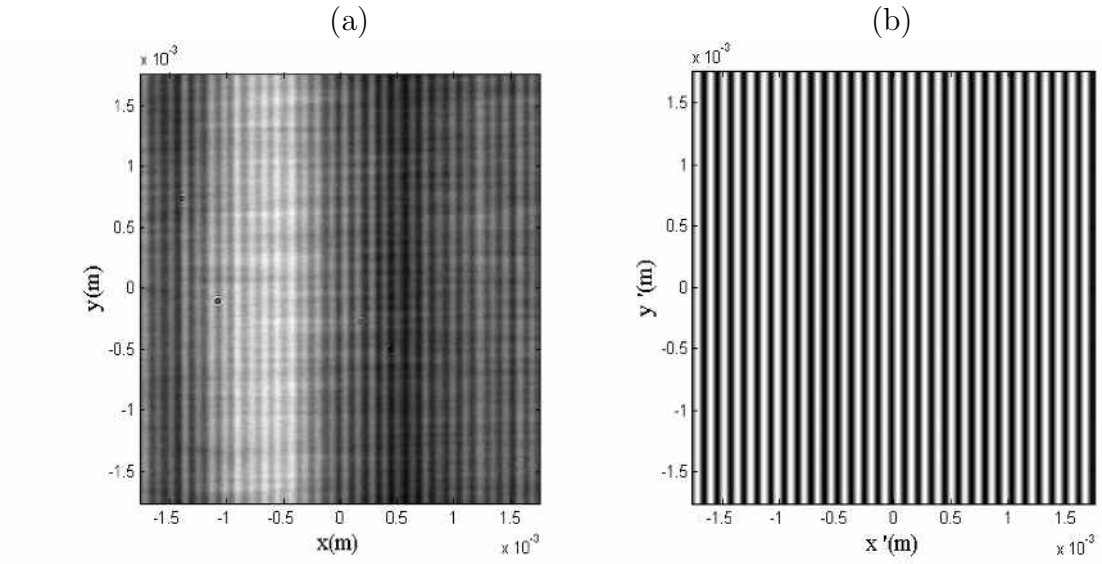

Fig. 7.14: Interference fringes without rotation from experiment (a), and simulation (b).

In the CCD sensor plane, the interference pattern is observed as bright and dark strips. The experimental interference pattern is shown in Fig. 7.14(a) and the simulated interference pattern is shown in Fig. 7.14(b). The rotation angle in this case is $\theta = 0\pi(or 0°)$. Two channels align along the x-axis (no rotation). The analysis of interferograms can be done by plotting the intensity profile of these inferference patterns along the horizontal axis. The intensity profile along the horizontal axis of the experiment and the simulation are presented in Fig. 7.15.

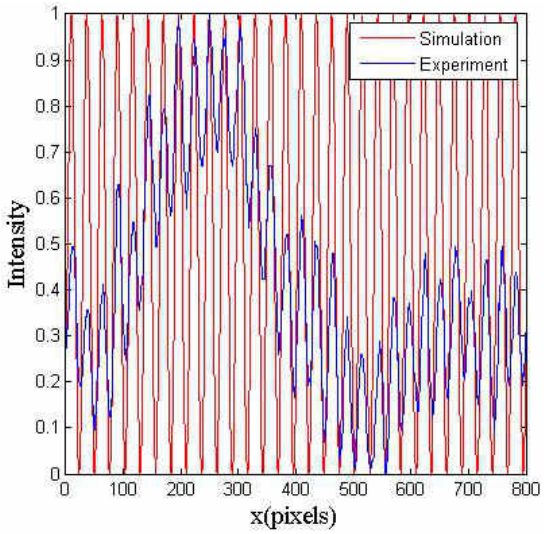

Fig. 7.15: Intensity profile of the interference fringes from simulation (red) and from experiment (blue) of Fig. 7.14.

To analyse the intensity profile of the interference pattern, the one-dimensional fast Fourier transform (1D-FFT) is applied to transform the intensity distribution in the space domain to the frequency domain. By using 1D-FFT, we can extract the frequencies forming the interference patterns. The frequency domains of the intensity distribution in the simulation and in the experiment are presented in Fig. 7.16.

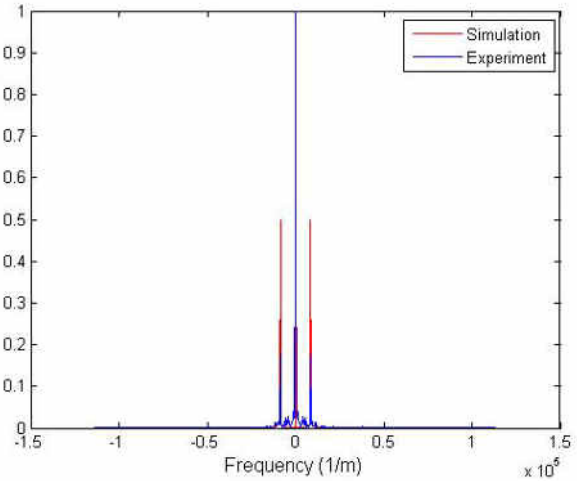

Fig. 7.16: FFT of the intensity distribution in simulation (red) and experiment (blue) when the two channels have no rotation ($\theta = 0°$).

From Fig. 7.16, there are three peaks. The central peak at zero comes from the background signal. The two peaks which are sysmetric around the central peak refer to the fringe's frequency. The distance from the two small peaks to the central peak is the value of the fringe's frequency. The fringe's frequency from the experiment is $8523m^{-1}$ whereas the calculated frequency is $8536m^{-1}$ as shown in Fig. 7.16. The results in Fig. 7.16 for the simulation and experiment agree well.

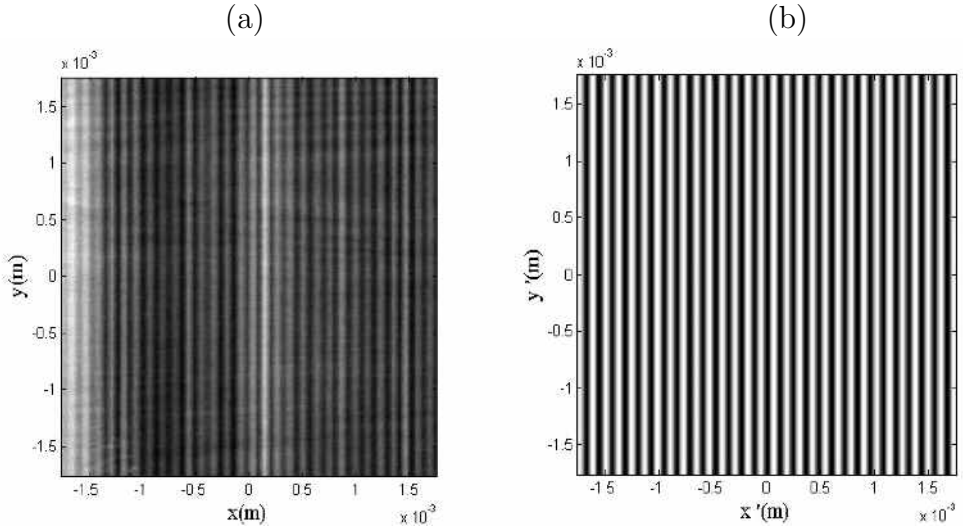

Fig. 7.17: Interference patterns with rotation angle $\theta = 12.6°$ from the experiment (a) and from the simulation (b).

For the rotation angle $\theta = 0.07\pi(12.6°)$, the experimented and the simulated interference patterns are shown in Fig. 7.17 (a) and (b), respectively. The intensity profiles are obtained (not presented here). By using 1D fast Fourier transform (1D-FFT), their intensity spectrum is as shown in Fig. 7.18.

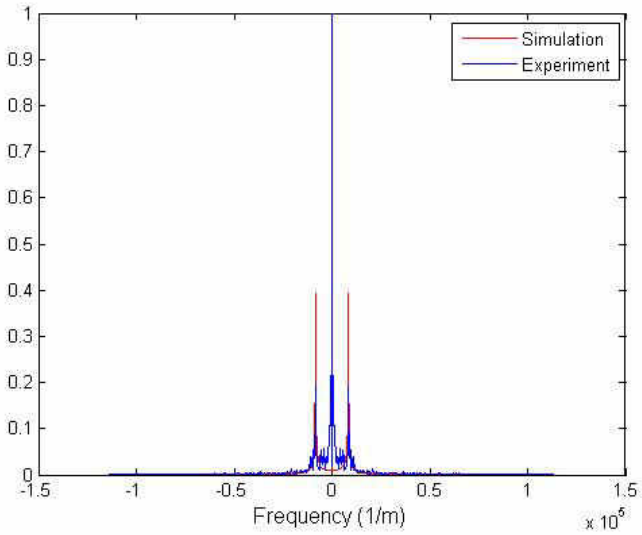

Fig. 7.18: FFT of the intensity distribution in simulation (red) and experiment (blue) with rotation angle $\theta = 12.6°$.

From the 1D-FFT in Fig. 7.18, there are three lobes. The central lobe at the origin comes from the background signal and the two lobes are symmetric to each other. In this case, the spatial frequency of the fringes with rotation angle $\theta = 12.6°$ is $8239m^{-1}$ (from the experiment). The calculated frequency is $8328m^{-1}$. From the FFT in Fig. 7.18, the peaks of the simulation (in red) and experiment (in blue) are located at the same positions.

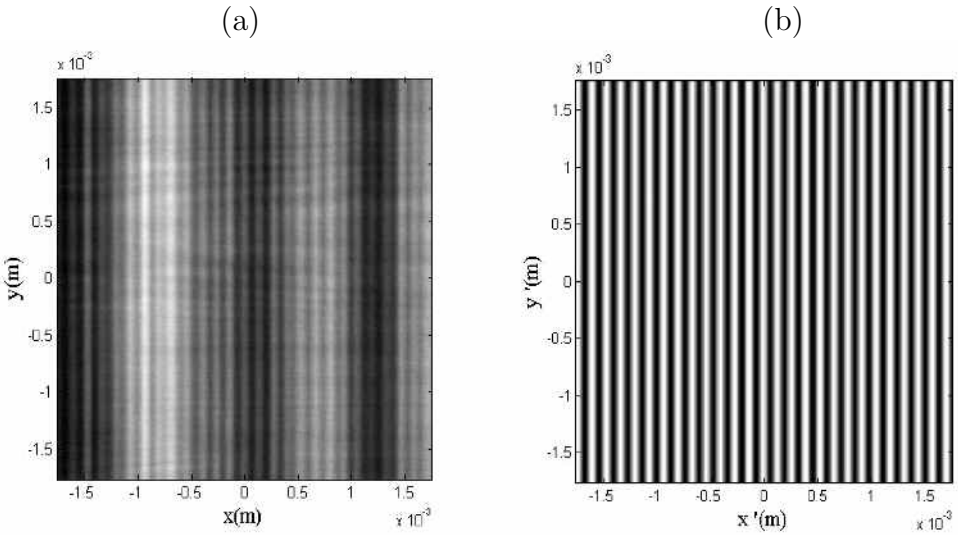

Fig. 7.19: Interference patterns of double-core pipe with $\theta = 30.6°$ from experiment (a) and simulation (b).

For the rotation angle equal to $0.17\pi(30.6°)$, the interference fringes are shown in Fig. 7.19. Fig. 7.19(a) shows the interference pattern from the experiment and Fig. 7.19(b) shows the interference pattern from the simulation.

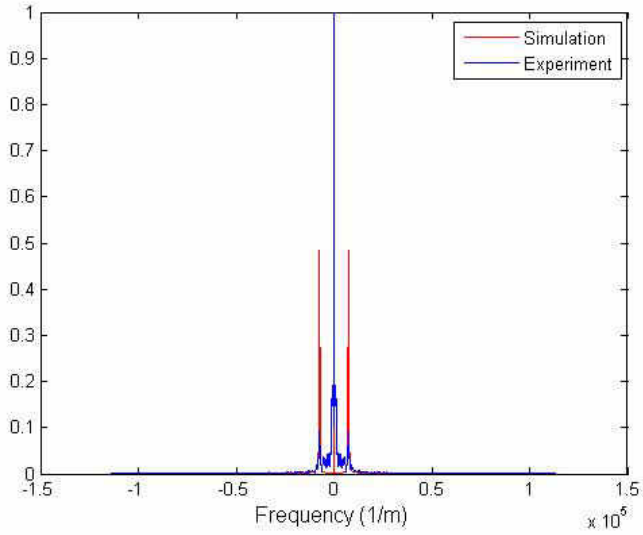

Fig. 7.20: FFT of the intensity distribution of double-core pipe with $\theta = 30.6°$.

The intensity profiles along the horizontal axis of the simulated and experimented fringes are obtained. After using 1D-FFT, the spectrum of the intensity distribution is as presented in Fig. 7.20. From the spectrum in Fig. 7.20, the spatial frequency of the interference pattern is $7382m^{-1}$ whereas the calculated spectrum is equal to $7353m^{-1}$. The result from the experiment agrees well with the simulation.

For the rotation angle $\theta = 0.25\pi(45°)$, the interference fringes are shown in Fig. 7.21 both experimentally (a) and numerically (b).

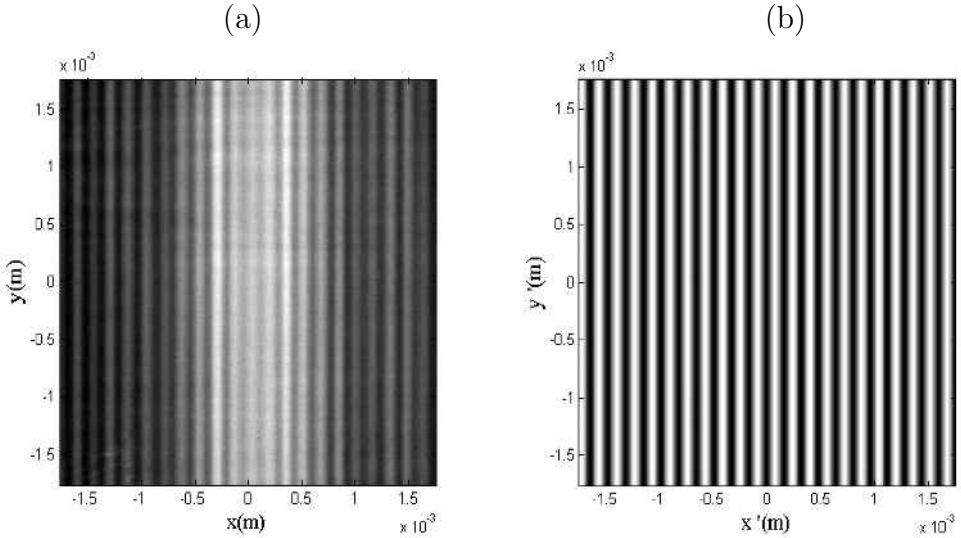

Fig. 7.21: Interference fringes of two channels with $\theta = 45°$ in experiment (a) and simulation (b).

The intensity profiles are plotted for both the experiment and simulation. The spectrum of the intensity profiles of the interference fringes is analysed by 1D-FFT. The result is presented in Fig. 7.22. The spatial frequency is equal to $6250m^{-1}$ in Fig. 7.22 whereas the calculated spatial frequency is $6034m^{-1}$.

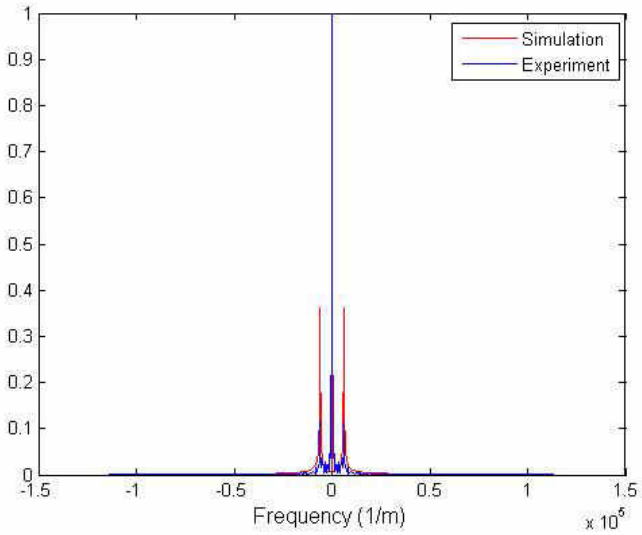

Fig. 7.22: FFT of the intensity distribution of double-core pipe with rotation angle $\theta = 45°$.

For the rotation angle $\theta = 0.4\pi(72°)$, the interference fringes are shown in Fig. 7.23 both experimentally (a) and numerically (b).

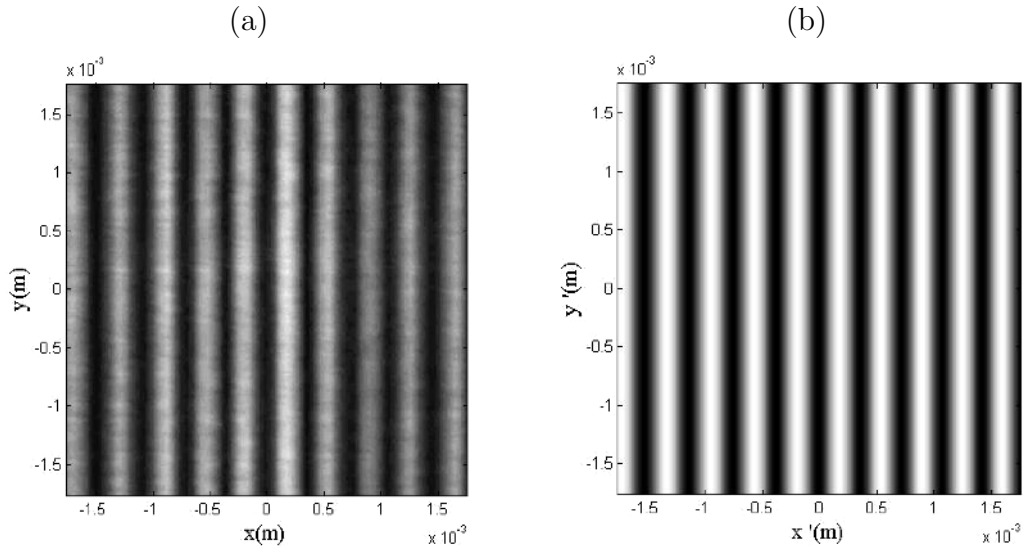

Fig. 7.23: (a) The experimented and (b) simulated interference fringes with rotation angle $\theta = 72°$.

The intensity profiles are plotted for both cases as shown in Fig. 7.24. The spectrum of the intensity profiles of the interference fringes is analysed by 1D-FFT. The result is presented in Fig. 7.25.The spatial frequency is equal to $2841m^{-1}$. The calculated spatial frequency according to Eq.(7.15) is equal to $2640m^{-1}$.

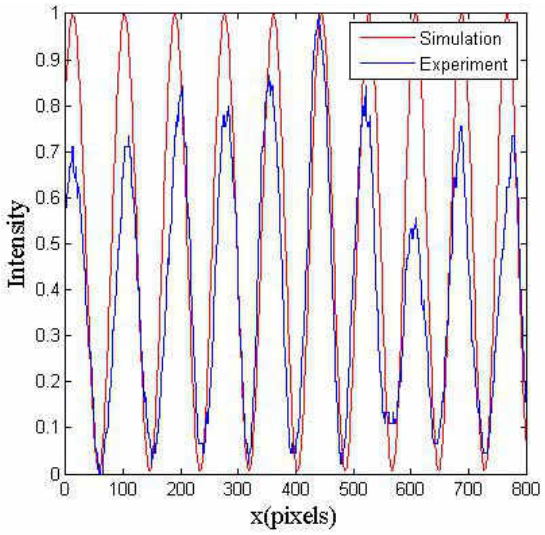

Fig. 7.24: Intensity profile of the interference fringes in Fig.7.23 of simulation (red) and of experiment (blue).

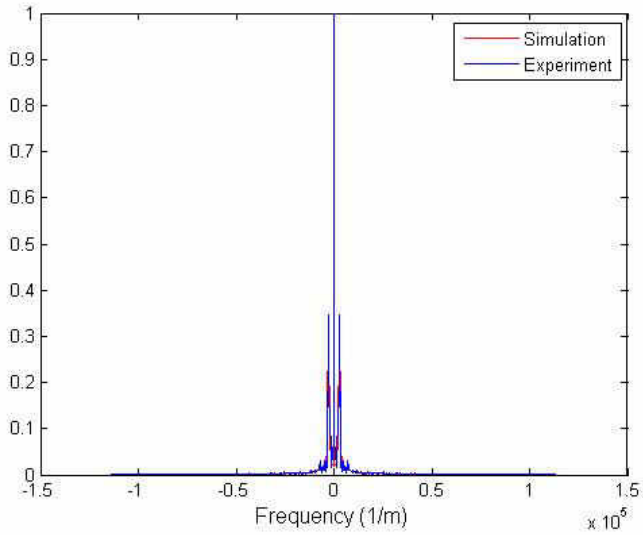

Fig. 7.25: FFT of the intensity profile in Fig. 7.24.

When the rotation angle increases to $\pi/2$, the fringes' frequency is not the lowest. Sub-fringes are observed inside each strip of bright fringes. This effect may come from the interference of higher waves (more than two waves). At a 90° of rotation angle, the intensity is very low due to light scattered from the first pipe and there is a small amount of light that can pass through the second pipe. Fig. 7.26 presents the tube with rotation angle $\theta = 90°$. The red arrow represents the direction of the incident light source.

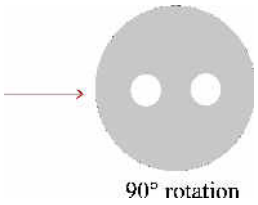

Fig. 7.26: Double-core configuration when rotation angle $\theta = 90°$.

The relationship between the spatial frequency and rotation angle of the double-core pipe is shown in Fig. 7.27 from FFT of the experimental results (blue), from the simulation (red), and from Eq.(7.15) (black). We can see that we are able to determine the distance between the two cores and their orientation.

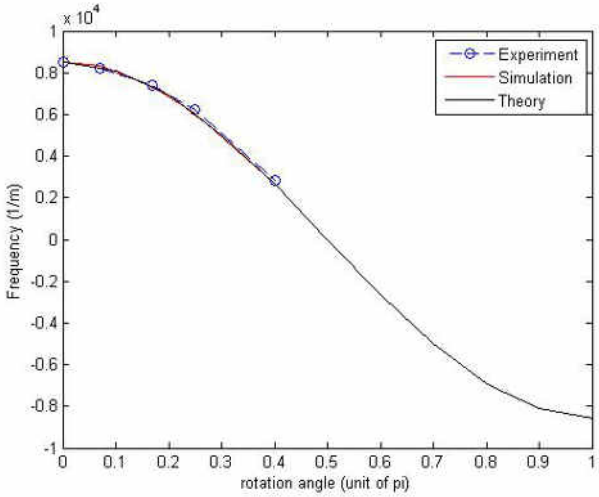

Fig. 7.27: Relationship between rotation angle and fringe's frequency.

The following table presents the fringe's frequency and fringe's space at different rotation angles from the experiment and simulation.

Angle(θ)	Experiment		Simulation	
	$F(m^{-1})$	$\delta x = \frac{1}{F}(m)$	$F(m^{-1})$	$\delta x = \frac{1}{F}(m)$
0°	8523	1.173×10^{-4}	8536	1.172×10^{-4}
12.6°	8239	1.214×10^{-4}	8328	1.201×10^{-4}
30.6°	7382	1.355×10^{-4}	7353	1.360×10^{-4}
45°	6250	1.600×10^{-4}	6034	1.657×10^{-4}
72°	2841	3.520×10^{-4}	2640	3.788×10^{-4}

Tab. 7.1: Data derived from different orientation angles of pipe.

From the intensity spectrum, the fringe frequency is obtained and the fringe spacing is the inverse of fringe frequency which is indicated in the Tab. 7.1. From the

previous section, we already know that the fringe spacing (δx) depends on the interdistance s and the rotation angle θ, as in Eq.(7.14).

When the double-core micropipe makes no rotation, the distances from the first and the second channel to the curvature of pipe, z_{p1} and z_{p2}, are equal. However, when the double-core pipe rotates with some angle, the distances z_{p1} and z_{p2} are different, as presented in Fig. 7.7. The following table shows the calculated distances z_{p1} and z_{p2} with different rotation angles. The calibrated value of the interdistance is $s = 0.2583mm$. The results in Tab. 7.2 match the calibrated value well.

Angle(θ)	$z_{p1}(mm)$	$z_{p2}(mm)$	B_1	B_2	$s(mm)$
0°	0.3875	0.3875	0.0471	0.0471	0.2578
12.6°	0.3593	0.4157	0.049	0.0453	0.2555
30.6°	0.3218	0.4532	0.0514	0.0428	0.2592
45°	0.2962	0.4788	0.0531	0.0412	0.2675
72°	0.2647	0.5103	0.0551	0.0391	0.2779

Tab. 7.2: Distances z_{p1} and z_{p2}, matrix elements B_1 and B_2, and interdistance s presented according to the orientation of pipe.

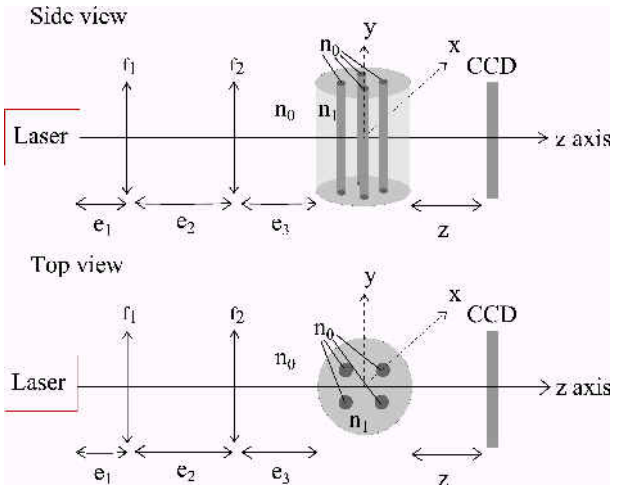

Fig. 7.28: Experimental set-up: top view and side view. The experimental parameters are $e1 = 46.05mm, f1 = 46.05mm, e2 = 300.57mm, f2 = 5.5mm, e3 = 13.20mm, z = 63.40mm$.

7.2.2 Quard-core pipe

For the experiment of quard-core pipe (model: FB 531Q), the experimental set-up is presented in Fig. 7.28. All parameters used in the experiment are indicated in the caption of Fig. 7.28. The configuration set-up is the same as in the case of the double-core pipe. The incident light source illuminates a quard-core pipe. The

quard-core pipe is made from the same material as the double-core pipe (quartz) with its refractive index $n_1 = 1.54427$. A CCD sensor is located at distance z from the quard-core pipe.

In the CCD plane, the interference pattern is observed as shown in Fig. 7.29(a) for the experiment and the simulated interference pattern is shown in Fig. 7.29(b).

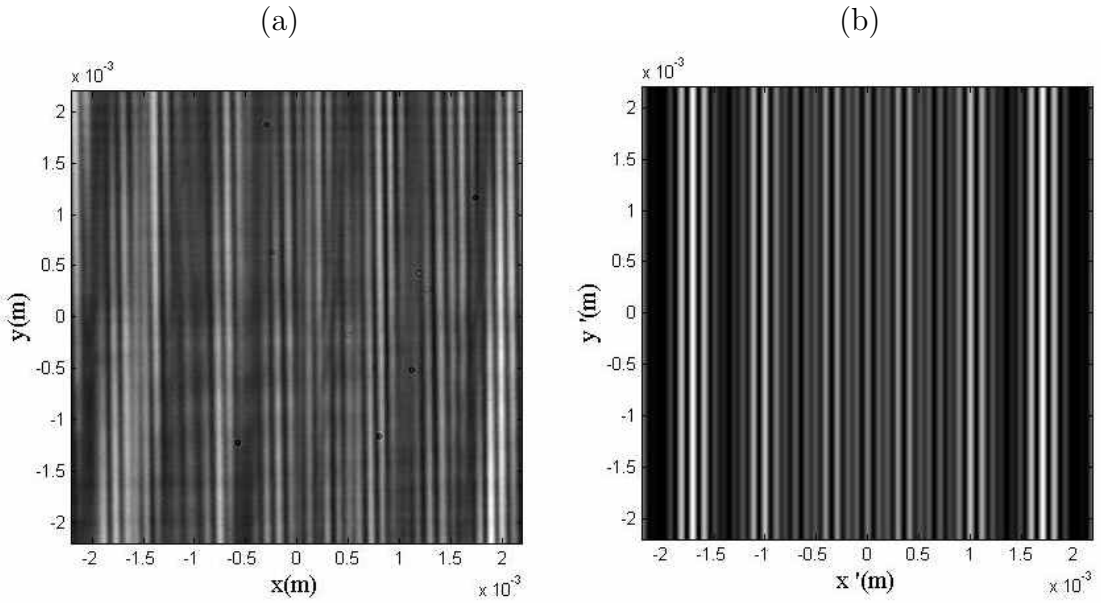

Fig. 7.29: Experimental interference pattern of quard-core pipe (a) and numerical interference pattern of quard-core pipe (b) without rotation.

The rotation angle in this case is $\theta = 0\pi, 0.51\pi (or 0°, 91.8°)$. The intensity profiles along the horizontal axis of the experiment and simulation are presented in Fig. 7.30.

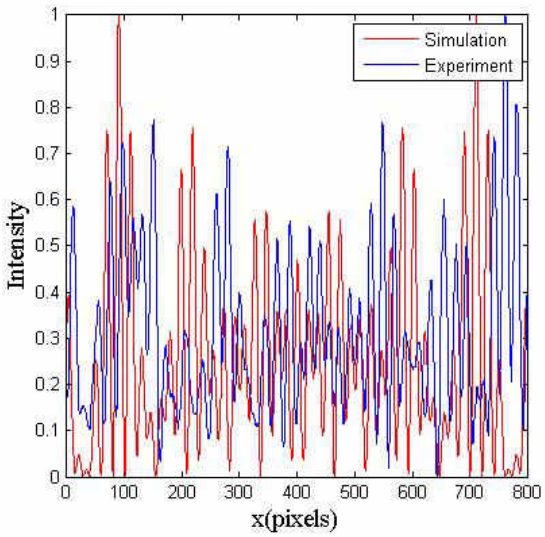

Fig. 7.30: Intensity profile of the interference fringes of simulation (red) and of experiment (blue).

To analyse the intensity profiles of the interference pattern, the one-dimensional

fast Fourier transform (1D-FFT) is applied to transform the intensity distribution in the space domain to the frequency domain. By using 1D-FFT, we can extract the spatial frequencies forming the interference patterns. The intensity spectrum in the simulation (in red) and in the experiment (in blue) are presented in Fig. 7.31.

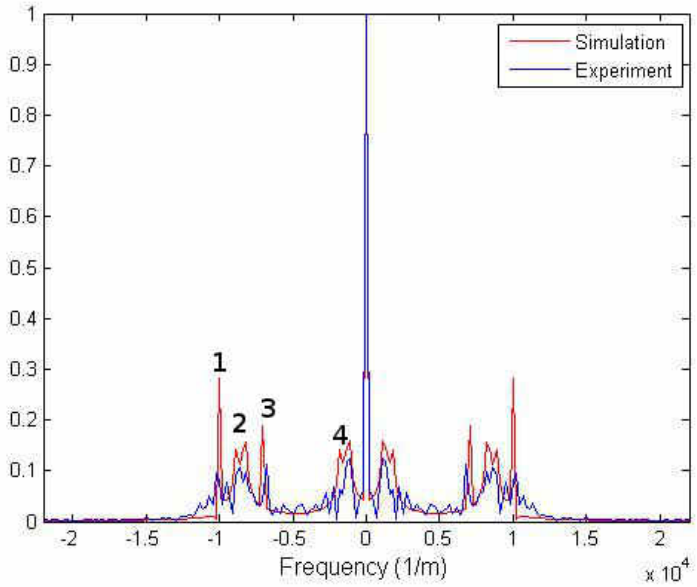

Fig. 7.31: FFT of the intensity distribution in simulation (red) and experiment (blue).

From the intensity spectrum, there are 9 peaks. The central peak comes from the background signal. The eight peaks on the two sides of the central peak are symmetric. One side of the central peak is considered. From the simulation, there are 4 frequencies: $10000m^{-1}, 8636m^{-1}, 7045m^{-1}, 1136m^{-1}$. From the experimental spectrum in Fig. 7.31, there are the following frequencies: $10230m^{-1}$, $8409m^{-1}$, $6818m^{-1}$, and $1364m^{-1}$. The fringes' frequencies of the simulation and experiment agree well.

Experiment		Simulation	
$F(m^{-1})$	$\delta x = \frac{1}{F}(m)$	$F(m^{-1})$	$\delta x = \frac{1}{F}(m)$
$F_1 = 10230$	9.775×10^{-5}	10000	1.000×10^{-4}
$F_2 = 8409$	1.189×10^{-4}	8636	1.158×10^{-4}
$F_3 = 6818$	1.467×10^{-4}	7045	1.419×10^{-4}
$F_4 = 1364$	7.331×10^{-4}	1136	8.803×10^{-4}

Tab. 7.3: Values of fringe frequency F and fringe spacing δx.

After the spatial frequency of the interference fringe is obtained, the space between fringes is derived from the inversion of the frequency as presented in Tab. 7.3.

Let us consider the spectrum in Fig. 7.31, where the highest frequency (peak1) is the result of the interference between channel 1 and channel 2. Peak3 comes from the interference between channel 3 and channel 4. The intermediate peak (peak2) between peak 1 and peak 2 has two consecutive peaks which are closed together. This intermediate peak (peak2) comes from crossed interference between channel 1 and 3 and channel 2 and 4. Peak4 relates to the interference between channel 1 and 4 and channel 2 and 3.

From the relation in the previous section, Eq.(7.16) and Eq.(7.17), we then obtain the interdistance between cores s. Peak1 in Fig. 7.31 corresponds to the interdistance between channel 1 and channel 2 $s_1 = 0.256mm$. Peak2 corresponds to the distance between channel 1 and channel 3 or channel 2 and channel 4 $s_2 = 0.242mm$. Peak3 corresponds to the distance between channel 3 and channel 4 $s_3 = 0.210mm$. Peak4 corresponds to the distance between channel 1 and channel 4 or channel 2 and channel 3 $s_4 = 0.048mm$. The calibrated value of s is $s = 0.25mm$. The value of s_1 is more than the values of s_2, s_3, and s_4 because the interdistance s_1 comes from the interference between channel 1 and 2 and these two columns are closer to the CCD sensor. Channel 3 and 4 are further from the CCD. Thus from the CCD point of view, the distance s_1 looks slightly greater than the others.

For the other rotation angles of quard-core pipe, the interference patterns are not the same as in the simulation because of various factors. The possible factors are: the precision in rotation is not accurate enough, so the interference pattern that we observed quite close to the case of rotation angle 0π; the alignement of the pipe is not in the vertical direction or its alignement makes some angle to the vertical axis; the effect of the cylindrical shape of the inner cores.

7.3 Conclusions

In this chapter, we show the possiblility of our model describing the interferogram introduced by a double- or quard-core pipe. With our model, we consider the cores of the pipe as extended light sources. Each extended light source is composed of many point sources. For mathematical description, the generalized Huygens-Fresnel integral with ABCD matrix formalism is proposed to describe the propagation of light through a multi-core pipe. The experimental and numerical results of the interference pattern of multi-core pipes are studied. For double-core pipe, light from two extended light sources interfered and caused the interference pattern observed in the CCD sensor. For quard-core pipe, light from the four extended light sources interfered and the interference pattern could be observed in the CCD camera.

In this work, the relation between fringes' frequency and the interdistance length is developed for both two and four channels. The interference patterns from the experiment and simulation of the rotated pipe are compared. The calculated and experimental spatial frequencies correspond to each other.

8. CONCLUSIONS AND PERSPECTIVES

For particle detection, many techniques have been developped such as particle imaging velocimetry (PIV), interferometric laser imaging for droplet sizing (ILIDS), Rainbow, laser Doppler anemometry (LDA), etc. However, these techniques cannot give three-dimensional information such as the 3D positions of the particle. The only technique that is able to give three-dimentional information is holography. In this thesis, the simplest configuration of holography, called digital in-line holography (DIH), is used to characterize the inclusions inside a droplet. The main advantage of this configuration is the simplification of the set-up.

In this work, we have been developed the DIH for characterization of inclusions inside a droplet. The generalized Huygens-Fresnel integral represented by an ABCD matrix is used to describe the propagation of light through the considered optical system. For the digital holography, a hologram is recorded by a CCD sensor and is reconstructed digitally by 2D fractional Fourier transform (2D-FRFT). In the best reconstruction plane, the image of the particle is recovered. This optimal plane of reconstruction corresponds to the optimal fractional order in 2D-FRFT which depends on the longitudinal location of the particle.

The DIH developed is used to characterize inclusions in a flow. In this previous model, the inclusions are considered as opaque disks, while the shape of the container (droplet or channel) is considered as a curved interface. This point of view allows us to take into account the simple aberration as astigmatism.

Following this direction, in the first part of chapter 3 of this thesis, we proposed a new model to describe the transmission function of opaque and transparent inclusions by Zernike polynomials. Thus, it is possible to describe a hologram in cases where an object (particle, bubble), as an inclusion or not, can be opaque or transparent, *i.e.* fully absorbed or partially absorbed.

The second part of chapter 3 described the droplet as a transparent object with different approximations: (i) opaque, (ii) quadratic phase, and (iii) quasi-spherical phase approximation. All three approximations are compared with Lorenz-Mie theory (LMT) and good results are obtained. The hologram and reconstruction image of the transparent inclusion inside a droplet are presented at the end of this chapter. In this study, we can interpret a transparent inclusion inside a droplet as a quasi-spherical approximation. In chapter 3, the size and three-dimensional positions of the opaque and transparent object can be characterized.

For a long exposure time experiment, the 3D positions in a droplet of the inclusions, their transverse velocity, and their trajectories inside the droplet are obtained. Another method to track the particle's trajectory is to take a series of hologram images and reconstruct them. This frame by frame method is not practical because it takes a long time to process each hologram. Therefore, we proposed the long exposure time method for tracking the trajectories of particles. The interference pattern recorded by

a CCD camera with a long exposure time is spread and blurred along the direction of movement of that particle. Blurring in the hologram image affects the resolution of the reconstructed image. Therefore, better resolution is necessary. A possible way to improve the resolution of the reconstructed image of inclusions is by changing the resolution of the CCD camera. If the shutter time of the camera is very long, longer trajectories of the inclusions can be observed. However, when the exposure time increases, the SNR value is very low. For longer trajectories, the movement in three dimentions can be visualized and the three components of velocity of the inclusion can be obtained. With this technique, the behaviour of the inclusions is observed inside a suspended droplet.

The model describing the arbitrary/irregular shape of an opaque and constant phase object can be used as a simulational model in the case of aggregated opaque and/or phase inclusions when they are inside a droplet or in the case of an ice crystal. In this study, the intensity profiles of the reconstructed opaque and phase inclusions are different. For the opaque inclusion, the lowest reconstructed intensity profile is at the centre of the profile, whereas the reconstructed intensity profile of phase inclusion is not lowest at the centre. From the difference of the reconstructed intensity profiles we can distinguish the opaque and phase inclusions when they are mixed together. Further experiments on aggregated opaque and phase inclusions inside a droplet have to be performed to confirm the simulation.

In case of non-spherical inclusions in a non-spherical or non-elliptical shell, we proposed interferometric imaging for analysis of the interference patterns. In this work, micro-pipes with two and four hollow channels are investigated. The channels are considered as solid cylindrical inclusions inside a cylindrical geometry. In the simulation, we generated two and four columns of point sources from the Dirac distribution which represented two and four channels inside a pipe. To describe the propagation of light through this system, the generalized Huygens-Fresnel integral based on ABCD matrix formalism is used. Then we can simulate the interferogram at the CCD plane. By plotting the intensity profiles along the horizontal axis of the interferogram and transforming the intensity distribution by 1D-FFT, the spatial fringe's frequency is analysed. When we know the resultant frequency, we then know the space between the two/four channels and their orientation in the pipe.

The aim of all of our studies is to characterize the inclusions inside a droplet. The droplet diameter in our studies is on millimetric scale and the inclusion diameter is varied from $5 - 20\mu m$. However, we still cannot characterize inclusions smaller than $5\mu m$ with our configuration set-up experimentally because we cannot separate the reconstructed particle from the background noise of the image. Therefore, the experiments have to be improved in order to increase the image quality or to get rid of background noise. In other word, the increasing signal-to-noise ratio (SNR) is very important to the image quality. The characterization of inclusions on a nanometric scale is also of interesting for future work. If we can fix the axial position of the particles in the drop experimentally, then we can compare the optimal fractional order obtained from the experiment and from the theoretical values. To fix the axial position of the particles in the droplet, an optical tweezer may be used to hold the particle in position. In the more genreal case, for smaller size droplets, the evaporation behaviour of the droplet should be considered. Moreover, the development of digital holography for measuring

the refractive index of the inclusions is very interesting.

To make the system close to realistic, we need to use a falling droplet instead of a suspended droplet. The motions of the inclusions inside a droplet will follow the flow inside the droplet when the droplet falls. There is no capillary effect introduced to the motions of inclusions as in the suspended droplet. The experimental set-up can be the same as we have used in this work (in-line configuration). The difference is in the system for falling droplets, the droplets can be monodisperse as line of droplets or polydisperse as spray of droplets. Moreover, the different particles can be characterized such as biological particles, ice crystal formation, and nano-particles inside a micro-bubble.

Appendix A

PROPAGATION BEFORE THE OBJECT'S PLANE

A.1 Matrix transfer of the system before the particle plane

For the system of droplet with inclusion as presented in the setup in Fig. A.1, the matrix transfer of the system before the particle plane, $M_1^{x,y}$, is:

$$M_1^{x,y} = M_{z_1} \times M_{R_1}^{x,y} \times M_{e_3} \times M_{f_2}^{x,y} \times M_{e_2} \times M_{f_1}^{x,y} \times M_{e_1} \tag{A.1}$$

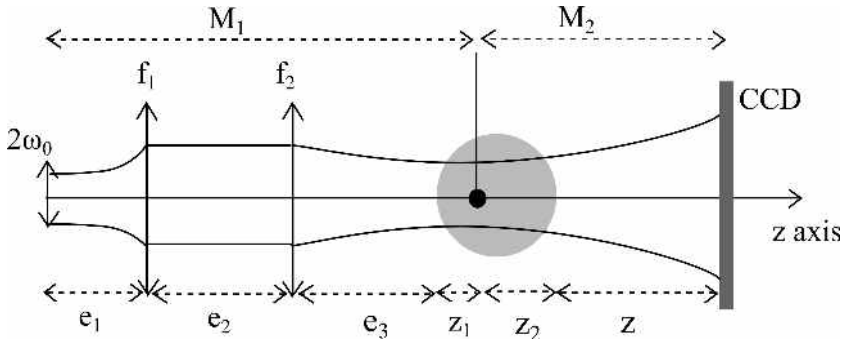

Fig. A.1: The configuration of numerical and experimental setup.

Each matrices are defined by:

$$M_{e_1} = \begin{pmatrix} 1 & e_1/n_0 \\ 0 & 1 \end{pmatrix} \qquad M_{f_1}^{x,y} = \begin{pmatrix} 1 & 0 \\ -1/f_1^{x,y} & 1 \end{pmatrix} \qquad M_{e_2} = \begin{pmatrix} 1 & e_2/n_0 \\ 0 & 1 \end{pmatrix}$$

$$M_{f_2}^{x,y} = \begin{pmatrix} 1 & 0 \\ -1/f_2^{x,y} & 1 \end{pmatrix} \qquad M_{e_3} = \begin{pmatrix} 1 & e_3/n_0 \\ 0 & 1 \end{pmatrix} \qquad M_{R_1}^{x,y} = \begin{pmatrix} 1 & 0 \\ \frac{n_0-n_1}{R_1^{x,y}} & 1 \end{pmatrix} \tag{A.2}$$

$$M_{z_1} = \begin{pmatrix} 1 & z_1/n_1 \\ 0 & 1 \end{pmatrix}$$

where n_0 is the refractive index of the air and n_1 is the refractive index of water. $R_1^{x,y}$ is the radius of curvature of the entrance side of the droplet. Other parameters are defined in Fig. A.1.

A.2 The complex amplitude at object plane

If the incident source is a gaussian light source, $G_0(\mu, \nu, z)$ can be written as

$$G_0(\mu, \nu, z) = \exp\left(-\frac{\mu^2 + \nu^2}{\omega_0^2}\right), \tag{A.3}$$

where (μ, ν) is the plane coordinates at the incident plane. ω_0 is the waist of the gaussian incident beam and $R(z)$ is the radius of curvature of the Gaussian beam and is defined as in Eq.(2.11). The complex amplitude at the object plane can be found from Fresnel integral as shown in the following equation:

$$\begin{aligned} G_1(\xi, \eta) = \frac{\exp(i\frac{2\pi}{\lambda}E_1)}{i\lambda\sqrt{B_1^x B_1^y}} \int_{\mathbb{R}^2} G_0 \ \exp\left(-\frac{\mu^2 + \nu^2}{\omega_0^2}\right) \exp\left(i\frac{\pi}{\lambda B_1^x}[A_1^x\mu^2 - 2\xi\mu + D_1^x\xi^2]\right) \\ \exp\left(i\frac{\pi}{\lambda B_1^y}[A_1^y\nu^2 - 2\eta\nu + D_1^y\eta^2]\right) d\mu \, d\nu \end{aligned} \tag{A.4}$$

Substitute Eq.(A.3) into Eq.(A.4), the field amplitude in the object plane is:

$$\begin{aligned} G_1(\xi, \eta) = \frac{\exp(i\frac{2\pi}{\lambda}E_1)}{i\lambda\sqrt{B_1^x B_1^y}} G_0 \exp\left[i\frac{\pi}{\lambda}\left(\frac{D_1^x}{B_1^x}\xi^2 + \frac{D_1^y}{B_1^y}\eta^2\right)\right] \int_{\mathbb{R}^2} \exp\left(-\frac{\mu^2 + \nu^2}{\omega_0^2}\right) \\ \exp\left(i\frac{\pi}{\lambda B_1^x}[A_1^x\mu^2 - 2\xi\mu]\right) \exp\left(i\frac{\pi}{\lambda B_1^y}[A_1^y\nu^2 - 2\eta\nu]\right) d\mu \, d\nu \end{aligned} \tag{A.5}$$

Then regroup the parameters μ and ν together. The Eq.(A.5) becomes:

$$\begin{aligned} G_1(\xi, \eta) = \frac{\exp(i\frac{2\pi}{\lambda}E_1)}{i\lambda\sqrt{B_1^x B_1^y}} G_0 \exp\left[i\frac{\pi}{\lambda}\left(\frac{D_1^x}{B_1^x}\xi^2 + \frac{D_1^y}{B_1^y}\eta^2\right)\right] \\ \int_\mu \exp\left[-\left(\frac{1}{\omega_0^2} - i\frac{\pi A_1^x}{\lambda B_1^x}\right)\mu^2\right] \exp\left(-2i\frac{\pi}{\lambda B_1^x}\xi\mu\right) \ d\mu \\ \int_\nu \exp\left[-\left(\frac{1}{\omega_0^2} - i\frac{\pi A_1^y}{\lambda B_1^y}\right)\nu^2\right] \exp\left(-2i\frac{\pi}{\lambda B_1^y}\eta\nu\right) \ d\nu \end{aligned} \tag{A.6}$$

Use the exponential integral formular in this form:

$$\int_{-\infty}^{+\infty} e^{-ax^2} e^{-2bx} dx = \sqrt{\frac{\pi}{a}} e^{\frac{b^2}{a}} \tag{A.7}$$

Then integrate Eq.(A.6) over μ and ν. Therefore, G_1 is

$$\begin{aligned} G_1(\xi,\eta) = \frac{\exp(i\frac{2\pi}{\lambda}E_1)}{i\lambda\sqrt{B_1^x B_1^y}} G_0 \exp\left[i\frac{\pi}{\lambda}\left(\frac{D_1^x}{B_1^x}\xi^2 + \frac{D_1^y}{B_1^y}\eta^2\right)\right] \\ \sqrt{\frac{\pi}{\left(\frac{1}{\omega_0^2} - \frac{i\pi}{\lambda}\frac{A_1^x}{B_1^x}\right)}} \exp\left[\frac{\left(\frac{i\pi}{\lambda B_1^x}\xi\right)^2}{\left(\frac{1}{\omega_0^2} - \frac{i\pi}{\lambda}\frac{A_1^x}{B_1^x}\right)}\right] \\ \sqrt{\frac{\pi}{\left(\frac{1}{\omega_0^2} - \frac{i\pi}{\lambda}\frac{A_1^y}{B_1^y}\right)}} \exp\left[\frac{\left(\frac{i\pi}{\lambda B_1^y}\eta\right)^2}{\left(\frac{1}{\omega_0^2} - \frac{i\pi}{\lambda}\frac{A_1^y}{B_1^y}\right)}\right] \end{aligned} \tag{A.8}$$

Rearrange the Eq.(A.8) to

$$\begin{aligned} G_1(\xi,\eta) = \frac{\exp(i\frac{2\pi}{\lambda}E_1)}{i\lambda\sqrt{B_1^x B_1^y}} G_0 \exp\left[i\frac{\pi}{\lambda}\left(\frac{D_1^x}{B_1^x}\xi^2 + \frac{D_1^y}{B_1^y}\eta^2\right)\right] K_1^x K_1^y \\ \exp\left[-\frac{\left(\frac{\pi\omega_0}{\lambda B_1^x}\right)^2 \xi^2}{\left(1 - i\frac{\pi\omega_0^2}{\lambda}\frac{A_1^x}{B_1^x}\right)}\right] \exp\left[-\frac{\left(\frac{\pi\omega_0}{\lambda B_1^y}\right)^2 \eta^2}{\left(1 - i\frac{\pi\omega_0^2}{\lambda}\frac{A_1^y}{B_1^y}\right)}\right] \end{aligned} \tag{A.9}$$

with

$$K_1^{x,y} = \left(\frac{\pi\omega_0^2}{1 - i\frac{\pi\omega_0^2}{\lambda}\frac{A_1^{x,y}}{B_1^{x,y}}}\right)^{1/2} \tag{A.10}$$

Then consider the denominators of the exponential term in Eq.(A.9). Multiply the term in exponential by $\left(1 + i\frac{\pi\omega_0^2}{\lambda}\frac{A_1^{x,y}}{B_1^{x,y}}\right)$ both numerator and denominator. Then the Eq.(A.9) becomes:

$$\begin{aligned} G_1(\xi,\eta) = \frac{\exp(i\frac{2\pi}{\lambda}E_1)}{i\lambda\sqrt{B_1^x B_1^y}} G_0 \exp\left[i\frac{\pi}{\lambda}\left(\frac{D_1^x}{B_1^x}\xi^2 + \frac{D_1^y}{B_1^y}\eta^2\right)\right] K_1^x K_1^y \\ \exp\left[-\frac{\left(\frac{\pi\omega_0}{\lambda B_1^x}\right)^2 \xi^2}{\left(1 - i\frac{\pi\omega_0^2}{\lambda}\frac{A_1^x}{B_1^x}\right)}\frac{\left(1 + i\frac{\pi\omega_0^2}{\lambda}\frac{A_1^x}{B_1^x}\right)}{\left(1 + i\frac{\pi\omega_0^2}{\lambda}\frac{A_1^x}{B_1^x}\right)}\right] \exp\left[-\frac{\left(\frac{\pi\omega_0}{\lambda B_1^y}\right)^2 \eta^2}{\left(1 - i\frac{\pi\omega_0^2}{\lambda}\frac{A_1^y}{B_1^y}\right)}\frac{\left(1 + i\frac{\pi\omega_0^2}{\lambda}\frac{A_1^y}{B_1^y}\right)}{\left(1 + i\frac{\pi\omega_0^2}{\lambda}\frac{A_1^y}{B_1^y}\right)}\right] \end{aligned} \tag{A.11}$$

Rearrange again. Then we get the following equation:

$$\begin{aligned} G_1(\xi,\eta) = \frac{\exp(i\frac{2\pi}{\lambda}E_1)}{i\lambda\sqrt{B_1^x B_1^y}} G_0 K_1^x K_1^y \exp\left[-\left(\frac{\xi^2}{\omega_{1_x}^2} + \frac{\eta^2}{\omega_{1_y}^2}\right)\right] \\ \exp\left[-i\frac{\pi}{\lambda}\left(\frac{\xi^2}{R_{1_x}} + \frac{\eta^2}{R_{1_y}}\right)\right], \end{aligned} \tag{A.12}$$

where $\omega_{1x,1y}$ is

$$\omega_{1_{x,y}} = \left(\frac{\lambda B_1^{x,y}}{\pi\omega_0}\right)\left[1 + \left(\frac{\pi\omega_0^2}{\lambda}\frac{A_1^{x,y}}{B_1^{x,y}}\right)^2\right]^{1/2}, \tag{A.13}$$

and $R_{1_{x,y}}$ is

$$R_{1_{x,y}} = -\frac{B_1^{x,y}}{D_1^{x,y} - \frac{A_1^x\left(\frac{\pi\omega_0^2}{\lambda B_1^{x,y}}\right)^2}{1+\left(\frac{\pi\omega_0^2}{\lambda}\frac{A_1^{x,y}}{B_1^{x,y}}\right)^2}} \tag{A.14}$$

where $\omega_{1_{x,y}}$ and $R_{1_{x,y}}$ are the beam radii and the beam curvature at the object plane, respectively.

Appendix B

PROPAGATION AFTER THE OBJECT'S PLANE

B.1 Matrix transfer of the system after the particle plane

The matrix transfer of the system between the particle plane and the CCD sensor, $M_2^{x,y}$, is:

$$M_2^{x,y} = M_z \times M_{R_2}^{x,y} \times M_{z_2} \tag{B.1}$$

Each matrices are defined by:

$$M_{z_2} = \begin{pmatrix} 1 & z_2/n_1 \\ 0 & 1 \end{pmatrix} \qquad M_{R_2}^{x,y} = \begin{pmatrix} 1 & 0 \\ \frac{n_1-n_0}{R_2^{x,y}} & 1 \end{pmatrix} \qquad M_z = \begin{pmatrix} 1 & z/n_0 \\ 0 & 1 \end{pmatrix} \tag{B.2}$$

where n_0 is the refractive index of air and n_1 is the refractive index of water. $R_1^{x,y}$ is the radius of curvature of the left side of the droplet. Other parameters are defined in Fig. A.1.

B.2 The complex amplitude at CCD plane

For the electric field recorded in the CCD sensor $G_2(x, y)$, it can be described by Fresnel integral as shown in the following equation.

$$\begin{aligned} G_2(x,y) = \frac{\exp(i\frac{2\pi}{\lambda}E_2)}{i\lambda\sqrt{B_2^x B_2^y}} \int_{\mathbb{R}^2} G_1(\xi,\eta)[1-T(\xi,\eta)] \\ \exp\left[i\frac{\pi}{\lambda B_2^x}(A_2^x\xi^2 - 2\xi x + D_2^x x^2)\right] \exp\left[i\frac{\pi}{\lambda B_2^y}(A_2^y\eta^2 - 2\eta y + D_1^y y^2)\right] d\xi\, d\eta \end{aligned} \tag{B.3}$$

or it can be devided into two terms:

$$G_2(x,y) = \frac{\exp(i\frac{2\pi}{\lambda}E_2)}{i\lambda\sqrt{B_2^x B_2^y}} \left[R(x,y) - O(x,y)\right]; \tag{B.4}$$

where $R(x, y)$ refers to the reference beam and $O(x, y)$ refers to the beam scattered from the object (is called the object beam). The reference beam is

$$R(x,y) = \int_{\mathbb{R}^2} G_1(\xi,\eta) \exp\left[i\frac{\pi}{\lambda B_2^x}(A_2^x\xi^2 - 2\xi x + D_2^x x^2)\right] \exp\left[i\frac{\pi}{\lambda B_2^y}(A_2^y\eta^2 - 2\eta y + D_1^y y^2)\right] d\xi\, d\eta \tag{B.5}$$

The object beam is

$$O(x,y) = \int_{\mathbb{R}^2} G_1(\xi,\eta)T(\xi,\eta) \exp\left[i\frac{\pi}{\lambda B_2^x}(A_2^x\xi^2 - 2\xi x + D_2^x x^2)\right] \exp\left[i\frac{\pi}{\lambda B_2^y}(A_2^y\eta^2 - 2\eta y + D_1^y y^2)\right] d\xi\, d\eta \tag{B.6}$$

B.2.1 Reference beam

From (B.5), substitute G_1 in (A.12) into the equation. Then the reference beam is:

$$\begin{aligned} R(x,y) = \int_{\mathbb{R}^2} \frac{\exp(i\frac{2\pi}{\lambda}E_1)}{i\lambda\sqrt{B_1^x B_1^y}} G_0 K_1^x K_1^y \exp\left[-\left(\frac{\xi^2}{\omega_{1_x}^2} + \frac{\eta^2}{\omega_{1_y}^2}\right)\right] \\ \exp\left[-i\frac{\pi}{\lambda}\left(\frac{\xi^2}{R_{1_x}} + \frac{\eta^2}{R_{1_y}}\right)\right] \exp\left[i\frac{\pi}{\lambda B_2^x}(A_2^x\xi^2 - 2\xi x + D_2^x x^2)\right] \\ \exp\left[i\frac{\pi}{\lambda B_2^y}(A_2^y\eta^2 - 2\eta y + D_1^y y^2)\right] d\xi\, d\eta \end{aligned} \tag{B.7}$$

Then regroup the parameters ξ and η together. The Eq.(B.7) becomes:

$$\begin{aligned} R(x,y) = \frac{\exp(i\frac{2\pi}{\lambda}E_1)}{i\lambda\sqrt{B_1^x B_1^y}} G_0 K_1^x K_1^y \exp\left[i\frac{\pi}{\lambda}\left(\frac{D_2^x}{B_2^x}x^2 + \frac{D_2^y}{B_2^y}y^2\right)\right] \\ \int_\xi \exp\left[-\left(\frac{1}{\omega_{1_x}^2} + i\frac{\pi}{\lambda}\frac{1}{R_{1_x}} - i\frac{\pi}{\lambda}\frac{A_2^x}{B_2^x}\right)\xi^2\right] \exp\left(-2i\frac{\pi x}{\lambda B_2^x}\xi\right)\, d\xi \\ \int_\eta \exp\left[-\left(\frac{1}{\omega_{1_y}^2} + i\frac{\pi}{\lambda}\frac{1}{R_{1_y}} - i\frac{\pi}{\lambda}\frac{A_2^y}{B_2^y}\right)\eta^2\right] \exp\left(-2i\frac{\pi y}{\lambda B_2^y}\eta\right)\, d\eta \end{aligned} \tag{B.8}$$

Use the exponential integral formular in Eq.(A.7). Therefore, the reference beam becomes:

$$\begin{aligned} R(x,y) = \frac{\exp(i\frac{2\pi}{\lambda}E_1)}{i\lambda\sqrt{B_1^x B_1^y}} G_0 K_1^x K_1^y \exp\left[i\frac{\pi}{\lambda}\left(\frac{D_2^x}{B_2^x}x^2 + \frac{D_2^y}{B_2^y}y^2\right)\right] \\ \sqrt{\frac{\pi}{\left(\frac{1}{\omega_{1_x}^2} + i\frac{\pi}{\lambda}\frac{1}{R_{1_x}} - i\frac{\pi}{\lambda}\frac{A_2^x}{B_2^x}\right)}} \exp\left[\frac{\left(i\frac{\pi x}{\lambda B_2^x}\right)^2}{\left(\frac{1}{\omega_{1_x}^2} + i\frac{\pi}{\lambda}\frac{1}{R_{1_x}} - i\frac{\pi}{\lambda}\frac{A_2^x}{B_2^x}\right)}\right] \\ \sqrt{\frac{\pi}{\left(\frac{1}{\omega_{1_y}^2} + i\frac{\pi}{\lambda}\frac{1}{R_{1_y}} - i\frac{\pi}{\lambda}\frac{A_2^y}{B_2^y}\right)}} \exp\left[\frac{\left(i\frac{\pi y}{\lambda B_2^y}\right)^2}{\left(\frac{1}{\omega_{1_y}^2} + i\frac{\pi}{\lambda}\frac{1}{R_{1_y}} - i\frac{\pi}{\lambda}\frac{A_2^y}{B_2^y}\right)}\right] \end{aligned} \tag{B.9}$$

or

$$R(x,y) = \frac{\exp(i\frac{2\pi}{\lambda}E_1)}{i\lambda\sqrt{B_1^x B_1^y}} G_0 K_1^x K_1^y K_2^x K_2^y \exp\left[i\frac{\pi}{\lambda}\left(\frac{D_2^x}{B_2^x}x^2 + \frac{D_2^y}{B_2^y}y^2\right)\right] \exp\left[-\frac{\left(\frac{\pi x}{\lambda B_2^x}\right)^2 \omega_{1_x}^2}{\left(1 + i\frac{\pi\omega_{1_x}^2}{\lambda}\left(\frac{1}{R_{1_x}} - \frac{A_2^x}{B_2^x}\right)\right)}\right] \exp\left[-\frac{\left(\frac{\pi y}{\lambda B_2^y}\right)^2 \omega_{1_y}^2}{\left(1 + i\frac{\pi\omega_{1_y}^2}{\lambda}\left(\frac{1}{R_{1_y}} - \frac{A_2^y}{B_2^y}\right)\right)}\right] \tag{B.10}$$

where $K_2^{x,y}$ is

$$K_2^{x,y} = \left[\frac{\pi\omega_{1_{x,y}}^2}{\left(1 + i\frac{\pi\omega_{1_{x,y}}^2}{\lambda}\left(\frac{1}{R_{1_{x,y}}} - \frac{A_2^{x,y}}{B_2^{x,y}}\right)\right)}\right]^{1/2} \tag{B.11}$$

Then consider the denominators of the exponential term in Eq.(B.10). Multiply the term in exponential by $\left(1 - i\frac{\pi\omega_{1_{x,y}}^2}{\lambda}\left(\frac{1}{R_{1_{x,y}}} - \frac{A_1^{x,y}}{B_1^{x,y}}\right)\right)$ both numerator and denominator. Then the Eq.(B.10) becomes:

$$\begin{aligned} R(x,y) = {} & \frac{\exp(i\frac{2\pi}{\lambda}E_1)}{i\lambda\sqrt{B_1^x B_1^y}} G_0 K_1^x K_1^y K_2^x K_2^y \exp\left[i\frac{\pi}{\lambda}\left(\frac{D_2^x}{B_2^x}x^2 + \frac{D_2^y}{B_2^y}y^2\right)\right] \\ & \exp\left[-\frac{\left(\frac{\pi x}{\lambda B_2^x}\right)^2 \omega_{1_x}^2}{\left(1 + i\frac{\pi\omega_{1_x}^2}{\lambda}\left(\frac{1}{R_{1_x}} - \frac{A_2^x}{B_2^x}\right)\right)} \frac{\left(1 - i\frac{\pi\omega_{1_x}^2}{\lambda}\left(\frac{1}{R_{1_x}} - \frac{A_2^x}{B_2^x}\right)\right)}{\left(1 - i\frac{\pi\omega_{1_x}^2}{\lambda}\left(\frac{1}{R_{1_x}} - \frac{A_2^x}{B_2^x}\right)\right)}\right] \\ & \exp\left[-\frac{\left(\frac{\pi y}{\lambda B_2^y}\right)^2 \omega_{1_y}^2}{\left(1 + i\frac{\pi\omega_{1_y}^2}{\lambda}\left(\frac{1}{R_{1_y}} - \frac{A_2^y}{B_2^y}\right)\right)} \frac{\left(1 - i\frac{\pi\omega_{1_y}^2}{\lambda}\left(\frac{1}{R_{1_y}} - \frac{A_2^y}{B_2^y}\right)\right)}{\left(1 - i\frac{\pi\omega_{1_y}^2}{\lambda}\left(\frac{1}{R_{1_y}} - \frac{A_2^y}{B_2^y}\right)\right)}\right] \end{aligned} \tag{B.12}$$

Rearrange the equation. Then

$$\begin{aligned} R(x,y) = {} & \frac{\exp(i\frac{2\pi}{\lambda}E_1)}{i\lambda\sqrt{B_1^x B_1^y}} G_0 K_1^x K_1^y K_2^x K_2^y \exp\left[i\frac{\pi}{\lambda}\left(\frac{D_2^x}{B_2^x}x^2 + \frac{D_2^y}{B_2^y}y^2\right)\right] \\ & \exp\left[-\frac{\left(\frac{\pi x}{\lambda B_2^x}\right)^2 \omega_{1_x}^2}{\left(1 + \left(\frac{\pi\omega_{1_x}^2}{\lambda}\right)^2\left(\frac{1}{R_{1_x}} - \frac{A_2^x}{B_2^x}\right)^2\right)}\right] exp\left[-\frac{\left(\frac{\pi x}{\lambda B_2^x}\right)^2 \omega_{1_x}^2\left(-i\frac{\pi\omega_{1_x}^2}{\lambda}\left(\frac{1}{R_{1_x}} - \frac{A_2^x}{B_2^x}\right)\right)}{\left(1 + \left(\frac{\pi\omega_{1_x}^2}{\lambda}\right)^2\left(\frac{1}{R_{1_x}} - \frac{A_2^x}{B_2^x}\right)^2\right)}\right] \\ & \exp\left[-\frac{\left(\frac{\pi y}{\lambda B_2^y}\right)^2 \omega_{1_y}^2}{\left(1 + \left(\frac{\pi\omega_{1_y}^2}{\lambda}\right)^2\left(\frac{1}{R_{1_y}} - \frac{A_2^y}{B_2^y}\right)^2\right)}\right] exp\left[-\frac{\left(\frac{\pi y}{\lambda B_2^y}\right)^2 \omega_{1_y}^2\left(-i\frac{\pi\omega_{1_y}^2}{\lambda}\left(\frac{1}{R_{1_y}} - \frac{A_2^y}{B_2^y}\right)\right)}{\left(1 + \left(\frac{\pi\omega_{1_y}^2}{\lambda}\right)^2\left(\frac{1}{R_{1_y}} - \frac{A_2^y}{B_2^y}\right)^2\right)}\right] \end{aligned} \tag{B.13}$$

or

$$R(x,y) = \frac{\exp(i\frac{2\pi}{\lambda}E_1)}{i\lambda\sqrt{B_1^x B_1^y}} G_0 K_1^x K_1^y K_2^x K_2^y \exp\left[-\frac{\pi}{\lambda}\left(\frac{N_x}{B_2^x}x^2 + \frac{N_y}{B_2^y}y^2\right)\right] \exp\left[i\frac{\pi}{\lambda}\left(\frac{M_x}{B_2^x}x^2 + \frac{M_y}{B_2^y}y^2\right)\right] \tag{B.14}$$

where

$$N_{x,y} = \frac{\left(\frac{\pi\omega_{1_x}^2}{\lambda B_2^x}\right)}{\left(1 + \left(\frac{\pi\omega_{1_x}^2}{\lambda}\right)^2 \left(\frac{1}{R_{1_x}} - \frac{A_2^x}{B_2^x}\right)^2\right)} \tag{B.15}$$

$$M_{x,y} = D_2^{x,y} + \frac{\left(\frac{\pi\omega_{1_x}^2}{\lambda B_2^x}\right)^2 \left(\frac{B_2^x}{R_{1_x}} - A_2^x\right)}{1 + \left(\frac{\pi\omega_{1_x}^2}{\lambda}\right)^2 \left(\frac{1}{R_{1_x}} - \frac{A_2^x}{B_2^x}\right)^2} \tag{B.16}$$

B.2.2 Object beam

From Eq.(B.6), the object beam is

$$O(x,y) = \int_{\mathbb{R}^2} G_1(\xi,\eta) T(\xi,\eta) \exp\left[i\frac{\pi}{\lambda B_2^x}(A_2^x\xi^2 - 2\xi x + D_2^x x^2)\right] \exp\left[i\frac{\pi}{\lambda B_2^y}(A_2^y\eta^2 - 2\eta y + D_1^y y^2)\right] d\xi\, d\eta \tag{B.17}$$

Substitute G_1 into Eq. (B.17).

$$O(x,y) = \int_{\mathbb{R}^2} \frac{\exp(i\frac{2\pi}{\lambda}E_1)}{i\lambda\sqrt{B_1^x B_1^y}} G_0 K_1^x K_1^y \exp\left[-\left(\frac{\xi^2}{\omega_{1_x}^2} + \frac{\eta^2}{\omega_{1_y}^2}\right)\right] \exp\left[-\frac{i\pi}{\lambda}\left(\frac{\xi^2}{R_{1x}} + \frac{\eta^2}{R_{1y}}\right)\right] T(\xi,\eta) \exp\left[i\frac{\pi}{\lambda B_2^x}(A_2^x\xi^2 - 2\xi x + D_2^x x^2)\right] \exp\left[i\frac{\pi}{\lambda B_2^y}(A_2^y\eta^2 - 2\eta y + D_1^y y^2)\right] d\xi\, d\eta \tag{B.18}$$

Rearrange the equation.

$$O(x,y) = \frac{\exp(i\frac{2\pi}{\lambda}E_1)}{i\lambda\sqrt{B_1^x B_1^y}} G_0 K_1^x K_1^y \exp\left[\frac{i\pi}{\lambda}\left(\frac{D_2^x}{B_2^x}x^2 + \frac{D_2^y}{B_2^y}y^2\right)\right] \int_{\mathbb{R}^2} \exp\left[-\left(\frac{\xi^2}{\omega_{1_x}^2} + \frac{\eta^2}{\omega_{1_y}^2}\right)\right] \exp\left[-\frac{i\pi}{\lambda}\left(\frac{\xi^2}{R_{1x}} + \frac{\eta^2}{R_{1y}}\right)\right] T(\xi,\eta) \exp\left[i\frac{\pi}{\lambda B_2^x}(A_2^x\xi^2 - 2\xi x)\right] \exp\left[i\frac{\pi}{\lambda B_2^y}(A_2^y\eta^2 - 2\eta y)\right] d\xi\, d\eta \tag{B.19}$$

Next, separate parameter ξ and η.

$$\begin{aligned} O(x,y) = & \frac{\exp(i\frac{2\pi}{\lambda}E_1)}{i\lambda\sqrt{B_1^x B_1^y}} G_0 K_1^x K_1^y \exp\left[\frac{i\pi}{\lambda}\left(\frac{D_2^x}{B_2^x}x^2 + \frac{D_2^y}{B_2^y}y^2\right)\right] \\ & \int_\xi \int_\eta \exp\left[-\left(\frac{1}{\omega_{1_x}^2} + i\frac{\pi}{\lambda}\left(\frac{1}{R_{1x}} - \frac{A_2^x}{B_2^x}\right)\right)\xi^2\right] T(\xi,\eta) \exp\left(-2i\frac{\pi x}{\lambda B_2^x}\xi\right) \\ & \exp\left[-\left(\frac{1}{\omega_{1_y}^2} + i\frac{\pi}{\lambda}\left(\frac{1}{R_{1y}} - \frac{A_2^y}{B_2^y}\right)\right)\eta^2\right] \exp\left(-2i\frac{\pi y}{\lambda B_2^y}\eta\right)\, d\xi\, d\eta \end{aligned} \tag{B.20}$$

From [60] Eq.(7), $T(\xi,\eta)$ is defined as

$$T(\xi,\eta) = \sum_{k=1}^{N} A_k \exp\left[-\frac{B_k}{b^2}\left(\xi^2 + R_{ell}^2\eta^2\right)\right] \tag{B.21}$$

Then Eq.(B.20) becomes:

$$\begin{aligned} O(x,y) = & \frac{\exp(i\frac{2\pi}{\lambda}E_1)}{i\lambda\sqrt{B_1^x B_1^y}} G_0 K_1^x K_1^y \exp\left[\frac{i\pi}{\lambda}\left(\frac{D_2^x}{B_2^x}x^2 + \frac{D_2^y}{B_2^y}y^2\right)\right] \\ & \int_\xi \int_\eta \exp\left[-\left(\frac{1}{\omega_{1_x}^2} + i\frac{\pi}{\lambda}\left(\frac{1}{R_{1x}} - \frac{A_2^x}{B_2^x}\right)\right)\xi^2\right] \exp\left(-2i\frac{\pi x}{\lambda B_2^x}\xi\right) \\ & \left(1 - e^{i\phi}\right) \sum_{k=1}^{N} A_k \exp\left[-\frac{B_k}{b^2}\left(\xi^2 + R_{ell}^2\eta^2\right)\right] \\ & \exp\left[-\left(\frac{1}{\omega_{1_y}^2} + i\frac{\pi}{\lambda}\left(\frac{1}{R_{1y}} - \frac{A_2^y}{B_2^y}\right)\right)\eta^2\right] \exp\left(-2i\frac{\pi y}{\lambda B_2^y}\eta\right)\, d\xi\, d\eta \end{aligned} \tag{B.22}$$

Rearrange Eq.(B.22) again, then the object beam is

$$\begin{aligned} O(x,y) = & \frac{\exp(i\frac{2\pi}{\lambda}E_1)}{i\lambda\sqrt{B_1^x B_1^y}} G_0 K_1^x K_1^y \exp\left[\frac{i\pi}{\lambda}\left(\frac{D_2^x}{B_2^x}x^2 + \frac{D_2^y}{B_2^y}y^2\right)\right]\left(1 - e^{i\phi}\right) \\ & \sum_{k=1}^{N} A_k \int_\xi \exp\left[-\left(\frac{1}{\omega_{1_x}^2} + \frac{B_k}{b^2} + i\frac{\pi}{\lambda}\left(\frac{1}{R_{1x}} - \frac{A_2^x}{B_2^x}\right)\right)\xi^2\right] \exp\left(-2i\frac{\pi x}{\lambda B_2^x}\xi\right) \\ & \int_\eta \exp\left[-\left(\frac{1}{\omega_{1_y}^2} + \frac{B_k}{b^2}R_{ell}^2 + i\frac{\pi}{\lambda}\left(\frac{1}{R_{1y}} - \frac{A_2^y}{B_2^y}\right)\right)\eta^2\right] \exp\left(-2i\frac{\pi y}{\lambda B_2^y}\eta\right)\, d\xi\, d\eta \end{aligned} \tag{B.23}$$

The coefficient B_k is a complex number so it has both real and imaginary part, $\Re(B_k)$ and $\Im(B_k)$, respectively. Therefore, the object beam can be written as:

$$
\begin{aligned}
O(x,y) = & \frac{\exp(i\frac{2\pi}{\lambda}E_1)}{i\lambda\sqrt{B_1^x B_1^y}} G_0 K_1^x K_1^y \exp\left[\frac{i\pi}{\lambda}\left(\frac{D_2^x}{B_2^x}x^2 + \frac{D_2^y}{B_2^y}y^2\right)\right](1-e^{i\phi})\sum_{k=1}^{N} A_k \\
& \int_\xi \exp\left[-\left(\frac{1}{\omega_{1_x}^2} + \frac{\Re(B_k)+i\Im(B_k)}{b^2} + i\frac{\pi}{\lambda}\left(\frac{1}{R_{1x}} - \frac{A_2^x}{B_2^x}\right)\right)\xi^2\right]\exp\left(-2i\frac{\pi x}{\lambda B_2^x}\xi\right)\, d\xi \\
& \int_\eta \exp\left[-\left(\frac{1}{\omega_{1_y}^2} + \frac{\Re(B_k)+i\Im(B_k)}{b^2}R_{ell}^2 + i\frac{\pi}{\lambda}\left(\frac{1}{R_{1y}} - \frac{A_2^y}{B_2^y}\right)\right)\eta^2\right] \\
& \exp\left(-2i\frac{\pi y}{\lambda B_2^y}\eta\right)\, d\eta
\end{aligned}
\tag{B.24}
$$

or

$$
\begin{aligned}
O(x,y) = & \frac{\exp(i\frac{2\pi}{\lambda}E_1)}{i\lambda\sqrt{B_1^x B_1^y}} G_0 K_1^x K_1^y \exp\left[\frac{i\pi}{\lambda}\left(\frac{D_2^x}{B_2^x}x^2 + \frac{D_2^y}{B_2^y}y^2\right)\right](1-e^{i\phi})\sum_{k=1}^{N} A_k \\
& \int_\xi \exp\left[-\left(\frac{1}{\omega_{1_x}^2} + \frac{\Re(B_k)}{b^2} + i\frac{\pi}{\lambda}\left(\frac{1}{R_{1x}} - \frac{A_2^x}{B_2^x} + \frac{\lambda\Im(B_k)}{\pi b^2}\right)\right)\xi^2\right]\exp\left(-2i\frac{\pi x}{\lambda B_2^x}\xi\right)\, d\xi \\
& \int_\eta \exp\left[-\left(\frac{1}{\omega_{1_y}^2} + \frac{\Re(B_k)}{b^2}R_{ell}^2 + i\frac{\pi}{\lambda}\left(\frac{1}{R_{1y}} - \frac{A_2^y}{B_2^y} + \frac{\lambda\Im(B_k)}{\pi b^2}R_{ell}^2\right)\right)\eta^2\right] \\
& \exp\left(-2i\frac{\pi y}{\lambda B_2^y}\eta\right)\, d\eta
\end{aligned}
\tag{B.25}
$$

Let

$$
\frac{1}{\omega_{1_{xeq}}^2} = \frac{1}{\omega_{1_x}^2} + \frac{\Re(B_k)}{b^2}, \qquad \frac{1}{\omega_{1_{yeq}}^2} = \frac{1}{\omega_{1_y}^2} + R_{ell}^2\frac{\Re(B_k)}{b^2} \tag{B.26}
$$

and

$$
\frac{1}{R_{1_{xeq}}} = \frac{1}{R_{1_x}} + \frac{\Im(B_k)\lambda}{\pi b^2}, \qquad \frac{1}{R_{1_{yeq}}} = \frac{1}{R_{1_y}} + R_{ell}^2\frac{\Im(B_k)\lambda}{\pi b^2} \tag{B.27}
$$

Then (B.25) becomes

$$
\begin{aligned}
O(x,y) = & \frac{\exp(i\frac{2\pi}{\lambda}E_1)}{i\lambda\sqrt{B_1^x B_1^y}} G_0 K_1^x K_1^y \exp\left[\frac{i\pi}{\lambda}\left(\frac{D_2^x}{B_2^x}x^2 + \frac{D_2^y}{B_2^y}y^2\right)\right](1-e^{i\phi})\sum_{k=1}^{N} A_k \\
& \int_\xi \exp\left[-\left(\frac{1}{\omega_{1_{xeq}}^2} + i\frac{\pi}{\lambda}\left(\frac{1}{R_{1_{xeq}}} - \frac{A_2^x}{B_2^x}\right)\right)\xi^2\right]\exp\left(-2i\frac{\pi x}{\lambda B_2^x}\xi\right)\, d\xi \\
& \int_\eta \exp\left[-\left(\frac{1}{\omega_{1_{yeq}}^2} + i\frac{\pi}{\lambda}\left(\frac{1}{R_{1_{yeq}}} - \frac{A_2^y}{B_2^y}\right)\right)\eta^2\right]\exp\left(-2i\frac{\pi y}{\lambda B_2^y}\eta\right)\, d\eta
\end{aligned}
\tag{B.28}
$$

Use the exponential integral in Eq. (A.7) $\int_{-\infty}^{+\infty} e^{-ax^2}e^{-2bx}dx = \sqrt{\frac{\pi}{a}}e^{\frac{b^2}{a}}$. The object

beam is

$$O(x,y) = \frac{\exp(i\frac{2\pi}{\lambda}E_1)}{i\lambda\sqrt{B_1^x B_1^y}} G_0 K_1^x K_1^y \exp\left[\frac{i\pi}{\lambda}\left(\frac{D_2^x}{B_2^x}x^2 + \frac{D_2^y}{B_2^y}y^2\right)\right]\left(1-e^{i\phi}\right)\sum_{k=1}^{N} A_k$$
$$\sqrt{\frac{\pi}{\frac{1}{\omega_{1_{x_{eq}}}^2} + i\frac{\pi}{\lambda}\left(\frac{1}{R_{1_{x_{eq}}}} - \frac{A_2^x}{B_2^x}\right)}} \exp\left[\frac{\left(i\frac{\pi x}{\lambda B_2^x}\right)^2}{\frac{1}{\omega_{1_{x_{eq}}}^2} + i\frac{\pi}{\lambda}\left(\frac{1}{R_{1_{x_{eq}}}} - \frac{A_2^x}{B_2^x}\right)}\right] \tag{B.29}$$
$$\sqrt{\frac{\pi}{\frac{1}{\omega_{1_{y_{eq}}}^2} + i\frac{\pi}{\lambda}\left(\frac{1}{R_{1_{y_{eq}}}} - \frac{A_2^y}{B_2^y}\right)}} \exp\left[\frac{\left(i\frac{\pi y}{\lambda B_2^y}\right)^2}{\frac{1}{\omega_{1_{y_{eq}}}^2} + i\frac{\pi}{\lambda}\left(\frac{1}{R_{1_{y_{eq}}}} - \frac{A_2^y}{B_2^y}\right)}\right]$$

or

$$O(x,y) = \frac{\exp(i\frac{2\pi}{\lambda}E_1)}{i\lambda\sqrt{B_1^x B_1^y}} G_0 K_1^x K_1^y \exp\left[\frac{i\pi}{\lambda}\left(\frac{D_2^x}{B_2^x}x^2 + \frac{D_2^y}{B_2^y}y^2\right)\right]\left(1-e^{i\phi}\right)\sum_{k=1}^{N} A_k$$
$$K_2^{x_{eq}} K_2^{y_{eq}} \exp\left[\frac{\left(i\frac{\pi x}{\lambda B_2^x}\right)^2}{\frac{1}{\omega_{1_{x_{eq}}}^2} + i\frac{\pi}{\lambda}\left(\frac{1}{R_{1_{x_{eq}}}} - \frac{A_2^x}{B_2^x}\right)}\right] \exp\left[\frac{\left(i\frac{\pi y}{\lambda B_2^y}\right)^2}{\frac{1}{\omega_{1_{y_{eq}}}^2} + i\frac{\pi}{\lambda}\left(\frac{1}{R_{1_{y_{eq}}}} - \frac{A_2^y}{B_2^y}\right)}\right] \tag{B.30}$$

where

$$K_2^{x,y_{eq}} = \left[\frac{\pi}{\frac{1}{\omega_{1_{x,y_{eq}}}^2} + i\frac{\pi}{\lambda}\left(\frac{1}{R_{1_{x,y_{eq}}}} - \frac{A_2^{x,y}}{B_2^{x,y}}\right)}\right]^{1/2} \tag{B.31}$$

Then consider the denominators of the exponential term of the object beam in Eq.(B.30). Multiply the term in exponential by $\left[1 - i\frac{\pi\omega_{1_{xeq,yeq}}^2}{\lambda}\left(\frac{1}{R_{1_{xeq,yeq}}} - \frac{A_1^{x,y}}{B_1^{x,y}}\right)\right]$ both numerator and denominator. Then the Eq.(B.30) becomes:

$$O(x,y) = \frac{\exp(i\frac{2\pi}{\lambda}E_1)}{i\lambda\sqrt{B_1^x B_1^y}} G_0 K_1^x K_1^y \exp\left[\frac{i\pi}{\lambda}\left(\frac{D_2^x}{B_2^x}x^2 + \frac{D_2^y}{B_2^y}y^2\right)\right]\left(1-e^{i\phi}\right)\sum_{k=1}^{N} A_k$$
$$K_2^{x_{eq}} K_2^{y_{eq}} \exp\left[\frac{\left(i\frac{\pi x}{\lambda B_2^x}\right)^2 \omega_{1_{x_{eq}}}^2}{1 + i\frac{\pi\omega_{1_{x_{eq}}}^2}{\lambda}\left(\frac{1}{R_{1_{x_{eq}}}} - \frac{A_2^x}{B_2^x}\right)} \frac{1 - i\frac{\pi\omega_{1_{x_{eq}}}^2}{\lambda}\left(\frac{1}{R_{1_{x_{eq}}}} - \frac{A_2^x}{B_2^x}\right)}{1 - i\frac{\pi\omega_{1_{x_{eq}}}^2}{\lambda}\left(\frac{1}{R_{1_{x_{eq}}}} - \frac{A_2^x}{B_2^x}\right)}\right] \tag{B.32}$$
$$\exp\left[\frac{\left(i\frac{\pi y}{\lambda B_2^y}\right)^2 \omega_{1_{y_{eq}}}^2}{1 + i\frac{\pi\omega_{1_{y_{eq}}}^2}{\lambda}\left(\frac{1}{R_{1_{y_{eq}}}} - \frac{A_2^y}{B_2^y}\right)} \frac{1 - i\frac{\pi\omega_{1_{y_{eq}}}^2}{\lambda}\left(\frac{1}{R_{1_{y_{eq}}}} - \frac{A_2^y}{B_2^y}\right)}{1 - i\frac{\pi\omega_{1_{y_{eq}}}^2}{\lambda}\left(\frac{1}{R_{1_{y_{eq}}}} - \frac{A_2^y}{B_2^y}\right)}\right]$$

After some mathematical development, the object beam is

$$O(x,y) = \frac{\exp(i\frac{2\pi}{\lambda}E_1)}{i\lambda\sqrt{B_1^x B_1^y}} G_0 K_1^x K_1^y \exp\left[\frac{i\pi}{\lambda}\left(\frac{D_2^x}{B_2^x}x^2 + \frac{D_2^y}{B_2^y}y^2\right)\right](1-e^{i\phi})\sum_{k=1}^{N} A_k K_2^{x_{eq}} K_2^{y_{eq}} \exp\left[-\frac{\pi}{\lambda}\left(\frac{N_{x_{eq}}}{B_2^x}x^2 + \frac{N_{y_{eq}}}{B_2^y}y^2\right)\right]\exp\left[i\frac{\pi}{\lambda}\left(\frac{M_{x_{eq}}}{B_2^x}x^2 + \frac{M_{y_{eq}}}{B_2^y}y^2\right)\right], \tag{B.33}$$

where

$$N_{x,y_{eq}} = \frac{\frac{\pi\omega_{1_{x,y_{eq}}}^2}{\lambda B_2^{x,y}}}{1+\left(\frac{\pi\omega_{1_{x,y_{eq}}}^2}{\lambda B_2^{x,y}}\right)^2\left(\frac{B_2^{x,y}}{R_1^{x,y}} - A_2^{x,y}\right)^2}, \tag{B.34}$$

and

$$M_{x,y_{eq}} = \frac{\left(\frac{\pi\omega_{1_{x,y_{eq}}}^2}{\lambda B_2^{x,y}}\right)^2\left(\frac{B_2^{x,y}}{R_1^{x,y}} - A_2^{x,y}\right)}{1+\left(\frac{\pi\omega_{1_{x,y_{eq}}}^2}{\lambda B_2^{x,y}}\right)^2\left(\frac{B_2^{x,y}}{R_1^{x,y}} - A_2^{x,y}\right)^2} \tag{B.35}$$

For the theoretical study in Chapter3, see Appendix D.1.

Appendix C

FRACTIONAL FOURIER TRANSFORMATION

Fractional Fourier transform (FRFT) is a generalized Fourier transform with $n-th$ power, where n is not an integer. This integral operator has various applications in signal processing. The FRFT is the Fourier transform of a function $f(x)$ as defined by

$$\mathcal{F}_\alpha[f](u) = \int K_\alpha(u,x) f(x) dx \tag{C.1}$$

where α is non-integer number. In the other word, α is the angle of the kernel operator. K_α is the kernel function with the properties of

symmetry:

$$K_\alpha(u,x) = K_\alpha(x,u) \tag{C.2}$$

inverse:

$$K_\alpha^{-1}(u,x) = K_\alpha^*(u,x) = K_{-\alpha}(x,u) \tag{C.3}$$

additivity:

$$K_{\alpha+\beta}(u,x) = \int K_\alpha(u,v) K_\beta(v,x) dv \tag{C.4}$$

In this work, the 2D fractional Fourier transform (2D-FRFT) of the intensity distribution is defined by

$$\mathcal{F}_\alpha[I(x,y)](x_a,y_a) = \int_{\mathbb{R}^2} K_{\alpha_x}(x,x_a) K_{\alpha_y}(y,y_a) I(x,y)\, dx\, dy \tag{C.5}$$

where $I(x,y) = G_2(x,y)\, \overline{G_2(x,y)}$ and the overbar refers to the complex conjugate.

$$\begin{aligned} I(x,y) &= G_2(x,y)\, \overline{G_2(x,y)} \\ &= \frac{1}{\lambda^2 B_2^x B_2^y} \left[|R|^2 - 2\Re[R\overline{O}] + |O|^2 \right] \end{aligned} \tag{C.6}$$

Here, the kernel operator $K_{\alpha_{x,y}}$ is defined by

$$K_{\alpha_p}(p,p_a) = C(\alpha_p) \exp\left(i\pi \frac{p^2 + p_a^2}{s_p^2 \tan\alpha_p} \right) \exp\left(-\frac{i2\pi p_a p}{s_p^2 \sin\alpha_p} \right) \tag{C.7}$$

$C(\alpha_p)$ is the coefficient and is defined as

$$C(\alpha_p) = \frac{\exp\left[-i\left(\frac{\pi}{4}sign(\sin\alpha_p) - \frac{\alpha_p}{2}\right)\right]}{|s_p^2 \sin\alpha_p|^{1/2}} \tag{C.8}$$

$p = x, y$. The parameter s_p is related to CCD parameter and is defined as $s_p^2 = N_p \cdot \delta_p^2$ where N_p is number of pixel and δ_p is pixel's size.

To do the numerical refocusing over the object, the quadratic phase in the interference term of the intensity distribution $2\Re[R\overline{O}]$ in Eq.(C.6) is considered. From Eq.(B.14) and Eq.(B.33), the quadratice phase in the interference term is:

$$\varphi = \frac{\pi}{\lambda}\left[\left(\frac{M_x - D_2^x}{B_2^x}\right)x^2 + \left(\frac{M_y - D_2^y}{B_2^y}\right)y^2\right] \tag{C.9}$$

Another quadratic phase is in the kernel of 2D-FRFT and it is denoted by φ_a as in the following equation:

$$\varphi_a = \pi\left(\frac{\cot\alpha_x}{s_x^2}x^2 + \frac{\cot\alpha_y}{s_y^2}y^2\right) \tag{C.10}$$

The reconstructed image is obtained by applying the 2D-FRFT to the intensity distribution of Eq.(C.6):

$$\begin{aligned}\mathcal{F}_{\alpha_x,\alpha_y}[I(x,y)] \propto \mathcal{F}_{\alpha_x,\alpha_y}\left[|R|^2 + |O|^2\right] - C(\alpha_x)C(\alpha_y)\int_{\mathbb{R}^2}|R\overline{O}|\exp[i(\varphi_a - \varphi)] \\ \exp\left[-2i\pi\left(\frac{x_a x}{s_x^2\sin\alpha_x} + \frac{y_a y}{s_y^2\sin\alpha_y}\right)\right]dx\,dy - C(\alpha_x)C(\alpha_y)\int_{\mathbb{R}^2}|R\overline{O}| \\ \exp[i(\varphi_a + \varphi)]\exp\left[-2i\pi\left(\frac{x_a x}{s_x^2\sin\alpha_x} + \frac{y_a y}{s_y^2\sin\alpha_y}\right)\right]dx\,dy\end{aligned} \tag{C.11}$$

The best reconstruction plane is reached when the quadratic phase is zero. Therefore:

$$\varphi_a \pm \varphi = 0 \tag{C.12}$$

with the above condition, the optimal fractional order α_x^{opt} and α_y^{opt} corresponded to the best hologram reconstruction are:

$$\alpha_x^{opt} = \arctan\left[\mp\frac{B_2^x\lambda}{s_x^2(M_x - D_2^x)}\right], \qquad \alpha_y^{opt} = \arctan\left[\mp\frac{B_2^y\lambda}{s_y^2(M_y - D_2^y)}\right] \tag{C.13}$$

Appendix D

FIELD AMPLITUDE IN MATRIX FORM

D.1 Field amplitude in object plane

A Gaussian beam in Eq.(A.3) can be written in matrix form as:

$$G_0(\mu,\nu) = \exp\left(-\rho^T Q_0^{-1}\rho\right) \tag{D.1}$$

where Q_0 is:

$$Q_0 = \begin{pmatrix} \omega_0^2 & 0 \\ 0 & \omega_0^2 \end{pmatrix} \tag{D.2}$$

and $\rho = (\mu \;\; \nu)^T$.

The transfer matrix M_1 described the propagation through the system between the incident plane and the object plane is defined as:

$$M_1 = \begin{pmatrix} A_1 & B_1 \\ C_1 & D_1 \end{pmatrix} \tag{D.3}$$

and each matrix element in Eq.(D.3) can be written as:

$$A_1 = \begin{pmatrix} A_1^x & 0 \\ 0 & A_1^y \end{pmatrix}, \quad B_1 = \begin{pmatrix} B_1^x & 0 \\ 0 & B_1^y \end{pmatrix}, \quad C_1 = \begin{pmatrix} C_1^x & 0 \\ 0 & C_1^y \end{pmatrix}, \quad D_1 = \begin{pmatrix} D_1^x & 0 \\ 0 & D_1^y \end{pmatrix} \tag{D.4}$$

Recall that the field amplitude in the object plane as in Eq.(A.12) are:

$$G_1(\xi,\eta) = \frac{\exp(ikE_1)}{i\lambda\sqrt{B_1^x B_1^y}} K_1^x K_1^y \exp\left[-\left(\frac{\xi^2}{\omega_{1_x}^2} + \frac{\eta^2}{\omega_{1_y}^2}\right)\right] \exp\left[-i\frac{\pi}{\lambda}\left(\frac{\xi^2}{R_{1_x}} + \frac{\eta^2}{R_{1_y}}\right)\right] \tag{D.5}$$

with

$$K_1^x = \left(\frac{\pi\omega_0^2}{1 - i\frac{\pi\omega_0^2}{\lambda}\frac{A_1^x}{B_1^x}}\right)^{1/2} \qquad K_1^y = \left(\frac{\pi\omega_0^2}{1 - i\frac{\pi\omega_0^2}{\lambda}\frac{A_1^y}{B_1^y}}\right)^{1/2} \tag{D.6}$$

Let consider $K_1^x K_1^y$:

$$
\begin{aligned}
K_1^x K_1^y &= \left(\frac{\pi\omega_0^2}{1 - i\frac{\pi\omega_0^2}{\lambda}\frac{A_1^x}{B_1^x}}\right)^{1/2} \left(\frac{\pi\omega_0^2}{1 - i\frac{\pi\omega_0^2}{\lambda}\frac{A_1^y}{B_1^y}}\right)^{1/2} \\
&= \pi\omega_0^2 \left(\frac{1}{1 - i\frac{\pi\omega_0^2}{\lambda}\frac{A_1^x}{B_1^x}}\right)^{1/2} \left(\frac{1}{1 - i\frac{\pi\omega_0^2}{\lambda}\frac{A_1^y}{B_1^y}}\right)^{1/2} \\
&= \pi \frac{\sqrt{B_1^x}}{\sqrt{\frac{B_1^x}{\omega_0^2} - i\frac{\pi}{\lambda}A_1^x}} \frac{\sqrt{B_1^y}}{\sqrt{\frac{B_1^y}{\omega_0^2} - i\frac{\pi}{\lambda}A_1^y}}
\end{aligned}
\tag{D.7}
$$

Then multiply by $\frac{1}{\sqrt{B_1^x B_1^y}}$:

$$
\begin{aligned}
\frac{K_1^x K_1^y}{\sqrt{B_1^x B_1^y}} &= \frac{\pi}{\sqrt{B_1^x B_1^y}} \frac{\sqrt{B_1^x}}{\sqrt{\frac{B_1^x}{\omega_0^2} - i\frac{\pi}{\lambda}A_1^x}} \frac{\sqrt{B_1^y}}{\sqrt{\frac{B_1^y}{\omega_0^2} - i\frac{\pi}{\lambda}A_1^y}} \\
&= \pi \frac{1}{\sqrt{\frac{B_1^x}{\omega_0^2} - i\frac{\pi}{\lambda}A_1^x}} \frac{1}{\sqrt{\frac{B_1^y}{\omega_0^2} - i\frac{\pi}{\lambda}A_1^y}}
\end{aligned}
\tag{D.8}
$$

or it can be written in the matrix form as:

$$
\frac{K_1^x K_1^y}{\sqrt{B_1^x B_1^y}} = \pi \frac{1}{\sqrt{\det\left(B_1 Q_0^{-1} - i\frac{\pi}{\lambda}A_1\right)}} \tag{D.9}
$$

The two exponential term in Eq.(D.5) can be written in the matrix form as:

$$
\exp\left[-\left(\frac{\xi^2}{\omega_{1_x}^2} + \frac{\eta^2}{\omega_{1_y}^2}\right)\right] \exp\left[-i\frac{\pi}{\lambda}\left(\frac{\xi^2}{R_{1_x}} + \frac{\eta^2}{R_{1_y}}\right)\right] = \exp\left[-\frac{\pi^2}{\lambda^2}\mathbf{r}^T Q_1^{-1}\mathbf{r}\right], \tag{D.10}
$$

where $\mathbf{r}^T = (\xi \;\; \eta)$. Q_1^{-1} is:

$$
Q_1^{-1} = B_1^{-1T}\left(Q_0^{-1} - i\frac{\pi}{\lambda}B_1^{-1}A_1\right)^{-1} B_1^{-1} - i\frac{\pi}{\lambda}D_1 B_1^{-1}, \tag{D.11}
$$

Therefore, the field amplitude in the object plane as in Eq.(D.5) can be written in the matrix form as:

$$
G_1(\mathbf{r}) = \frac{\pi}{i\lambda} \frac{\exp(ikE_1)}{\sqrt{det\left(B_1 Q_0^{-1} - i\frac{\pi}{\lambda}A_1\right)}} \exp\left[-\frac{\pi^2}{\lambda^2}\mathbf{r}^T Q_1^{-1}\mathbf{r}\right], \tag{D.12}
$$

and $k = \frac{2\pi}{\lambda}$ and E_1 is an optical path between the incident plane and the object plane.

D.2 Field amplitude in CCD plane

The transfer matrix M_2 described the propagation through the system between the object plane and the CCD plane is defined as:

$$M_2 = \begin{pmatrix} A_2 & B_2 \\ C_2 & D_2 \end{pmatrix} \tag{D.13}$$

and each matrix element in Eq.(D.13) can be written as:

$$A_2 = \begin{pmatrix} A_2^x & 0 \\ 0 & A_2^y \end{pmatrix}, \quad B_2 = \begin{pmatrix} B_2^x & 0 \\ 0 & B_2^y \end{pmatrix}, \quad C_2 = \begin{pmatrix} C_2^x & 0 \\ 0 & C_2^y \end{pmatrix}, \quad D_2 = \begin{pmatrix} D_2^x & 0 \\ 0 & D_2^y \end{pmatrix} \tag{D.14}$$

Recall that the field amplitude in the CCD plane as in Eq.(B.3) are:

$$\begin{aligned} G_2(x,y) = \frac{\exp(i\frac{2\pi}{\lambda}E_2)}{i\lambda\sqrt{B_2^x B_2^y}} \int_{\mathbb{R}^2} G_1(\xi,\eta)[1-T(\xi,\eta)] \\ \exp\left[i\frac{\pi}{\lambda B_2^x}(A_2^x\xi^2 - 2\xi x + D_2^x x^2)\right] \exp\left[i\frac{\pi}{\lambda B_2^y}(A_2^y\eta^2 - 2\eta y + D_1^y y^2)\right] d\xi\, d\eta \end{aligned} \tag{D.15}$$

or

$$\begin{aligned} G_2(x,y) = \frac{\exp(i\frac{2\pi}{\lambda}E_2)}{i\lambda\sqrt{B_2^x B_2^y}} \exp\left[\frac{i\pi}{\lambda}\left(\frac{D_2^x}{B_2^x}x^2 + \frac{D_2^y}{B_2^y}y^2\right)\right] \int_{\mathbb{R}^2} G_1(\xi,\eta)[1-T(\xi,\eta)] \\ \exp\left[i\frac{\pi}{\lambda B_2^x}(A_2^x\xi^2 - 2\xi x)\right] \exp\left[i\frac{\pi}{\lambda B_2^y}(A_2^y\eta^2 - 2\eta y)\right] d\xi\, d\eta \end{aligned} \tag{D.16}$$

In this case, the particle transmission function $T(\xi,\eta)$ is replaced by $p(s,\theta)$ as defined in the following equation:

$$\begin{aligned} p(s,\theta) &= [1 - A(s,\theta)\exp(i\Phi(s,\theta))]\, Z_0^0(s,\theta) \\ &= \left[1 - \sum_{n,m} \gamma_n^m Z_n^m(s,\theta)\right] Z_0^0(s,\theta) \end{aligned} \tag{D.17}$$

$Z_n^m(s,\theta)$ is Zernike polynomials which is defined as:

$$Z_n^m(s,\theta) = R_n^{|m|}(s)e^{im\theta}, \qquad 0 \le s \le 1,\ 0 \le \theta \le 2\pi \tag{D.18}$$

Therefore, the field amplitude in the CCD plane as in Eq.(D.14) becomes:

$$\begin{aligned} G_2(x,y) = \frac{\exp(i\frac{2\pi}{\lambda}E_2)}{i\lambda\sqrt{B_2^x B_2^y}} \exp\left[\frac{i\pi}{\lambda}\left(\frac{D_2^x}{B_2^x}x^2 + \frac{D_2^y}{B_2^y}y^2\right)\right] \int_{\mathbb{R}^2} G_1(\xi,\eta)[1-p(s,\theta)] \\ \exp\left[i\frac{\pi}{\lambda}(\frac{A_2^x}{B_2^x}\xi^2 + \frac{A_2^y}{B_2^y}\eta^2)\right] \exp\left[-i\frac{2\pi}{\lambda}(\frac{A_2^x}{B_2^x}\xi x + \frac{A_2^y}{B_2^y}\eta y)\right] d\xi\, d\eta \end{aligned} \tag{D.19}$$

The amplitude $G_1(\xi,\eta)$ can be written in the matrix form $G_1(\mathbf{r})$ as in Eq.(D.12). The term outside the integral in Eq.(D.19) can be written as:

$$\frac{\exp(i\frac{2\pi}{\lambda}E_2)}{i\lambda\sqrt{B_2^x B_2^y}}\exp\left[\frac{i\pi}{\lambda}\left(\frac{D_2^x}{B_2^x}x^2+\frac{D_2^y}{B_2^y}y^2\right)\right]=\frac{\exp(i\frac{2\pi}{\lambda}E_2)}{i\lambda\sqrt{\det(B_2)}}\exp\left[i\frac{\pi}{\lambda}\mathbf{r'}^T B_2^{-1}D_2\mathbf{r'}\right], \quad \text{(D.20)}$$

where the vector $\mathbf{r'}^T=(x\ \ y)$, and E_2 is an optical path between the object plane and the CCD plane.

From Eq.(D.19), the field amplitude in the CCD plane can be written in the matrix form as:

$$\begin{aligned}G_2(\mathbf{r'})=&\frac{\exp(i\frac{2\pi}{\lambda}E_2)}{i\lambda\sqrt{\det(B_2)}}\exp\left[i\frac{\pi}{\lambda}\mathbf{r'}^T B_2^{-1}D_2\mathbf{r'}\right]\int_{\mathbb{R}^2}G_1(\mathbf{r})[1-p(s,\theta)]\\&\exp\left[i\frac{\pi}{\lambda}\mathbf{r}^T B_2^{-1}\mathbb{A}_2\mathbf{r}\right]\exp\left[-i\frac{2\pi}{\lambda}\mathbf{r}^T B_2^{-1}\mathbf{r}\right]d\mathbf{r}\end{aligned} \quad \text{(D.21)}$$

Substitute $G_1(\mathbf{r})$ from Eq.(D.12) into Eq.(D.21), then the field $G_2(\mathbf{r'})$ becomes:

$$\begin{aligned}G_2(\mathbf{r'})=&\frac{\exp(i\frac{2\pi}{\lambda}E_2)}{i\lambda\sqrt{\det(B_2)}}\exp\left[i\frac{\pi}{\lambda}\mathbf{r'}^T B_2^{-1}\mathbb{D}_2\mathbf{r'}\right]\frac{\pi}{i\lambda}\frac{\exp(ikE_1)}{\sqrt{\det\left(B_1Q_0^{-1}-i\frac{\pi}{\lambda}A_1\right)}}\\&\int_{\mathbb{R}^2}\exp\left[-\frac{\pi^2}{\lambda^2}\mathbf{r}^T Q_1^{-1}\mathbf{r}\right][1-p(s,\theta)]\exp\left[i\frac{\pi}{\lambda}\mathbf{r}^T B_2^{-1}A_2\mathbf{r}\right]\exp\left[-i\frac{2\pi}{\lambda}\mathbf{r}^T B_2^{-1}\mathbf{r}\right]d\mathbf{r}\end{aligned} \quad \text{(D.22)}$$

Then we will change the variable $\mathbf{r}$ and $\mathbf{r'}$ to the dimensionless variables $\mathbf{s}=2\mathbf{r}/D$ and $\mathbf{s'}=2\mathbf{r'}/D$ where D is the particle's diameter. Therefore, the Eq.(D.22) becomes

$$\begin{aligned}G_2(\mathbf{s'}D/2)=&-\frac{\pi}{\lambda^2}\frac{\exp(i\frac{2\pi}{\lambda}E_1+E_2)}{\sqrt{\det(B_2)\det\left(B_1Q_0^{-1}-iA_1\right)}}\exp\left[i\frac{\pi D^2}{4\lambda}\mathbf{s'}^T B_2^{-1}D_2\mathbf{s'}\right]\\&\int_{\mathbb{R}^2}\exp\left[-i\mathbf{s}^T L_2\mathbf{s}\right][1-p(s,\theta)]\exp\left[-i2\pi\mathbf{s}^T P_2\mathbf{s'}\right]\frac{D^2}{4}\,d\mathbf{s}\end{aligned} \quad \text{(D.23)}$$

with

$$L_2=\frac{\pi D^2}{4\lambda}B_2^{-1}A_2+i\left(\frac{\pi D}{2\lambda}\right)^2 Q_1, \qquad P_2=\frac{D^2}{4\lambda}B_2^{-1} \quad \text{(D.24)}$$

Let $\boldsymbol{\sigma}=P_2\mathbf{s'}$, then the integration in Eq.(D.24) changes to the form:

$$\begin{aligned}G_2(DP_2^{-1}\boldsymbol{\sigma}/2)=&-\frac{\pi D^2}{4\lambda^2}\frac{\exp(i\frac{2\pi}{\lambda}E_1+E_2)}{\sqrt{\det(B_2)\det\left(B_1Q_0^{-1}-iA_1\right)}}\exp\left[i\frac{\pi D^2}{4\lambda}\boldsymbol{\sigma}^T S_2\boldsymbol{\sigma}\right]\\&\int_{\mathbb{R}^2}[1-p(s,\theta)]\exp\left[-i\mathbf{s}^T L_2\mathbf{s}\right]\exp\left[-i2\pi\mathbf{s}^T\boldsymbol{\sigma}\right]\,d\mathbf{s}\end{aligned} \quad \text{(D.25)}$$

where $S_2 = P_2^{-1T} D_2 B_2^{-1} P_2^{-1}$.

D.3 Intensity distribution in the CCD plane

The intensity distribution recorded by the CCD sensor is:

$$\begin{aligned} I &= |G_2(DP_2^{-1}\boldsymbol{\sigma}/2)|^2 \\ &= \frac{\pi D^2}{4\lambda^2} \frac{|G(\boldsymbol{\sigma}) - G_0^0(\boldsymbol{\sigma}) + \epsilon G_n^m(\boldsymbol{\sigma})|^2}{\left|\sqrt{\det(B_2)\det\left(B_1 Q_0^{-1} - i\frac{\pi}{\lambda}A_1\right)}\right|^2}, \end{aligned} \tag{D.26}$$

where $G(\boldsymbol{\sigma})$ is

$$G(\boldsymbol{\sigma}) = \int_{\mathbb{R}^2} \exp\left[-i\mathbf{s}^T L_2 \mathbf{s}\right] \exp\left[-i2\pi \mathbf{s}^T \boldsymbol{\sigma}\right] \, d\mathbf{s} \tag{D.27}$$

and

$$G_n^m(\boldsymbol{\sigma}) = \sum_{n,m} \gamma_n^m \times \int_{\mathbb{R}^2} Z_0^0(s,\theta) Z_n^m(s,\theta) \exp\left[-i\mathbf{s}^T L_2 \mathbf{s}\right] \exp\left[-i2\pi \mathbf{s}^T \boldsymbol{\sigma}\right] \, d\mathbf{s} \tag{D.28}$$

For an opaque particle, we have only the second term $G_0^0(\boldsymbol{\sigma})$ and the value of $\epsilon = 0$. For a phase particle, the value of epsilon $\epsilon = 1$.

Appendix E

CALCULATION OF $G(\boldsymbol{\sigma})$ AND $G_n^m(\boldsymbol{\sigma})$

E.1 Calculation of $G(\boldsymbol{\sigma})$

From Eq.(D.27), the integral $G(\boldsymbol{\sigma})$ is

$$G(\boldsymbol{\sigma}) = \int_{\mathbb{R}^2} \exp\left[i\mathbf{s}^T L_2 \mathbf{s}\right] \exp\left[-i2\pi \mathbf{s}^T \boldsymbol{\sigma}\right] \, d\mathbf{s} \tag{E.1}$$

Denoted that L_2 and $\mathbf{s}$ are

$$L_2 = \frac{\pi D^2}{4\lambda} B_2^{-1} A_2 + i\left(\frac{\pi D}{2\lambda}\right)^2 Q_1, \qquad \mathbf{s} = \frac{2\mathbf{r}}{D} = \frac{2}{D}\begin{pmatrix} x \\ y \end{pmatrix} \tag{E.2}$$

Then Eq.(D.1) becomes

$$G(\boldsymbol{\sigma}) = \int_x \int_y \exp\left[i\frac{4}{D^2} L_2 (x^2 + y^2)\right] \exp\left[-i\frac{4\pi}{D}(x+y)\boldsymbol{\sigma}\right] \, dx \, dy \tag{E.3}$$

Rearrange the variable x and y.

$$G(\boldsymbol{\sigma}) = \int_x \exp\left[i\frac{4}{D^2} L_2 x^2\right] \exp\left[-i\frac{4\pi}{D}\boldsymbol{\sigma} x\right] \, dx \int_y \exp\left[i\frac{4}{D^2} L_2 y^2\right] \exp\left[-i\frac{4\pi}{D}\boldsymbol{\sigma} y\right] \, dy \tag{E.4}$$

Use the integral exponential formula : $\int e^{-ax^2} e^{-2bx} dx = \sqrt{\frac{\pi}{a}} e^{\frac{b^2}{a}}$. Then the Eq.(E.4) becomes:

$$G(\boldsymbol{\sigma}) = \frac{\pi}{-i\frac{4}{D^2} L_2} \exp\left[\frac{\left(\frac{i2\pi\boldsymbol{\sigma}}{D}\right)^2}{-i\frac{4}{D^2} L_2}\right] \exp\left[\frac{\left(\frac{i2\pi\boldsymbol{\sigma}}{D}\right)^2}{-i\frac{4}{D^2} L_2}\right] \tag{E.5}$$

or

$$G(\boldsymbol{\sigma}) = \frac{i\pi D^2}{4L_2} \exp\left[-i\frac{\pi^2\boldsymbol{\sigma}^2}{L_2}\right] \exp\left[-i\frac{\pi^2\boldsymbol{\sigma}^2}{L_2}\right] \tag{E.6}$$

The $G(\boldsymbol{\sigma})$ can be written in matrix form as:

$$G(\boldsymbol{\sigma}) = \frac{i\pi}{\sqrt{\det(L_2)}} \exp\left[-i\pi^2 \boldsymbol{\sigma}^T L_2^{-1} \boldsymbol{\sigma}\right] \tag{E.7}$$

E.2 Calculation of $G_n^m(\boldsymbol{\sigma})$

The $G_n^m(\boldsymbol{\sigma})$ in Eq.(D.28) can be written as:

$$G_n^m(\sigma,\varphi) = \sum_{n,m} \gamma_n^m \times \int_{\mathbb{R}^2} Z_0^0(s,\theta) Z_n^m(s,\theta) \exp\left[-i\mathbf{s}^T L_2 \mathbf{s}\right] \exp\left[-i2\pi\sigma \cdot s\cos(\theta-\varphi)\right]\ s\,ds\,d\theta \tag{E.8}$$

where $\boldsymbol{\sigma} = \sigma\exp(i\varphi)$ and $\mathbf{s} = s\,\exp(i\theta)$. To get the semi-analytical solution of this integral, first write the $\exp\left[-i\mathbf{s}^T L_2\mathbf{s}\right]$ as the following equation:

$$\exp\left[-i\mathbf{s}^T L_2\mathbf{s}\right] = \exp\left[i\frac{1}{2}s^2\left(L_{2(1,1)} + L_{2(2,2)}\right) + i\frac{1}{2}s^2\left(L_{2(1,1)} - L_{2(2,2)}\right)\cos(2\theta)\right] \tag{E.9}$$

Then expand the second term of Eq.(E.9) by using β-coefficients:

$$\exp\left[i\frac{1}{2}s^2\left(L_{2(1,1)} - L_{2(2,2)}\right)\cos(2\theta)\right] = \sum_{q=-\infty}^{+\infty}\sum_{p=0}^{\infty} i^q \cdot \beta_{|2q|+2p}^{|2q|}(\delta)\cdot Z_{|2q|+2p}^{2q}(s,\theta) \tag{E.10}$$

where $\delta = \frac{1}{2}\left(L_{2(1,1)} - L_{2(2,2)}\right)$. The expansion coefficients $\beta_{|2q|+2p}^{|2q|}$ can be expressed explicitly in terms of the hypergeometric functions ${}_2F_3$ [57] as:

$$\begin{aligned}\beta_{|2q|+2p}^{|2q|}(\delta) = {} & d_0^0(-1)^r(2|2q|+4r+1)\left(\frac{1}{2}\delta\right)^{|2q|+2r} \\ & \times {}_2F_3\left(\begin{matrix} r+\frac{1}{2} & |2q|+r+\frac{1}{2} \\ \frac{1}{2} & |2q|+2r+\frac{3}{2} \end{matrix}\ \begin{matrix} \\ |2q|+2r+1 \end{matrix}; -\frac{1}{4}\delta^2\right),\end{aligned} \tag{E.11}$$

for the case of $2r-p=0$ and

$$\begin{aligned}\beta_{|2q|+2p}^{|2q|}(\delta) = {} & d_0^1(-1)^r(2|2q|+4r-1)\left(\frac{1}{2}\delta\right)^{|2q|+2r} \\ & \times {}_2F_3\left(\begin{matrix} r+\frac{1}{2} & |2q|+r+\frac{1}{2} \\ \frac{3}{2} & |2q|+2r+1 \end{matrix}\ \begin{matrix} \\ |2q|+2r+\frac{1}{2} \end{matrix}; -\frac{1}{4}\delta^2\right),\end{aligned} \tag{E.12}$$

for the case of $2r-p=1$. The coefficients d_0^0 and d_0^1 are defined as:

$$d_0^0 = \frac{(2r)!(2|2q|+2r)!}{r!(|2q|+r)!(2|2q|+4r+1)!} \tag{E.13}$$

and

$$d_0^1 = \frac{(2r)!(2|2q|+2r)!}{r!(|2q|+r)!(2|2q|+4r)!} \tag{E.14}$$

substitute Eq.(E.10) into Eq.(E.8), we see that there is the product of two Zernike polynomials as

$$Z_n^m(s,\theta)\cdot Z_{|2q|+2p}^{2q}(s,\theta) \tag{E.15}$$

From [79], Eq.(40)-(44), this product is:

$$Z_n^m(s,\theta)\cdot Z_{|2q|+2p}^{2q}(s,\theta)=\sum_t A_{n,|2q|+2p,t}^{m,2q,m+2q}\cdot Z_t^{m+2q}(s,\theta) \tag{E.16}$$

This summation over is

$$t=max\left(|m+2q|,|m-|2q|-2p|\right)(2)\left(n+|2q|+2p\right) \tag{E.17}$$

$a(2)b$ is $a, a+2, ..., b$ where $b-a$ is non-negative and even. The coefficients A can be given in terms of Wigner or Clebsch-Gordon coefficients [96], Eq.(23).

$$A_{j,l,n}^{i,k,m}=\left|C_{\frac{i}{2},\frac{k}{2},\frac{m}{2}}^{\frac{j}{2},\frac{l}{2},\frac{n}{2}}\right|^2 \tag{E.18}$$

The integral Eq.(E.8) is:

$$\begin{aligned}G_n^m(\sigma,\varphi)=\sum_{n,m}\gamma_n^m\times\int_0^1\int_0^{2\pi}Z_0^0(s,\theta)Z_n^m(s,\theta)\exp\left[-i2\pi\sigma\cdot s\cos(\theta-\varphi)\right]\\ \exp\left[i\frac{1}{2}s^2\left(L_{2(1,1)}+L_{2(2,2)}\right)+i\frac{1}{2}s^2\left(L_{2(1,1)}-L_{2(2,2)}\right)\cos(2\theta)\right]\ s\,ds\,d\theta\end{aligned} \tag{E.19}$$

Substitute Eq.(E.10) to Eq.(E.19), then

$$\begin{aligned}G_n^m(\sigma,\varphi)=\sum_{n,m}\gamma_n^m\times\int_0^1\int_0^{2\pi}Z_0^0(s,\theta)Z_n^m(s,\theta)\exp\left[-i2\pi\sigma\cdot s\cos(\theta-\varphi)\right]\\ \exp\left[i\frac{1}{2}s^2\left(L_{2(1,1)}+L_{2(2,2)}\right)\right]\sum_{q=-\infty}^{+\infty}\sum_{p=0}^{\infty}i^q\cdot\beta_{|2q|+2p}^{|2q|}(\delta)\cdot Z_{|2q|+2p}^{2q}(s,\theta)\ s\,ds\,d\theta\end{aligned} \tag{E.20}$$

From the product of two Zernike polynomials in Eq.(E.16), the $G_n^m(\sigma,\varphi)$ becomes

$$\begin{aligned}G_n^m(\sigma,\varphi)=\sum_{n,m}\gamma_n^m\times\int_0^1\int_0^{2\pi}\exp\left[-i2\pi\sigma\cdot s\cos(\theta-\varphi)\right]\exp\left[i\frac{1}{2}s^2\left(L_{2(1,1)}+L_{2(2,2)}\right)\right]\\ \sum_{q=-\infty}^{+\infty}\sum_{p=0}^{\infty}\sum_t A_{n,|2q|+2p,t}^{m,2q,m+2q}\cdot Z_t^{m+2q}(s,\theta)i^q\cdot\beta_{|2q|+2p}^{|2q|}(\delta)\ s\,ds\,d\theta\end{aligned} \tag{E.21}$$

or

$$G_n^m(\sigma,\varphi) = \sum_{q=-\infty}^{+\infty}\sum_{n,m,p}^{\infty}\sum_{t}\gamma_n^m \cdot A_{n,|2q|+2p,t}^{m,2q,m+2q} \cdot i^q \cdot \beta_{|2q|+2p}^{|2q|}(\delta) \int_0^1\int_0^{2\pi} \exp\left[-i2\pi\sigma \cdot s\cos(\theta-\varphi)\right] \exp\left[i\frac{1}{2}s^2\left(L_{2(1,1)}+L_{2(2,2)}\right)\right] \cdot Z_t^{m+2q}(s,\theta)\; s\,ds\,d\theta \tag{E.22}$$

The equation in this form is similar to the Eq.(3) in [81]. From [81] in Section 2.2, the semi-analytical solution of $G_n^m(\sigma,\varphi)$ becomes

$$G_n^m(\sigma,\varphi) = 2\pi \sum_{q=-\infty}^{+\infty}\sum_{n,m,p}^{\infty}\sum_{t}\gamma_n^m \cdot (-i)^{m+q} \cdot A_{n,|2q|+2p,t}^{m,2q,m+2q} \cdot \beta_{|2q|+2p}^{|2q|}(\delta) \cdot V_t^{m+2q}(2\pi\sigma,\chi) \cdot e^{i(m+2q)\varphi} \tag{E.23}$$

in which [81], Eq.(19-20)

$$V_n^m(r,f) = \varepsilon_m exp(if) \cdot \sum_{l=1}^{\infty}(-2if)^{l-1}\sum_{j=0}^{P}\upsilon_{lj} \cdot \frac{J_{|m|+l+2j}(r)}{l(r)^l} \tag{E.24}$$

where

$$\upsilon_{lj} = (-1)^P\left(|m|+l+2j\right)\binom{|m|+j+l-1}{l-1} \cdot \binom{j+l-1}{l-1}\binom{l-1}{P-j} / \binom{Q+l+j}{l}, \tag{E.25}$$

for $l = 1,2,3,...$ and $j = 0,1,2,...,P$. $Q = \frac{n+|m|}{2}$ and $P = \frac{n-|m|}{2}$. For odd $m < 0$, $\varepsilon_m = -1$ and otherwise $\varepsilon_m = 1$.

Appendix F

THE DEVELOPMENT OF THICKNESS FUNCTION $\triangle(\boldsymbol{r})$

Let's consider a sphere as in Fig. F.1. This figure shows ray analysis in x-z plane.

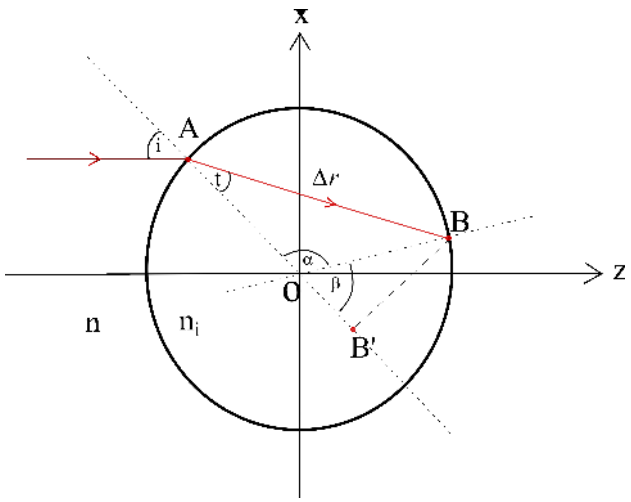

Fig. F.1: This image shows the entrance and the refracted ray of the droplet.

Point A is a point on a sphere where the ray enters to a droplet and point B is a point where the ray leaves the droplet. Consider triangle ABO, from the law of cosines, the thickness function can be written as

$$(\triangle \boldsymbol{r})^2 = \frac{D^2}{4} + \frac{D^2}{4} - 2\frac{D^2}{4}\cos\alpha \tag{F.1}$$

where α is the angle between the line $\overline{OA}$ and $\overline{OB}$ as shown in Fig. F.1. From the Snell's law, the incident angle and the refracted angle is related to

$$n\ \sin(i) = n_i\ \sin(t), \tag{F.2}$$

where i and t are incident and refracted angle, respectively. Then we know that the refracted angle related to the incident angle and the ratio of refractive index as

$$\sin(t) = \frac{n}{n_i}\sin(i). \tag{F.3}$$

Consider the right triangle ABB', then

$$\sin(t) = \frac{\overline{BB'}}{\triangle \boldsymbol{r}} \qquad \text{or} \qquad \overline{BB'} = \frac{n}{n_i} \triangle \boldsymbol{r} \sin(i) \tag{F.4}$$

The summation between the angle α and β is $\alpha + \beta = 180^\circ$ or $\beta = 180^\circ - \alpha$. By considering the right triangle OBB', sine of β is

$$\begin{aligned} \sin(\beta) &= \frac{\overline{BB'}}{D/2} \\ \overline{BB'} &= \frac{D}{2}\ \sin(\beta), \qquad \beta = 180^\circ - \alpha \\ &= \frac{D}{2}\ \sin(180^\circ - \alpha) = \frac{D}{2}\ \sin(\alpha) \end{aligned} \tag{F.5}$$

Then compare Eq.(F.4) and Eq.(F.5), we have:

$$\triangle \boldsymbol{r} = \frac{D}{2} \frac{n_i}{n} \frac{\sin(\alpha)}{\sin(i)} \tag{F.6}$$

From Eq.(F.1), we already know that

$$\begin{aligned} (\triangle \boldsymbol{r})^2 &= \frac{D^2}{2}(1 - \cos\alpha) \\ \cos\alpha &= 1 - \frac{2}{D^2}(\triangle \boldsymbol{r})^2 \end{aligned} \tag{F.7}$$

With trigonometry identity $cos^2\alpha + sin^2\alpha = 1$, then Eq.(F.6) becomes:

$$\begin{aligned} \triangle \boldsymbol{r} &= \frac{D}{2} \frac{n_i}{n} \frac{\sqrt{1 - \cos^2\alpha}}{\sin(i)} \\ &= \frac{D}{2} \frac{n_i}{n} \frac{\sqrt{1 - \left(1 - \frac{2}{D^2}(\triangle \boldsymbol{r})^2\right)^2}}{\sin(i)} \\ &= \frac{D}{2} \frac{n_i}{n} \frac{\sqrt{1 - \left(1 - \frac{4}{D^2}(\triangle \boldsymbol{r})^2 + \frac{4}{D^4}(\triangle \boldsymbol{r})^4\right)}}{\sin(i)} \\ &= \frac{D}{2} \frac{n_i}{n} \frac{\sqrt{\frac{4}{D^2}(\triangle \boldsymbol{r})^2 \left(1 - \frac{1}{D^2}(\triangle \boldsymbol{r})^2\right)}}{\sin(i)} \\ &= \frac{D}{2} \frac{n_i}{n} \frac{2}{D}(\triangle \boldsymbol{r}) \frac{\sqrt{\left(1 - \frac{1}{D^2}(\triangle \boldsymbol{r})^2\right)}}{\sin(i)} \\ \frac{n}{n_i} \sin(i) &= \sqrt{\left(1 - \frac{1}{D^2}(\triangle \boldsymbol{r})^2\right)} \\ (\triangle \boldsymbol{r})^2 &= D^2 \left[1 - \left(\frac{n}{n_i}\right)^2 \sin^2 i\right] \end{aligned} \tag{F.8}$$

With $\cos^2 i + \sin^2 i = 1$, the Eq.(F.8) becomes

$$\begin{aligned}(\triangle \boldsymbol{r})^2 &= D^2 \left[1 - \left(\frac{n}{n_i}\right)^2 \left(1 - \cos^2 i\right)\right] \\ (\triangle \boldsymbol{r})^2 &= D^2 \left[1 - \left(\frac{n}{n_i}\right)^2 + \left(\frac{n}{n_i}\right)^2 \cos^2 i\right]\end{aligned} \tag{F.9}$$

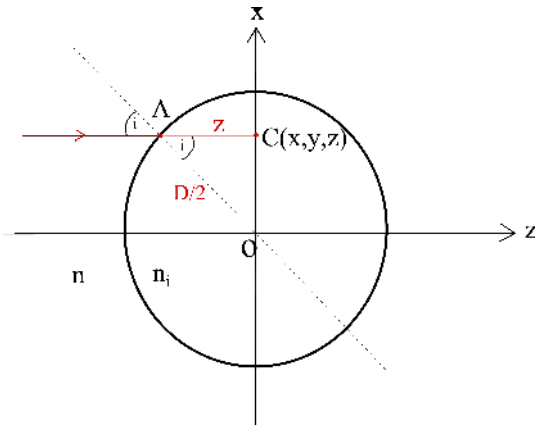

Fig. F.2: This image shows the incident angle with respect to parameters z and $D/2$

Consider the right triangle ACO in Fig. F.2, cos i is

$$\cos\ i = \frac{z}{D/2} \tag{F.10}$$

and

$$\begin{aligned}z &= \sqrt{\frac{D^2}{4} - x^2 - y^2} \\ &= \frac{D}{2}\sqrt{1 - \frac{(x^2+y^2)}{D^2/4}}\end{aligned} \tag{F.11}$$

Then cos i is

$$\begin{aligned}\cos\ i &= \frac{\frac{D}{2}\sqrt{1 - \frac{(x^2+y^2)}{D^2/4}}}{D/2} \\ \cos^2 i &= 1 - \frac{(x^2+y^2)}{D^2/4}\end{aligned} \tag{F.12}$$

By recalling that $\boldsymbol{r} = \boldsymbol{s}D/2$, therefore the thickness function can be written as:

$$\triangle \boldsymbol{r} = D \cdot \left(1 - c^2 \boldsymbol{s}^2\right)^{1/2} \tag{F.13}$$

where $c = n/n_i$ and $0 < c < 1$.

Appendix G

POSSIBLILITY TO ADD NOISE IN THE HOLOGRAM

From chapter 4 in section 4.5, we can add noise into the hologram. First part, we create a grid where the noise is obtained as shown in Fig. 4.22 (a) with $k1 = 2$. The scaling of this grid is then enlarged to the scaling of the hologram. MATLAB code for this part is:

```
% number
N = 5;
% create a grid
[X,Y] = meshgrid(-N : k1 : N, -N : k1 : N);
% generate grid's value randomly
Z = rand(size(X), size(Y));
```

Next, the other grid that have the same pixel number ($k2 = 1$) as the hologram grid (we called hologram-like grid) is generated by

```
% create another grid
[XI,YI] = meshgrid(-N : k2 : N, -N : k2 : N);
```

Unfortunately, the pixel sizes of both grids (noise grid and hologram-like grid) are not equal (noise grid has pixel size equals to 2 and hologram-like grid has pixel size equals to 1). We thus realize an interpolation or resampling of the noise grid in the hologram-like grid. The interpolation process is

```
% 2D interpolate the 1st grid to the 2nd grid
ZI = interp2(X,Y,Z,XI,YI);
```

Now Fig. 4.22 (b) is the generated hologram-like grid with the same pixel number as the hologram. Fig. 4.23 is the resulting noise grid that derived from the interpolation between Fig. 4.22 (a) and (b). Finally, in the hologram, noise can be added into our simulated hologram as presented in Fig. 4.25(c).

BIBLIOGRAPHY

[1] X. Yu, M. Cross, C. Liu, D. C. Clark, D. T. Haynie, M. K. Kim, "Measurement of the traction force of biological cells by digital holography", Biomedical Optics Express, 3, 153-159 (2011)

[2] X. Yu, M. Cross, C. Liu, D. C. Clark, D. T. Haynie, M. K. Kim, "Quantitative imaging of surface deformation on substrata due to cell motility by digital holography", Biomedical Optics and 3D Imaging, Optical Society of America, DSu4C.6 (2012)

[3] X. Yu, J. Hong, C. Liu, M. Cross, D. T. Haynie, M. K. Kim, "Four-dimensional motility tracking of biological cells by digital holography microscopy", J. Biomed. Opt.,19, 045001 (2014)

[4] I. Peruhov, E. Mihaylova, "Applications of holographic microscopy in life sciences", Chapter13, InTech (2013)

[5] K. Alm, Z. El-Schich, M. F. Miniotis, A. G. Wingren, B. Janicke, S. Oredsson, "Cells and holograms-holograms and digital holographic microscopy as a tool to study the morphology of living cells", Chapter14, InTech (2013)

[6] Y. Yang, G. N. Sze-To, Christopher Y. H. Chao, "Estimation of the aerodynamic sizes of single bacterium-Laden expiratory aerosols using stochastic modeling with experimental validation", Aerosol Sci. Technol., 46, 1-12 (2012)

[7] B. Lighthart,J. Kim, "Simulation of airborne microbial droplet transport", Appl. Environ. Microbiol., 55, 2349-2355 (1989)

[8] S. S. Lakdawala, K. Subbarao, "The ongoing battle against influenza: the cahllenge of flu transmission, Nature Medicine, 18, 1468-1470 (2012)

[9] Ottavio A. Vittori, Vittorio Prodi, "Scavenging of atmospheric particles by icce crystals", Journal of the Atmospheric Sciences, 24, 533-538 (1967)

[10] Matthew J. Berg, Gorden Videen, "Digital holographic imaging of aerosol particles in flight", Journal of Quantitative Spectroscopy and Radiative Transfer, 112, 1776-1783 (2011)

[11] C.S. Handscomb, M. Kraft, A.E. Bayly, "A new model for the drying of droplets containing suspended solids after shell formation", Chem. Eng. Sci., 64, 228-246 (2009)

[12] G. Derkachov, K. Kolwas, D. Jakubczyk, M. Zientara, and M. Kolwas, "Drying of a microdroplet of water suspension of nanoparticles: from surface aggregates to microcrystal", J. Phys. Chem. C, 112, 16919-16923 (2008)

[13] K. Uno, K. Hayashi, T. Hayashi, K. Ito, H. Kitano, "Particle adsorption in evaporating droplets of polymer latex dispersions on hydrophilic and hydrophobic surfaces", Colloid Polum. Sci., 276, 810-815 (1998)

[14] C. Zeng, H. Bissig, A.D. Dinsmore, "Particles on drolets: from fundamental physics to novel materials", Solid State Communications, 139, 547-556 (2006)

[15] Adrian G. Bailey, "The science and technology of electrostatic powder sprayin, transport and coating", Journal of Electrostatics, 45, 85-120 (1998)

[16] Anatol Jaworek, Andrzej Krupa, Arkadiusz T. Sobczyk, Artur Marchewicz, Michal Szudyga, Teresa Antes, Wamadeva Balachandran, Francesco Di Natale, Claudia Carotenuto, "Submicron particles removal by charged sprays. Fundamentals", Journal of Electrostatics, 71, 345-350 (2012)

[17] W. Balachandran, A. Krupa, W. Machowski, A. Jaworek, "Smoke precipitation by charged water aerosol", Journal of Electrostatics, 51-52, 193-199 (2001)

[18] J. Sheng, E. Malkiel, J. Katz, "Single beam two-views holographic particle image velocimetry", Appl. Opt., 42, 235-250 (2003)

[19] S. Satake, T. Kunugi, K. Sato, T. Ito, H. Kanamori, Jun Taniguchi, "Measurement of 3D flow in a micro-pipe via micro digital holographic particle tracking velocimetry", Meas. Sci. Technol., 17, 1647 (2006)

[20] H. W. Lu, F. Bottausci, J. D. Fowler, A. L. Bertozzi, C. Meinhart, C.J. Kim, "A study of EWOD-driven droplets by PIV investigation", The Royal Society of Chemistry, 8, 456-461 (2008)

[21] G. E. Elsinga, F. Scarano, B. Wieneke, B. W. van Oudheusden, "Tomographic particle image velocimetry", Exp. Fluids., 41, 933-947 (2006)

[22] M. I. Smith, V. Bertola, "Particle velocimetry inside Newtonian and non-Newtonian droplets impacting a hydrophobic surface", Exp. Fluids., 50, 1385-1391 (2011)

[23] C. F. Hess, D. L'esperance, "Droplet imaging velocimeter and sizer: a two-dimensional technique to measure droplet size", Exp. Fluids., 47, 171-182 (2009)

[24] F. Onofri, L. Bergougnoux, J. L. Firpo, J. Misguich-Ripault, "Size, velocity, and concentration in suspension measurements of spherical droplets and cylindrical jets", Appl. Opt., 38, 4681-4690 (1999)

[25] C. Bisgaard, "Velocity fields around spheres and bubbles investigated by laser-doppler anemometry", J. Non-Newtonian Fluid Mechanics, 12, 283-302 (1983)

[26] J. Costes,J. P. Couderc, "Study by laser doppler anemometry of the turbulent flow induced by a rushton turbine in a stirred tank: influence of the size of the units-I. mean flow and turbulence", Chemical Engineering Science, 43, 2751-2764 (1988)

[27] Slavica Ristic, "Laser Doppler anemometry and its application in wind tunnel tests", Scientific Technical Review, 8, 64-75 (2007)

[28] C. Tropea, "Laser Doppler anemometry: recent developments and future challenges", Meas. Sci. Technol., 6, 605-619 (1995)

[29] Dantec dynamics, a Nova Instruments Company: Measurement principles of LDA, Denmark (2013)

[30] H. Shen, S. Coëtmellec, G. Gréhan, M. Brunel, "Interferometric laser imaging for droplet sizing revisited: elaboration of transfer matrix", Appl. Opt., 51, 5357-5368 (2012)

[31] S. Saengkaew, G. Godard, J. B. Blaisot, G. Gréhan, "Experimental analysis of global rainbow technique: sensitivity of temperature and size distribution measurements to non-spherical droplets", Exp. Fluids, 47, 839-848 (2009)

[32] D. Gabor, "A new microscopic principle", Nature, 161, 777-8 (1948)

[33] E. N. Leith, J. Upathnieks, "Reconstructed wavefronts and communication theory", J. Opt. Soc. Am., 52, 1123-1130 (1962)

[34] E. N. Leith, J. Upathnieks, "Wavefront reconstruction with diffused illumination and threedimensional objects", J. Opt. Soc. Am., 54, 1295-1301 (1964)

[35] J. W. Goodman, R. W. Lawrence, "Digital image formation from electronically detected holograms", Appl. Phy. Lett., 11, 77-79 (1967)

[36] U. Schnars, W. Jueptner, "Digital holography, digital hologram recording, numerical reconstruction, and related techniques", Springer, Germany (2005)

[37] K. M. Leung, A. C. Cheung, B. C. Liu, H. K. Woo, C. Sun, X. Q. Shi, S. T. Lee, "Measuring thermal conductivity of CVD diamond and diamond-like films on silicon substrates by holographic interferometry", Diamond and rRelated Materials, 8, 1607-1610 (1999)

[38] S. Seebacher, W. Osten, T. Baumbach, W. Jüptner, "The determination of material parameters of microcomponents using digital holography", Opt. Las. Eng., 36, 103-126 (2001)

[39] D. Young, K. Jungling, T. Williamson, E. Nichols, "Holographic interferometry measurement of the thermal refractive index coefficient and thermal expansion coefficient of Nd:YAG and Nd: YALO", Quantum Electronics, IEEE Journal of, 8, 720-721 (1972)

[40] R. Wynne, J. L. Daneu, T. Y. Fan, "Thermal coefficients of the expansion and refractive index in YAG", Appl. Opt., 38, 3282-3284 (1999)

[41] B. Kemper, D. Carl, J. Schnekenburger, I. Bredebusch, W. Domschke, G. von Bally, "Applying digital-holographic microscopy to living tumor cells", SPIE Newsroom. DOI: 10.1117/2.1200608.0364, (2006)

[42] G. Coppola, P. Ferraro, M. Iodice, S. De Nicola, A. Fnizio, S. Grilli, "A digital holography microscope for complete characterization of microelectromechanical systems", Meas. Sci. Technol., 15, 529-539 (2004)

[43] U. Schnars, W. P. O. Jüptner, "Digital recording and numerical reconstruction of holograms", Meas. Sci. Technol., 13, R85-R101 (2002)

[44] C. Trujillo, S. Sema, F. Monroy, J. Garcia-Sucerquia, "Convolution algorithm for numerical reconstruction of digitally recorded holograms with an extended field of view", Photonics Letters of Poland, 2, 171-173 (2010)

[45] P. Picart, P. Tankam, D. Mounier, Z. Peng, J. Li, "New convolution algorithms for reconstructing extended objects encoded in digitally recorded holograms", Fringe 2009, Springer, Berlin, Heidelberg

[46] J. Weng, J. Zhong, C. Hu, "Phase reconstruction of digital holography with the peak of the two-dimensional Gabor wavelet transform", Appl. Opt., 48, 3308-3316 (2009)

[47] W. L. Anderson, H. Diao, "Two-dimensional wavelet transform and application to holographic particle velocimetry", Appl. Opt., 34, 249-255 (1995)

[48] G. Rajshekhar, S. Siva, P. Rastogi, "Estimation of displacement derivatives in digital holographic interferometry using a two-dimensional space-frequency distribution", Opt. Express, 18, 18041-18046 (2010)

[49] F. Sattar, G. Salomonsson, "The use of a filter bank and the Wigner-Ville distribution for time-frequency representation", IEEE Transactions on Signal Processing, 47, 1776-1783, (1999)

[50] J. Hormigo, G. Cristobal, "Image segmentation using the Wigner-Ville distribution", Advances in Imaging and Electron Physics, 131, 65-80, (2004)

[51] L. Onural, M.T. zgen, "Extraction of three-dimensional object-location information directly from in-line holograms using Wigner analysis", J. Opt. Soc. Am. A, 9, 252-260 (1992)

[52] P. Pellat-Finet, "Fresnel diffraction and the fractional-order Fourier transform", Opt. Lett., 19, 1388-1390 (1994)

[53] P. Pellat-Finet, G. Bonnet, "Fractional order Fourier transform and Fourier optics", Opt. Commun., 111, 141-154 (1994)

[54] V. Namias, "The fractional order Fourier transform and its application to quantum mechanics", J. Inst. Math. Appl., 25, 245-265 (1980)

[55] S. Coëtmellec, D. Lebrun, C. zkul, "Application of the two-dimensional fractional order Fourier transformation to particle field digital holography", J. Opt. Soc. Am. A, 19, 1537-1546 (2002)

[56] S. Coëtmellec, D. Lebrun, C. zkul, "Characterization of diffraction patterns directly from in-line holograms with fractional Fourier transform", Appl. Opt., 41, 312-319 (2002)

[57] F. Nicolas, S. Coëtmellec, M. Brunel, D. Allano, D. Lebrun, "Application of the fractional Fourier transformantion to digital holography recorded by an elliptical, astigmatic Gaussian beam", J. Opt. Soc. Am. A, 22, 2569-2577 (2005)

[58] N. K. Nishchal, J. Joseph, K. Singh, "Securing information using fractional Fourier transform in digital holography", Opt. Commun., 235, 253-259, (2004)

[59] X. Wang, D. Zhao, L. Chen, "Image encryption based on extended fractional Fourier transform and digital holography technique", Opt. Commun., 260, 449-453, (2006)

[60] N. Verrier, S. Coëtmellec, M. Brunel, D. Lebrun, "Digital in-line holography in thick optical systems: application to visualization in pipes", Appl. Optl., 47, 4147-4157 (2008)

[61] M. Brunel, H. Shen, S. Coëtmellec, D. Lebrun, K. Ait Ameur, "Femtosecond digital in-line holography with the fractional Fourier transform: application to phase-contrast metrology", Appl. Phys. B, 106, 583-591 (2012)

[62] M. Malek, D. Allano, S. Coëtmellec, C. Özkul, D. Lebrun, "Digital in-line holography for three-dimensional-two-components particle tracking velocimetry", Meas. Sci. Technol., 15, 1537-1546 (2004)

[63] F. Nicolas, S. Coëtmellec, M. Brunel, D. Lebrun, "Digital in-line holography with a sub-picosecond laser beam", Opt. Commun., 268, 27-33 (2006)

[64] A. W. Lohmann, "Image rotation, Wigner rotation, and the fractional Fourier transform", J. Opt. Soc. Am. A, 10, 2181-2186, (1993)

[65] J. Hua, L. Liu, G. Li , "Extended fractional Fourier transforms", J. Opt. Soc. Am. A, 12, 3316-3322, (1997)

[66] E. Hecht, "Optics", 4th ed., Pearson Education, Inc., publishing as Addison Wesley, San Francisco (2002)

[67] M. Fatih, H. M. Ozaktas, "Accumulated Gouy phase shift in Gaussian beam propagation through first-order optical systems", J. Opt. Soc. Am. A, 14, 2190-2194 (1997)

[68] H. M. Ozaktas, Z. Zalevsky, M. A. Kutay, "The fractional Fourier transform with applications in optics and signal processing", John Wiley and Sons Ltd., England (2001)

[69] Stuart A. Collins, JR., "Lens-system diffraction integral written in terms of matrix optics", J. Opt. Soc. Am., 60, 1168-1177 (1970)

[70] C. Palma, V. Bagini, "Extension of the Fresnel transform to ABCD systems", J. Opt. Soc. Am., 14, 1774-1779 (1997)

[71] J. J. Wen, M. Breazeale, "A diffraction beam field expressed as the superposition of Gaussian beams", J. Acoust. Soc. Am., 83, 1752-1177 (1970)

[72] M. Brunel, H. Shen, S. Coëtmellec, D. Lebrun, "Extended ABCD matrix formailsm for the description of femtosecond diffraction patterns; application to femtosecond digital in-line holography with anamorphic optical systems", Appl. Opt., 51, 1137-1148 (2012)

[73] L. M. Mugnier, "Conoscopic holography: toward three-dimensional reconstructions of opaque objects", Appl. Opt., 34, 1363-1371 (1995)

[74] E. Wolf, "Three-dimensional structure determination of semi-transparent objects from holographic data", Opt. Commun., 248, 41-50 (2005)

[75] F. Palacios, J. Ricardo, D. Palacios, E. Gonalves, J. L. Valin, R. De Souza, "3D image reconstruction of transparent microscopic objects using digital holography", Opt. Commun., 248, 41-50 (2005)

[76] W. J. Tango, "The circle polynomials of Zernike and their application in optics", Appl. Phys., 13, 327-332 (1977)

[77] V. N. Mahajan, "Zernike annular polynomials and optical aberrations of systems with annular pupils", Appl. Opt., 33, 8125-8127 (1994)

[78] H. Ozaktas, Z. Zalevsky, M. Kutay, "The fractional Fourier transform: with applications in optics and signal processing", Wiley (2001)

[79] A. J. E. M. Janssen, "Computation of Hopkins' 3-circle integrals using Zernike expansions", J. Eur. Opt. Soc. Rapid. Publi., 6, 11059 (2011)

[80] A. J. E. M. Janssen, "Extended Nijboer-Zernike approach for the computation of optical point-spread function", J. Opt. Soc. Am. A, 19, 849-857 (2002)

[81] S. van Haver, A. J. E. M. Janssen, "Advanced analytical treatment and efficient computation of the diffration integrals in the extended Nijboer-Zernike theory", J. Eur. Opt. Soc. Rapid. Publi., 8, 11059 (2013)

[82] V. Ashok Narayanan, K. M. M. Prabhu, "The fractional Fourier transform: theory, implementation and error analysis", Microprocessors and Microsystems, 27, 511-521 (2003)

[83] X. Wu, S. Meunier-Guttin-Cluzel, Y. Wu, S. Seangkaew, D. Lebrun, M. Brunel, L. Chen, S. Coëtmellec, K. Cen, G. Grehan, "Holography and micro-holography of particle fields: A numerical standard", Opt. Comm., 285, 3013-3020 (2012)

[84] J. Goodman, "Introduction to Fourier optics", Roberts and company publishers, PLACE (2005)

[85] M. Mori, "Discovery of the double exponential transformation and its developments", Publ. RIMS, Kyoto Univ.,41, 897-935 (2005)

[86] M. Brunel, H. Shen, S. Coëtmellec, D. Lebrun, K. Ait Ameur, "Phase contrast metrology using digital in-line holography: general models and reconstruction of phase discontinuities", J. Quantitative Spectroscopy and Radiative Transfer, 126, 113-121 (2013)

[87] M. Brunel, S. Coëtmellec, G. Gréhan, H. Shen, "Interferometric out-of-focus imaging simulator for irregular rough particles", J. Europ. Opt. Soc. Rap. Public., 9, 14008 (2014)

[88] N. Verrier, C. Rémacha, M. Brunel, D. Lebrun, S. Coëtmellec, "Micropipe flow visualization using digital in-line holographic microscopy", Opt. Express, Vol. 18, Iss. 8, 78077819 (2010).

[89] N. Verrier, S. Coëtmellec, M. Brunel, D. Lebrun, A. J. E. M. Janssen, "Digital in-line holography with an elliptical, astigmatic Gaussian beam: wide-angle reconstruction", J. Opt. Soc. Am. A, 25, 1459-1466 (2008)

[90] W. Xu, M.H. Jericho, H.J. Kreuzer, I.A. Meinertzhagen, "Tracking particles in four dimensions with in-line holographic microscopy", Opt. Lett., 28, 164-166 (2003)

[91] W. Yang, A. B. Kostinski, R. A. Shaw, "Phase signatre for particle detection with digital in-line holography", Opt. Lett., 31, 1399-1401 (2006)

[92] F. Dubois, C. Schockaert, N. Callens, C. Yourassowsky, "Focus plane detection criteria in digital holography microscopy by amplitude analysis", Opt. Express, 14, 5895-5908 (2006)

[93] C. Remacha, "Étude et développement d'un dispositif d'holographie numérique pour la mesure de taille de gouttes dans les tours aéroréfrigérantes", Ph.D. Thesis, University of Rouen (2012)

[94] H. Wang, A. Qin, M. Huang, "Autofocus method for digital holographic reconstruction of microscopic object", Symposium on Photonics and Optoelectronics, 1-4 (2009)

[95] R. Feng, R. J. Farris, "Influence of processing conditions on the thermal and mechanical properties of SU8 negative photoresist coating", Diamond and rRelated Materials, 8, 1607-1610 (1999)

[96] W. J. Tango, "The circle polynomials of Zernike and their application in optics", Appl. Phys., 13, 327-332 (1977)

[97] H. Meng, G. Pan, Y. Pu, S. H. Woodward, "Holographic particle image velocimetry: from film to digital recording", Meas. Sci. Technol., 15, 673-685 (2004)

[98] W. Yang, A. B. Kostinski, R. A. Shaw, "Depth-of-focus reduction for digital in-line holography of particle fields", Opt. Lett., 11, 1303-1305 (2005)

[99] F. Dubois, N. Callens, C. Yourassowsky, M. Hoyos, P. Kurowski, O. Monnom, "Digital holographic microscopy with reduced spatial coherence for three-dimensional particle flow analysis", Appl. Opt., 45, 864-871 (2006)

[100] S. H. Lee, Y. Roichman, G. R. Yi, S. H. Kim, S. M. Yang, A. van Blaaderen, P. van Oostrum, D. G. Grier, "Characterizing and tracking single colloidal particles with video holographic microscopy", Opt. Express, 15, 18275-18282 (2007)

[101] N. Salah, G. Godard, D. Lebrun, P. Paranthoën, D. Allano, S. Coëtmellec, "Application of multiple exposure digital in-line holography to particle tracking in a Benard-von Karman vortiex flow", Meas. Sci. Technol., 19, 1-7 (2008)

[102] L. Dixon, F. C. Cheong, D. G. Grier, "Holographic particle-streak velocimetry", Opt. Express, 19, 4393-4398 (2011)

[103] D. Lebrun, L. Méés, D. Fréchou, S. Coëtmellec, M. Brunel, D. Allano, "Long time exposure digital in-line holography for 3-D particle trajectography", Opt. Express, 21, 23522-23530 (2013)

[104] W. Wichitwong, S. Coëtmellec, D. Lebrun, D. Allano, G. Gréhan, M. Brunel, "Long exposure time digital in-line holography for the trajectoography of micronic particles within a suspended millimatric droplet", Opt. Commun, 326, 160-165 (2014)

[105] S. Coëtmellec, W. Wichitwong, G. Gréhan, D. Lebrun, M. Brunel, A. J. E. M. Janssen, "Digital in-line holography assessment for general phase and opaque particle", Opt. Commun, 326, 160-165 (2014)

[106] E. Wolf, "Three-dimensional structure determination of semi-transparent objects from holographic data", Opt. Commun, 1, 153-156 (1969)

[107] E. Stoykova, F. Yaras, A. O. Yontem, H. Kang, L. Onural, P. Hamel, Y. Delacrétaz, I. Bergoënd, C. Artire, C. Depeursinge, "Optical reconstruction of transparent objects with phase-only SLMs", Opt. Express, 21, 28246-28257 (2013)